T.C. İSTANBUL KÜLTÜR UNIVERSITY
INSTITUTE OF GRADUATE STUDIES

SEISMIC RESPONSE OF SEISMICALLY ISOLATED STRUCTURES WITH TRIPLE FRICTION PENDULUM BEARINGS

Masters of Applied Science Thesis

Ismail Iyal ADAMU

1700004538

Department: Civil Engineering

Programme: Structural Engineering

Supervisor: Assist. Prof Dr. Gökhan YAZICI

AUGUST 2019

T.C. İSTANBUL KÜLTÜR UNIVERSITY
INSTITUTE OF GRADUATE STUDIES

SEISMIC RESPONSE OF SEISMICALLY ISOLATED STRUCTURES WITH TRIPLE FRICTION PENDULUM BEARINGS

Masters of Applied Science Thesis

Ismail Iyal ADAMU

1700004538

Date of Submission: 2 September 2019

Date of defence examination: 2 August 2019

Supervisor and Chairperson:
Assist. Prof Dr. Gökhan YAZICI
Members of Examining Committee:
Assist. Prof Dr. Erdal COŞKUN
Assoc. Prof Dr. Sami And KILIÇ (Boğaziçi University)

AUGUST 2019

ACKNOWLEDGEMENT

I would like to express my sincere appreciation to Assist. Prof. Dr. Gökhan YAZICI for his guidance, time and patience throughout thesis meetings. I would also like to thank my family for their support and encouragement throughout my whole life.

University : **İstanbul Kültür University**
Institute : **Institute of Graduate Studies**
Department : **Civil Engineering**
Programme : **Structural Engineering**
Supervisor : **Assist. Prof. Dr. Gökhan YAZICI**
Degree Awarded and Date : **MSc Thesis - August 2019**

ABSTRACT

SEISMIC RESPONSE OF SEISMICALLY ISOLATED STRUCTURES WITH TRIPLE FRICTION PENDULUM BEARINGS

Ismail Iyal Adamu

Seismic isolation is an earthquake resistant design approach used to modify the natural period of a structure to make it less responsive to earthquake ground motions. This study investigates the seismic response of structures isolated with triple friction pendulum isolation bearings. Firstly, the working principles of seismic isolation and the design principles of isolation bearings are explained. This is followed by the evaluation of the design procedures for seismically isolated structures in TBDY 2019 and ASCE 7-16. The reductions in base shear, story shear, floor accelerations and interstory drifts for a model isolated structure in comparison to fixed base values, as well as the hysteresis loops for triple friction pendulum bearings were evaluated for 10 far-field and 11 near-field ground motions with magnitudes $6.5 \leq M \leq 7.1$. The finite element models for the fixed based and the isolated model structures were created and analyzed using OpenSEES. Moreover, the effect of variation of TFP surfaces friction coefficient on base shear and isolator displacement were also studied through a parametric study.

Keywords: Seismic Isolation, Triple friction pendulum system, OpenSEES, Seismic Response, Earthquake Resistant Design

Science Code: 624.03.01

Üniversite	**:**	**İstanbul Kültür Üniversitesi**
Enstitüsü	**:**	**Lisansüstü Eğitim Enstitüsü**
Anabilim Dalı	**:**	**İnşaat Mühendisliği**
Programı	**:**	**Yapı Mühendisliği (İngilizce)**
Tez Danışmanı	**:**	**Assist. Prof. Dr. Gökhan YAZICI**
Tez Türü ve Tarihi	**:**	**Yüksek Lisans – Ağustos 2019**

KISA ÖZET

ÜÇLÜ SÜRTÜNMELİ SARKAÇ MESNETLİ SİSMİK YALITIMLI YAPILARIN DEPREM YÜKLERİ ALTINDA DAVRANIŞI

Ismail Iyal Adamu

Sismik yalıtım, yapının doğal titreşim periyodunu değiştirmek suretiyle deprem hareketlerinden daha az etkilenmesini amaçlayan bir depreme dayanıklı tasarım yaklaşımıdır. Bu çalışmada, üçlü sürtünmeli sarkaç mesnetlerine oturan yapıların deprem yükleri altında davranışı incelenmektedir. İlk olarak, sismik yalıtımın çalışma prensipleri ve sismik yalıtım mesnetlerinin tasarım prensipleri açıklanmıştır. Bunu takiben, TBDY 2019 ve ASCE 7-16 yönetmeliklerinin sismik yalıtımlı yapılar için öngördüğü tasarım prosedürleri değerlendirilmiştir. Sismik yalıtımlı bir model yapı için taban kesme kuvveti, kat kesme kuvvetleri, kat ivmeleri ve kat ötelemelerinin sabit tabanlı durum için elde edilen değerlere göre azalımı ve üçlü sürtünmeli sarkaç mesnetlerinin histeresis çevrimleri, büyüklükleri $6.5 \leq M \leq 7.1$ arasında değişen 10 uzak fay ve 11 yakın fay deprem için değerlendirilmiştir. Sabit tabanlı ve sismik yalıtımlı yapı modellerinin sonlu eleman modelleri OpenSEES yazılımı aracılığıyla oluşturulmuş ve analiz edilmiştir. Buna ek olarak, üçlü sürtünmeli sarkaç mesnetlerinin dış kayma yüzeylerindeki sürtünme katsayısındaki değişimin taban kesme kuvveti ve izolatör yer değiştirmelerinin üzerindeki etkileri parametrik bir çalışmayla incelenmiştir.

Anahtar Kelimeler: Sismik İzolasyon, Üçlü Sürtünmeli Sarkaç Sistemi, OpenSEES, Deprem Yükleri Altında Davranış, Depreme Dayanıklı Tasarım

Bilim Dalı Sayısal Kodu: 624.03.01

TABLE OF CONTENTS

LIST OF FIGURES

LIST OF TABLES

LIST OF ABBREVIATIONS

SGIA: Sabiha Gökçen International Airport

ASCE: American Society of Civil Engineers

PGA: Peak Ground Acceleration

PGV: Peak ground velocity

MFPS: Multi-Friction Pendulum Structures

SLE: Service Level Earthquake

DBE: Design Based Earthquake

MCE: Maximum Considered Earthquake

FEMA: Federal Emergency Management Agency

NHERP: National Earthquake Hazards Reduction Program

TSC: Turkish Building Code

OPENSEES: Open System for Earthquake Engineering Simulation

TFP: Triple Friction Pendulum

PEER: Pacific Earthquake Engineering Research Centre

PTFE: Polytetrafluoroethylene

SFP: Single Friction Pendulum

SEAONC: Structural Engineers Association of Northern California

UBC: Uniform Building Code

AASHTO: American Association of State Highway and Transportation Officials

EPS: Earthquake Protection Systems

TCL: Tool Command Language

THA: Time History Analysis

LIST OF SYMBOLS

a_1, a_2, a_3, a_4: Bearing rate parameter (sec/m)

A_b : Bonded rubber area (m^2)

b: Shortest plan dimension (m)

β: Damping ratio

β_s, β_b: Superstructure and base damping ratio

B_D, B_M: Design and maximum damping correction factor

c_s, c_b: Superstructure and base damping coefficients

C: Damping coefficient

d: Longest plan dimension (m)

d: Friction pendulum displacement capacities (m)

d_1, d_2, d_3, d_4: Friction pendulum displacement capacities 1, 2, 3 and 4 (m)

D_D, D_M: Design and maximum displacement (m)

D_{TD}, D_{TM}: Total design and total maximum displacement (m)

D: Bearing displacement (m)

e: Eccentricity (m)

ε: separation parameter

E_c: Bearing compressive modulus (MPa)

E_c: Concrete elastic modulus (MPa)

E_s: Steel elactic modulus (MPa)

Es: Structure energy (kN.m)

Ed: Dissipated energy (kN.m)

Ek: Kinetic energy (kN.m)

Ee: Elastic strain energy (kN.m)

Ev: Viscous damping energy (kN.m)

Eh: Hysteretic damping energy (kN.m)

EDC: Energy dissipation circle (kN.m)

g: Acceleration due to gravity m/s^2

F: Lateral force (kN)

F_f: Frictional force (kN)

F_s: Story force (kN)

F_a, F_v: Site coefficients for short and 1s period spectral acceleration

G: Shear modulus (MPa)

h_x: Story height (m)

h_1, h_2, h_3 h_4: Friction pendulum height 1, 2, 3 and 4 (m)

h: Friction pendulum height (m)

k_s, k_b: Superstructure and base stiffness (kN/m)

k: Lateral force distribution correction coefficient

K: Stiffness (kN/m)

K_d: Bearing stiffness (kN/m)

K_{eff}: Effective bearing stiffness (kN/m)

K_D, K_D: Design and maximum stiffness (kN/m)

K_H , K_v: Bearing horizontal and vertical stiffness (kN/m)

m_s, m_b: Superstructure and base mass (kg)

M: Mass of structure (kg)

η_D, η_M: Design and maximum damping correction factor

φ: Mode shape

θ: Sliding bearing angle (rad)

P_T: The effective translational period (s)

ρ_c: Mass per unit volume concrete (kg/m)

ρ_c: Mass per unit volume steel (kg/m)

σ_{yb}: Bearing yield strength (MPa)

σ_y: Yield strength (MPa)

σ_c: Compressive strength (MPa)

Q: Bearing characteristic force strength (kN)

R: Friction pendulum radius (m)

R_{eff}: Effective pendulum bearing (m)

R_1, R_2, R_3 R_4: Friction pendulum radius 1, 2, 3 and 4 (m)

R_{eff1}, R_{eff2}, R_{eff3} R_{eff4}: Friction pendulum radius 1, 2, 3 and 4 (m)

R: Modification Factor

R_I: Modification factor

S_{ae}: Spectral acceleration (m/s^2)

S_D, S_M: Design and maximum spectral acceleration (g)

S_s: Spectral acceleration at short period (s)

S_1: Spectral acceleration at 1s (s)

S_{D1}, S_{M1}: Design and maximum spectral acceleration at 1s (m/s^2)

S_1, S_2, S_3, S_4: Sliding plate surface 1, 2, 3 and 4

S: Shape factor

t_r : The total thickness of rubber (m)

T: Period (s)

T_d: Bearing period (s)

T_{eff}: Effective bearing period (s)

T_D, T_M: Design and maximum structural period (s)

μ_1, μ_2, μ_3, μ_4: Friction coefficient 1, 2, 3 and 4 (m)

$\ddot{u}_t$: Total acceleration (g)

$\ddot{u}_r$: Relative acceleration or structural acceleration (g)

$\ddot{u}_g$: Ground motion acceleration (g)

$\dot{u}$: Relative velocity (m/s)

u: Relative displacement (m)

μ: Friction coefficient

V_D, V_M: Design and maximum base shear (kN)

V_{st}: Total unreduced shear-force of structure above the base level (kN)

V_S : Total reduced shear force on elements above the base level (kN)

ω: Natural frequency (rad/s)

ω_s, ω_b: Superstructure and base mass (rad/s)

w: Effective weight of the structure above the isolation (kN)

w_x: Story weight (kN)

W_s: Effective weight of the structure above the isolation excluding base level (kN)

x: Level (m)

y: Distance between centre of rigidity to plan corner (m)

γ: Mass ratio

CHAPTER 1

INTRODUCTION

1.1 Background

Isolation, by definition, involves the separation or the reduction of interaction between two or more objects. In the context of a seismic design, "seismic isolation" is essentially the separation of the structure from the ground with a flexible layer to mitigate damaging effects of earthquake strong ground motion. The study of seismic isolation systems for structures dates back to 1885 when an Englishman John Milne constructed the system for a replica building model in Tokyo that incorporated ball bearings and dished cast iron plates [1]. Modern seismic isolation systems as well as the analysis and design procedures outlined in design codes used today are products of decades of research, field reports, and advances in bearing manufacturing and testing technologies. Recently, there are hundreds of seismically isolated buildings in United States, Japan and China [2]. Countries such as Turkey, Chile, Greece and Italy are also adopting the use of seismic isolation to protect important structures such as hospitals, airports and historical buildings.

1.2 Seismic Isolator Applications in Turkey

In 1999 a high magnitude earthquake hit Kocaeli, Turkey causing considerable damages to residential and industrial structures [3]. This traumatic event brought awareness and triggered the need of earthquake proof structures in anticipation of future seismic events. Isolators in Turkey are majorly used in hospitals, airports and historical buildings. Examples of the large-scale isolated projects include Adana Integrated Health Campus, Isparta City Hospital, Sabiha Gökçen International Airport. Other applications of seismic isolated structures in Turkey are briefly listed in [4]–[10].

Adana Integrated Health Campus in Figure 1.1 was constructed in 2017 at the city of Adana South-East region of Turkey. This partly medical, rehabilitation and psychiatric health centre was the second largest isolated building in the world having an area of 430,000m^2 and supported by a total of 1512 base isolators [11][12].

Figure 1.1: Adana Integrated Health Campus [11]

Isparta City Hospital Figure 1.2 was built in 2016 in the city of Isparta. The building is use for medical purpose, also it is mentioned to be among the largest isolated buildings in the world with an area of approximately 221,000m^2 which is supported by 903 frictional pendulum isolators [13].

Figure 1.2: Isparta City Hospital [14]

Sabiha Gökçen International Airport Figure 1.3 is the second airport in Istanbul finished in 2001. SGIA is a steel structure of 200,000m^2 in area categorized among the largest isolated structure with 296 frictional pendulum isolators. The airport terminal serves for both international and domestic flights [15].

Figure 1.3: Sabiha Gökçen International Airport [15]

1.3 General

Seismic isolation is one of the techniques used to mitigate damages and loss of lives due to earthquake strong ground motion. Although, the use of seismic isolation systems may increase the initial construction cost of a structure, enhanced seismic performance of the structure can decrease the direct and indirect financial losses in addition to providing life safety. Seismic retrofitting of existing structures with isolator systems provide similar economic advantages [16]. Seismic isolation systems work by increasing the vibration period of the structure beyond the fundamental period of the earthquake ground motion, thereby reducing the amplification of the inertial loads due to resonance effect [17][18][19][20]. Seismic isolation systems modify the natural period of a structure by making the structure more flexible.

Rigid structures are more prone to seismic effects; more rigidity causes more force resistance. Normally rigid structures have a period very close to zero because when earthquake ground motion is excited on them, acceleration due to inertial forces is same as the ground motion acceleration of the structures however flexible structures generally have longer period which are on average greater than 2s, having very low transmitted acceleration making the building to stay at almost stationary with very minimal inter-story drift [21]. Figure 1.4 shows the behaviour of the isolated and fixed based structure during earthquake, the isolated based structure is shown to have no direct contact with the ground which makes it less prone to seismic effect. The increase in period reduces the acceleration, inter-story drift and story shear amount to an acceptable and safe value. The reduction of acceleration keeps the structure in the elastic or nearly elastic range [22].

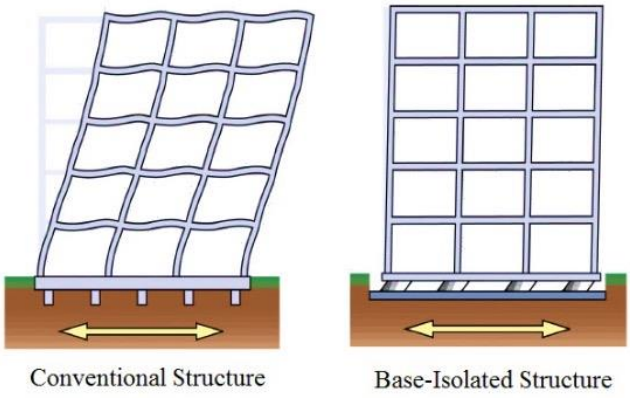

Figure 1.4: Behavior of Isolated and Fixed Based Structures [23]

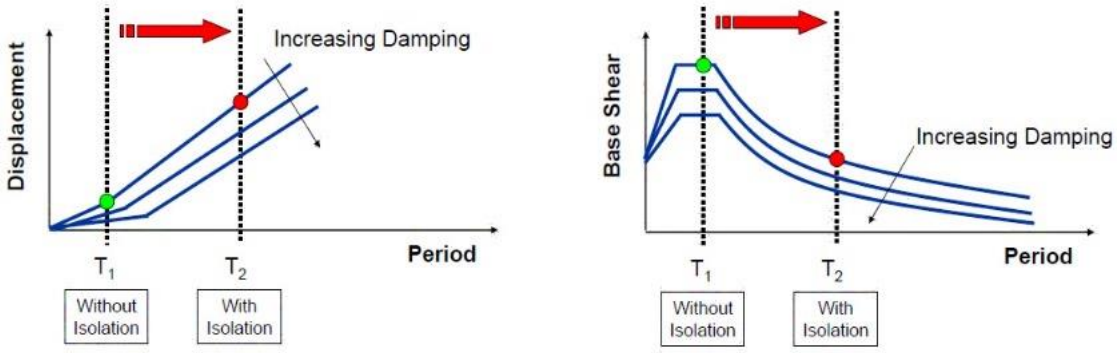

Figure 1.5: Isolated and Fixed Based Structure Displacement and Base Shear [17]

Decrease in accelerations reduces non-structural damages and the decrease in inter-story drift makes both structural and non-structural element damage less. In Figure 1.5, while isolators decrease acceleration, the displacements of the isolation increase. Increasing damping decreases the maximum displacement of the isolation system [24]. Lessening of the displacements by the dampers in isolated system is effective but it may lead to an increase in floor acceleration and story drifts because the dampers transfer energy to the higher modes which in-return increase their responses and negate the effect of base isolation. Highly damped systems with more than 20% damping may cause increase in drifts and shear forces of base isolated buildings, but if dampers of lower ratio are used displacement will be reduced and will not increase floor accelerations and story drifts to higher values [25].

1.4 Literature Review

This literature review investigates some studies made by researchers on the effects of seismic isolation systems on structures. In [21] an existing 15 story moment frame shear wall hospital building in Izmir was examined, model same as the original was designed with isolators introduced to the foundation. Efficiency assessment was performed on isolated model and the original fixed model with inter-storey drift ratio and floor accelerations as controlling parameters. The models were analysed using response spectrum and fast non-linear analysis, the results conclude that the drift inter drift ratio and peak floor accelerations values obtained from the isolated building system are far less from the limitations specified. Furthermore, similar analysis was performed on a 10- story and 5-story building having same condition with the previous analysed building which yields similar result. Sap2000 analysis on a regular and irregular planned 5-storey reinforced concrete school building with high damped rubber isolation system designed to a capable period (Td) of 2.10 sec, maximum capable period (Tm) of 2.50 secs and damping ratio of 15%. The lateral stiffness of base isolators, lateral displacements, rubber bearing mechanical parameters, bearing dimension were all designed according to ASCE code. For each building plan, isolated and fixed base structural models were drawn to make a comparative analysis. The result of this analysis shows a high increase in period between the isolated and non-isolated structure. Also, the base shear forces and moments values were significantly deduced due to decoupling of the structure from the ground. Moreover, the story displacements of the isolated structure were more than the displacements of the fixed base structure which can be eliminated using other techniques [26].

Near-fault studies in [27]–[29] suggest that for intense and high pulse motions supplementary dampers are vital in reducing the excess story displacements although they might increase the acceleration and drifts of the structure. Studies by [19] using 3D non-linear analysis stated that after using isolator the building period was increased from 0.58 to 2s and the variables calculated were found to be within the safety limits. Furthermore, the isolator reduced the effects of the earthquake to the building by about 70% and base shear force was reduced by 32%. The acceleration of the building was also examined, fixed base acceleration values have reach 1.0 g level and it increase as the story height increase, whereas in the base isolator situations the acceleration values do not increase with the change in storeys height. Moreover, in [15] 108 story skyscraper studies concluded that, seismic isolation will not be of advantage to high-rise structures or where wind load is more critical than the earthquake load and added that for fixed based structures with long period, introducing seismic isolation system will not be of much effect to the performance of the building under seismic action. Darama states that the period of a fixed based structure should be lower than 2 seconds for seismic isolation to be effective. Studies from [18][30][31] also gave similar conclusion on the effect of isolation system on structures. Multiple friction pendulum scaled shake table test in [32] under a severe earthquake of 1.047g in PGA (1940 El Centro earthquake) shows the maximum roof acceleration was merely up to 0.396g. Further experiments were performed under Kobe and TCU084 Chi-Chi earthquakes, the results from tests show that the MFPS isolator can mitigate the acceleration response in the range of 70 to 90 percent. Triple friction pendulum bearing in Istanbul Sabiha Gökçen international airport terminal met and surpassed the performance objectives under DBE and MCE design while achieving an 80% reduction in the base shear relative to the fixed-base building model, it significant decrease 83% and 90% of the story drift and floor acceleration. Analysis on all types of frictional pendulum in [33] shows significant decrease in base shear, maximum story drift. Triple friction bearing reduced the most among the three types of pendulum due to is more adaptive behaviour. Another analysis [34] compares double and triple friction pendulum at different ground motions, triple friction pendulum outperforms the double friction pendulum for small PGAs but yields opposite outcome for higher PGAs records. In conclusion, friction pendulum bearings efficiencies depend on the conditions of their application.

1.5 Thesis Structure

Chapter 2 presents basic knowledge of seismic isolation system components and their characteristics. In conclusion, the design procedures for seismic isolation systems are briefly stated based on ASCE, TSC2019, FEMA and NHERP guidelines.

In chapter 3 the geometry, sections and materials details of research analysis model are presented. Also, the chapter shows the lateral static design analysis of ASCE7-16 and TSC2019. Section 3.5.1 and 3.5.2 discusses ground motion selection with acceleration and displacement plots in time history analysis. Also, acceleration response spectra plot and matching of spectrums to site response spectrum were presented.

Chapter 4 discusses the results from analyses in chapter 3. Time history analysis comparison of story force, acceleration, and inter-story drift between fixed and TFP isolated structure on OpenSees. Furthermore, checking ground motions force-displacement bilinear model and their compliance with TFP isolator total effective displacement of regimes. Lastly, examining the effect of friction coefficient due to material change and contamination of outer and inner surfaces on base shear and isolator displacement.

Chapter 5 provides concluding remarks on thesis findings.

Appendix A presents the design of TFP.

CHAPTER 2

SEISMIC ISOLATION

2.1 Ideology of Seismic Isolation

An insight on the response of seismically isolated structures can be obtained by studying the behaviour of a simple 2-DOF isolated building model shown in Figure 2.1. The structural elements were assumed to be linearly elastic and within the linear viscous damping. The stiffness and damping were estimated by an equivalent linearization process.

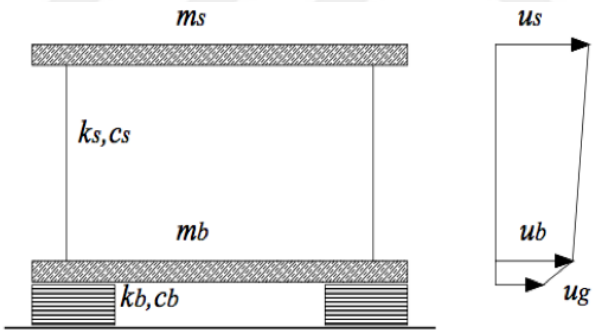

Figure 2.1: Two degree of freedom model for isolated system [35].

This model and equations are summaries from [35][36], The result of the analysis was expressed in terms of relative displacements and absolute acceleration. The base and superstructure angular frequencies ω_s, ω_b are calculated by equations (2.1) and (2.2).

$$\omega_s = \sqrt{\frac{k_s}{m_s}} \tag{2.1}$$

$$\omega_b = \sqrt{\frac{k_b}{(m_s + m_b)}} \tag{2.2}$$

A square ratio of the two frequencies gives the separation parameter (ε) mainly ranging from 0.1 to 0.01. Also, division of the superstructure mass with the summation of base mass and superstructure mass gives the mass ratio (γ). This mass ratio generally has a value below 1. Damping β_s, β_b for the superstructure and base system are computed using equations (2.3) and (2.4).

$$\beta_s = \frac{c_s}{2m_s\omega_s} \tag{2.3}$$

$$\beta_b = \frac{c_b}{(2\omega_b\,(m_s+m_b))} \tag{2.4}$$

c_s and c_b are the damping coefficients for superstructure and base structures. The natural vibration periods and modes of the system can be determined by matrices in equations (2.5) and (2.6).

$$M = \begin{bmatrix} m_b & 0 \\ 0 & m_s \end{bmatrix} \tag{2.5}$$

$$K = \begin{bmatrix} k_b + k_s & k_s \\ k_s & -k_s \end{bmatrix} \tag{2.6}$$

The frequencies can be obtained by the determinant of equation (2.7) and substitution for M and K matrices.

$$det\ |k - \omega_n^2\, m| \tag{2.7}$$

Mode deformation shape during structural motion is computed in equation (2.8);

$$|k - \omega_n^2 m|\ \varphi_n = 0 \tag{2.8}$$

2.2 Isolation System Performance

To achieve a good functioning seismic isolation system one has to consider if the isolation is necessary to begin with. [23] states that (a) isolators work better when the weight of the structure is large (b) the period of the structure before isolation should be less than 1s, and (c) the structure is founded on stiff soil. Moreover, [30] study summarized some of the key points necessary to achieve good performance from a seismic isolation system. The isolator should have low lateral resistance for better flexibility, in addition sufficient rigidity is needed to resist unnecessary movements due to wind for good serviceability. Furthermore, good vertical rigidity and good tension resistance are important to prevent bulging in the case of rubber bearings and to resist uplifting.

2.3 Elastomeric Rubber Bearings

Elastomeric bearings are isolators typically made of natural rubber providing horizontal stiffness with reinforcing steel plates to resist vertical loads of a structure. Also, the steel plates prevent the bearing from bulging effect due to compressive force in Figure 2.2. These bearings are produced through a method called vulcanization. stiffness and damping of an elastomeric bearing depends very much on the vulcanization process with the elastomer.

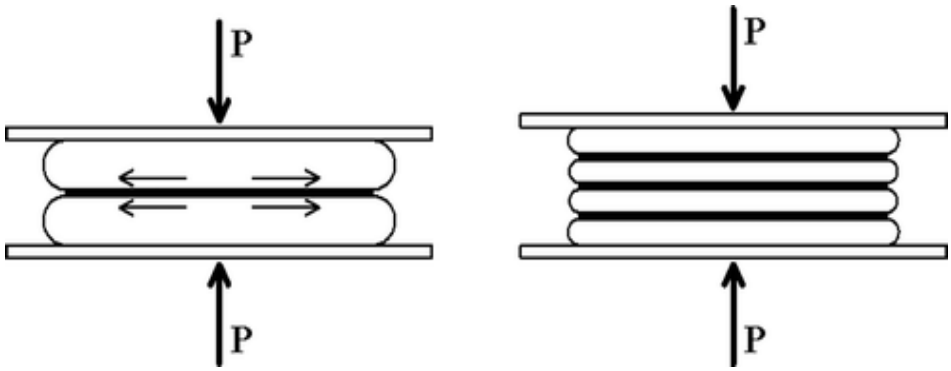

Figure 2.2: Elastomeric Bearing Bulging [37]

2.3.1 Low Damping Rubber Bearing

Low-damping natural rubber systems have very low damping ratios and they are generally used with additional damping devices unlike high-damping natural rubber bearings which have higher damping ratios. Low-damping natural rubber in Figure 2.3(a) exhibits approximately 150% shear strain with a nearly linear shear stress-strain behaviour before it stiffens to plasticity. Natural rubber with hardness of 50 is typically used for seismic applications having a shear modulus (G) that ranges from 0.65 MPa to 0.9 MPa. The equivalent damping ratio for low-damping natural rubber ranges between 2% and 3% at 100% shear strain [22].

2.3.2 High Damping Rubber Bearings

Energy dissipation in high-damping rubber bearings is achieved by special compounding of the elastomer. Damping ratios generally range between 7% and 14% of critical. The shear modulus of high-damping elastomers generally ranges between 0.35 MPa (50 psi) and 1.4 MPa (200 psi) [20].

2.3.3 Lead Rubber Bearings

Lead-rubber bearings differ from normal damped natural rubber bearings due to the presence of a lead plug in Figure 2.3(b) that is inserted at the centre of the bearing. The lead plug deforms plastically under shear deformation, enhancing the energy dissipation capabilities related to the rubber bearing.

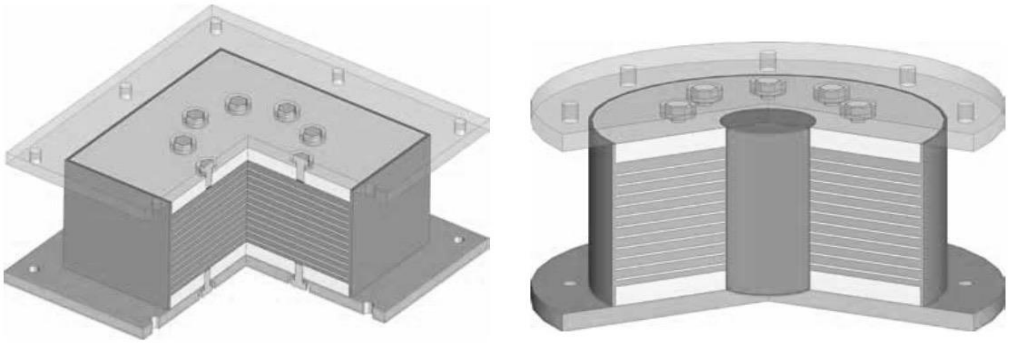

(a) (b)

Figure 2.3: (a) Damped Rubber Bearing (b) Lead Rubber Bearing [38]

2.4 Frictional Bearings

2.4.1 Single Friction Bearings

Single frictional pendulum is composed of a curved steel sliding surface and articulated slider made from steel. Energy dissipation (damping) is provided by friction (μ) between the composite bearing material and the stainless-steel overlay that is shown in the Figure 2.4(a) and 2.4(b). During an earthquake, the articulated slider moves on the surface along a displacement capacity *d*. The cause of friction is the materials mainly polytetrafluoroethylene (PTFE) and bimetallic sheets used on the sliders surface because it exhibits very good viscoelastic behaviour. Pendulum bearings are advantageous to use due to their restoring ability. Flat slider friction bearing has no restoring ability and do not return to initiation point after sliding but can used in combination with elastomeric bearings [39].

(a) (b)

Figure 2.4: (a) Flat Slider Bearing [40] (b) Single Friction Pendulum [39]

2.4.2 Double Friction Pendulum

Second generation friction pendulum in Figure 2.5 has two (2) sliding surfaces S_1, S_2 with friction coefficients μ_1, μ_2. The pendulum dimension is composed of two radii R_1, R_2, heights h_1, h_2 and displacement capacities d_1, d_2 resulting to a total displacement of $d_1 + d_2$. This bearing can be design for two earthquake levels having different frictional coefficients μ_1, μ_2, radii R_1, R_2 and displacement capacities. DFP's primary advantage is the cost savings that can be achieved through their more compact size and adaptive behaviour [41]. Also, double friction pendulum bearing is more effective than triple friction pendulum under higher peak ground acceleration records [34].

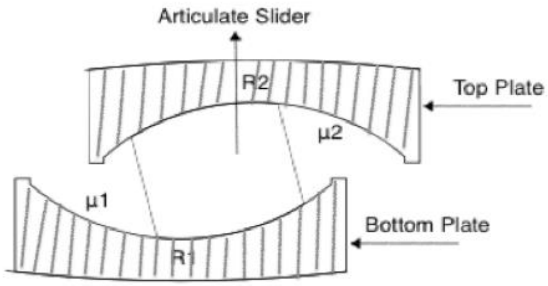

Figure 2.5: Double Friction Pendulum

2.4.3 Triple Friction Pendulum

Triple friction pendulum isolator Figure 2.6 is called third generation bearing because of being adaptive in its performance according to demand, displacement capacity and speed variation which prevents excessive variation in the friction coefficients [42]. Due to it is adaptive behaviour, triple friction pendulum application is wide and can be used in both near and far fault regions because of its different hysteretic properties at different stages of displacement. Its adaptive behaviour provides solutions for uncertain performance of seismic isolations systems under near-field ground motions [43]. Triple pendulum isolator eliminates the use of supplementary dampers in the case of near-field excitation due to its adaptive behaviour and variation in friction which reduces acceleration and displacements in an efficient-balance manner. The major benefit of this triple friction isolator is that, it enables the system to be optimized for multiple performance objectives in terms of different motions and hazard levels [41]. [32] mentioned that the main aim of developing multi-frictional isolators including triple friction pendulum is to improve the durability and upgrade the earthquake-proof capability of the traditional SFP isolator under near-source excitations and strong ground motions with long predominant periods. Triple friction pendulum also depends on its load capacity, sliding regimes, frictions, bearing displacement and ground excitation condition. Triple friction pendulum is composed of four (4) sliding surfaces, two inner surfaces S_1, S_2which are the smallest and two outer surfaces S_3, S_4 with friction coefficients μ_1 μ_2 μ_3 μ_4. Also, the pendulum dimensions are characterized by radii R_1, R_2, R_3 and R_4, heights h_1, h_2, h_3 and h_4, displacement capacities d_1, d_2, d_3 and d_4. Generally, the dimension of the isolator is designed to have similar values, sliding surfaces 2 and 3 are equal (R_2=R_3 and d_2=d_3) also sliding surfaces 1 and 4 (R_1=$R_4$and d_1 = d_4).

It is not must for the dimension parameters to be equal, they can differ according to their application conditions.

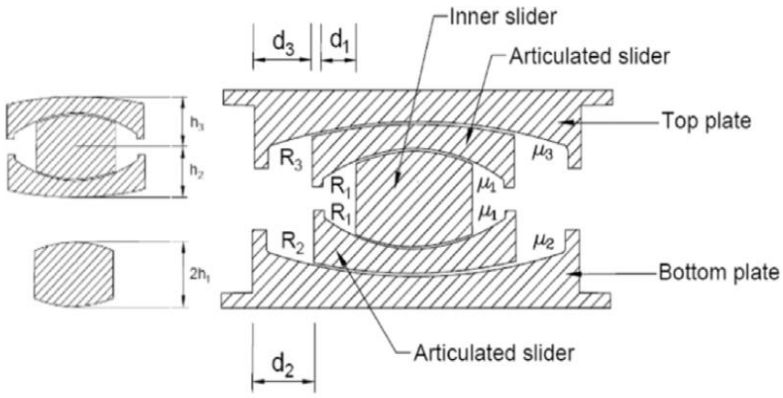

Figure 2.6: Triple Friction Pendulum [44]

2.5 Friction of PTFE Coating Material

Polytetrafluoroethylene (PTFE) is plastic material that is commonly used and worked on friction pendulum bearing interface providing the necessary friction needed for dissipation. The material has a diameter generally larger than 250mm, AASHTO 1999 recommends that the material should at least be 1.66m after compression. Also, non-corrosive bimetallic filler materials can be used together with PTFE to increase friction of bearing (e.g bronze, lead and stainless steel). The friction efficiency of PTFE material is affected by velocity, pressure, temperature and contamination. The friction coefficient of PTFE on steel is 0.02-0.03 for slow sliding rates. Typical seismic velocities and pressures in bridge bearings increases friction coefficient to a values of 0.10-0.15 depending on lubrication [45].

2.5.1 Effect of Pressure on Velocity and Friction

Coulomb friction model is often used in mathematical representation of friction coefficient but friction bearing interface is velocity dependent. Figure 2.7 is a function of the maximum and minimum friction values at ambient temperature (20^{o}C) throughout the range of velocity at a certain normal pressure value on the surface. Prior to sliding, the static friction force linked with static coefficient of friction must be overcome. Once the sliding starts the friction force drops to a minimum value then rises at higher velocities values until it steadies at the maximum friction force.

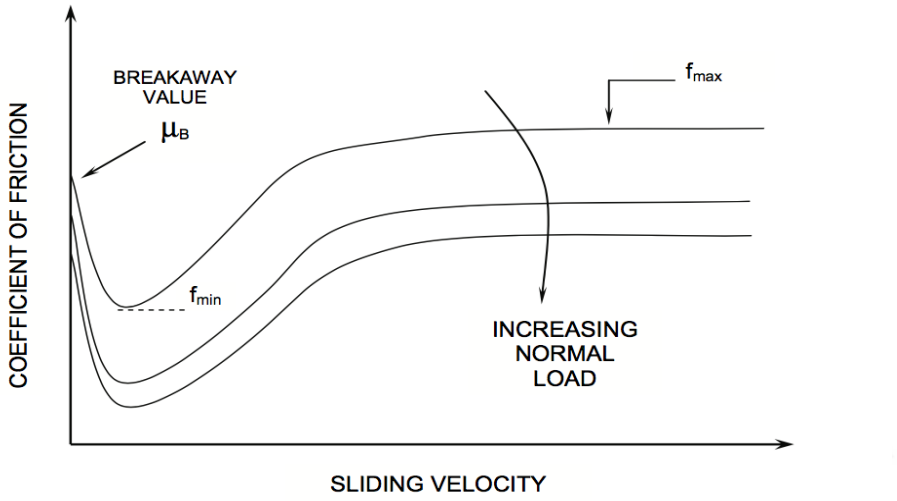

Figure 2.7: Friction coefficient of PTFE-polished stainless steel [45]

Increase in interface pressure leads to decrease in friction coefficient. This decrease in friction coefficient is mostly due to compression of the interface material. Summarized from [20], friction coefficient change due to pressure is computed in equation (2.9).

$$\mu = \frac{F}{N} = \frac{SA_r}{P_r A_r} = \frac{S_o}{P_r} + \alpha \tag{2.9}$$

where S is the shear strength of the interface in equation (2.10), P_r is the pressure over the real area of contact, A_r is the area of contact dependent to the deformation level and α correction constant.

$$s = s_o + \alpha P_r \tag{2.10}$$

2.5.2 Effect of Temperature on Velocity and Friction

During sliding, the interface material (PTFE) temperature on the surface providing friction resistance change from the normal ambient temperature. This heating effect is due to shear of friction material surface which causes deformation and directly affect the roughness. The change in temperature in Figure 2.8 shows that friction coefficient increases at temperatures below 20^{o}C.

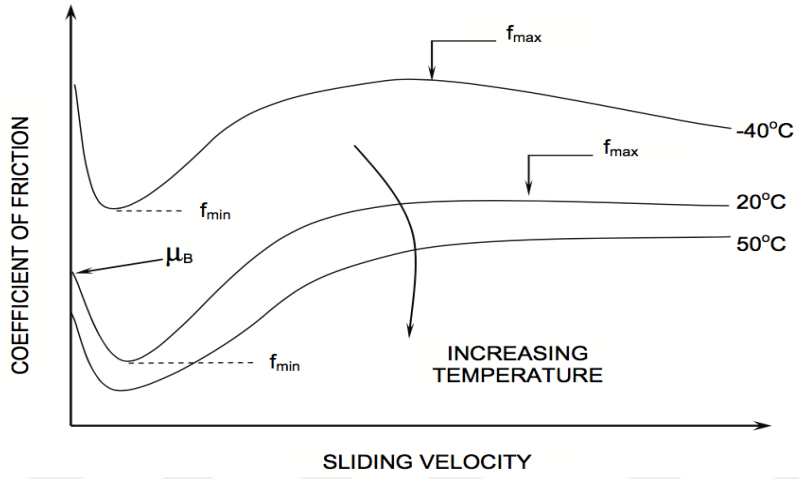

Figure 2.8: Friction coefficient of PTFE-polished stainless steel [20]

2.5.3 Effect of Contaminant on Friction

Contamination of the sliding bearing interface causes increase in friction by other component of friction due to third body effects and due to abrasion of the stainless steel. This change in mechanical property is reduced or eliminated by rubber sealing of the whole bearing and downward installation of the stainless-steel surface with the friction material. Friction bearings are unlikely to be contaminated in the sliding interface unless the bearing is disassembled at the construction site before installation or the bearing is sealed wrongly [47][48]. Moreover, double and triple friction bearings may contaminate debris slowly after a time even when sealed based on the condition and their upward installation of stainless-steel surfaces containing the interface.

2.6 Mechanical Behaviour of Isolation Systems

2.6.1 Viscous Behaviour

Viscous behaviour force dissipation is proportional to velocity and performance of a damper within the elastic limit Figure 2.9(a). Viscous damping is an ideal and convenient type of damping to handle mathematically which is used in the fundamental solution of differential equation of a motion. This force is zero at the maximum displacement and therefore does not contribute to the effective stiffness of the isolation system.

2.6.2 Hysteretic Behaviour

This behaviour is mostly realized during deformation of solids when the friction between the internal planes shear as the material deforms which mostly illustrates the inelastic portion of the structural when the elasticity of the structures is lost Figure 2.9(b). This behaviour deals with the cracking and breaking portion of the structure. The force-displacement relation of the isolator may be approximated by a bilinear curve.

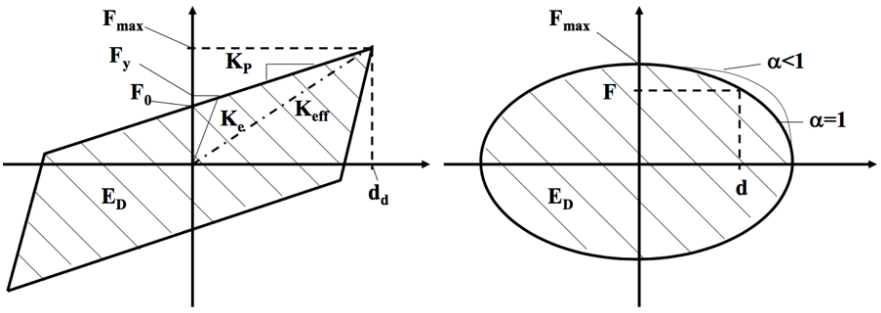

(a) (b)

Figure 2.9: (a) Hysteretic (b) Viscous Behavior [45]

Most of the seismic design are force and displacement considered. However, earthquake is in fact an energy originated event. From [19] summary, the energy concept is more fundamental phenomenon to think about because forces and displacements arise as consequences of this energy. Energy of an earthquake should be equal to the sum of energy stored within the structure (E_S) and the dissipated energy (E_d) in equation (2.11) to (2.13).

$$E = E_s + E_d \tag{2.11}$$

$$E_s = E_k + E_e \tag{2.12}$$

$$E_d = E_v + E_h \tag{2.13}$$

Where E is the total energy of the structure or work done by the structure counteracting the shear force by ground motion. The structure actualizes this storage by converting the earthquake energy into kinetic energy (E_k) and elastic strain energy (E_e) during its swinging. The amount of energy dissipated by the structure (E_d) has two components, called viscous damping energy (E_V) and hysteretic damping energy (E_h). Earthquake within the elastic limit has low intensity, in this case the total structural energy or work done should be summation of energy stored within the structure (E_S) and viscous damping energy (E_V) in equation (2.14).

$$E = E_e + E_k + E_v \tag{2.14}$$

For high intensity earthquake (exceeds elastic limits) the total structural energy is the summation of energy stored within the structure (E_S), viscous damping energy (E_V) and hysteretic damping energy (E_h) because high intensity earthquakes causes damages.

2.7 Code Design of Seismic Isolators

The seismic isolation design requirement was founded by the Structural Engineers Association of Northern California (SEAONC), this design requirement is later modified and used in uniform building code (UBC) in 1986 which is the first official code for seismic Isolation design. The (SEAONC) guidelines book emphasis that the equivalent lateral-force analysis and seismic demand level are required for design, in the recent American code of seismic isolation design, a structure is analysed using response spectrum or time history analysis the results most be checked with equivalent lateral-force method [1][2].

2.7.1 Static Design

The forces and minimum displacements are calculated with formulas derived based on constant velocity assumption [1]. The displacement of the structure is classified into three levels; (D_D) design displacement which is DBE dependent, total design displacement (D_{TD}) and (D_{TM}) as the total maximum displacement dependent to MCE. Static analysis is necessary to give idea on the minimum criteria for design. Static analysis is efficient without further analysis according to [48] if ;

a) Structure is located at a site with soil coefficient < 0.60g determined by checking the spectral acceleration maps.
b) Soil classification is between A-D.
c) Structures height above the isolation plane is less than 65 feet (19.812m) or less than 5 stories.
d) Isolated system effective period at maximum displacement T_M should not exceed 3.0 seconds
e) Effective design period displacement T_D is three times greater than the elastic period of the fixed-base structure.
f) Superstructure plane is regular.
g) Effective stiffness at design displacement of the isolation system has a value that is greater than 1/3 of the effective stiffness at 20% of design displacement.
h) Isolation system has a restoring force required by code.
i) Isolation system force deflection properties are not dependent to the rate of loading.
j) Effect of the isolation system to maximum capable earthquake (MCE) displacements does not lessen the S_{M1}/S_{D1} times the total design displacements.

2.7.2 Linear Equivalent Static Design Procedure

According to codes, linear analysis on structures is needed to know the preliminary design requirements. This seismic isolated static analysis method is given in FEMA 365 [49], 2009 NHERP [50], ASCE 7-16 [51] and TSC2019 [52].

Turkish Code (TSC 2019):

Turkish design code for isolator design is like ASCE 7-05/10 with some additional coefficient from Eurocode.

- Design Displacement

  Equation (2.15) is the design displacement (D_D) of seismic motion in which (S_{ae}), serves as the spectral acceleration and (η_D), (η_M) in equation (2.16) represents the correction factor for damping.

$$D_D = 1.3\left[\frac{g}{4\pi^2}\right]T_D^2\eta_D S_{ae} \tag{2.15}$$

$$\eta_D, \eta_M = \sqrt{\frac{10}{5+\zeta}} \tag{2.16}$$

  Where,

  ζ =damping ratio.

- Period at the Design Displacement

  (T_D) in equation (2.17) is the design structural period which is proportional to the design stiffness (K_D) and angular frequency (ω).

$$T_D = 2\pi\sqrt{\frac{\omega}{K_D g}} \tag{2.17}$$

- Maximum Displacement

  (D_M) in equation (2.18) is the design displacement of seismic motion in which (S_{ae}), serves as the design spectral acceleration and (η_M) is the maximum considered correction factor for damping.

$$D_M = 1.3\left[\frac{g}{4\pi^2}\right]T_M^2\eta_M S_{ae} \tag{2.18}$$

- Period at the Maximum Displacement

  Equation (2.19) represents the maximum structural period (T_M) which is proportional to the Maximum stiffness (K_M) and angular frequency (ω).

$$T_M = 2\pi\sqrt{\frac{\omega}{K_M\, g}} \tag{2.19}$$

- Total Displacement

  The total design displacement (D_{TD}) and the total maximum displacement (D_{TM}) of components of the isolation system in equation (2.20) and (2.21) includes additional displacement due to actual and accidental torsion.

$$D_{TD} = D_D \left[1 + y\frac{12e}{b^2 + d^2}\right] \tag{2.20}$$

$$D_{TM} = D_M \left[1 + y\frac{12e}{b^2 + d^2}\right] \tag{2.21}$$

  Where;

  e = eccentricity

  y = distance between centre of rigidity to plan corner

  b = shortest plan dimension

  d = longest plan dimension

- Lateral Forces

  Equation (2.22) and (2.23) calculates the (V_D), (V_M) the shear forces above the isolator with modification factor R as the denominator factor.

$$V_D = \frac{S_{ae}.W.\eta_D}{R} \tag{2.22}$$

$$V_M = \frac{S_{ae}.W.\eta_M}{R} \tag{2.23}$$

The story lateral force (F_s) is distributed over the height (x) of the structure above the isolation interface using equation (2.24).

$$F_s = \frac{V_D\, w_x\, h_x}{\sum_i^n w_i\, h_i} \tag{2.24}$$

American Code ASCE 7-16:

- Design Displacement

  This is the minimum lateral earthquake displacement (D_D) in equation (2.25) that isolator should resist,

$$D_D = \left[\frac{g}{4\pi^2}\right]\frac{S_{D1}T_D}{B_D} \tag{2.25}$$

Where (S_{D1}) is are the design spectral response acceleration parameter at 1s, (B_D) is the design damping ratio factors at design level in Table 2.1.

Table 2.1: Design and Maximum Damping Correction Ratio Factor [50]

B_D, B_M	B_D, B_M
0.8	≤ 2%
1.0	5%
1.2	10%
1.35	15%
1.5	20%
1.7	30%
1.9	40%
2.0	≥50%

- Effective Period at the Design Displacement

  The effective period (T_D) of an isolated building equation (2.26) at the design displacement is determined using (K_D) design stiffness of the isolation system.

$$T_D = 2\pi\sqrt{\frac{W}{K_D\, g}} \tag{2.26}$$

- Maximum Displacement

  The maximum displacement of the isolation system (D_M) equation (2.27) represents the most critical direction of horizontal response.

$$D_M = \left[\frac{g}{4\pi^2}\right]\frac{S_{M1}T_M}{B_M} \tag{2.27}$$

- Effective Period at the Maximum Displacement

  Equation (2.28), The effective period (T_M) of the isolated building at the maximum displacement is determined using (K_M) maximum stiffness of the isolation system.

$$T_M = 2\pi\sqrt{\frac{W}{K_M\, g}} \tag{2.28}$$

- Total Displacement

  Equations (2.29) and (2.30) represents the total design displacement (D_{TD}) and the total maximum displacement (D_{TM}) of components of the isolation system shall include additional displacement due to actual and accidental torsion calculated considering the spatial distribution of the effective stiffness of the isolation system at the design displacement and the most disadvantageous location of mass eccentricity.

$$D_{TD} = D_D\left[1 + \left(\frac{y}{P_T^2}\right)\frac{12e}{b^2 + d^2}\right] \tag{2.29}$$

$$D_{TM} = D_M \left[1 + \left(\frac{y}{P_T^2}\right) \frac{12e}{b^2 + d^2}\right] \quad (2.30)$$

Where;

e = eccentricity

y = distance between centre of rigidity to plan corner

b = shortest plan dimension

d = longest plan dimension

P_T = The effective translational period of the isolation system to the effective to torsional period of the isolation system ratio normally taken as a value less than 1.0

Total maximum displacement value (D_{TM}) should be ≥ 1.15 D_M provided that the isolation system is shown by calculation to be configured to resist torsion.

- Lateral Forces

The superstructure shear force V_{st} in equation (2.32) computes the shear force above the isolator. The foundation, and all other structural components and elements below the isolation system shall be designed and constructed to withstand a minimum lateral seismic force, V_b in equation (2.31).

$$V_b = K_D D_D \quad (2.31)$$

$$V_{st} = V_b \left(\frac{W_s}{W}\right)^{(1-2B_m)} \quad (2.32)$$

The value of V_s shall be computed with equation (2.33),

$$V_S = \frac{V_{st}}{R_I} \tag{2.33}$$

R_I is the response modification factor value required for design of the structure above the isolation system. The shear force, V_s, shall be distributed over the height of the structure above the isolation interface with equation (2.34).

$$F_x = \frac{V_s w_x h_x^k}{\sum_i^n w_i h_i^k} \tag{2.34}$$

At each level designated as *x*, the force F_x shall be applied over the area of the building in accordance with the weight, w_x, distribution at that level, h_x and *k* is story force distribution correction parameter.

2.8 Dynamic Design

Dynamic analysis is a conservative analysis that gives results according to the behaviour of the seismic ground motion. Based on ASCE code, dynamic Analysis is necessary if the period at maximum displacement of the structure (T_M) is greater or equal 3.0 seconds, the soil class is E or F, the structure located is within 6.2 miles (10km) of active fault and the period at design displacement (T_D) is three times greater than the elastic fixed base period of the structure above isolators [1].

2.8.1 Response Spectrum Dynamic Design

Normally, response spectrum analysis is used to design a superstructure which essentially remains elastic for design earthquake ground motions. The acceleration value of response spectrum depends mainly on the seismic design category and site-soil class. These parameters give the short period (S_s) and 1s period (S_1) acceleration [53]. Figure 2.10 shows the response spectrum design curve.

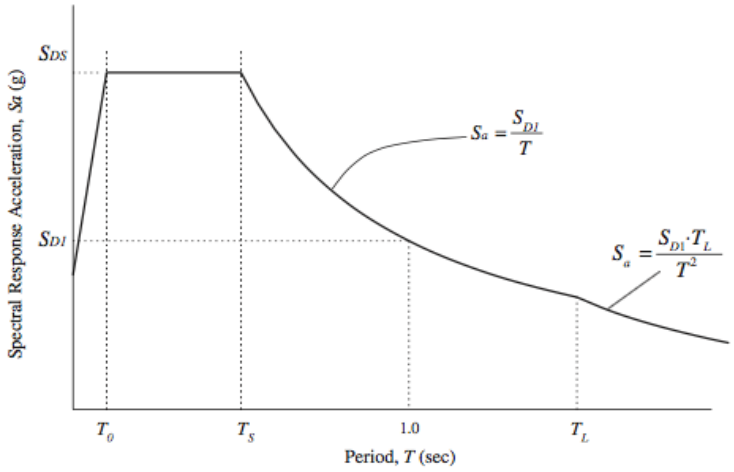

Figure 2.10: Design Response Spectrum [54]

Isolated structures modal response spectrum analysis should have damping equivalent to the lesser value between effective damping of the isolation system or 30% of critical. To determine the total design displacement and total maximum displacement of the structure, 100% of the motion should be used in the most critical excitation direction and 30% of it in the perpendicular axis. Moreover, If the total design displacement (D_{TD}) determined by response spectrum analysis is found to be less than the value in equivalent linear static analysis or the total maximum displacement (D_{TM}) determined by response spectrum analysis is found to be less than the value of (D_{TM}), response analysis parameters are increased to (D_{TD}) value, or the (D_{TM}) value [55].

Service Level Earthquake (SLE)

Service level earthquake is the least earthquake design level use in design analysis. During motion, the structures are considered not to have any damages but displacements of non-structural elements may be expected [55]. An SLE has 50% probability of being exceeded in 30 years or 43-year return period [56]. This level is included in design to account for the smallest acceleration value needed to activate the isolator. It is a very important level in the design of frictional pendulum isolators. Service level earthquake is approximately about 50% - 60% of Design level earthquake in [57].

Design Basis Earthquake (DBE)

This earthquake is used in preliminary design phase of isolator displacement and resistance. Design base earthquakes have 10% probability of being exceeded in 50 years or 475-year return period [56][58]. The earthquake motions at the design stage may cause fixable damages to the structure and human injuries. This design performances value in equation (2.35) and (2.36) gives the engineer an idea on the behaviour of the structure to be expected.

$$S_{Ds} = \frac{2}{3} F_a S_s \quad (2.35)$$

$$S_{D1} = \frac{2}{3} F_v S_1 \quad (2.36)$$

F_a and F_v are site coefficients given in Table 2.3 and 2.4.

Maximum Capable Earthquake (MCE)

The maximum capable earthquake level calculated in equation (2.37) is the level which has 2% probability of ground motion exceeding 50 years or 2475-year return period[49][55]. This level is for final design analysis of the structure for protection of both the structure and the non-structural materials.

The displacement at (MCE) level is the average of peak values calculated from seven nonlinear response history analyses records according to ASCE/SEI 7-10 and ASCE/SEI 7-16 standards. The maximum considered earthquake motions may cause permanent structural damages and loss of lives.

$$S_M = \frac{3}{2} S_D \quad (2.37)$$

Table 2.2: Short period site class coefficient [53]

Site Class	$S_s \leq 0.25$	$S_s = 0.5$	$S_s = 0.75$	$S_s = 1.0$	$S_s \geq 1.25$
A	0.8	0.8	0.8	0.8	0.8
B	1.0	1.0	1.0	1.0	1.0
C	1.2	1.2	1.1	1.0	1.0
D	1.6	1.4	1.2	1.1	1.0
E	2.5	1.7	1.2	0.9	0.9

Table 2.3: 1s period site class coefficient [53]

Site Class	$S_1 \leq 0.1$	$S_1 = 0.2$	$S_1 = 0.3$	$S_1 = 0.4$	$S_1 \geq 0.5$
A	0.8	0.8	0.8	0.8	0.8
B	1.0	1.0	1.0	1.0	1.0
C	1.7	1.6	1.5	1.4	1.3
D	2.4	2.0	1.8	1.6	1.5
E	3.5	3.2	2.8	2.4	2.4

2.8.2 Response History Dynamic Design

Response history analysis is based on direct ground motion records recorded by site seismogram, this analysis is used mainly for maximum structural design [60]. Ground motions are applied to the structure to see the displacement and other structural parameter values for the design. Response history design analysis requires no less than three design based scaled ground motion records with each having two horizontal and a vertical component for uplift check and the maximum response of three motion is used for design [55]. If seven or more ground motion records are used for response history analysis, the average of all responses of the parameter shall be used for design.

2.9 Isolators Characteristic Design

2.9.1 Rubber Bearings.

The stiffness parameter (K) and characteristic force strength (Q) are the important aspects of rubber bearing design, the horizontal stiffness (K_H) provided by the rubber is good in resisting shear forces. The vertical stiffness (K_v) is resisted by the steel shims between rubbers which confines the isolator together and stops bulging effect. General design according to AISC code in Figure 2.11 and equations (2.38) to (2.52) were summarized from studies [22][23][45] and FEMA 365.

$$K_H = \frac{GA_r}{T_r} \tag{2.38}$$

G is the shear modulus, T_r as the total thickness of rubber and A_B is the bonded rubber area. The compressive modulus (E_c) in equation (2.39) due to weight of the structure changes according to the shape factor (S) of the bearing.

$$E_c = 6GS^2 \tag{2.39}$$

The dimensionless geometric parameter shape factor (S) of a single rubber layer of a bearing can be computed by equation (2.40).

$$S = \frac{A_L}{A_b} \tag{2.40}$$

Vertical stiffness and horizontal stiffness are mathematically proportional.

$$K_v = \frac{E_c A_r}{T_r} = \frac{6GS^2 A_r}{T_r} = 6S^2 K_H \tag{2.41}$$

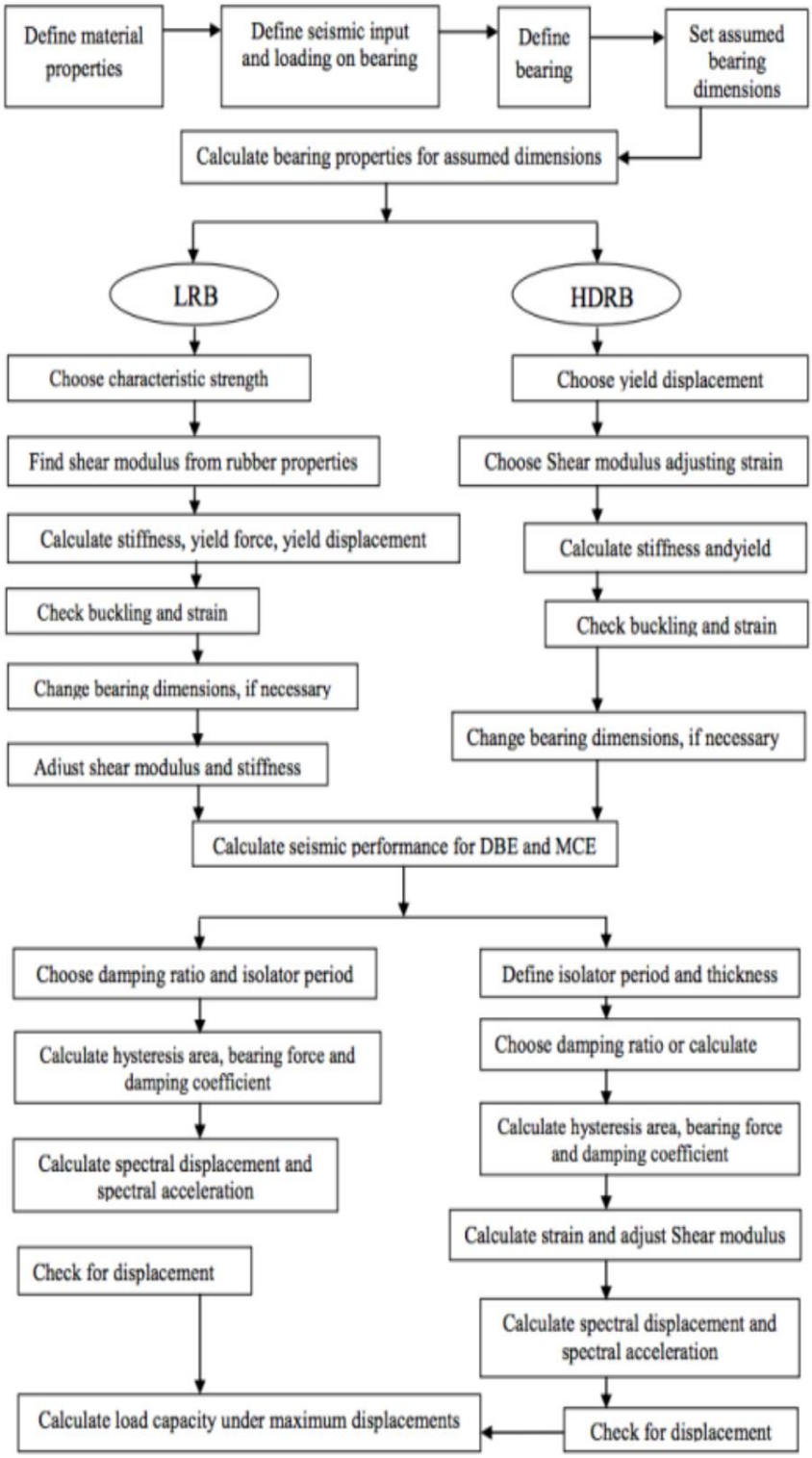

Figure 2.11: Design process of rubber bearings [23]

Lead rubber bearing stiffness (K_{HL}) equation (2.42) and damped rubber bearing stiffness (K_H) have similar equations except for the Force (Q_d) from the yield strength of the lead in equation (2.43) where, (d) is the horizontal of the lead.

$$K_{HL} = K_H + \frac{Q_d}{d} \tag{2.42}$$

$$Q_d = \left(\frac{\pi D^2}{4}\right) \sigma_{yb} \tag{2.43}$$

2.9.2 Frictional Pendulum Bearings.

Single friction pendulum isolator design involves few process and computation presented in Table 2.4 by AASHTO 1999 recommended specification [20]. The sliding interface material and thickness is chosen to achieve effective friction, the thickness of the steel plate is selected to resist the applied loads by providing necessary characteristic stiffness. Friction isolators have a normal pendulum like behaviour Figure 2.12 with a lateral force (F) needed to impose a lateral displacement (u) in equation (2.48). The frictional force (F_f) at the sliding interface is expressed as friction coefficient (μ) multiplied by weight of the structure (W) equation (2.47). The frictional pendulum isolator depends on the friction coefficient of the sliding surface for dissipation.

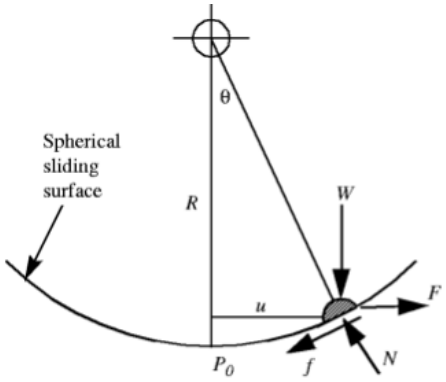

Figure 2.12: Friction pendulum free body diagram [61]

Table 2.4: AASHTO 1999 specification for friction pendulum bearing design [20]

	Recommendation
I.	The thickness of interface sheet (mostly PTFE material) should be at least 1.6 mm after compression for effectiveness.
II.	The stainless-steel sliding surface should be smoothened to a high degree of reflectivity with little to no roughness. AASHTO (1999) recommends that the arithmetic average (R_a) surface roughness should be ≤ 0.8 micrometres after finishing. This roughness limit is set for well friction sheet lining.
III.	The stainless steel should preferably be of type 316 conforming to ASTM A240 American code. This stainless-steel selection is important to avoid corrosion of the bearing.
IV.	The stainless-steel sliding plate thickness should be ≥1.5 mm for surfaces having a maximum dimension of <300 mm and ≥2.3 mm for surfaces having a maximum dimension <900 mm. Plates with higher dimensions' thickness should be verified by testing of full-size bearings at representative loads and velocities.
V.	Materials that are not corrosion-resistant are recommended not to be in contact with non-metallic liner materials. Materials that are not corrosion resistance may hinder with the frictional coefficients.
VI.	Lubricated bearings should be of PTFE and concave. The diameter of the concave region should be ≤ 8mm and a depth < 2mm. Also, the region should cover 20 to 30 percent of the PTFE surface. The lubricant should be silicone grease that is effective at very low temperatures.

$$T_d = 2\pi\sqrt{\frac{R}{g}} \tag{2.44}$$

$$T_{eff} = 2\pi\sqrt{\frac{W}{g\,K_{eff}}} \tag{2.45}$$

Effective and normal period of friction pendulum isolator are calculated by equation (2.44) and (2.45). Sliding angle (*θ)* for small values is defined in equation (2.46) where *D* is the bearing top displacement.

$$\theta = \frac{D}{R-h} \tag{2.46}$$

where, R-h is the effective radius of a curvature (R_{eff}) of the sliding surface.

$$F_f = \mu W \tag{2.47}$$

$$F = \frac{W}{R} D + \mu W \tag{2.48}$$

Dividing equations (2.47) and (2.48) by displacement (D), the normal and effective stiffness of the friction pendulum is derived from equation (2.49) and (2.50).

$$K_d = \frac{W}{R} \tag{2.49}$$

$$K_{eff} = \frac{W}{R} + \frac{\mu W}{D} \tag{2.50}$$

Energy dissipation per force-displacement cycle (E.D.C) is provided in equation (2.51)

$$EDC = 4\mu WD \tag{2.51}$$

Effective damping (β) is given in equation (2.52)

$$\beta = \frac{EDC}{2\pi K D^2} \tag{2.52}$$

These listed equations above also change with the type of friction pendulum used, sliding angle (θ) changes when displacement increases and the amount of sliding plates in the case of triple friction pendulum isolators. Refer to [62][41] for further design procedures.

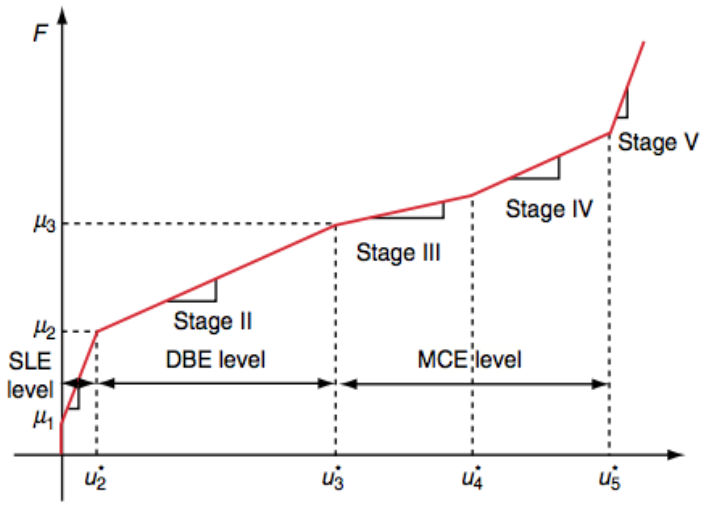

Figure 2.13: Triple Friction Pendulum Design Stages [57]

Triple frictional pendulum design is not as direct as the design of a single pendulum, it takes five stages to reach the maximum design displacement Figure 2.10. Each stage has its specific design displacements in Figure 2.13. The stage I is designed according to service level earthquake (SLE) having ground acceleration of 50% of DBE, II stage is designed to undergo a displacement of design base earthquake (DBE), stage III/IV are designed according to maximum considered earthquake displacement (MCE) which is 150% of DBE, and stage V is aimed to cover for displacements above MCE [34][57]. Refer to Appendix A for triple frictional pendulum design.

Fenz and Constantinou behaviour models is based on the forces on the free body diagram of each slider plate in Figure 2.15. The theory is characterized by friction coefficients μ_1 μ_2 μ_3 μ_4, radii R_1, R_2, R_3 and R_4, heights h_1, h_2, h_3 and h_4 and displacement capacities d_1, d_2, d_3 and d_4. Five (5) main motion Transitions (I II III IV and V) in Figure 2.14 formulated in Table 2.5. This formulation is according to assumptions;

1. friction coefficient($\mu_2 = \mu_3 < \mu_1 < \mu_4$),
2. surface radii (R_{eff1}=R_{eff4}>> R_{eff2}=R_{eff3})
3. Displacement capacities $d_2 > (\mu_1 - \mu_2)R_{eff2}$, $d_3 > (\mu_4 - \mu_3)R_{eff3}$ and
4. $d_1 > (\mu_4 - \mu_1)R_{eff1}$

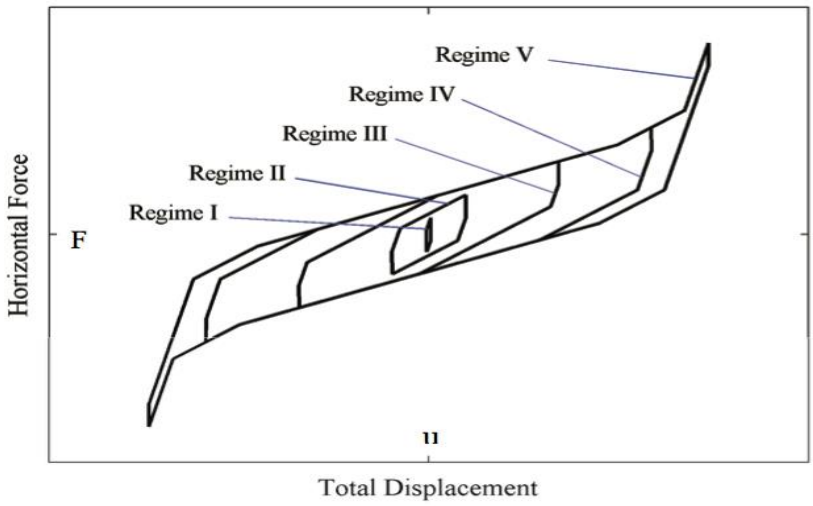

Figure 2.14: Triple Friction Pendulum Force-Displacement Hysteresis Loop [63]

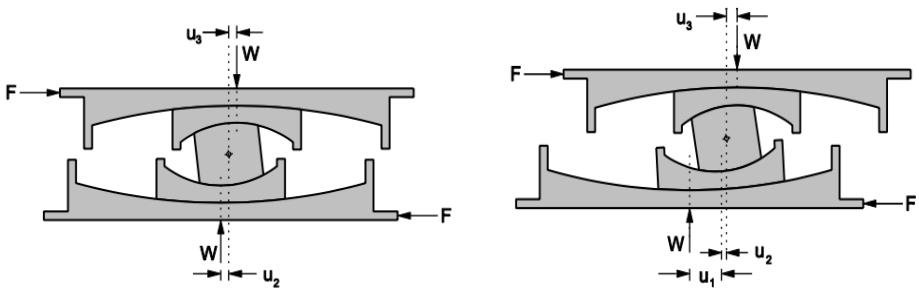

I II

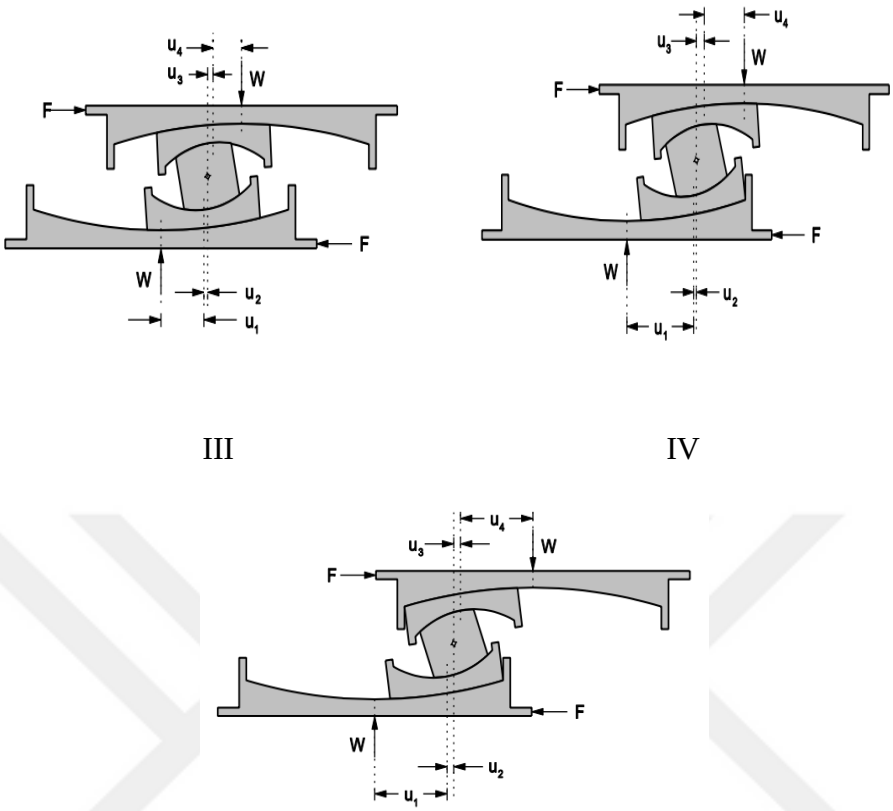

Figure 2.15: Triple Friction Pendulum Regimes [41]

Regime I

This is the stage where motion begins, this motion starts at the inner sliding plates 2 and 3 only. The motion starts when the horizontal excitation force F = F_{f2}= F_{f3}. Sliding stops when F = F_{f1} and when displacement (u^*) is reached.

Regime II

Sliding continuous on 3 and starts at surface 1 when F = $F_{f1}$and when the displacement (u^*) is reached. The motion continuous up to the second stage displacement (u^{**}) before stopping at F = F_{f4}.

Regime III

Sliding stops at surface 3, then sliding on surface 1 and 4 occurs when F = F_{f4} and displacement (u^{**}) is reached. At force F_{dr1} transition ends with displacement (u_{dr1}) upon reaching surface 1 restrainer.

Regime IV

When the motion hits surface 1 restrain a reactive force $F_{dr1}$is forms, the sliding continuous on surface 4 and starts at 2 at force F_{dr1} with displacement (u_{dr1}) ending it is transition at a total displacement u_{dr4} and corresponding force F_{dr4}.

Regime V

Upon hitting the surface 4 restrain, motion begins on surface 2 and 3 at displacement u_{dr4} and corresponding force F_{dr4}. The motion stops upon reaching design displacement $u_{max} > u_{dr4}$.

Table 2.5: Force-Displacement Equations [41]

Regime	Description	Force-Displacement Relationship
I	Sliding on surfaces 2 and 3 only	$F = \frac{W}{R_{eff2}+R_{eff3}}u + \frac{F_{f2}R_{eff2}+F_{f3}R_{eff3}}{R_{eff2}+R_{eff3}}$ *Valid until:* $F = F_{f1},\ u = u^{*} = (\mu_1-\mu_2)R_{eff2} + (\mu_1-\mu_3)R_{eff3}$
II	Motion stops on surface 2; Sliding on surfaces 1 and 3	$F = \frac{W}{R_{eff1}+R_{eff3}}u + \frac{F_{f1}(R_{eff1}-R_{eff2}) + F_{f2}R_{eff2} + F_{f3}R_{eff3}}{R_{eff1}+R_{eff3}}$ *Valid until:* $F = F_{f4},\ u = u^{**} = u^{*} + (\mu_4-\mu_1)(R_{eff1}+R_{eff3})$
III	Motion is stopped on surfaces 2 and 3; Sliding on surfaces 1 and 4	$F = \frac{W}{R_{eff1}+R_{eff4}}u + \frac{F_{f1}(R_{eff1}-R_{eff2}) + F_{f2}R_{eff2} + F_{f3}R_{eff3} + F_{f4}(R_{eff4}-R_{eff3})}{R_{eff1}+R_{eff4}}$ *Valid until:* $F = F_{dr1} = \frac{W}{R_{eff1}}d_1 + F_{f1},\ u = u_{dr1} = u^{**} + d_1\left(1+\frac{R_{eff4}}{R_{eff1}}\right) - (\mu_4-\mu_1)(R_{eff1}+R_{eff4})$
IV	Slider contacts restrainer on surface 1; Motion remains stopped on surface 3; Sliding on surface 2 and 4	$F = \frac{W}{R_{eff2}+R_{eff4}}(u-u_{dr1}) + \frac{W}{R_{eff1}}d_1 + F_{f1}$ *Valid until:* $F = F_{dr4} = \frac{W}{R_{eff4}}d_4 + F_{f4},\ u = u_{dr4} = u_{dr1} + \left[\left(\frac{d_4}{R_{eff4}}+\mu_4\right) - \left(\frac{d_1}{R_{eff1}}+\mu_1\right)\right](R_{eff2}+R_{eff4})$
V	Slider bears on restrainer of surface 1 and 4; Sliding on surfaces 2 and 3	$F = \frac{W}{R_{eff2}+R_{eff3}}(u-u_{dr4}) + \frac{W}{R_{eff4}}d_4 + F_{f4}$

Assumptions: (1) $R_{eff1} = R_{eff4} \gg R_{eff2} = R_{eff3}$, (2) $\mu_2 = \mu_3 < \mu_1 < \mu_4$, (3) $d_1 > (\mu_4-\mu_1)R_{eff1}$, (4), $d_2 > (\mu_1-\mu_2)R_{eff2}$
(5) $d_3 > (\mu_4-\mu_3)R_{eff3}$

Alternative triple friction pendulum model on software is series model, this model has three single friction pendulums connected in series characterize by three different radii R_1, R_2, R_3, friction coefficients μ_1, μ_2, μ_3 and displacement capacitiesd_1, d_2, d_3.

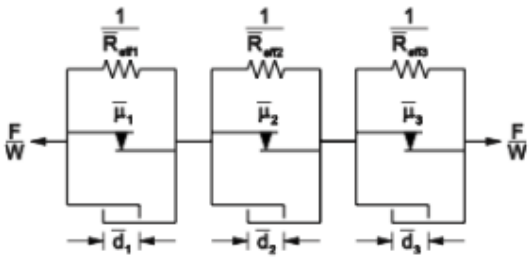

Figure 2.16: Triple Friction Pendulum series model [42]

[64] mentioned during their research that previous structural analysis software have no applicable hysteresis rules or nonlinear elements available that can be used to exactly model triple friction pendulum bearings for response-history analysis. Series model in Figure 2.16 is used in old versions of analysis software to characterize the behaviour of triple friction pendulum. Though, the behaviour of the triple friction pendulum is not exactly series arrangement of single concave friction pendulum however it is similar.

Table 2.6: TFP Conversion to Series Model Configuration [64]

	Coefficients of friction	Radii of curvature	Nominal displacement capacity	Rate parameter
Element 1	$\bar{\mu}_1=\mu_2=\mu_3$	$\bar{R}_{eff\,1}=R_{eff\,2}+R_{eff\,3}$	$\bar{d}_1=d_{tot}{}^{a}-(\bar{d}_2+\bar{d}_3)$	$\bar{a}_1=\frac{1}{2}\frac{(a_2+a_3)}{2}$
Element 2	$\bar{\mu}_2=\mu_1$	$\bar{R}_{eff\,2}=R_{eff\,1}-R_{eff\,2}$	$\bar{d}_2=\frac{R_{eff\,1}-R_{eff\,2}}{R_{eff\,1}}d_1$	$\bar{a}_2=\frac{R_{eff\,1}}{R_{eff\,1}-R_{eff\,2}}a_1$
Element 3	$\bar{\mu}_3=\mu_4$	$\bar{R}_{eff\,3}=R_{eff\,4}-R_{eff\,3}$	$\bar{d}_3=\frac{R_{eff\,4}-R_{eff\,3}}{R_{eff\,4}}d_4$	$\bar{a}_3=\frac{R_{eff\,4}}{R_{eff\,4}-R_{eff\,3}}a_4$

[a] Note: d_{tot} is the total displacement capacity of the actual bearing. Alternatively, parameter $\bar{d}_1$ may be left unspecified (infinite displacement capacity).

Fenz and Constantinou in Table 2.6 present modifications to convert triple friction pendulum isolator to series model, these parameters and additional gap link elements can be used to closely captures the hysteresis behaviour of triple friction pendulum in software like Sap2000.

CHAPTER 3

STRUCTURAL MODELLING

3.1 Model

The thesis analysis model is a simple four (5) story low-rise reinforced concrete residential building in Figure 3.1 located in Bakirkoy Istanbul, Turkey at coordinate 40.98116 and 28.886032 in Figure 3.4, with 10% probability of being exceeded in 50 years or 475-year return period and design spectrum and site parameters in Table 3.2.

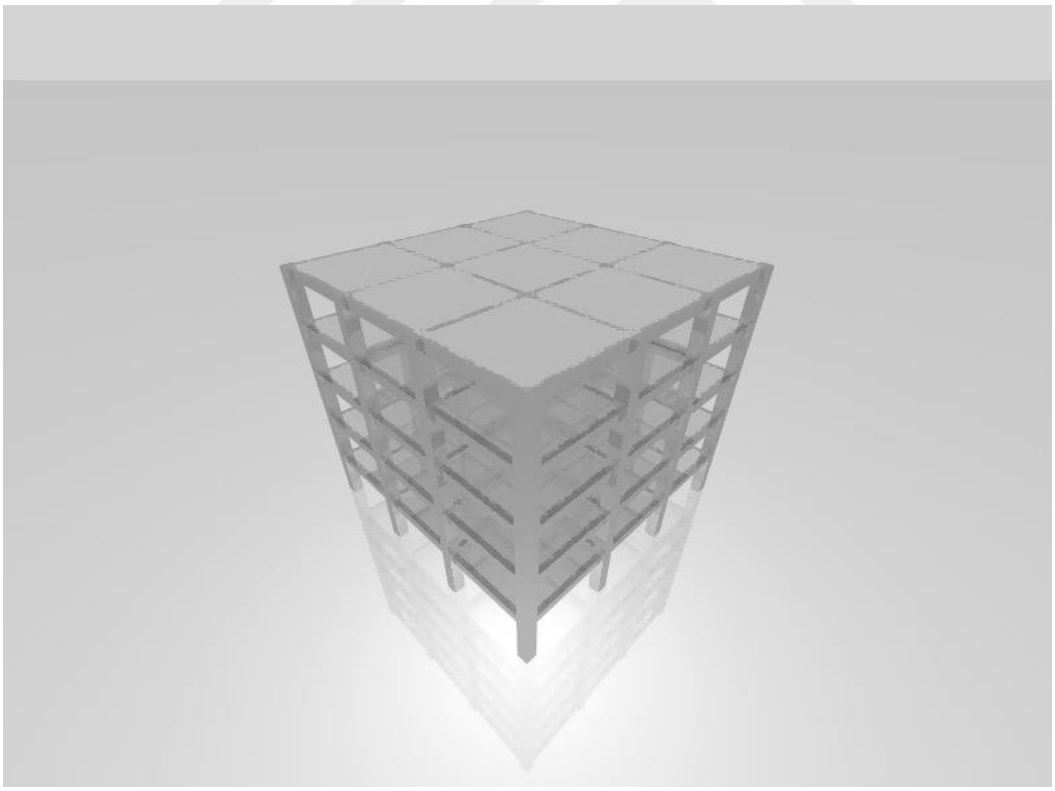

Figure 3.1: Structural Model

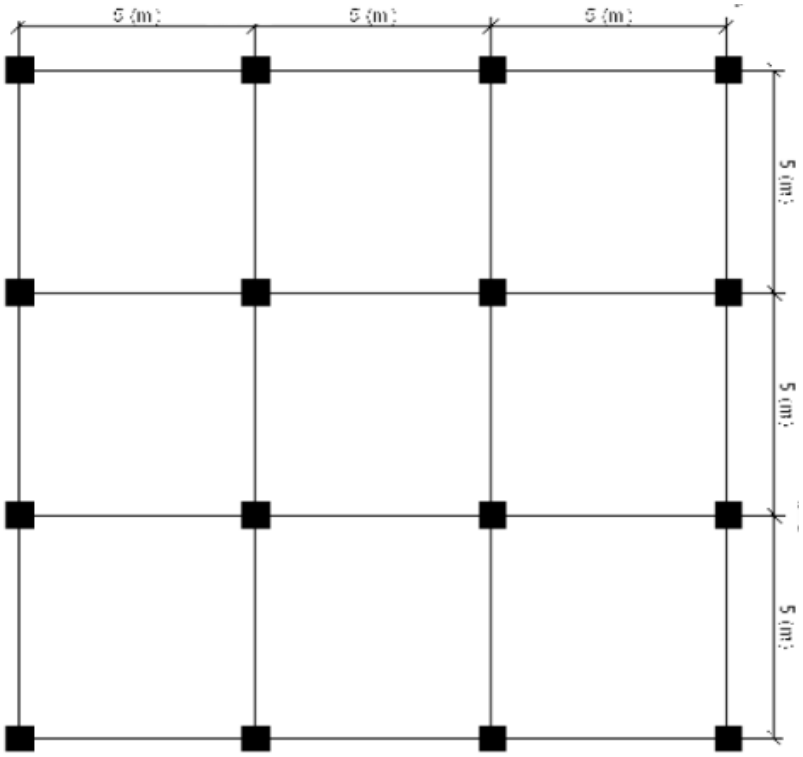

Figure 3.2: Geometric Plan X-Y

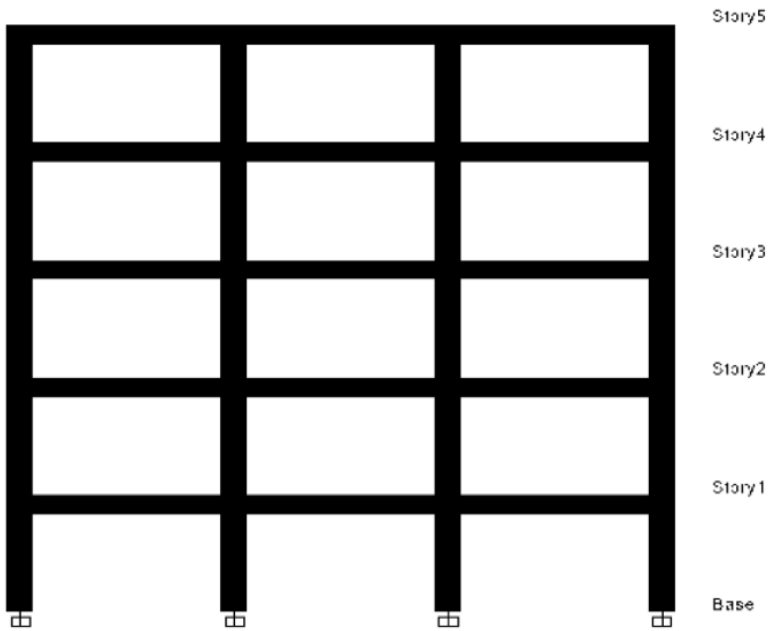

Figure 3.3: Geometric Plan X-Z

The building is designed according Turkish code (TSC2019) with geometrical plan dimension of 15m to x-axis, 15m to the y-axis and 15m to vertical axis in Figure 3.2 and Figure 3.3. The building has a slab thickness 0.15m connected to the elements in Table 3.1 compose of concrete with compressive strength (σ_c) of 25Mpa, mass per unit volume (ρ_c) of 2500kg/m and elastic modulus (E_c) of 31000Mpa. The steel reinforcement used has a yield strength (σ_y)of 250MPa, mass per unit volume (ρ_s) of 7850kg/m and elastic modulus (E_s) of 200000MPa.

Table 3.1: Structural Element Properties

Section Property	Dimension (m)	Cross-section Area(m)	Length (m)	Moment of Inertia y-axis (m4)	Moment of Inertia y-axis (m4)	Torsional Inertia (m4)	Self-weight factor
Column	0.6m x 0.6m	0.36	3	0.0108	0.0108	0.018252	1
Beam	0.5m x 0.3m	0.15	5	0.001125	0.003125	0.002817371	1

The structure is assigned a gravity load composed of dead load (assigned 2KN/m^2 + self-weight) and 2KN/m2 live load at each floor. The structure has a mass source combination of 1.0DL + 0.3LL given in TSC2019. This design parameters and loads give the floor loads in Table 3.2.

Table 3.2: Building site Parameters

Site Class	S_S	S_1	S_{DS}	S_{D1}	PGA	PGV
C	1.169	0.319	1.403	0.479	0.480	29.464

Where,

S_s: 5% damped, spectral response acceleration parameter at short periods as defined

S_1: 5% damped, spectral response acceleration parameter at a period of 1 s

S_{DS}: The design spectral response acceleration parameter at short periods

S_{D1}: The design spectral response acceleration parameter at a 1-s period

PGA: Peak ground acceleration

PGV: Peak ground velocity

Table 3.3: Floor Loads

Floor	Mass (Ton)	Weight (KN)
5	205.228	2013.291
4	226.828	2225.187
3	226.828	2225.187
2	226.828	2225.187
1	226.828	2225.187

Table 3.4: Analysis Mode periods

Fixed	1st mode	2nd mode	3rd mode
Etabs	0.500	0.149	0.076
Opensees	0.522	0.154	0.077

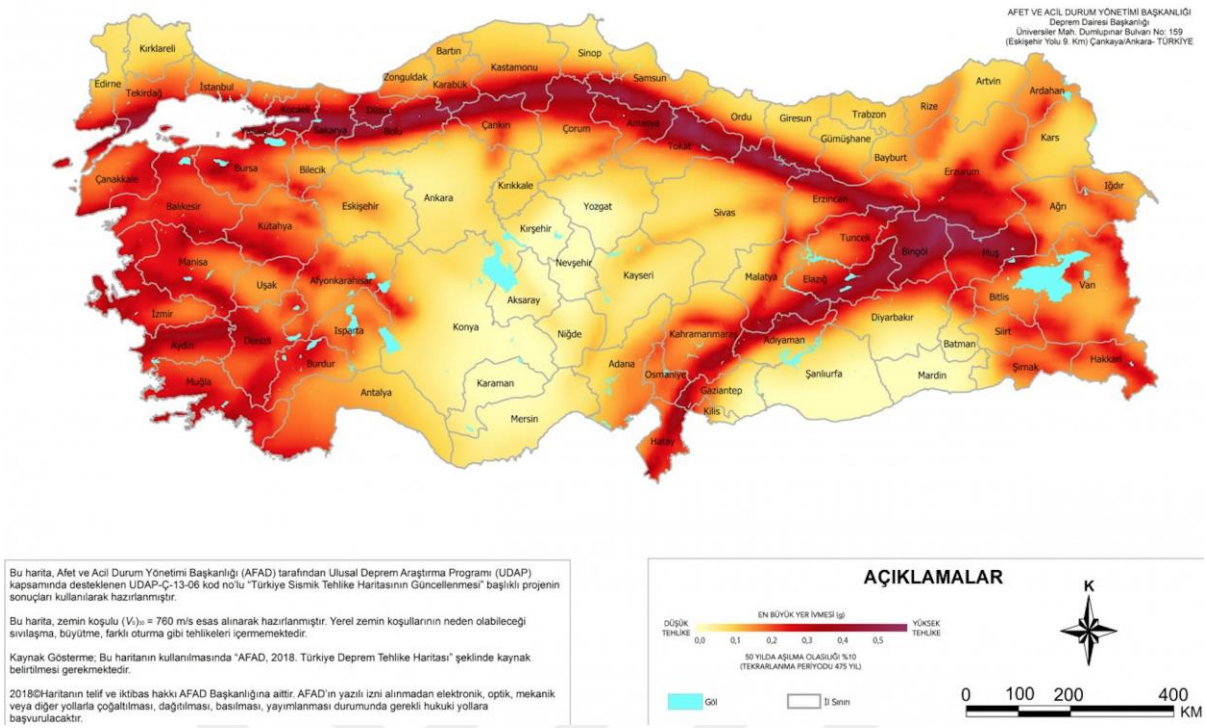

Figure 3.4: Turkey's Seismic Map [65]

Triple friction isolator Table 3.5 is applied in Figure 3.1 fixed model having analysis periods in Table 3.4, the isolator is designed according to the spectral displacement of the building region in Appendix A. The geometry and characteristic of the designed isolator is approximately same as the long-period medium displacement capacity triple friction pendulum used in [57] following the representative sizes manufactured by EPS Inc.

Table 3.5: Triple Friction Pendulum Parameters

Effective Radius for TFP(m)				TFP Velocity Dependent Friction				Displacement Capacities(m)		TFP Rate Parameter (sec/m)	
R_{eff1}	R_{eff2}	R_{eff3}	R_{eff4}	μ_1	μ_2	μ_3	μ_4	d_2=d_3	d_1=d_3	a_2=a_3	a_1=a_4
1.62	0.405	0.405	1.62	0.02 0.05	0.01 0.01	0.01 0.01	0.05 0.1	0.14	0.4	100.0	100.0

3.2 Opensees

Opensees is an open source software developed by University of California in 2000s. The program was developed using TCL programming language and it is aim is to provide easy simulation of earthquake records for researchers and academicians. The software has graphical representation limitations, postprocessors are needed for data charts. Opensees models are created by coding, nodes are created at each beam and column points and assigned masses for modal analysis. Constraints are assigned at each ground floor nodes to restrain movements, diaphragms are assigned for direction restrains in upper building floors and a geometric transformation is assigned to convert local axis to global. Isolated structures have extra commands for material definition and friction coefficient. The building elements are designed as linear or non-linear and for isolated building, bearing element is assigned. Load at each floor in Table 3.2 is equally divided at all floor nodes and assigned structural damping is constructed using first mode period with built-in Rayleigh damping command. Gravity and modal built-in analysis commands are assigned to construct solution. Ground motion time-series is constructed at each excitation axis before time-history-analysis command are set to perform analysis.

3.3 Equivalent Lateral Force Seismic Isolator Analysis

Table 3.6 and 3.7 designs are based on section 3.1 values and section 2.8.1.1 formulations, seismic site class coefficients to be used in codes design given in Table 3.3. Similar site parameters are used in both codes for the static analysis. Isolator effective period (T_{eff}) and damping ratio (β) are taken as 3.0s and 20% respectively in both codes.

In TSC2019, combination 1.0DL + 0.3LL is used as the mass source for weight and modification factor (R) as 1 for load reduction. Design superstructure base shear (V_x) is computed as 1102.120kN. For ASCE 7-16, 1.0DL + 0.25LL as mass source and a modification factor (R) of 2 for seismic load reduction. The shape parameter (k) for the force distribution is computed as 1.4. The base shear (V_b), total unreduced superstructure (V_{st}), and reduced superstructure (V_s) are 2076.334kN, 1892.334kN and 946.167kN respectively.

Table 3.6: TSC 2019 Equivalent Lateral Method

Floors	h(m)	wi(kN)	$w_x h_x$	$\frac{w_x h_x}{\sum w_x h_x}$	F_x (kN)
1	3	2225.187	6675.561	0.069	75.883
2	6	2225.187	13351.122	0.138	151.767
3	9	2225.187	20026.683	0.207	227.650
4	12	2225.187	26702.244	0.275	303.533
5	15	2013.291	30199.365	0.311	343.286

$a = \frac{w_x h_x}{\sum w_x h_x}$ story force distribution coefficient.

$F_x = a.V_x$ story force

Table 3.7: ASCE 7-16 Equivalent Lateral Method

Floors	h(m)	wi(kN)	$w_x h_x^k$	$\frac{w_x h_x^k}{\sum w_x h_x^k}$	F_x
1	3	2202.679	10254.65265	0.042	39.652
2	6	2202.679	27062.1906	0.111	104.643
3	9	2202.679	47740.912	0.195	184.603
4	12	2202.679	71417.54916	0.292	276.155
5	15	1990.783	88216.87543	0.361	341.114

$C_{vx} = \frac{w_x h_x^k}{\sum w_x h_x^k}$ story force distribution coefficient.

$F_x = C_{vx}.V_{st}$ story force

3.4 Time History Analysis

3.4.1 Validation of Triple Friction Pendulum Model

One-story building model having a fundamental fixed base period of 0.2s in [64] is verified on Opensees with force-displacement curve and drift(m) as verification values. The model stands on a triple friction pendulum with properties presented in Table 3.8. The model in Figure 3.5 has a damping ratio of 0.25% with an approximate base weight (W_b) to superstructure weight (W_s) ratio as 0.5 and a total weight of 50KN on each isolator. All frame elements are assumed to be massless and rigidly connected.

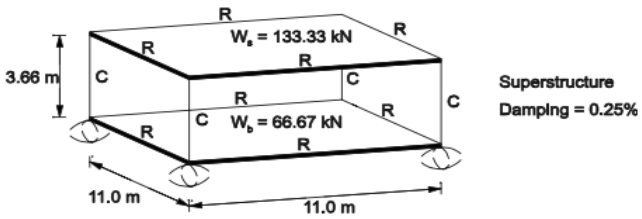

Section Property	Area (mm^2)	Moments of Inertia (mm^4)	Torsion Constant (mm^4)	Shear Area (mm^2)	Mass (kg)	Weight (kN)
"Column" (C)	5.0×10^6	6.851×10^7	1.0×10^6	5.0×10^6	0	0
"Rigid" (R)	5.0×10^6	1.0×10^{11}	1.0×10^6	5.0×10^6	0	0

Figure 3.5: Verification Isolated structure[64]

Table 3.8: Isolator Properties [64]

Actual properties from testing (Fenz and Constantinou 2008b)				
Surface 1	$R_{eff\,1}$=435 mm	μ_1=0.02−0.04	d_1=64 mm	a_1=0.10 sec/mm
Surface 2	$R_{eff\,2}$=53 mm	μ_2=0.01−0.02	d_2=19 mm	a_2=0.10 sec/mm
Surface 3	$R_{eff\,2}$=53 mm	μ_3=0.01−0.02	d_3=19 mm	a_3=0.10 sec/mm
Surface 4	$R_{eff\,4}$=435 mm	μ_4=0.06−0.13	d_4=64 mm	a_4=0.10 sec/mm
Properties of series elements				
Element 1	$\bar{R}_{eff\,1}$=106 mm	$\bar{\mu}_1$=0.01−0.02	$\bar{d}_1$=−	$\bar{a}_1$=0.05 sec/mm
Element 2	$\bar{R}_{eff\,2}$=382 mm	$\bar{\mu}_2$=0.02−0.04	$\bar{d}_2$=56.2 mm	$\bar{a}_2$=0.11 sec/mm
Element 2	$\bar{R}_{eff\,3}$=382 mm	$\bar{\mu}_3$=0.06−0.13	$\bar{d}_3$=56.2 mm	$\bar{a}_3$=0.11 sec/mm

The triple friction pendulum validation analysis results in Figure 3.6 and Figure 3.7 were from integration of motion equations and Sap2000 using 180 component of 1940 El Centro record (PGA of 0.31g) as a unidirectional excitation along single lateral axis, record is available from the PEER NGA database. The ground motion was scaled by a factor of 2.15 to magnify the displacement values to trigger all sliding regimes.

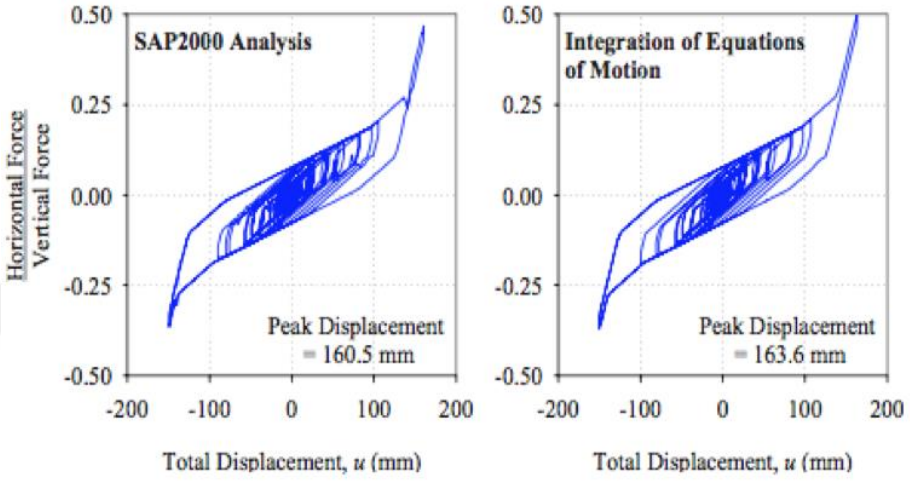

Figure 3.6: Force-Displacement Curves for SAP2000 and Numerical Integration of Equations of Motion[64]

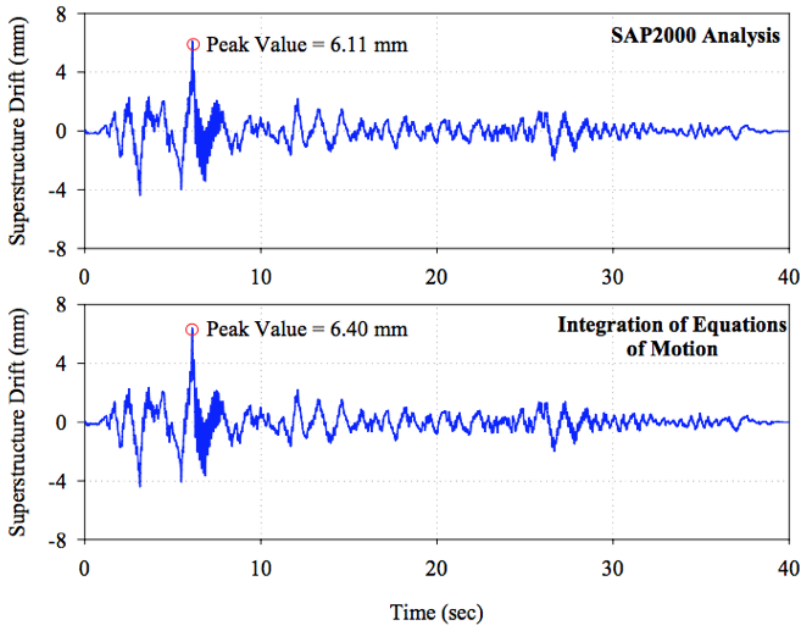

Figure 3.7: Structure Drift from Sap2000 and integration of motion equation [64]

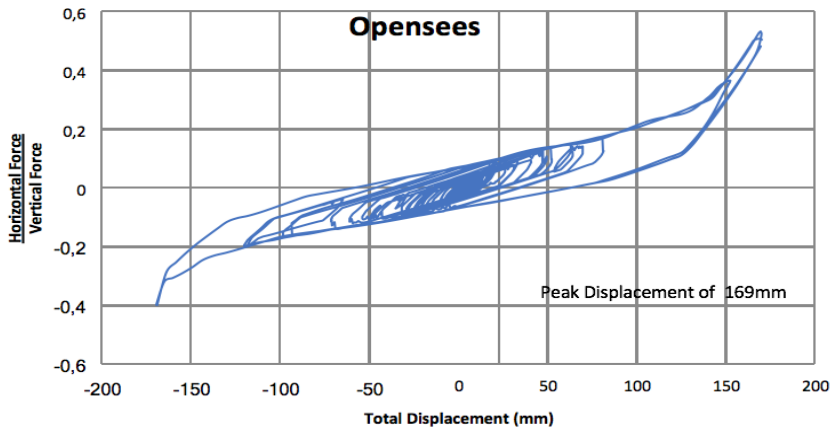

Figure 3.8: Verified Force-Displacement Curve

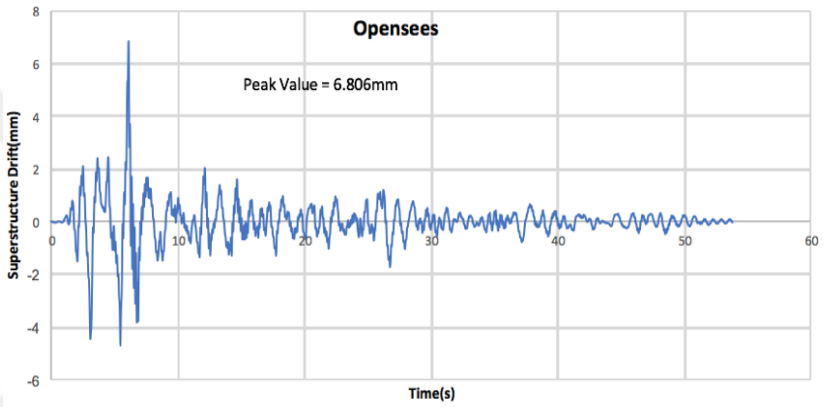

Figure 3.9: Verified Story Drift

Figure 3.8 and Figure 3.9 shows Opensees verified results plot. The force-displacement and story drift values show negligible difference which are due to convergence and analysis commands used.

3.5 Ground Motions

3.5.1 Selection of Ground Motions

According to ASCE 7-05/7-10 site ground motions should be selected from detailed events with magnitudes, fault distance, source and site condition. For sites lacking the required number of appropriate ground motion sets needed for analysis, appropriate simulated ground motion sets should be used to reach the number required. Three or more sets of ground motion are used in non-linear analysis, for three sets of analyses performed, the maximum value of the three

responses is used. Furthermore, if seven sets of ground motion were used to perform analysis, the average value of the seven peak responses is used. It is permissible to use sets of records beyond 3 or 7 sets but yields no significant variance. Moreover, site condition is essential to selection of ground motion. Soils at sites are classified based on their textures and behaviour during earthquake starting from soil class A (Hard rock) to soil class F (Clay). This soil classification is based on 100ft(30m) of the soil profile, sites lacking data are permitted to be estimated by soil and geologic design professionals after tests [53]. Ten (10) far-field and eleven near-field (11) ground motions with magnitude $6.5 \leq M \geq 7.6$ in Table 3.9 and Table 3.10 were selected from the list of records presented in FEMA [66]. The ground accelerations and displacements are shown in Figure 3.10 to Figure 3.51.

Table 3.9: Far-Field Ground Motion Records.

No.	Name and Station	Component	Year	Soil Type	Magnitude, M	PGA(g)
1.	Duzce, Turkey – Bolu	0	1999	D	7.1	0.739
2.	Kobe, Japan– Nishi Akashi	0	1995	C	6.9	0.474
3.	Kobe, Japan – Shin Osaka	90	1995	D	6.9	0.212
4.	Kocaeli, Turkey – Arcelik	0	1999	C	7.5	0.204
5.	Imperial Valley – Delta	352	1979	D	6.5	0.334
6.	Hector Mine - Hector	90	1999	C	7.1	0.273
7.	San Farnendo – L.A Hollywood	90	1971	D	6.6	0.225
8.	Northridge- Beverly Hills	279	1994	D	6.7	0.477
9.	Manji, Iran - Abbar	L	1990	C	7.4	0.485
10.	Landers - Coolwater	LN	1992	D	7.3	0.282

Table 3.10: Near-Field Ground Motion Records.

No.	Name and Station	Component	Year	Soil Type	Magnitude, M	PGA(g)
1.	Erzincan, Turkey – Erzincan	EW	1992	D	6.7	0.490
2.	Cape Mondecino – Petrolia	0	1992	C	7.0	0.591
3.	Duzce, Turkey – Duzce	270	1999	D	7.1	0.503
4.	Imperial Valley06 – Bonds Corner	140	1979	D	6.5	0.586
5.	Nahanni Canada – Site 2	240	1985	C	6.8	0.44
6.	Chi Chi Taiwan - TCU067	E	1999	C	7.6	0.500
7.	Superstition Hills – P. T. S	315	1987	D	6.5	0.384
8.	Loma Prieta – Saratoga	0	1989	C	6.9	0.501
9.	Northridge01- Sylmar	090	1994	C	6.7	0.395
10.	Northridge01- Saticoy	090	1994	D	6.7	0.281
11.	Imperial Valley06 – Chihuahua	282	1979	D	6.5	0.254

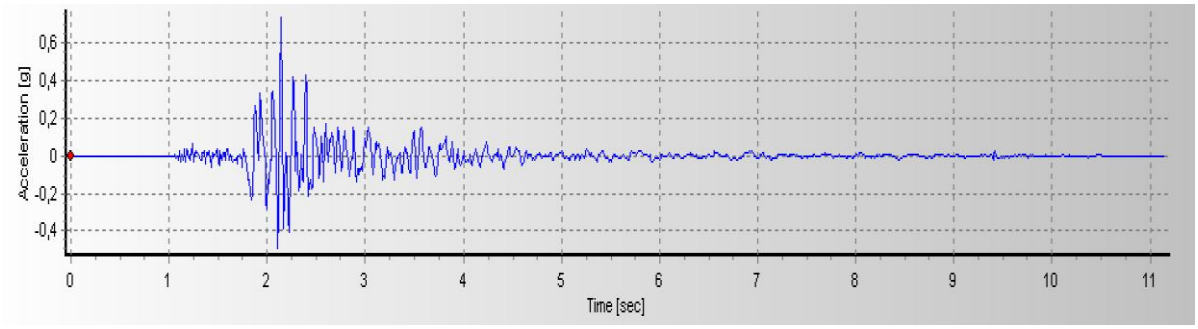

Figure 3.10: Bolu Ground Acceleration

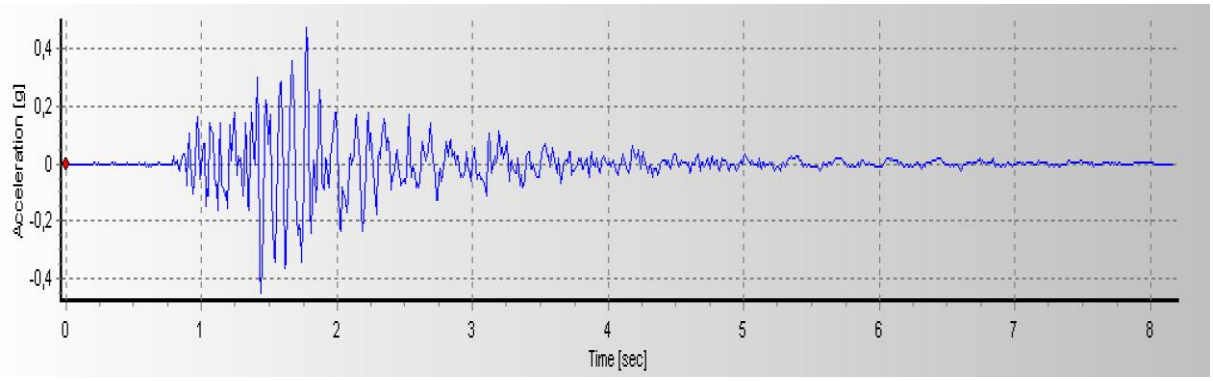

Figure 3.11: Nishi Akashi Ground Acceleration

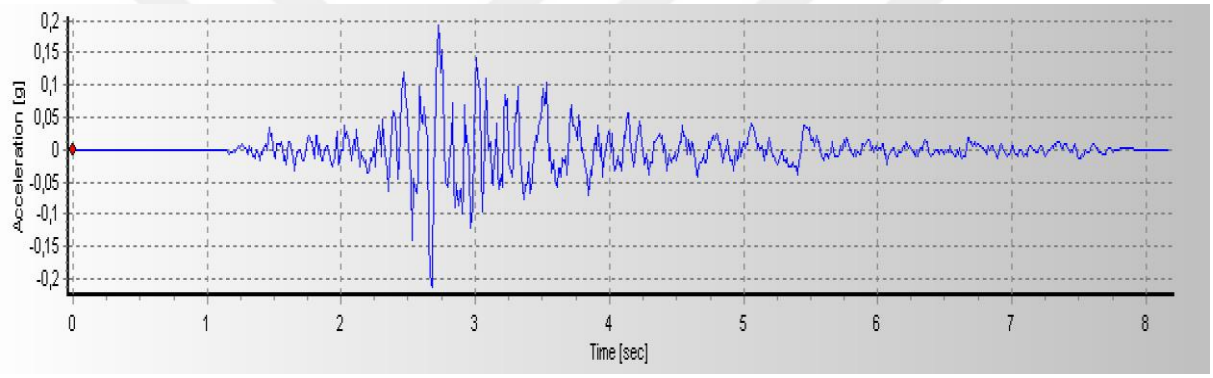

Figure 3.12: Shin Osaka Ground Acceleration

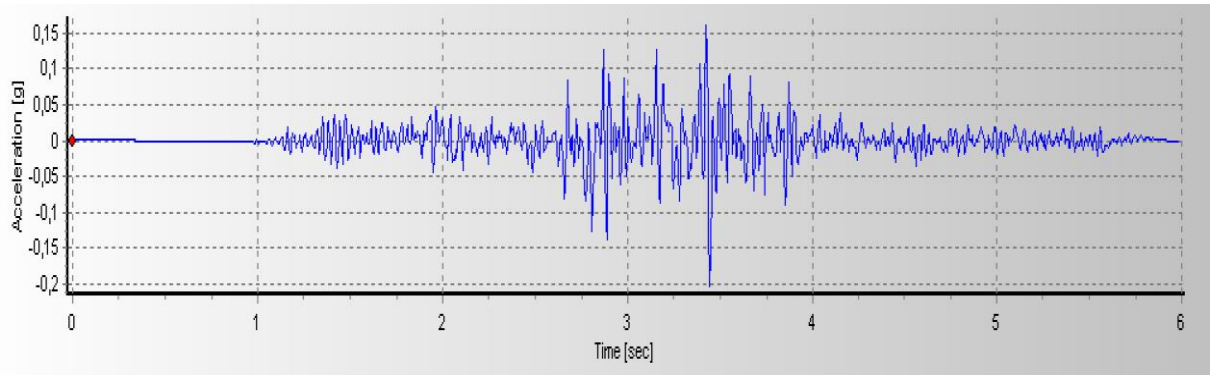

Figure 3.13: Arcelik Ground Acceleration

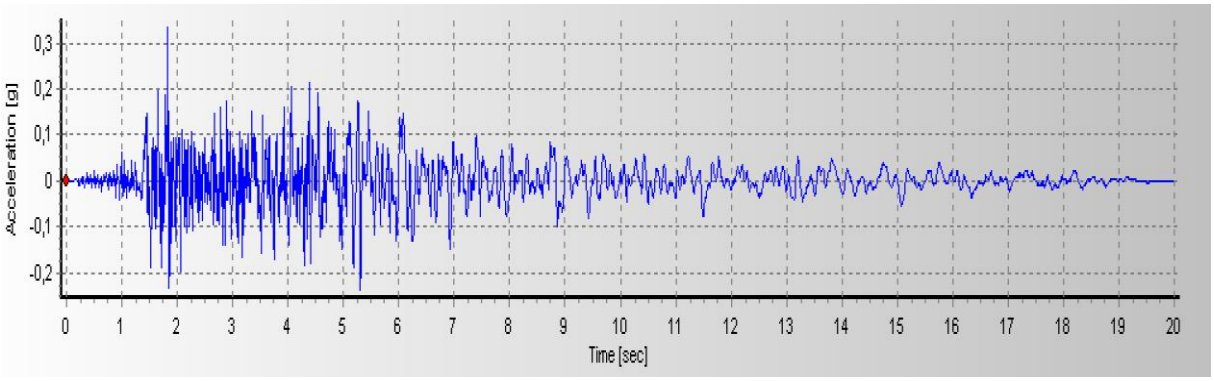

Figure 3.14: Delta Ground Acceleration

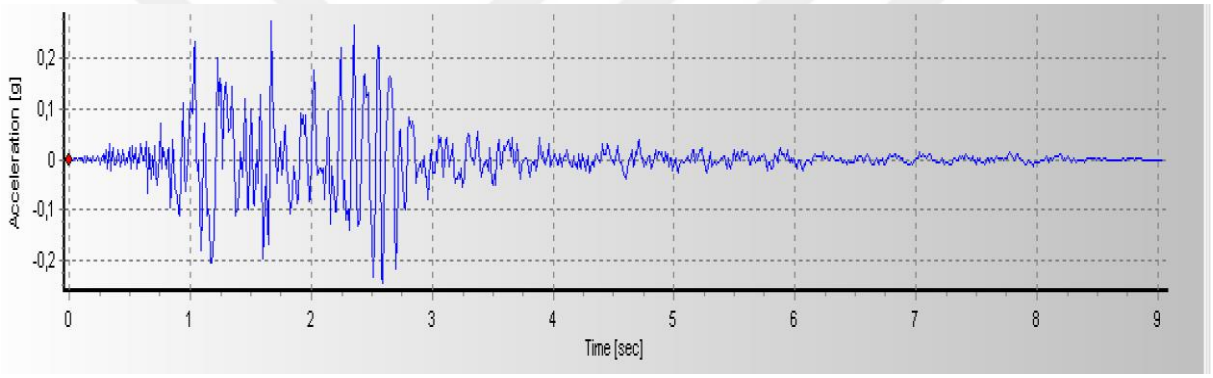

Figure 3.15: Hector Ground Acceleration

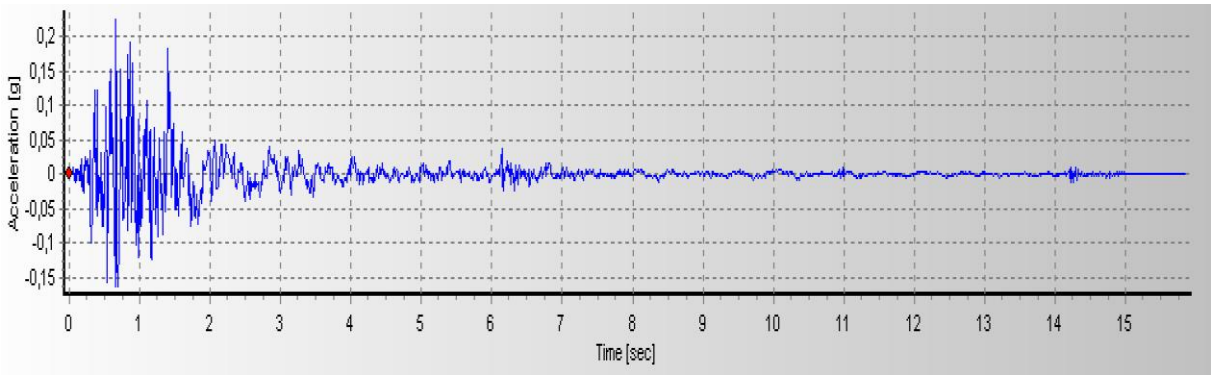

Figure 3.16: L.A Hollywood Ground Acceleration

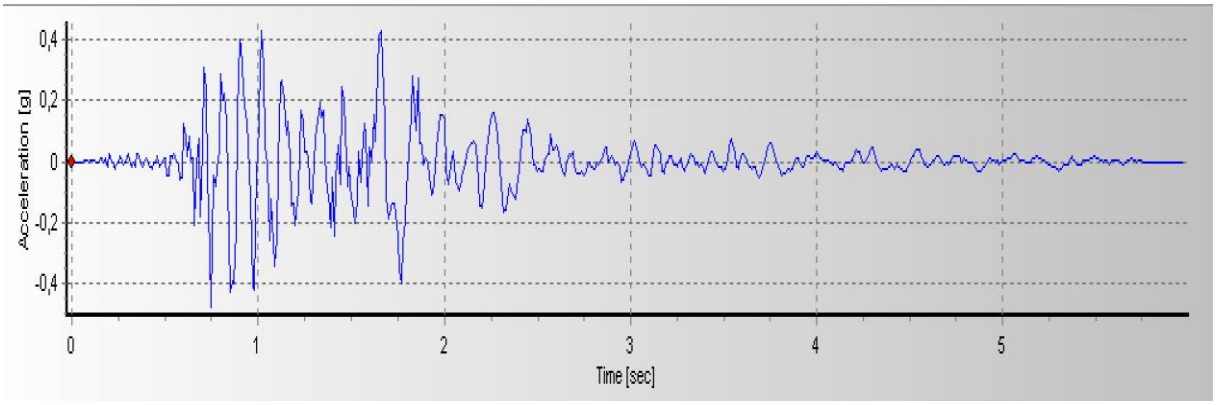

Figure 3.17: Beverly Hills Ground Acceleration

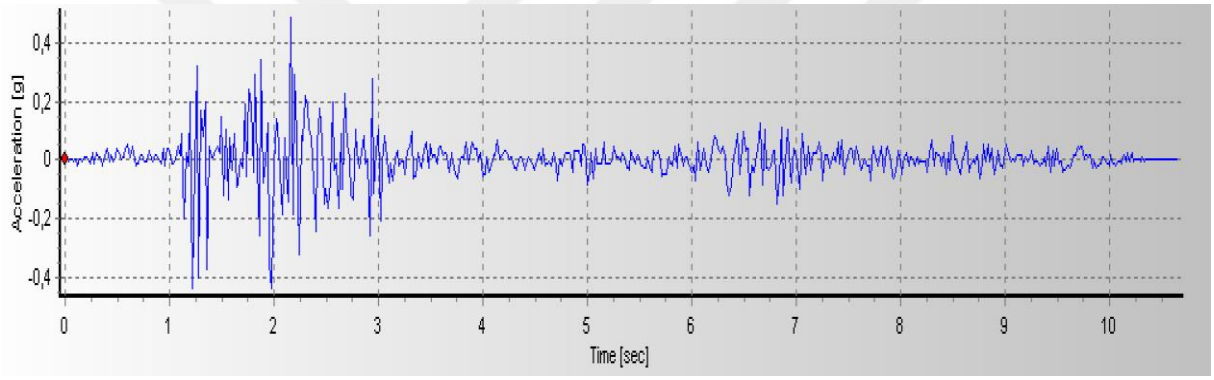

Figure 3.18: Abbar Ground Acceleration

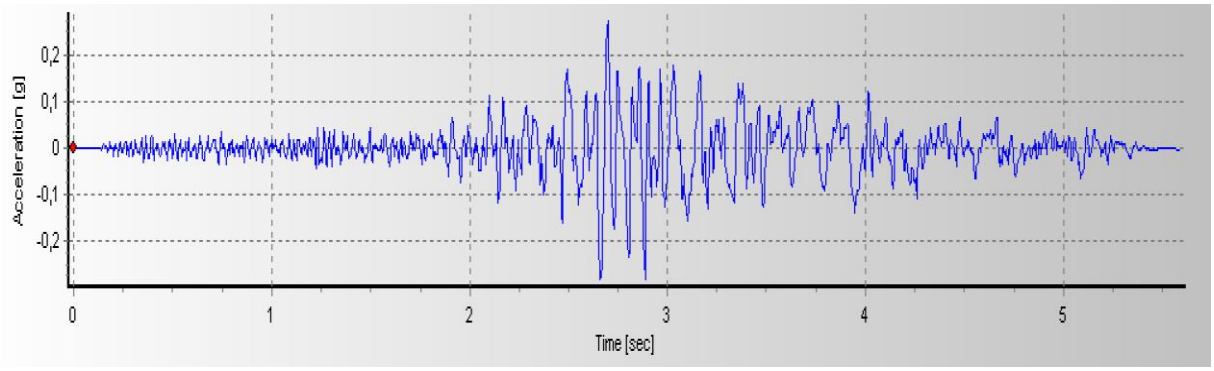

Figure 3.19: Coolwater Ground Acceleration

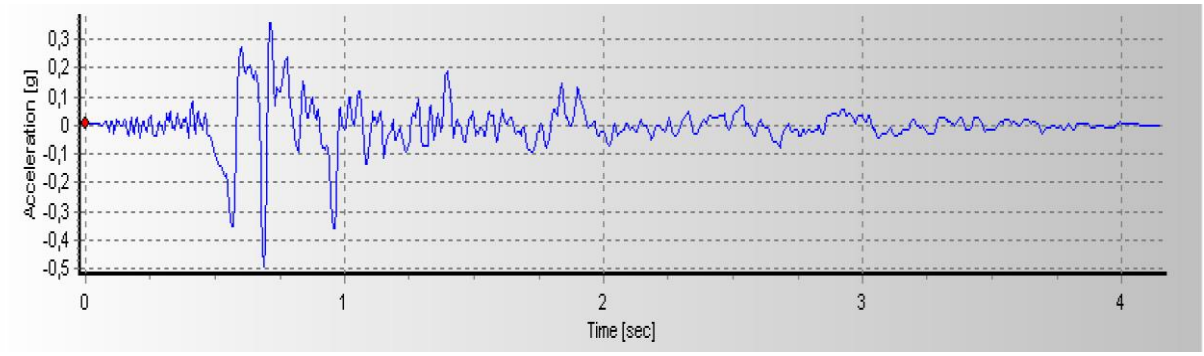

Figure 3.20: Erzincan Ground Acceleration

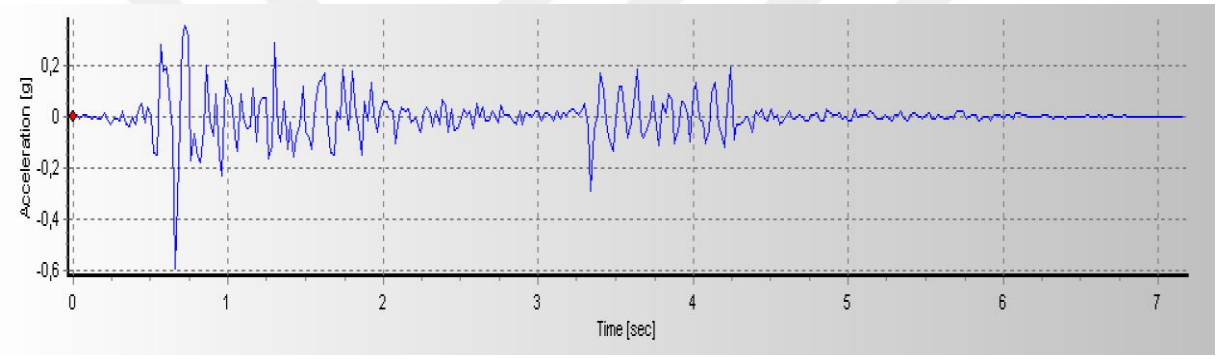

Figure 3.21: Petrolia Ground Acceleration

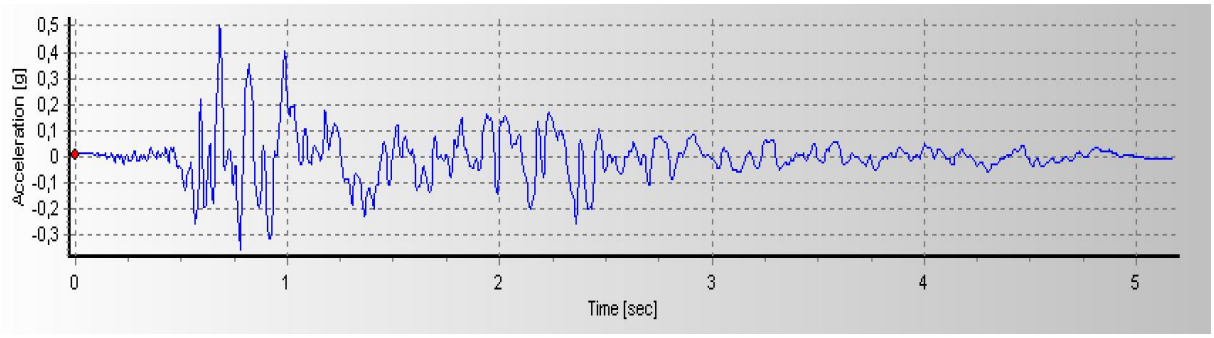

Figure 3.22: Duzce Ground Acceleration

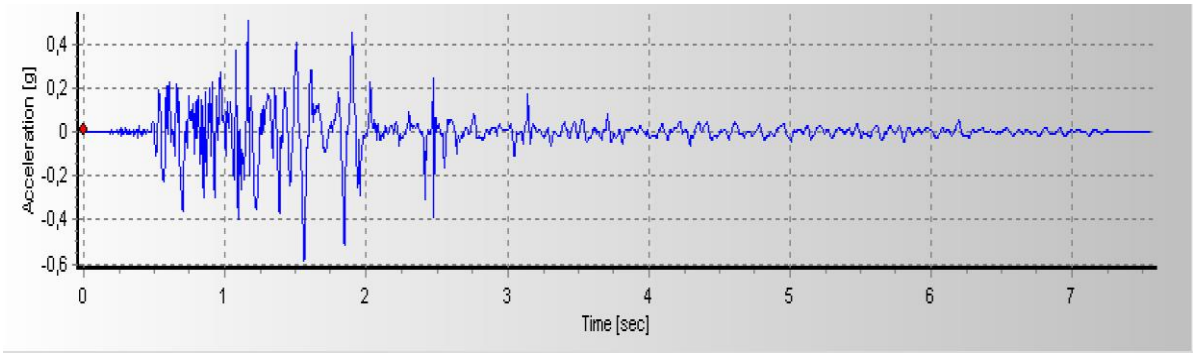

Figure 3.23: Bonds Corner Ground Acceleration

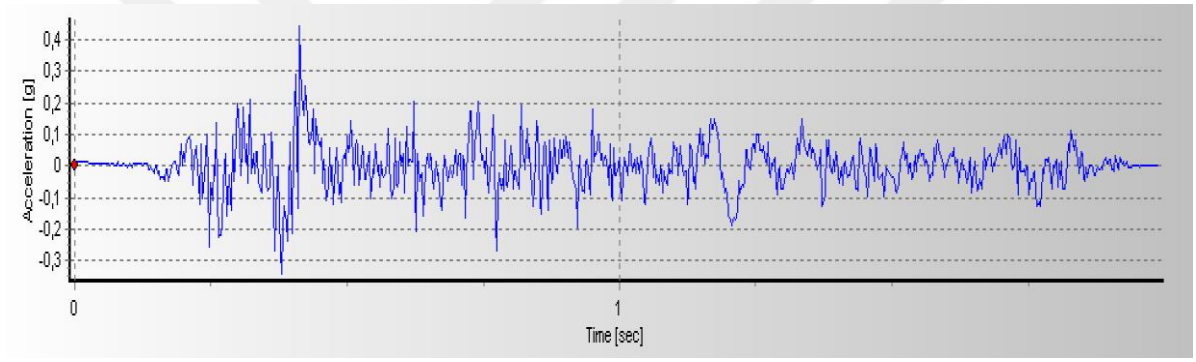

Figure 3.24: Nahanni Site 2 Ground Acceleration

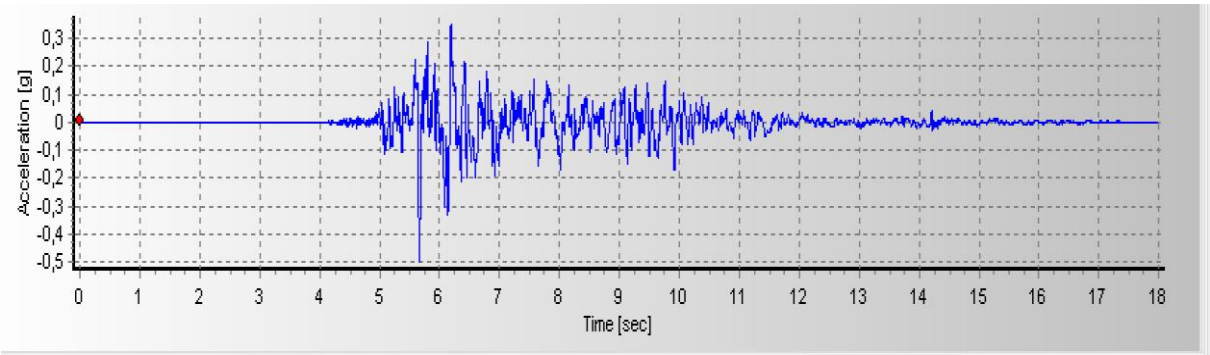

Figure 3.25: ChiChi TCU067 Ground Acceleration

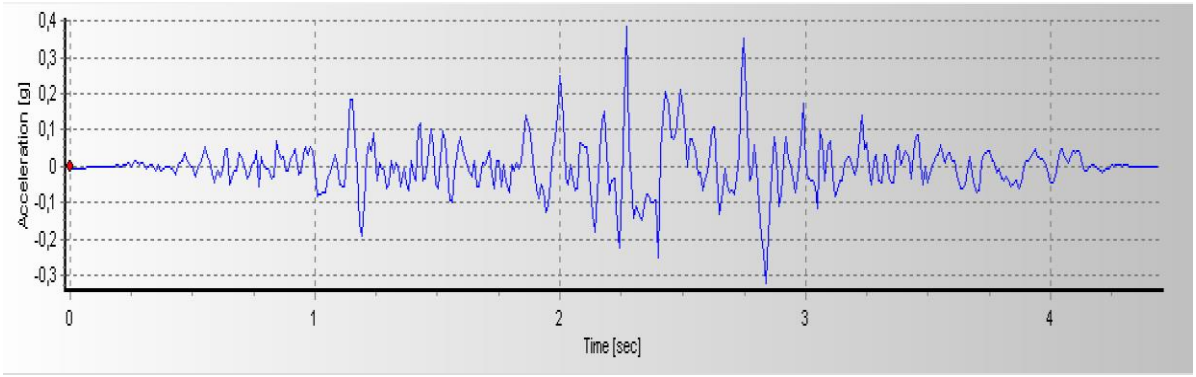

Figure 3.26: Parachute Test Site Ground Acceleration

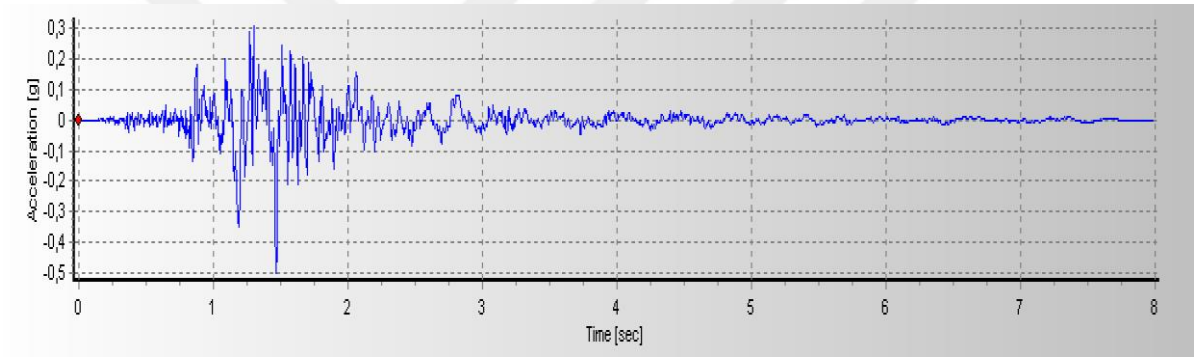

Figure 3.27: Saratoga Ground Acceleration

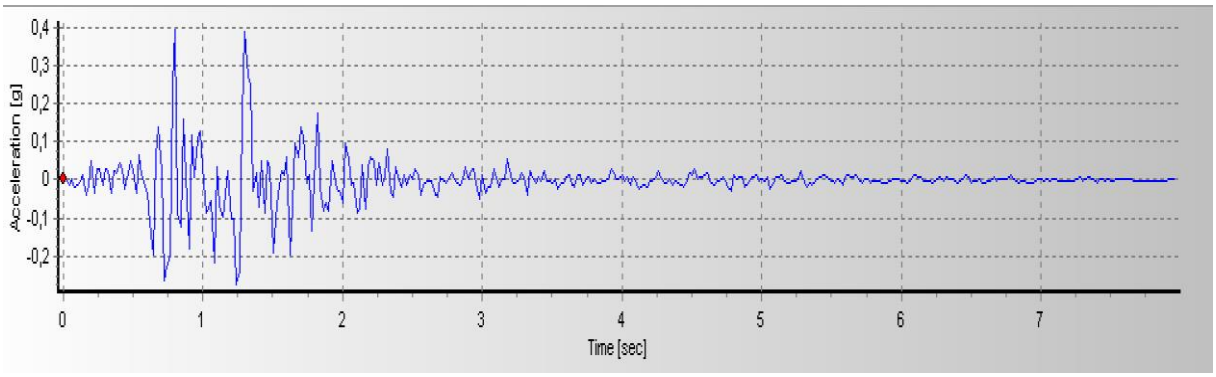

Figure 3.28: Sylmar Ground Acceleration

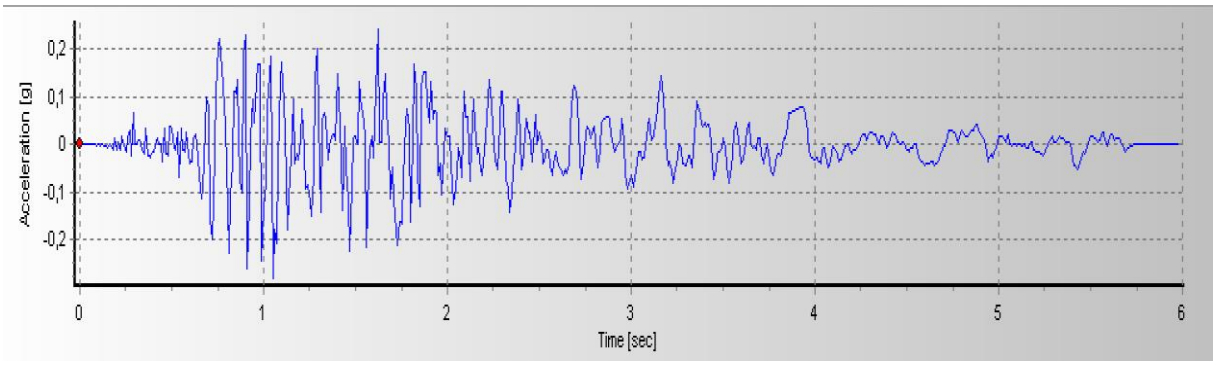

Figure 3.29: Saticoy Ground Acceleration

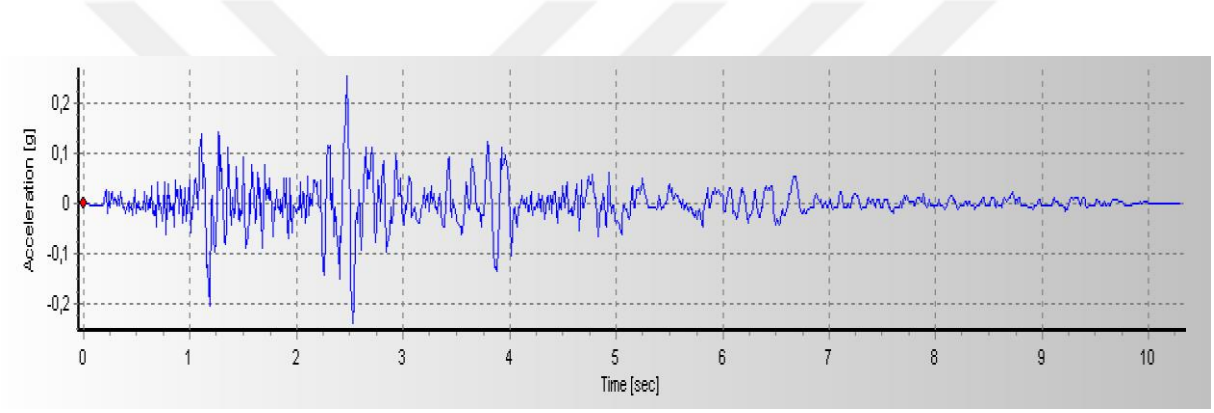

Figure 3.30: Chihuahua Ground Acceleration

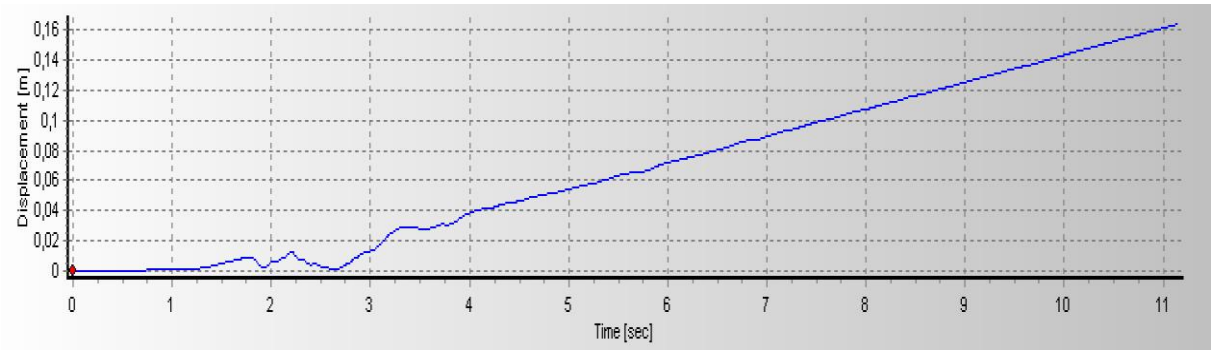

Figure 3.31: Bolu Ground Displacement

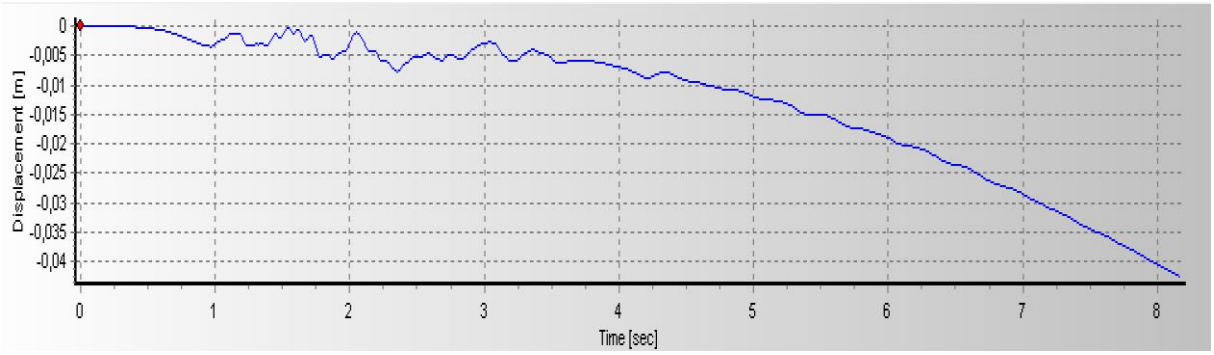

Figure 3.32: Nishi Akashi Ground Displacement

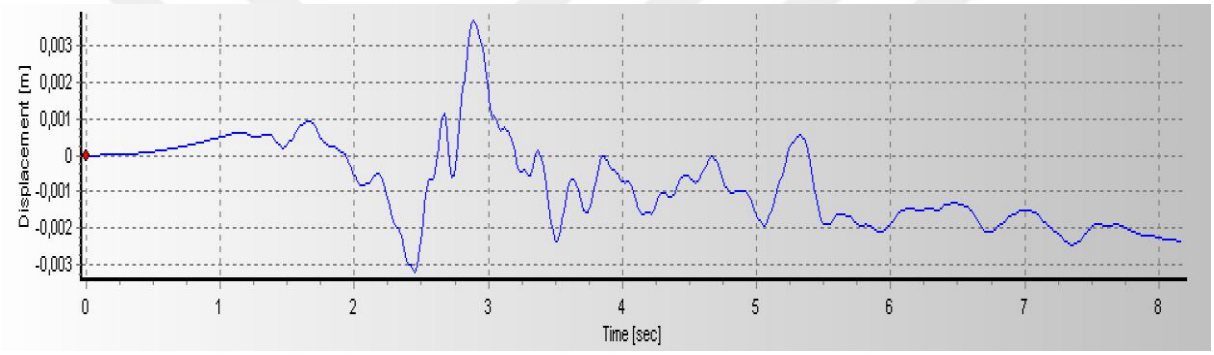

Figure 3.33: Shin Osaka Ground Displacement

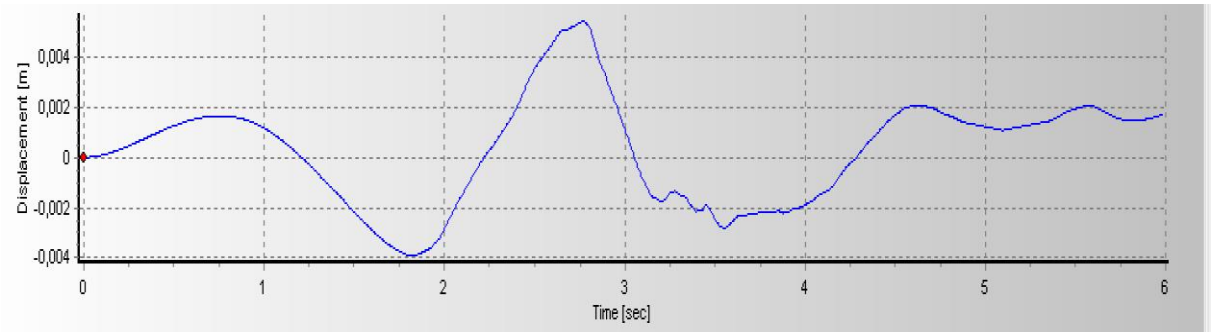

Figure 3.34: Arcelik Ground Displacement

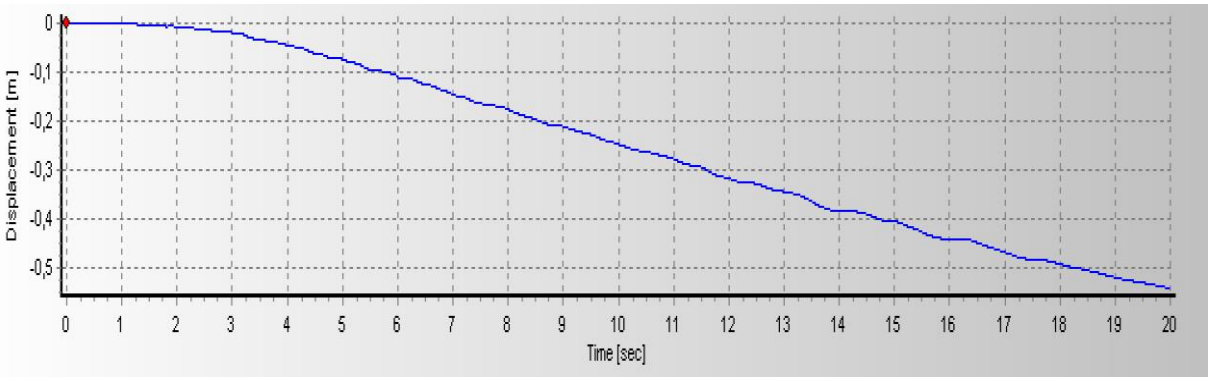

Figure 3.35: Delta Ground Displacement

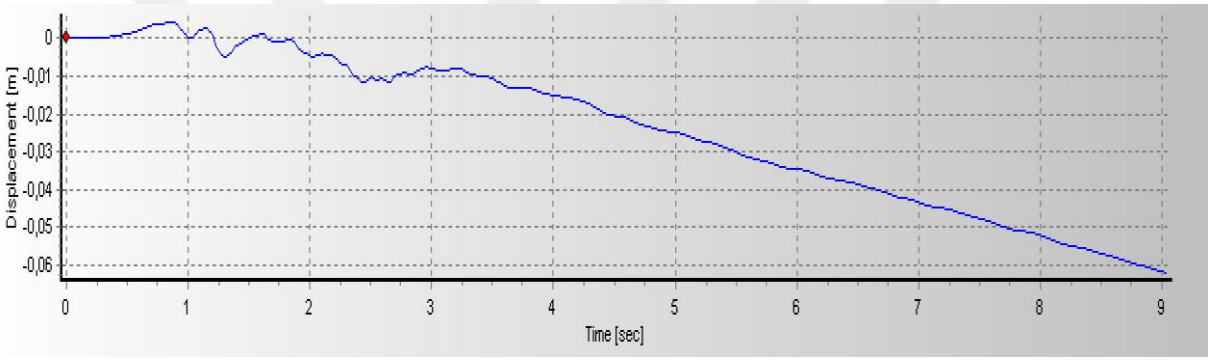

Figure 3.36: Hector Ground Displacement

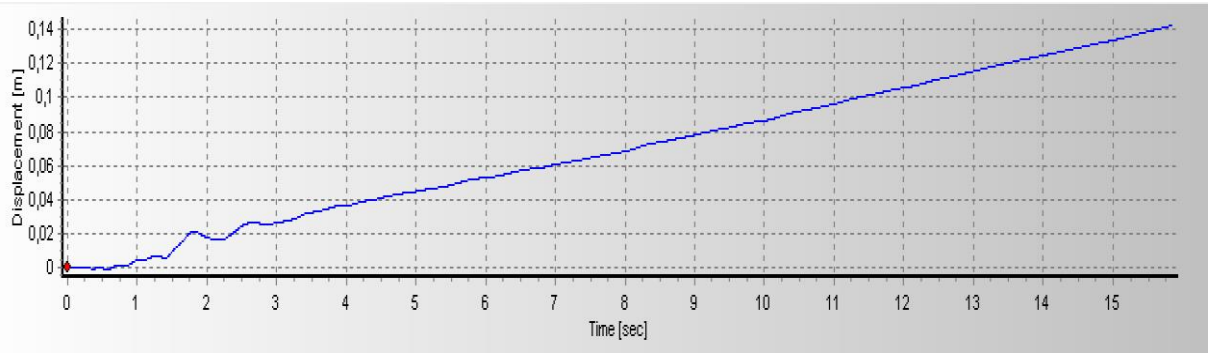

Figure 3.37: L.A Hollywood Ground Displacement

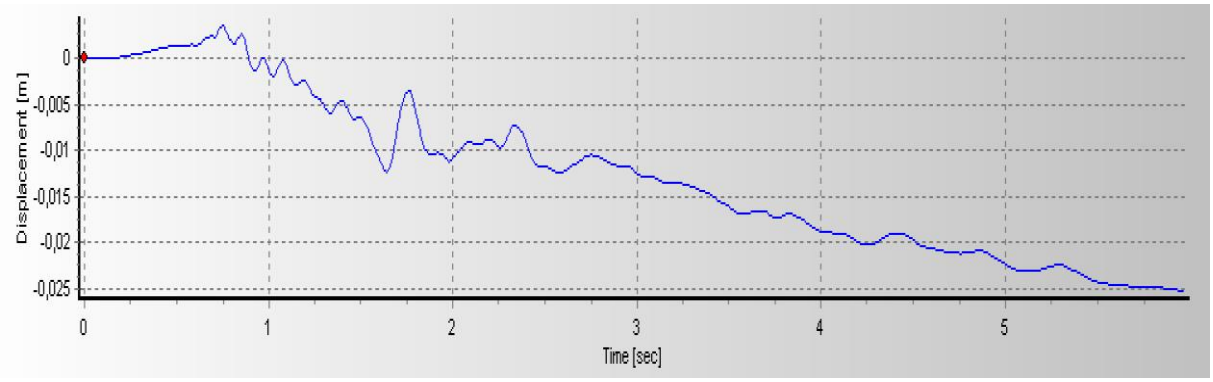

Figure 3.38: Beverly Hills Ground Displacement

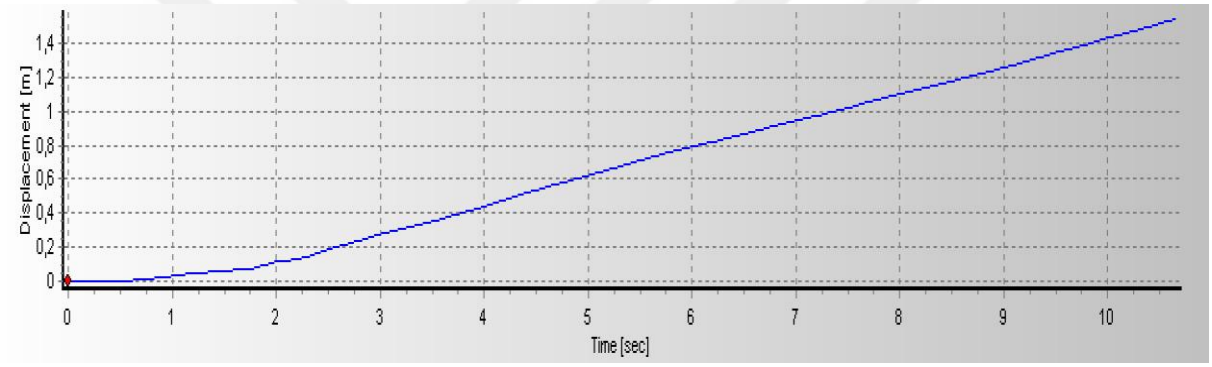

Figure 3.39: Abbar Ground Displacement

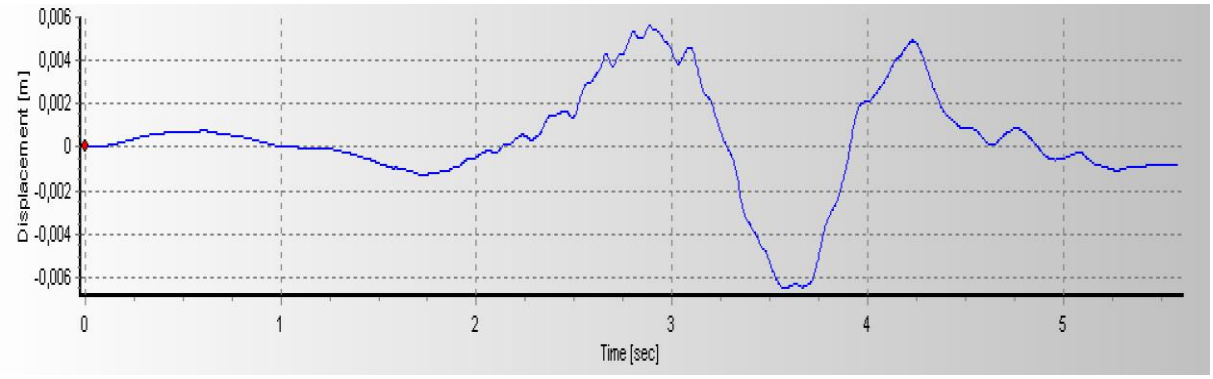

Figure 3.40: Coolwater Ground Displacement

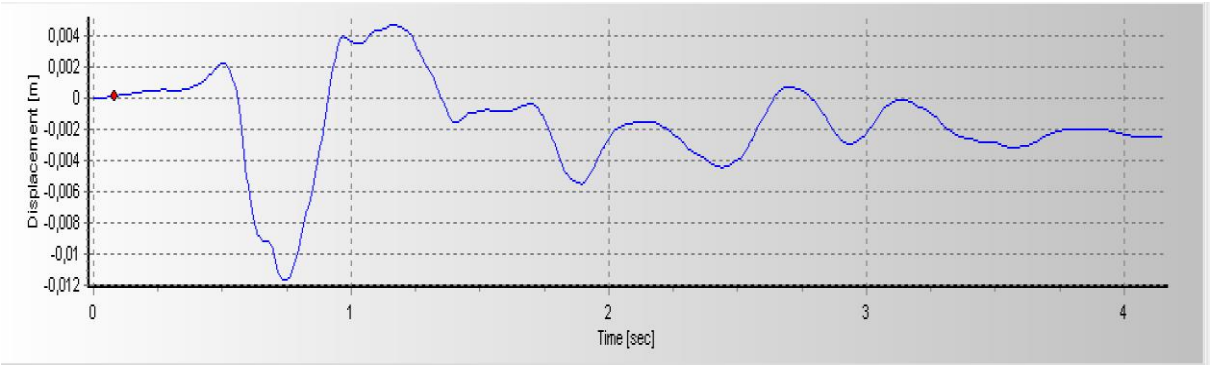

Figure 3.41: Erzincan Ground Displacement

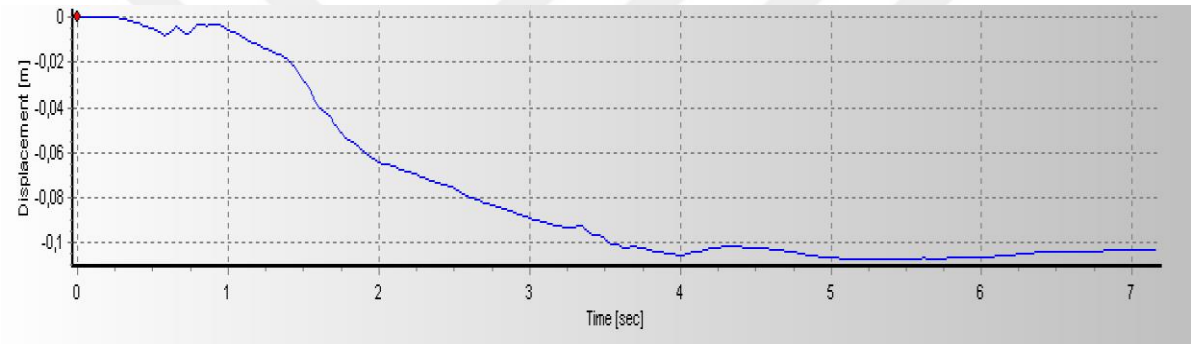

Figure 3.42: Petrolia Ground Displacement

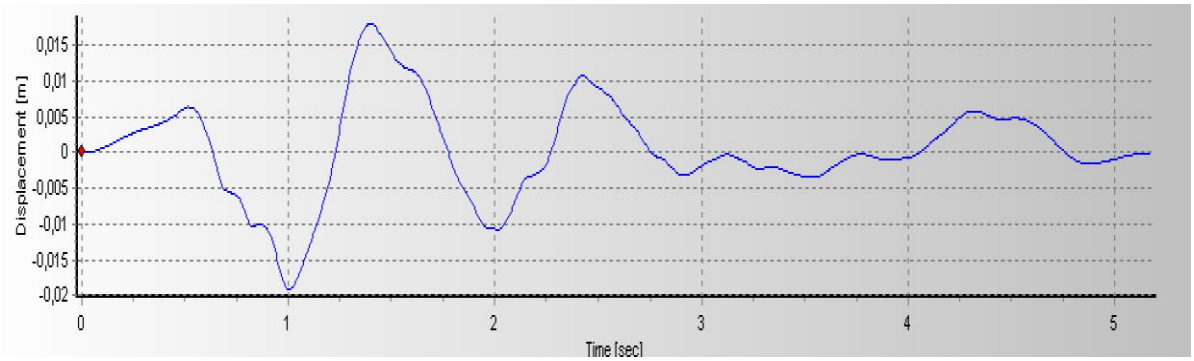

Figure 3.43: Duzce Ground Displacement

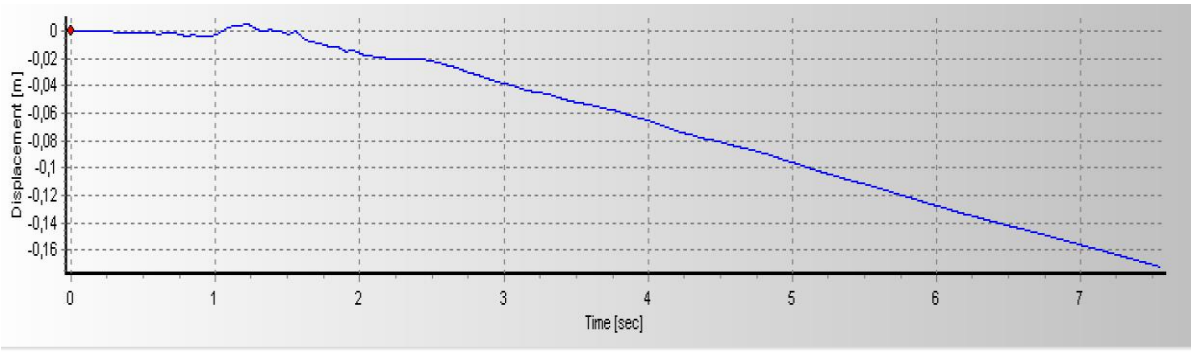

Figure 3.44: Bonds Corner Ground Displacement

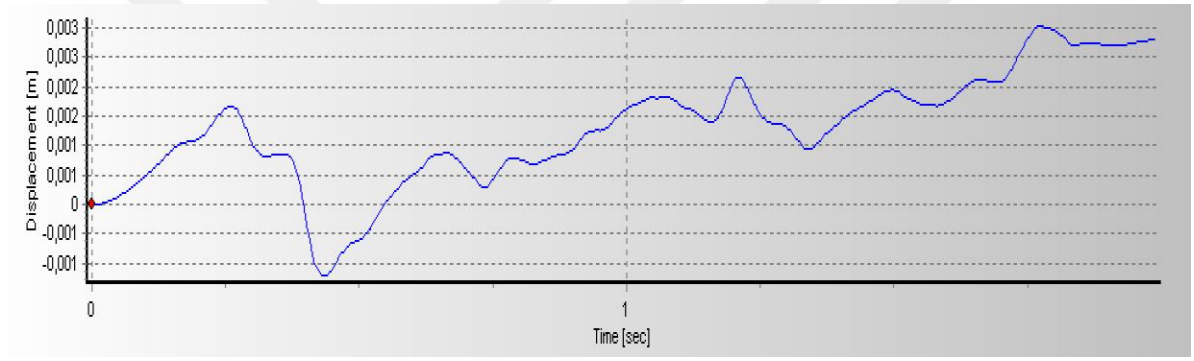

Figure 3.45: Nahanni Site 2 Ground Displacement

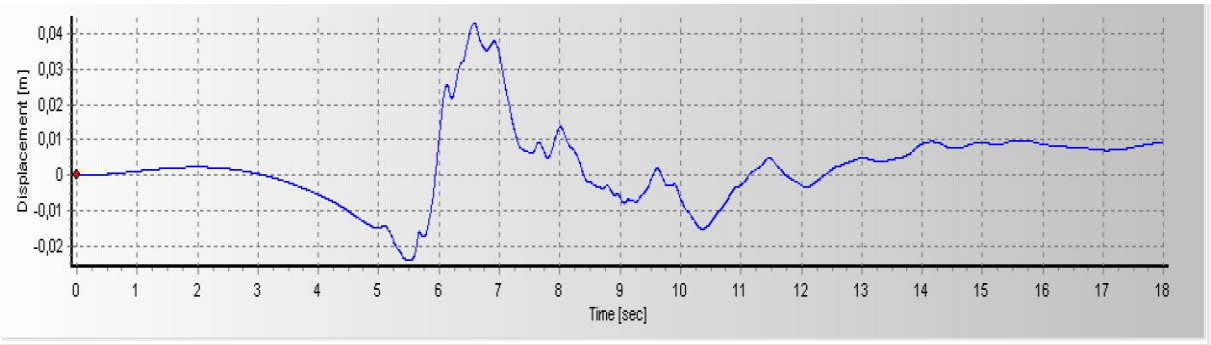

Figure 3.46: ChiChi TCU067 Ground Displacement

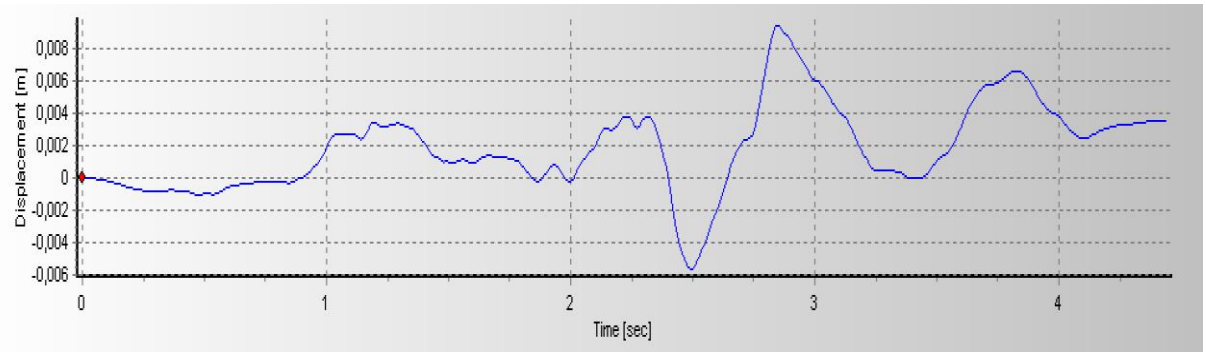

Figure 3.47: Parachute Test Site Ground Displacement

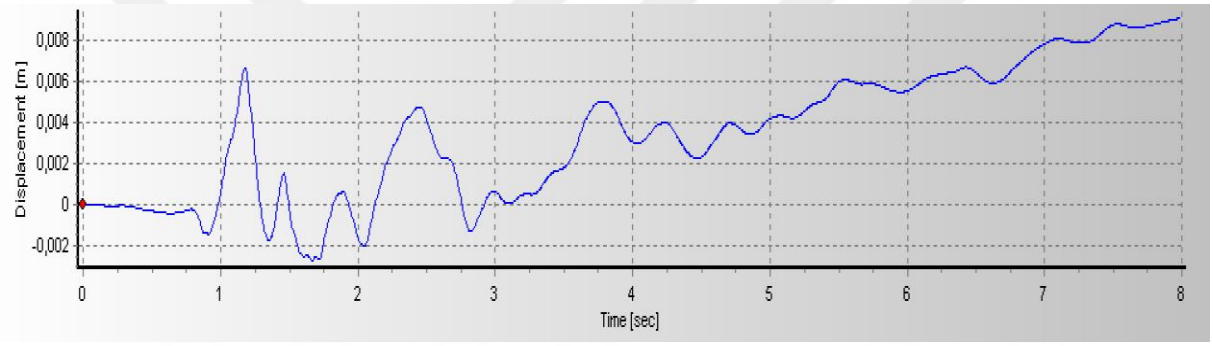

Figure 3.48: Saratoga Ground Displacement

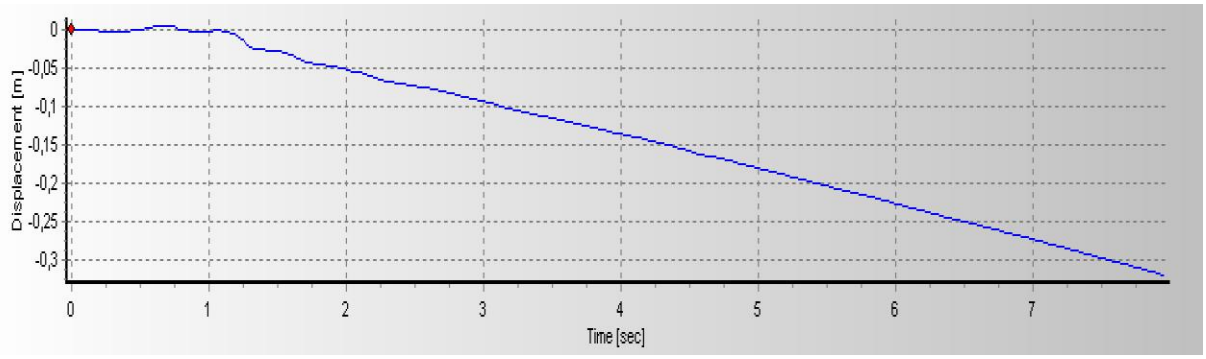

Figure 3.49: Sylmar Ground Displacement

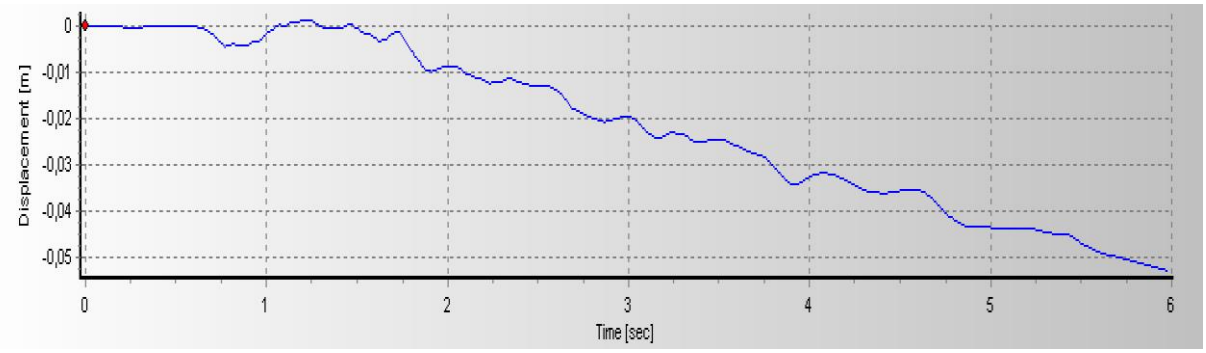

Figure 3.50: Saticoy Ground Displacement

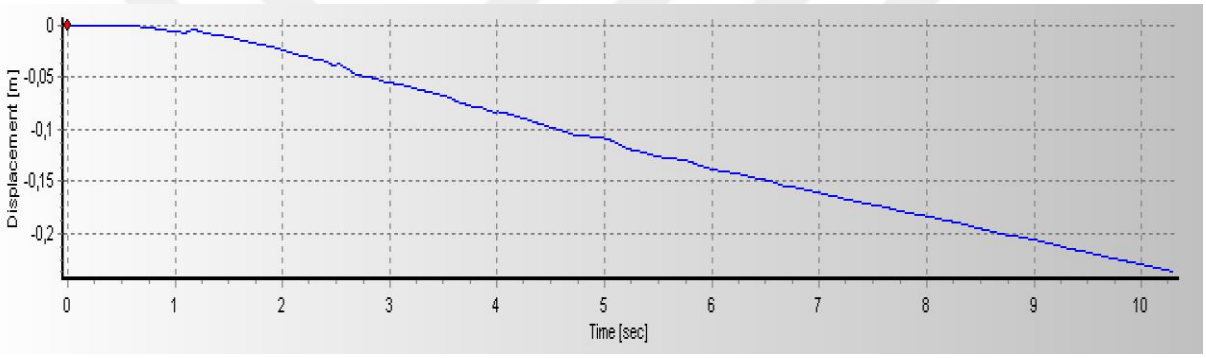

Figure 3.51: Chihuahua Ground Displacement

3.5.2 Ground Motion Scaling.

There are different approaches that are used in scaling of motion record but there is no agreement amongst experts on which approach is preferable for THA [67]. The most widely used method is matching the 5%-damped spectral acceleration of ground motion at fundamental natural period of 1s S(T_1,5%) with site spectrum at 1s [67][68]. The seismic parameters for the analysis structure region is presented in Table3.3, These parameters plot the site spectrum curve in Figure 3.52.

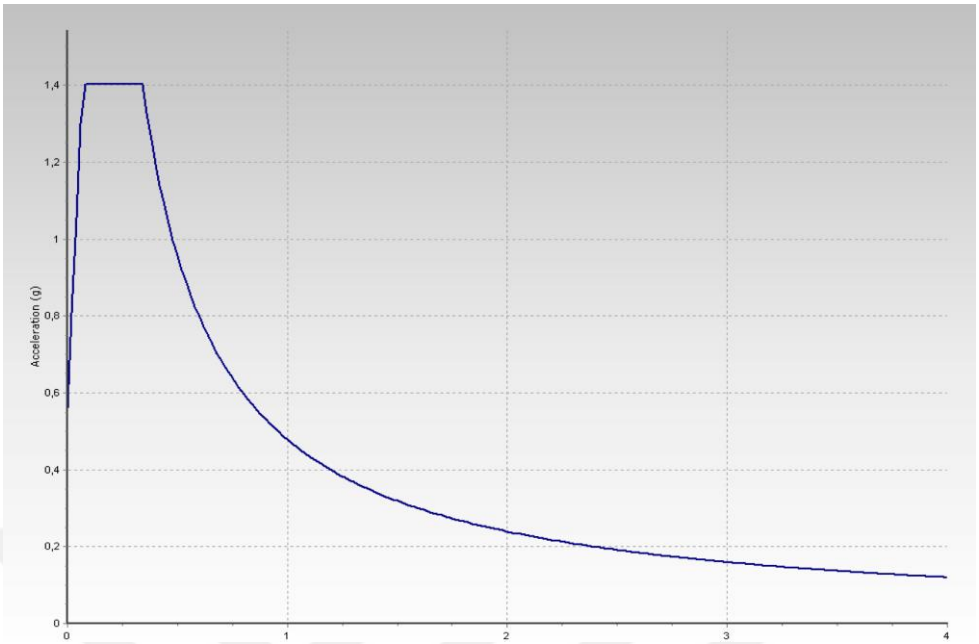

Figure 3.52: Site Response Spectrum

Earthquake records were scaled records to a target response spectrum for the considered site. Ground motions are scaled such that the 5% damped response spectra value of motions are not less than the site design response spectrum periods ranging from 0.2T to 1.5T, T is the fundamental period of the structure in the fundamental mode (1^{st} mode) for the direction of response being analysed [53]. Variation in some seismic hazard parameters such as duration, frequency, magnitude of different ground motions scaled at the same Sa (T1,5%) may result in the diverse level of response and damage to a given structure. So, use of only one ground motion may not provide enough assurance that the structure will have the same response when subjected to another ground motion record with the same Sa (T1,5%) [68]. Matched Spectrums of records in Figure 3.53 to Figure 3.75 with scaling factors in Table 3.11 and Table 3.12 are very important in analysis providing reduction in record-to-record variability of the input and output result.

Table 3.11: Scaled Far-Field Ground Motion.

Ground Motions	Scaling factor
Duzce, Turkey – Bolu	0.99
Kobe, Japan– Nishi Akashi	1.30
Kobe, Japan – Shin Osaka	2.67
Kocaeli, Turkey – Arcelik	5.53
Imperial Valley – Delta	1.98
Hector Mine - Hector	2.58
San Farnendo – L.A Hollywood	3.05
Northridge- Beverly Hills	1.28
Manji, Iran - Abbar	1.38
Landers - Coolwater	2.02

Table 3.12: Scaled Near-Field Ground Motions.

Ground Motions	Scaling factor
Erzincan, Turkey – Erzincan	1.30
Cape Mondecino – Petrolia	1.31
Duzce, Turkey – Duzce	1.12
Imperial Valley06 – Bonds Corner	1.24
Nahanni Canada – Site 2	1.97
Chi Chi Taiwan - TCU067	1.44

Superstition Hills – P. T. S	1.49
Loma Prieta – Saratoga	2.05
Northridge01- Sylmar	1.62
Northridge01- Saticoy	2.1
Imperial Valley06 – Chihuahua	2.7

Mean matched spectrum of the ten far-field and eleven near-field ground motions is represented in Figure 3.76 and Figure 3.77. Also, scaling helps to enhance some of the frequencies within the record. Thorough check is important for pulse records, if pulse is needed in analysis, records with required characteristics are to be used and be ensured that these characteristics are conserved after matching [69].

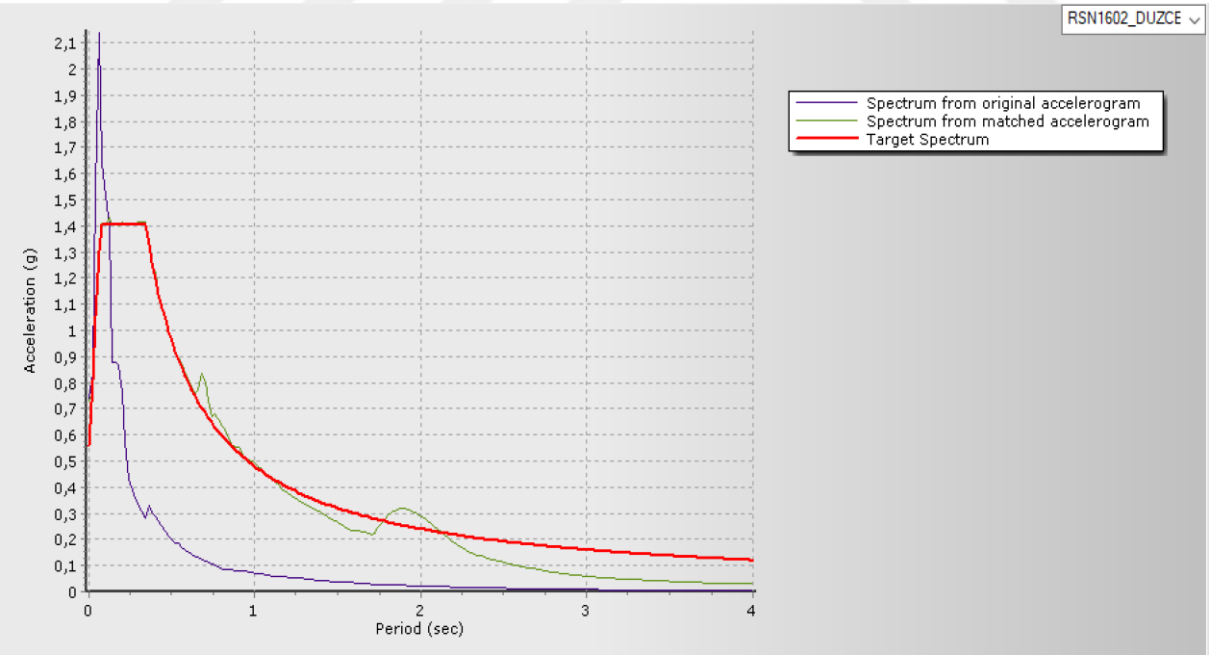

Figure 3.53: Bolu 5% Matched Spectrum

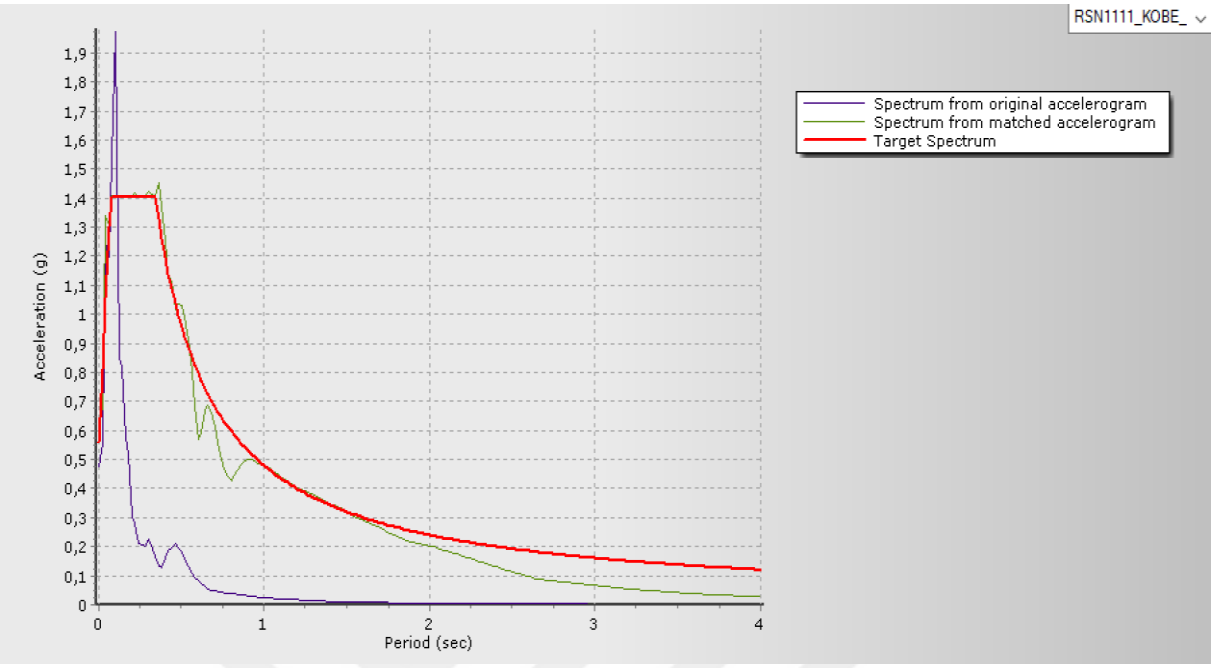

Figure 3.54: Nishi Akashi 5% Matched Spectrum

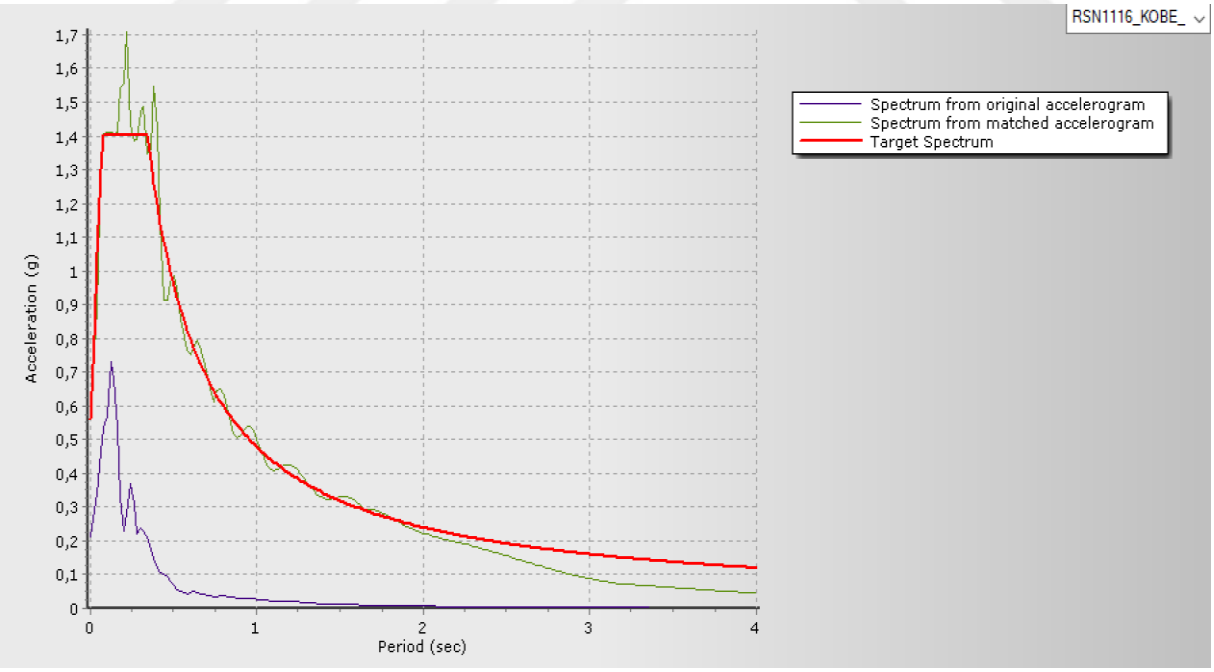

Figure 3.55: Shin Osaka 5% Matched Spectrum

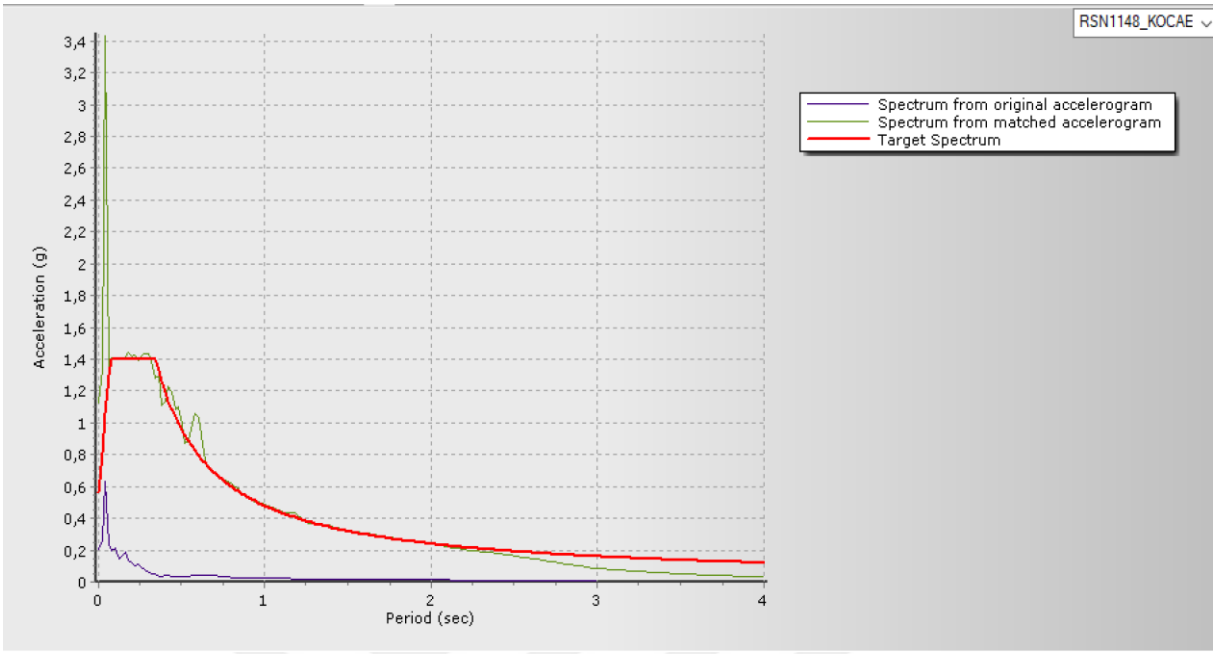

Figure 3.56: Arcelik 5% Matched Spectrum

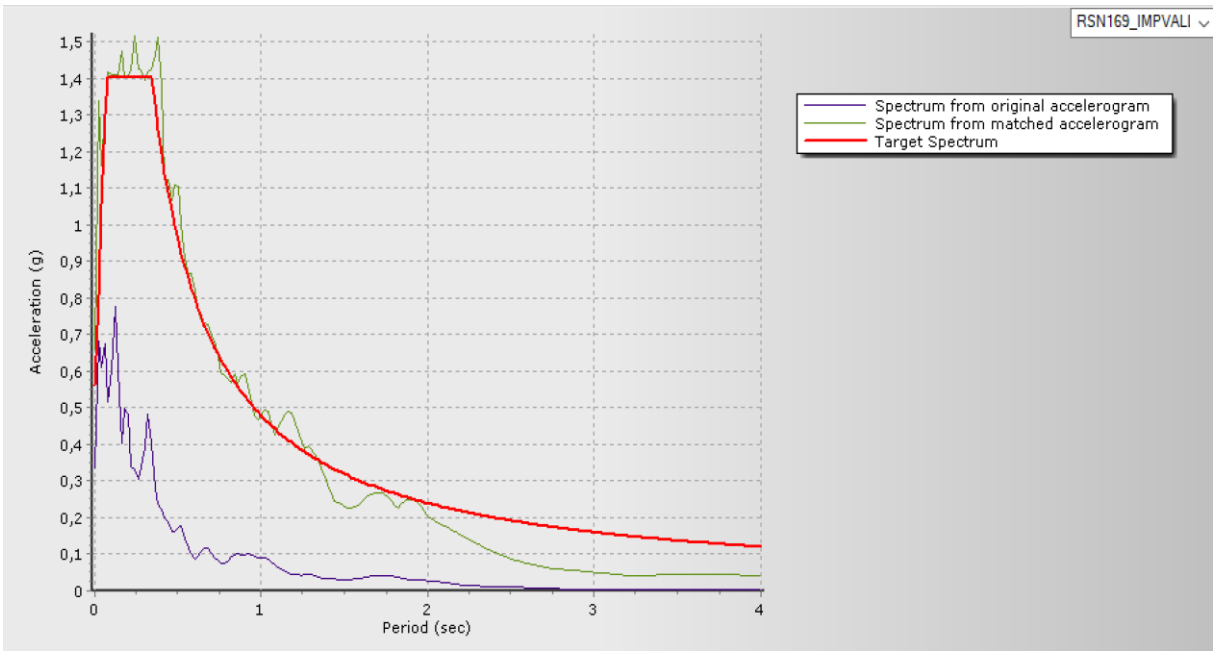

Figure 3.57: Delta 5% Matched Spectrum

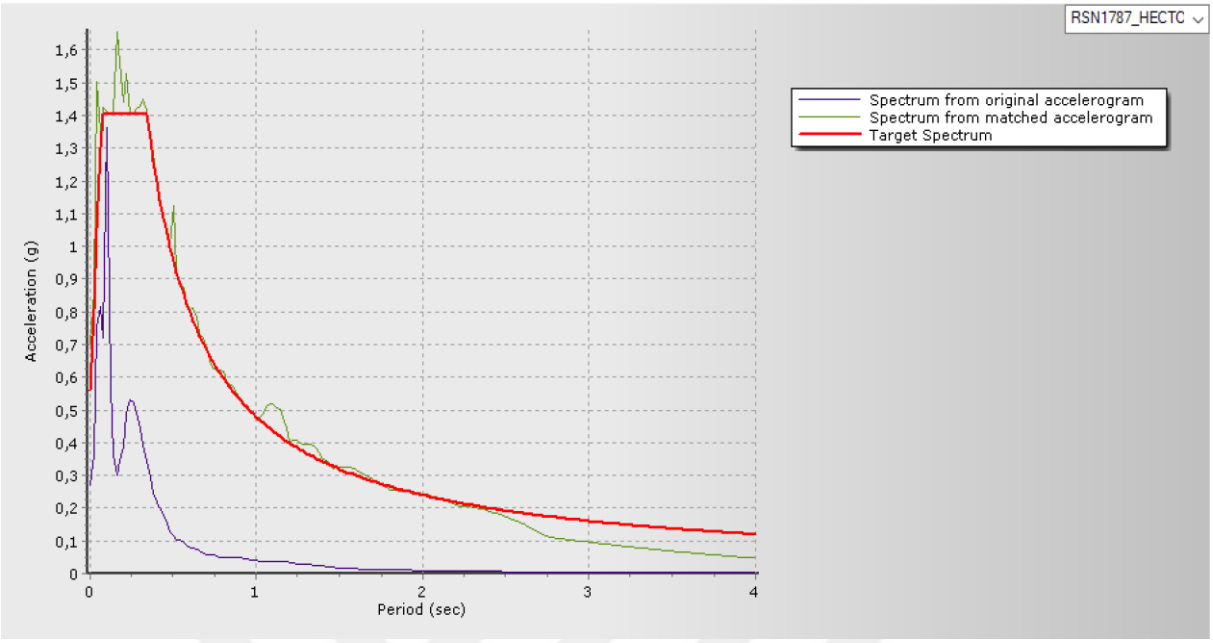

Figure 3.58: Hector 5% Matched Spectrum

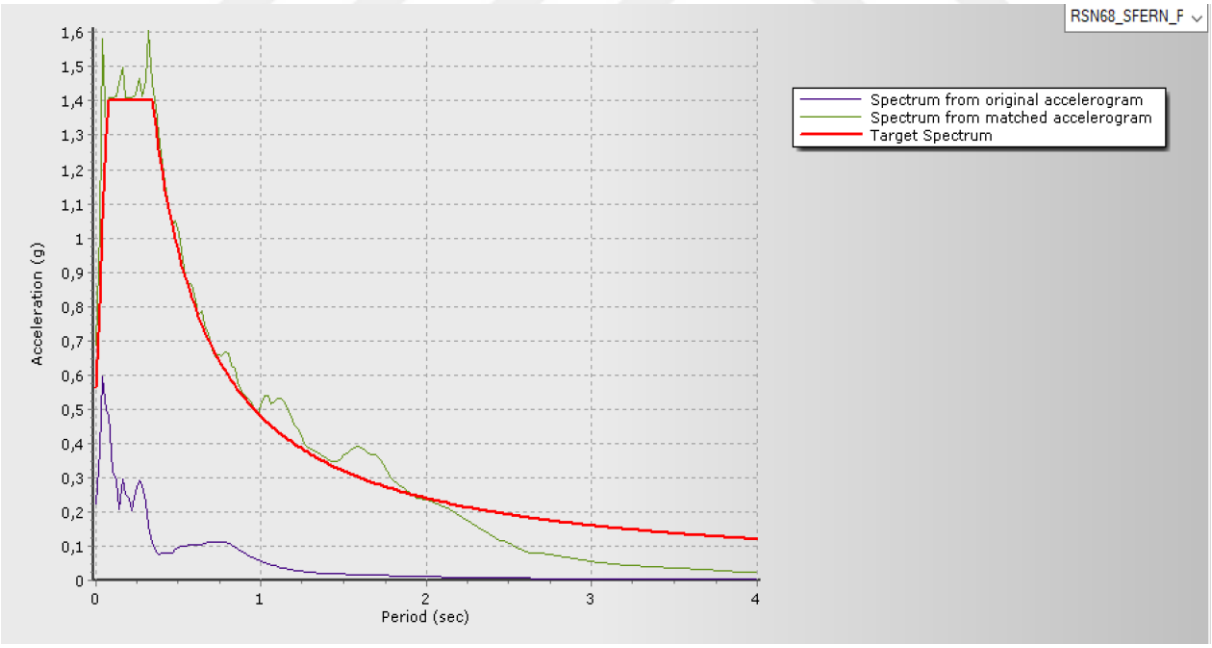

Figure 3.59: L.A Hollywood 5% Matched Spectrum

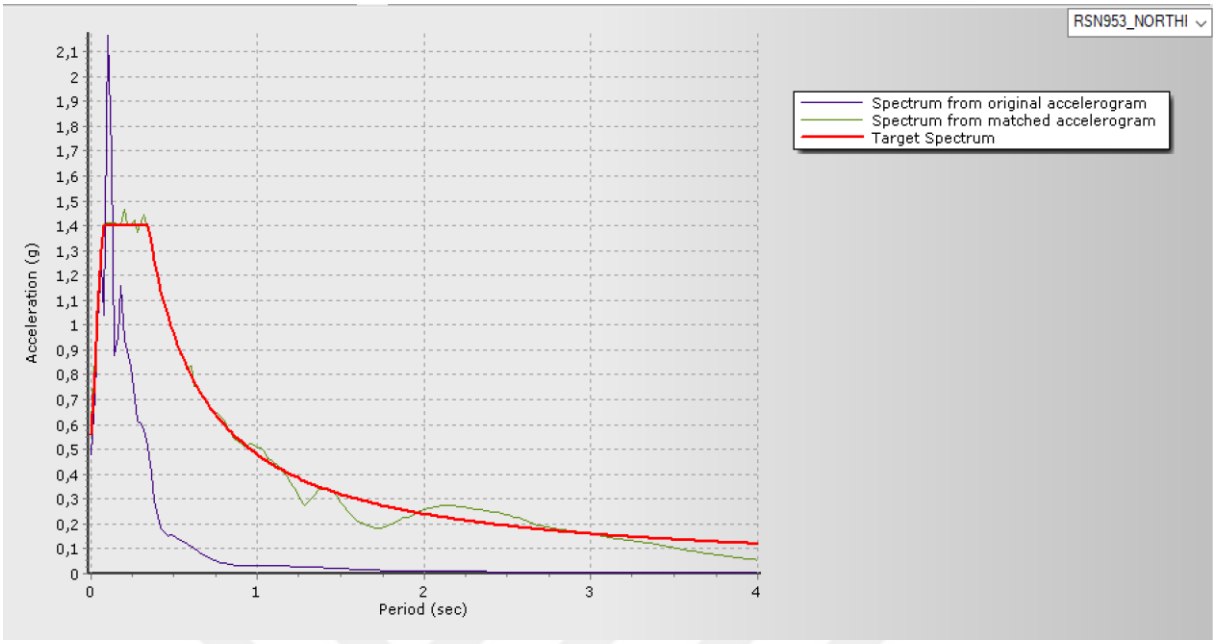

Figure 3.60: Beverly Hills 5% Matched Spectrum

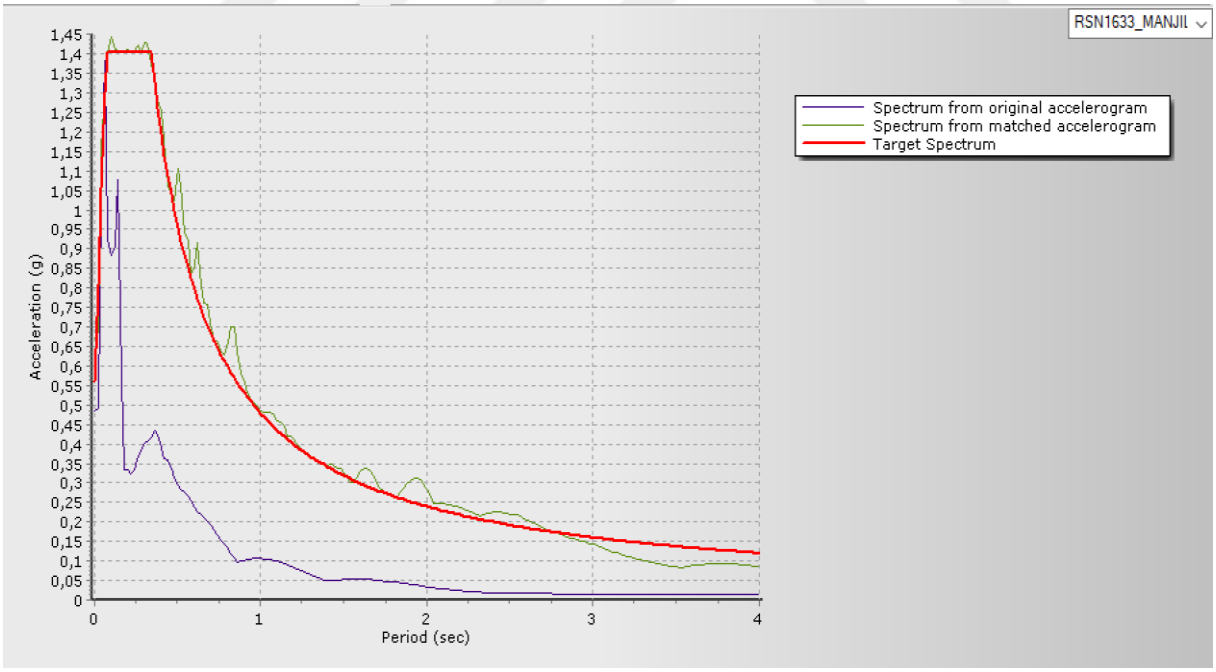

Figure 3.61: Abbar 5% Matched Spectrum

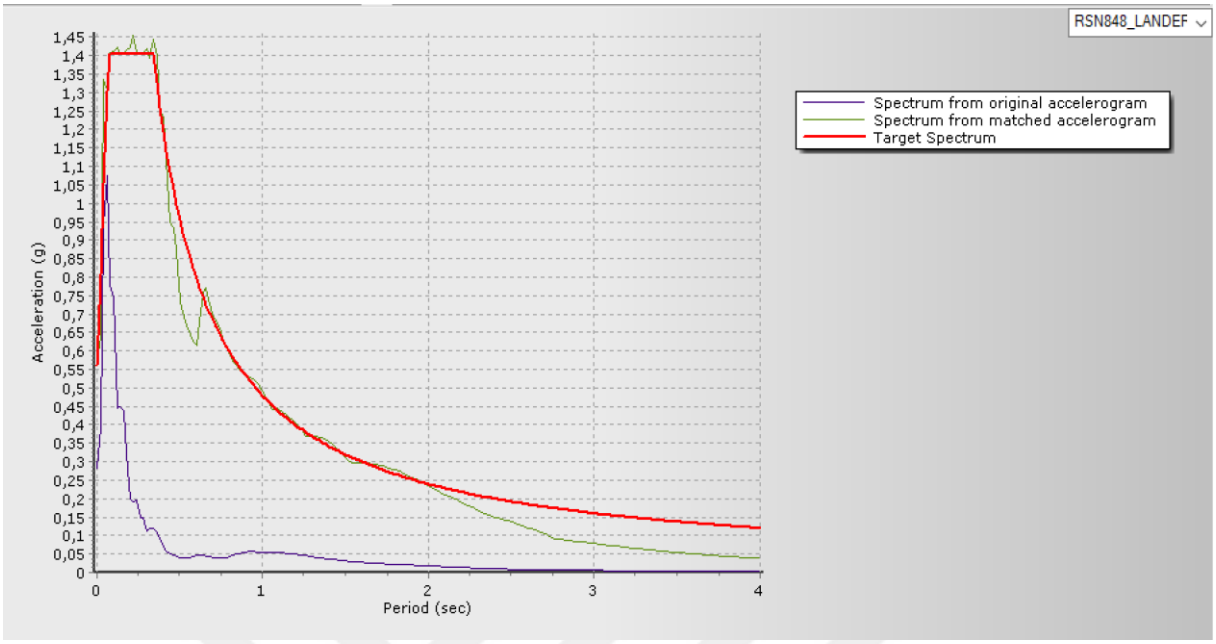

Figure 3.62: Coolwater 5% Matched Spectrum

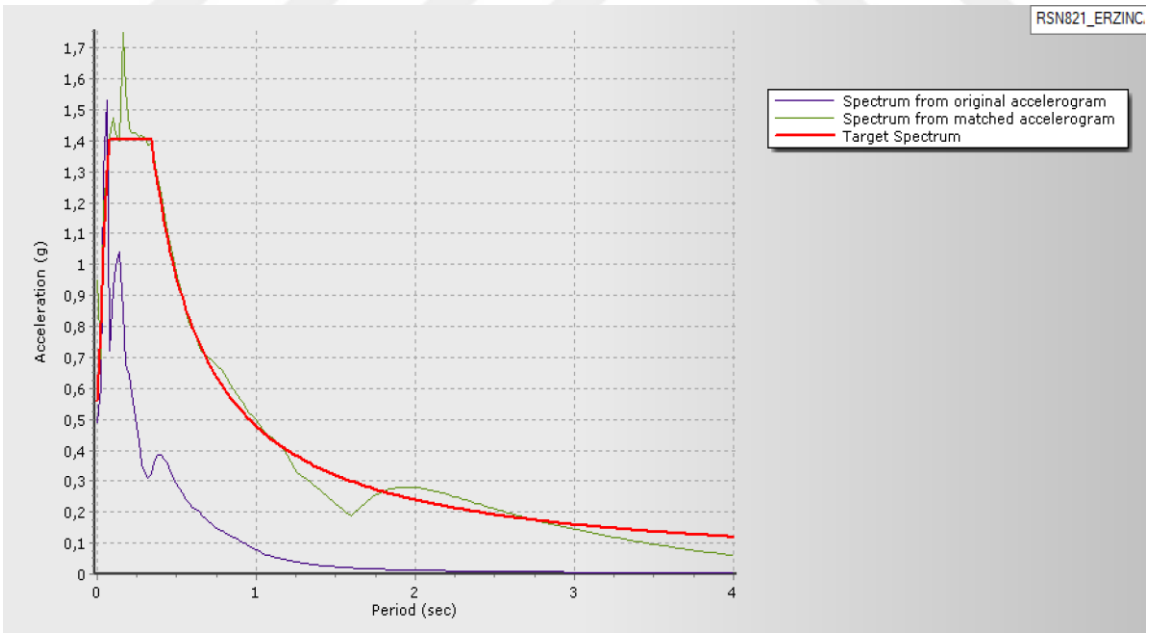

Figure 3.63: Erzincan 5% Matched Spectrum

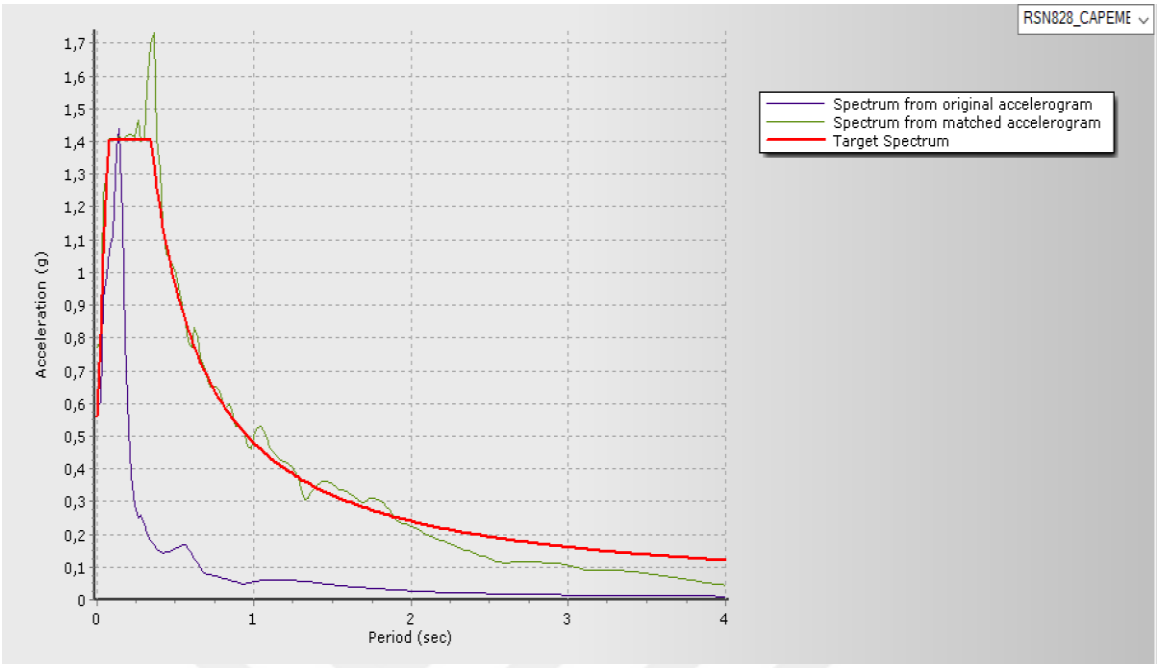

Figure 3.64: Petrolia 5% Matched Spectrum

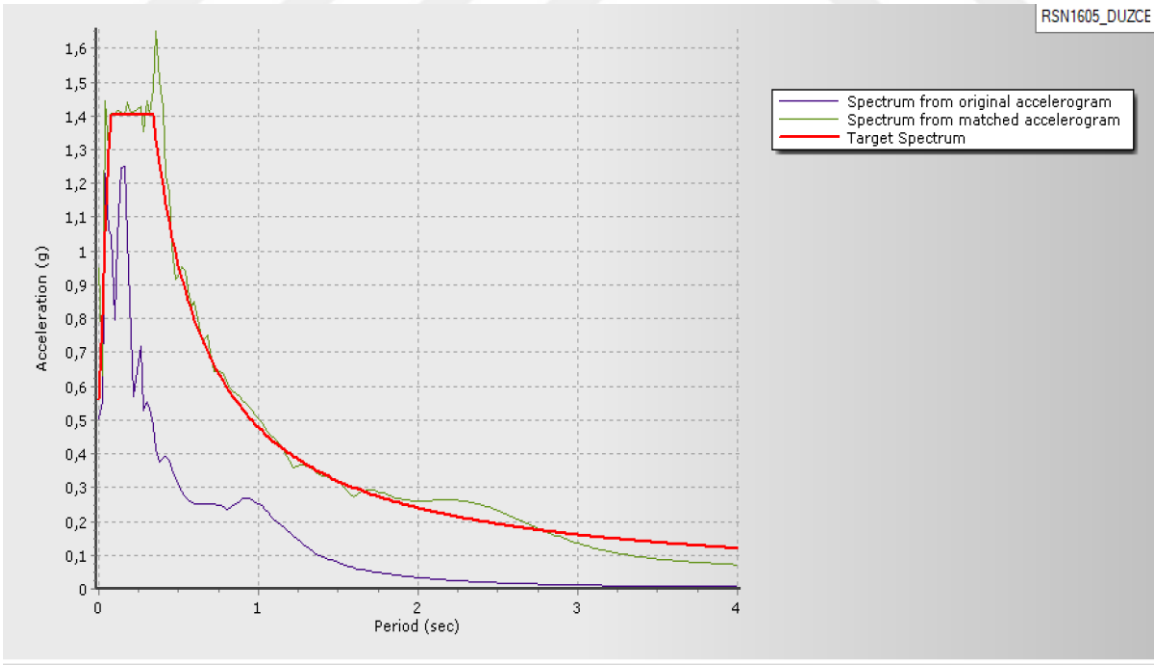

Figure 3.65: Duzce 5% Matched Spectrum

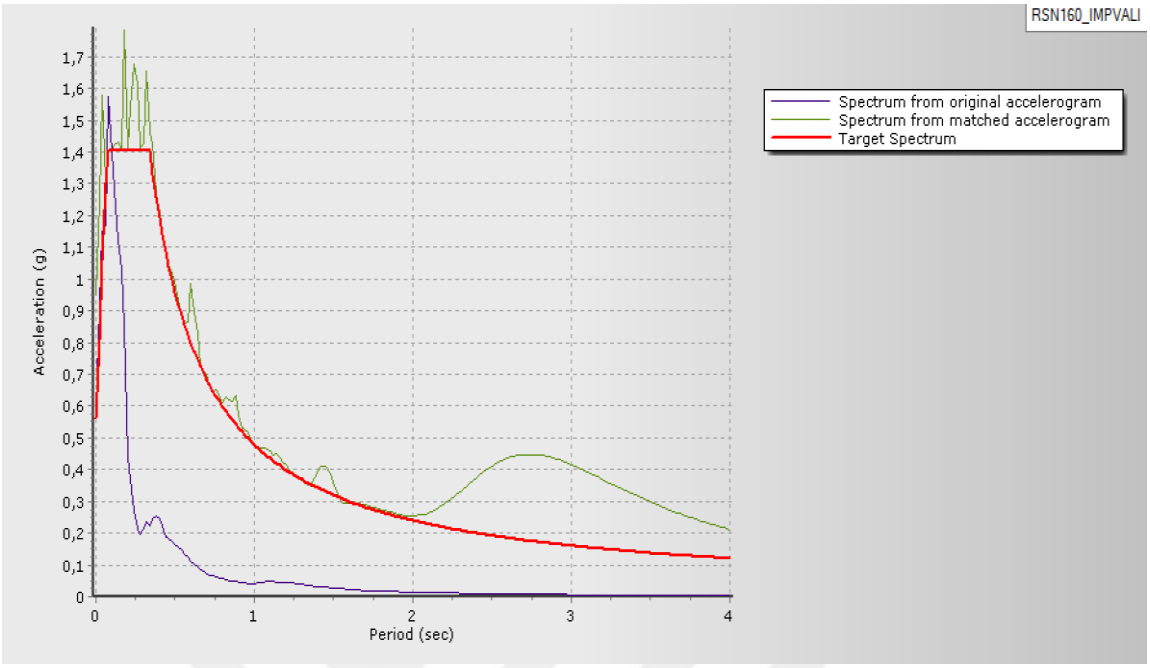

Figure 3.66: Bonds Corner 5% Matched Spectrum

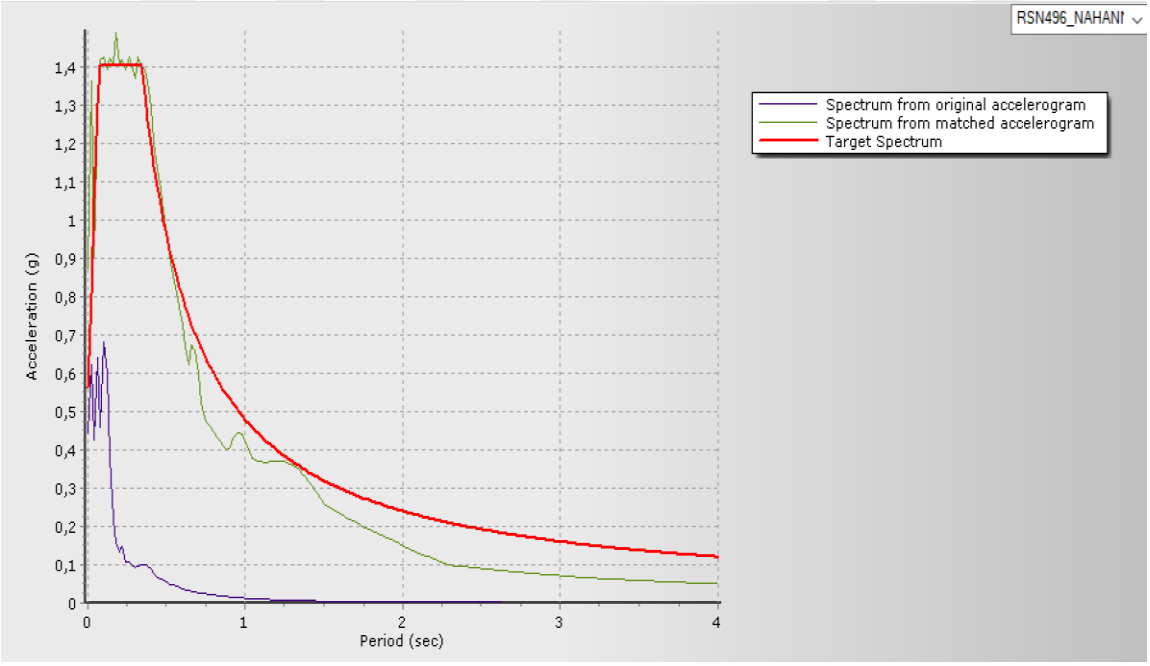

Figure 3.67: Nahanni Site 2 5% Matched Spectrum

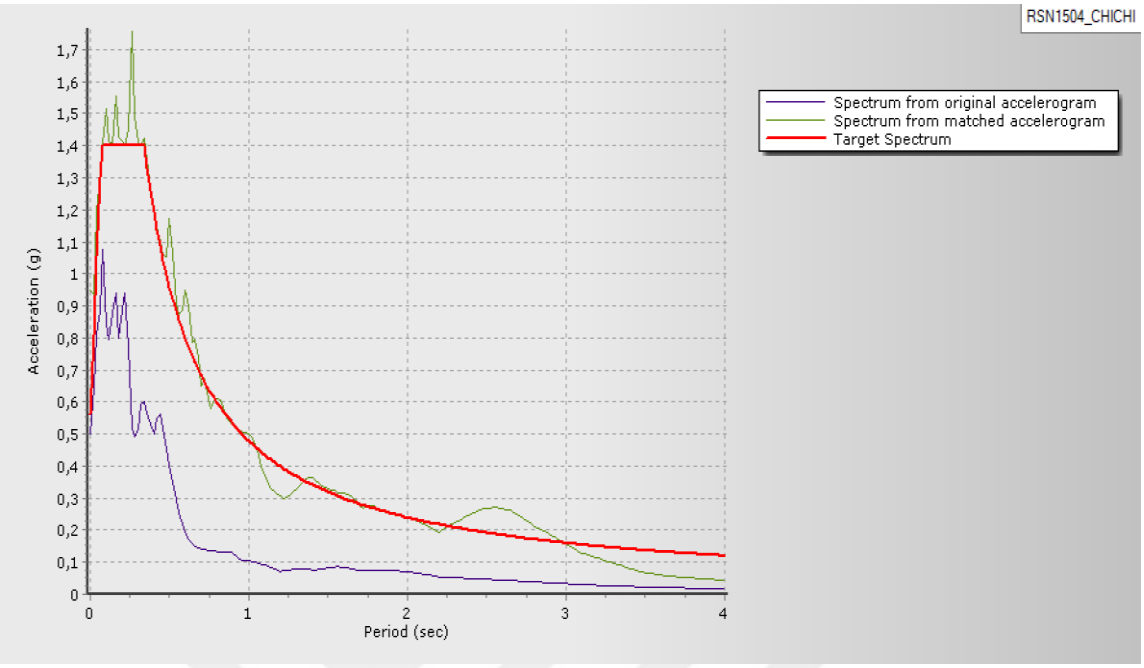

Figure 3.68: ChiChi TCU067 5% Matched Spectrum

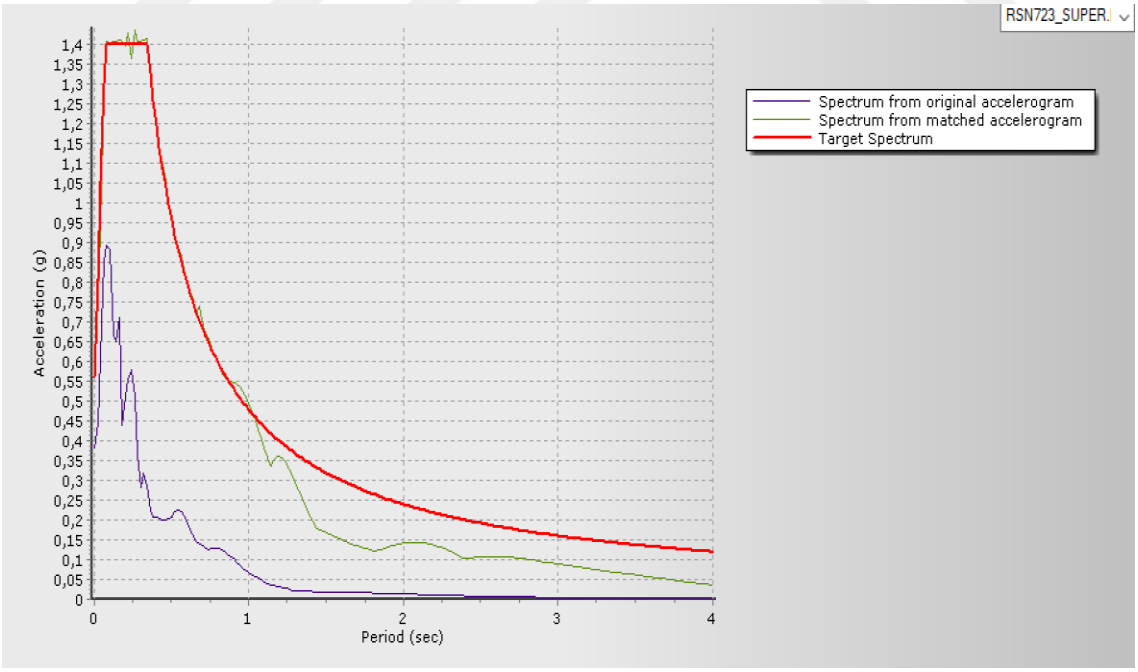

Figure 3.69: Parachute Test Site 5% Matched Spectrum

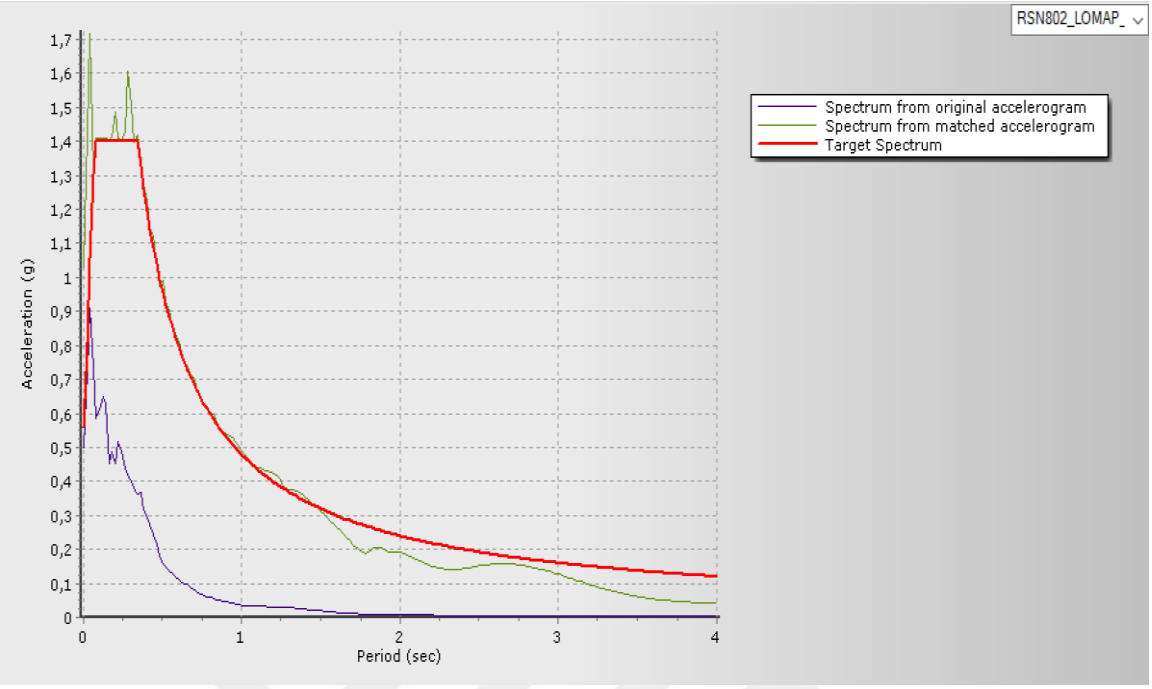

Figure 3.70: Saratoga 5% Matched Spectrum

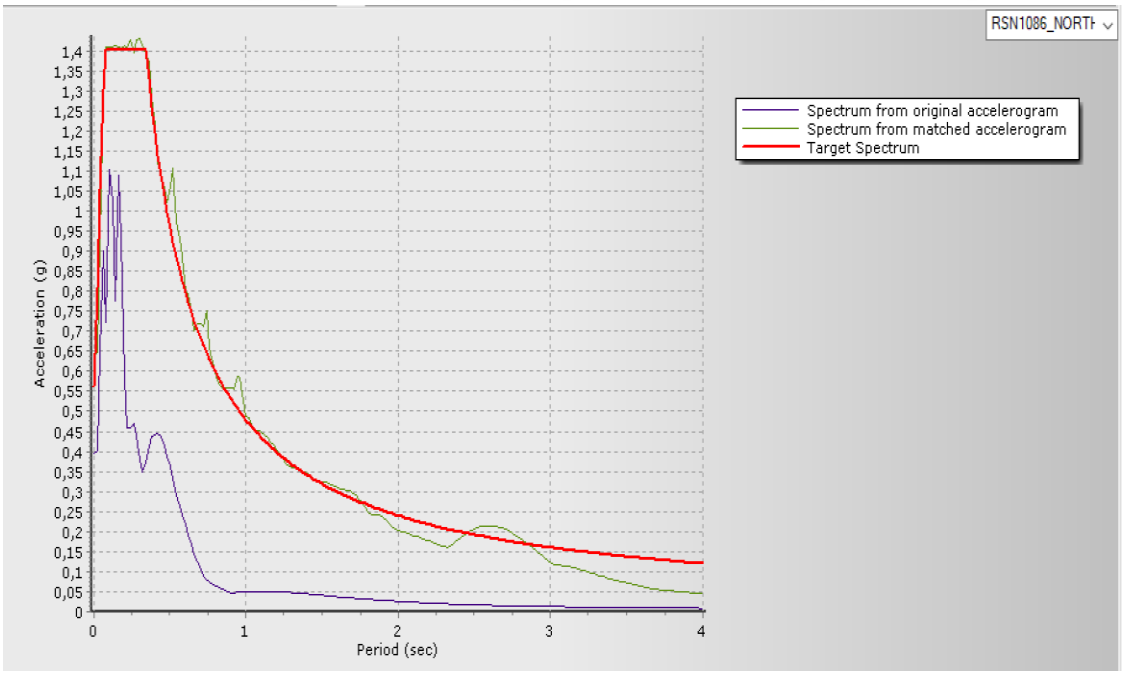

Figure 3.71: Sylmar 5% Matched Spectrum

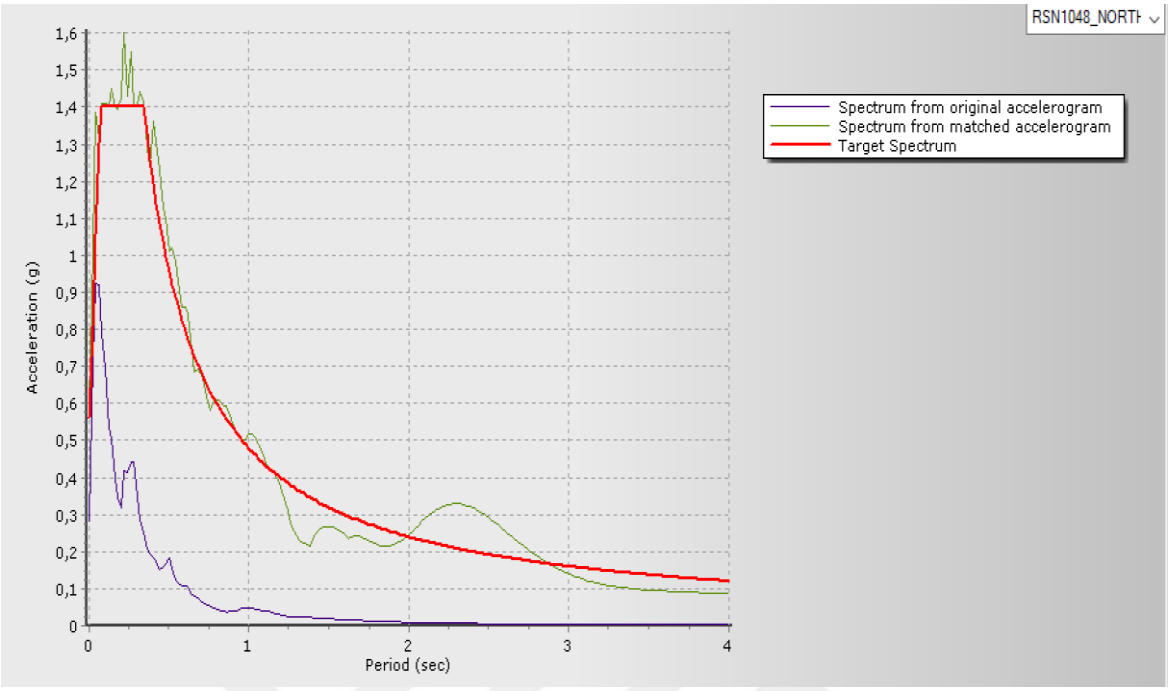

Figure 3.72: Saticoy 5% Matched Spectrum

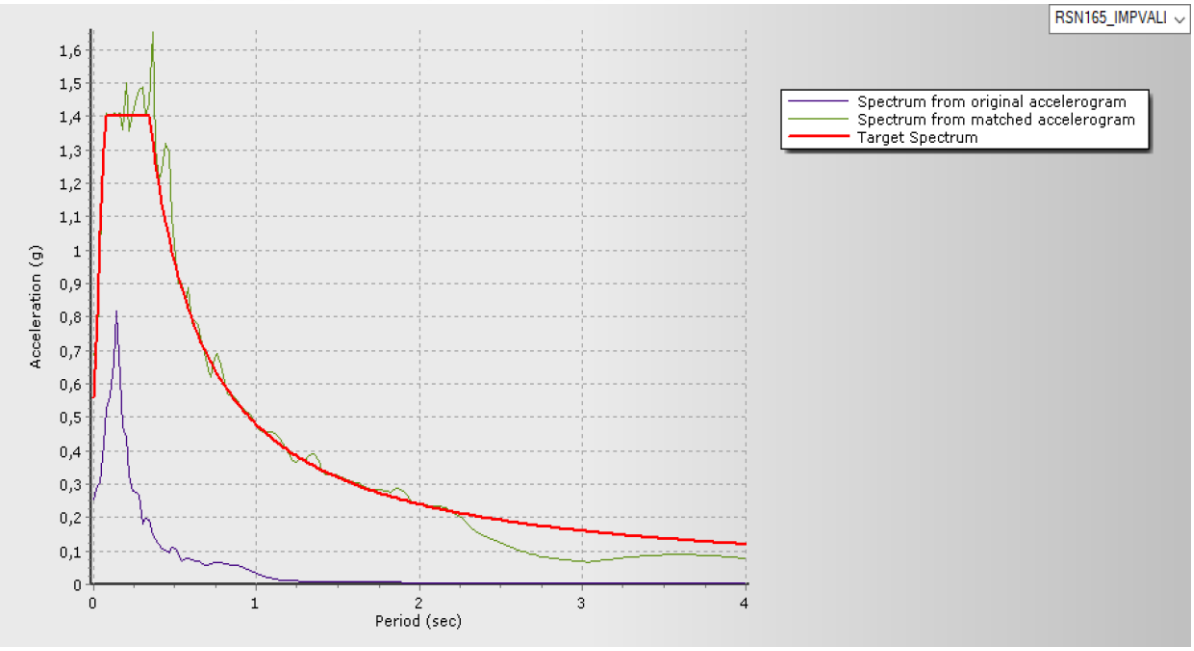

Figure 3.73: Chihuahua 5% Matched Spectrum

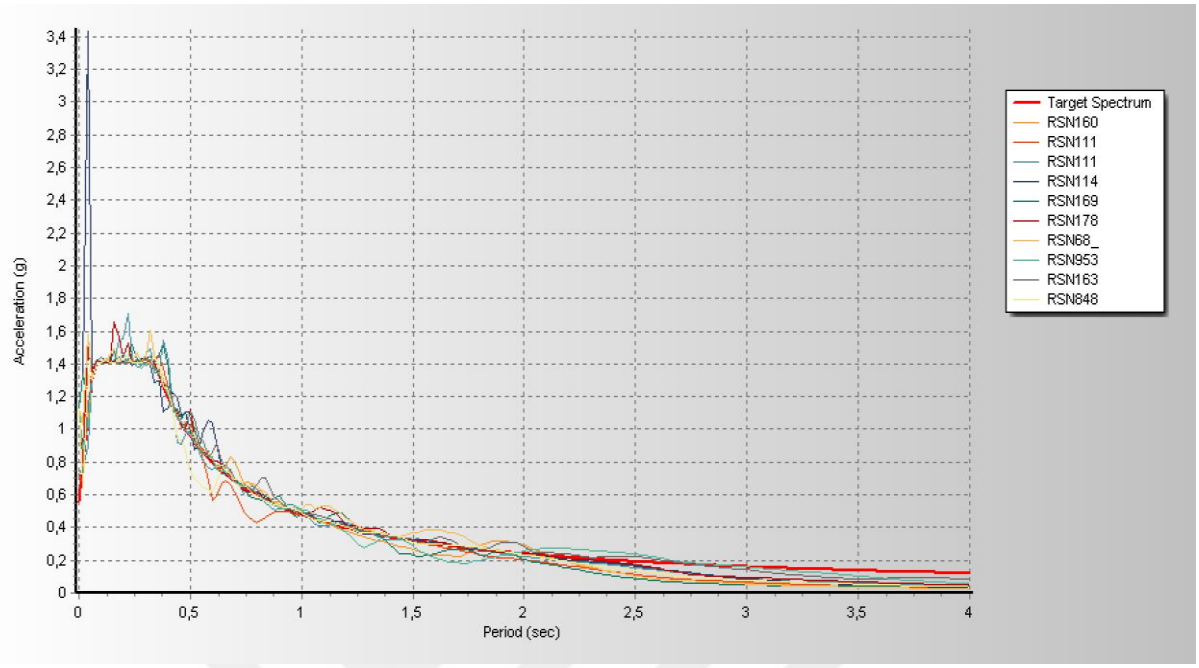

Figure 3.74: Far-Field 5% Target Spectrum and Matched Ground Motion Spectrums

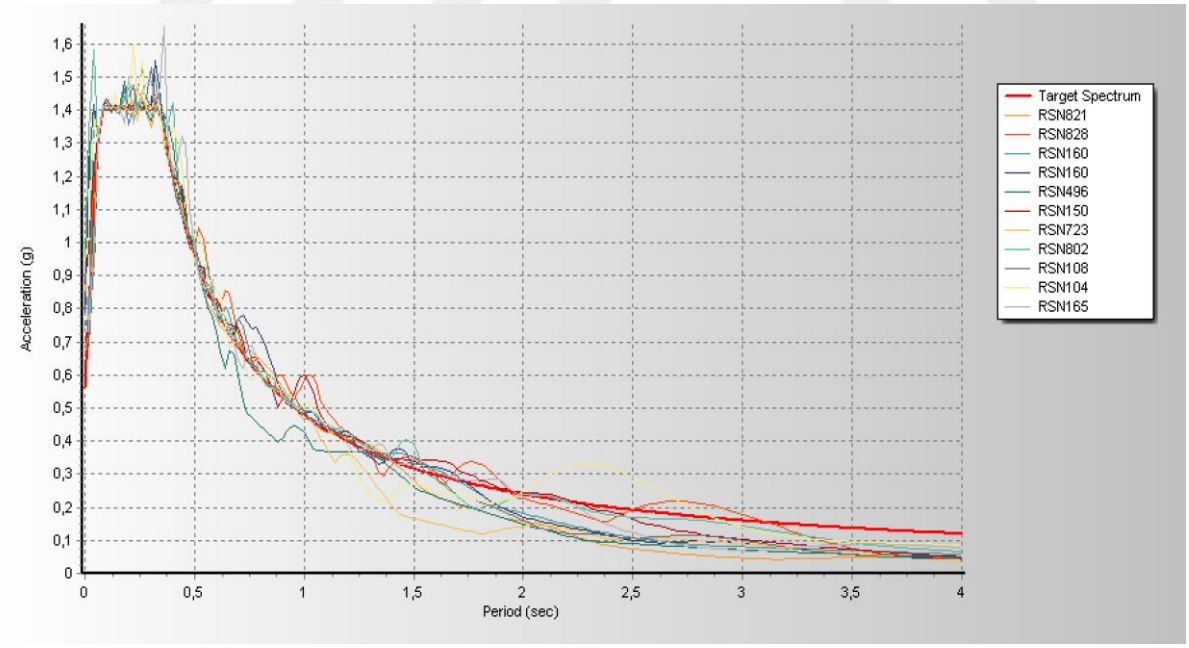

Figure 3.75: Near-Field 5% Target Spectrum and Matched Ground Motion Spectrums

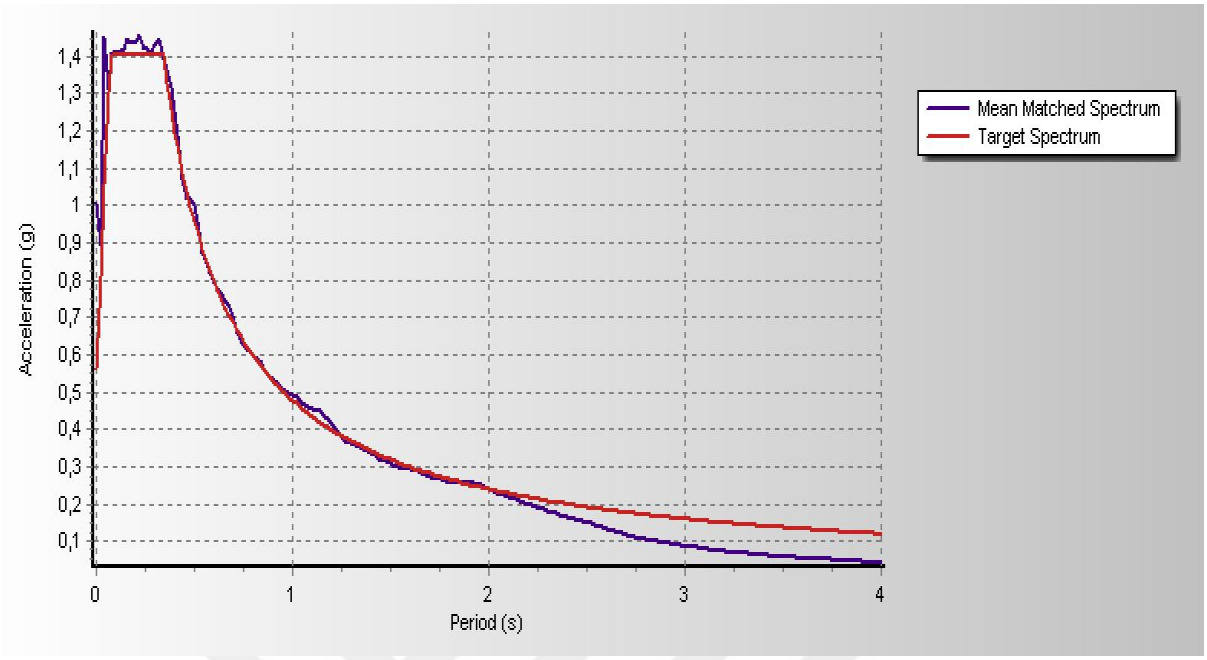

Figure 3.76: Far-Field 5% Target Spectrum and 5% Mean Spectrum

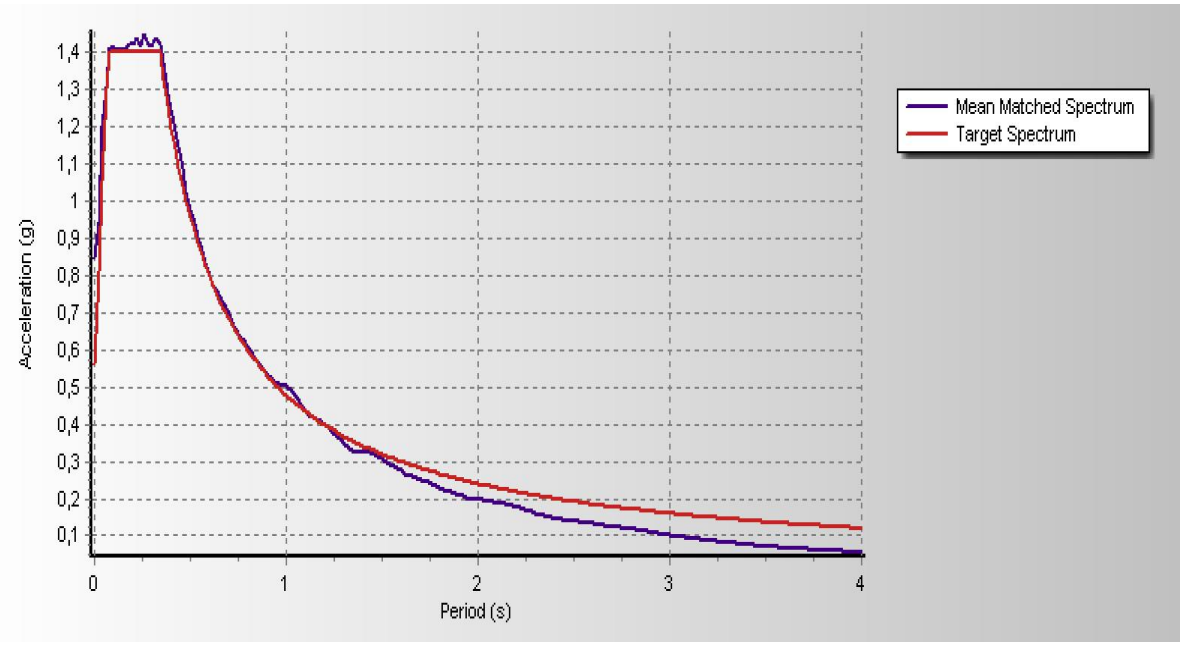

Figure 3.77: Near-Field 5% Target Spectrum and 5% Mean Spectrum

CHAPTER 4

ANALYSIS RESULTS

4.1 General

Time history analysis (THA) of fixed and TFP isolated building models were analysed using Opensees under different horizontal ground motions scaled to region response spectrum to simulate the real site behaviour and assess the structural performance. The fixed based and TFP isolated structure periods were obtained through modal analysis. The fixed period of 0.52s was increased to a period value approximately 6 times after application of triple frictional pendulum isolator. The analysis results show significant decrease in story acceleration, story shear and inter-story drift. As shown in Figure 1.5, these parameters decrease with increase in the structural fundamental period but in contrary to the story displacement. The con of increasing the structural period is that it may increase bearing displacements. In addition, the effect of varying frictional coefficient of the surfaces are assessed to check the base shear and bearing displacement effects. Moreover, influence of the change on bearing friction due to factors such as contamination is evaluated.

4.2 Performance of TFP Isolated Structure

4.2.1 Story Shear

Story shear decreases with increase in story height as shown in Figure 4.1-4.21. It also shown that rigid structures such as fixed based exhibit greater story shear. TFP isolators have drastically decreased story shear of the structure. The isolator reduced up to 90% respectively of story shear in most analysed motion records. The isolation system is observed to be more effective in far-field ground motions with a maximum reduction of 96%.

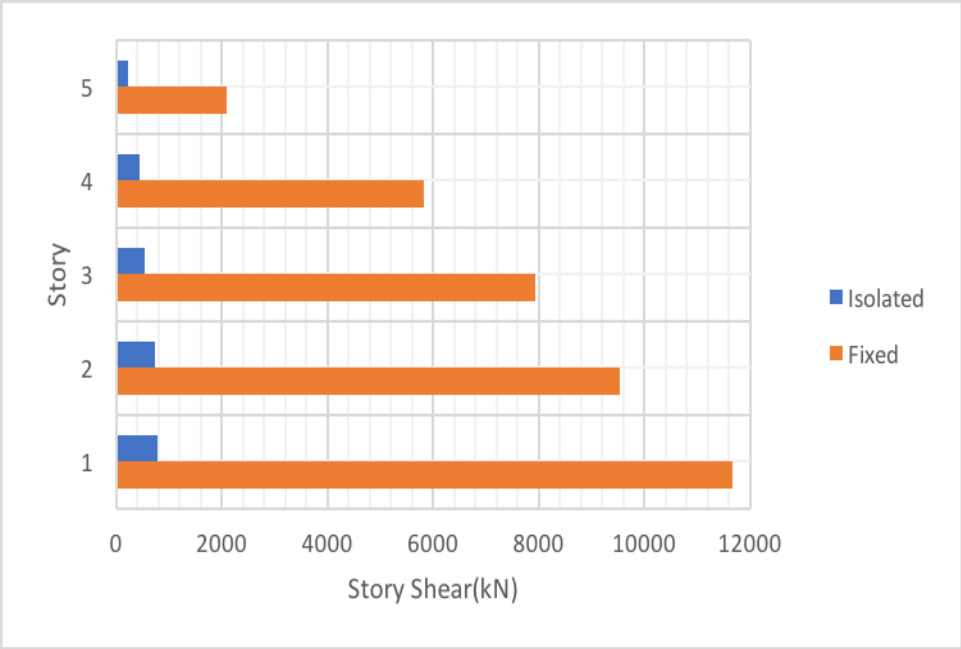

Figure 4.1: Maximum Base Shear Bolu – X direction

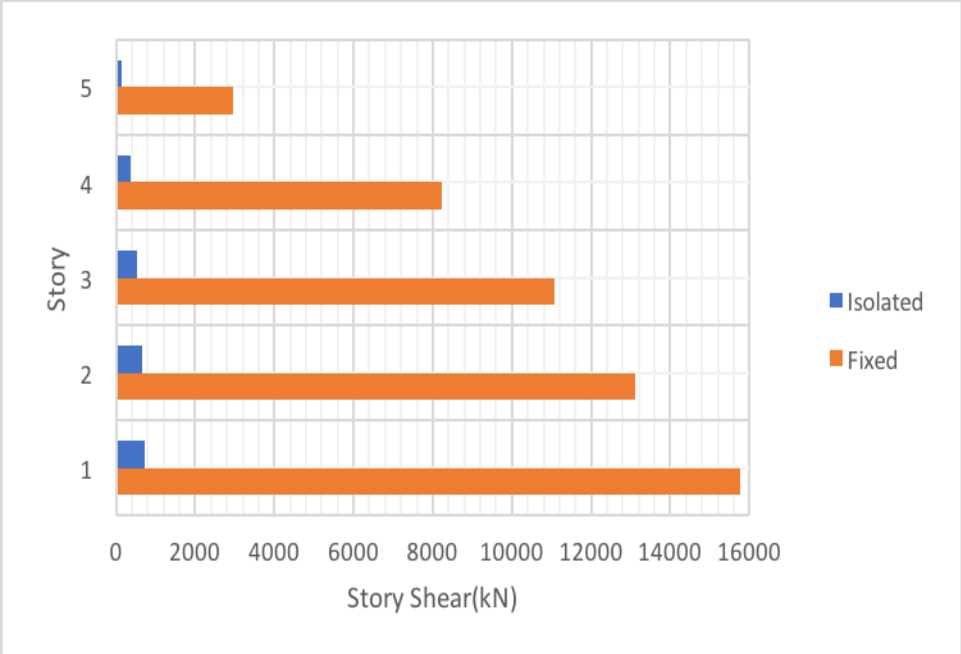

Figure 4.2: Maximum Base Shear Nishi Akashi – X direction

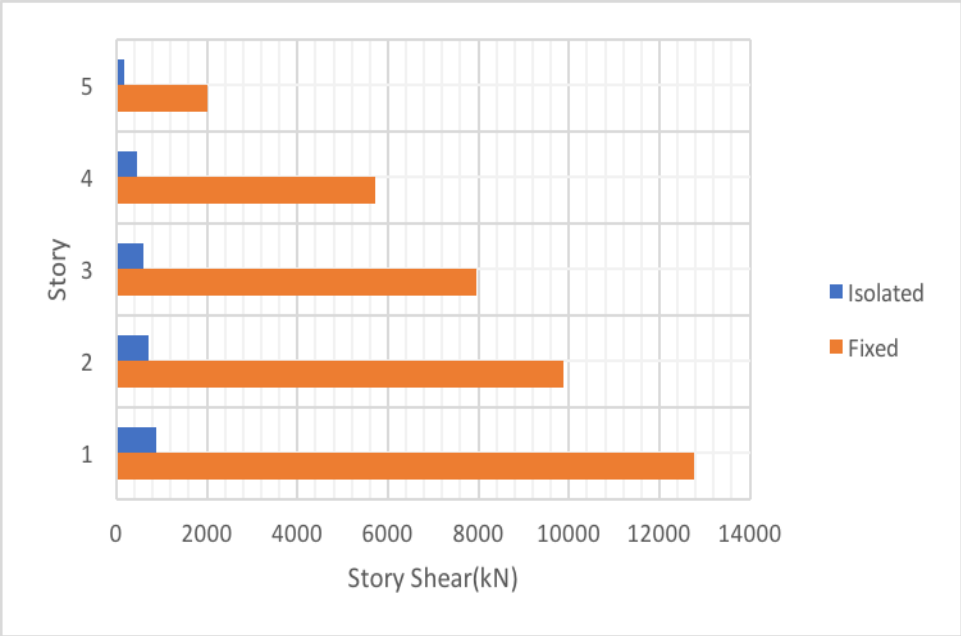

Figure 4.3: Maximum Base Shear Shin Osaka – X direction

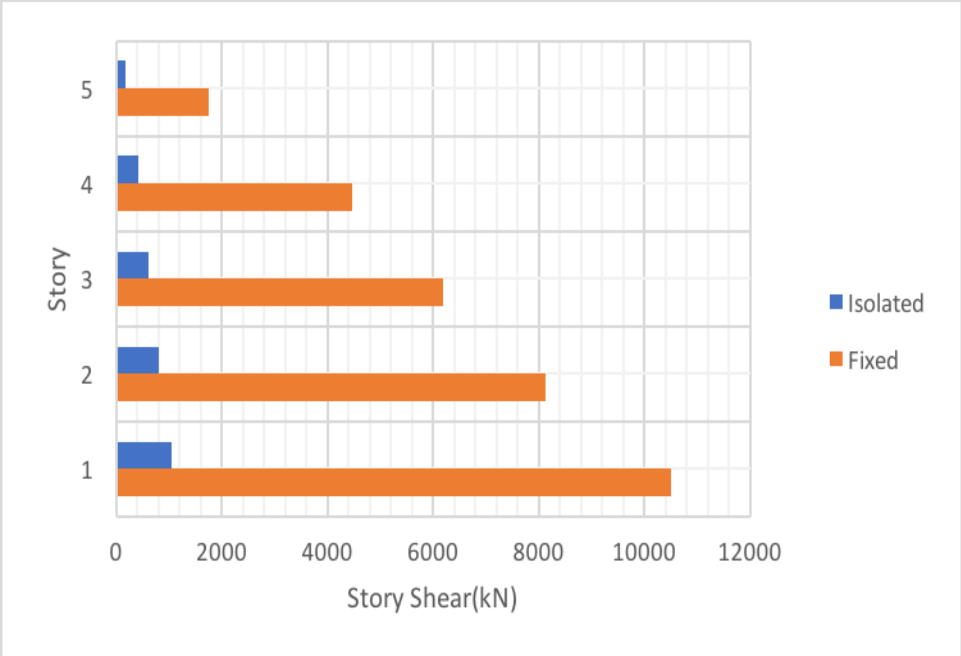

Figure 4.4: Maximum Base Shear Arcelik – X direction

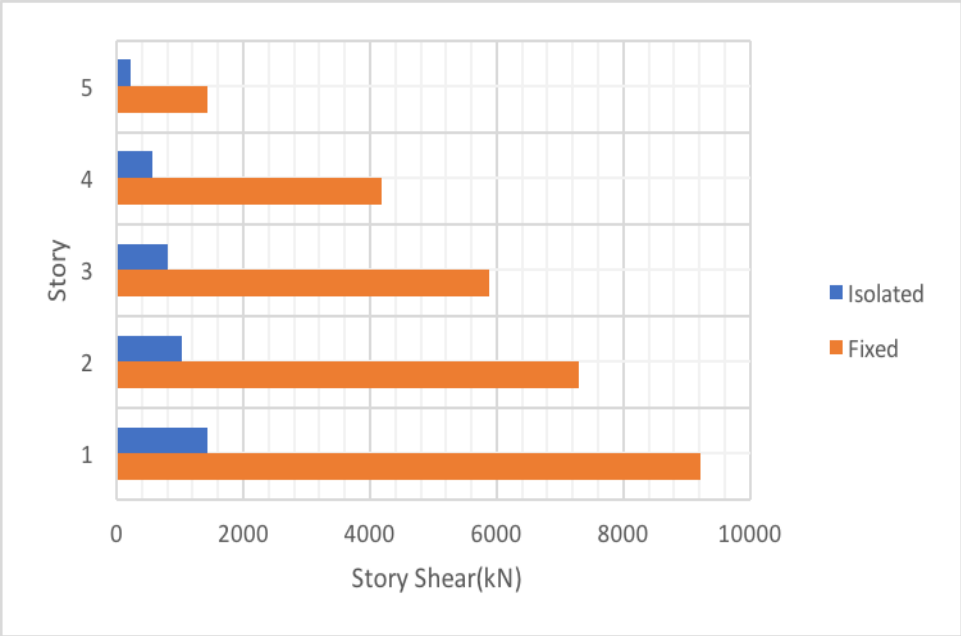

Figure 4.5: Maximum Base Shear Delta – X direction

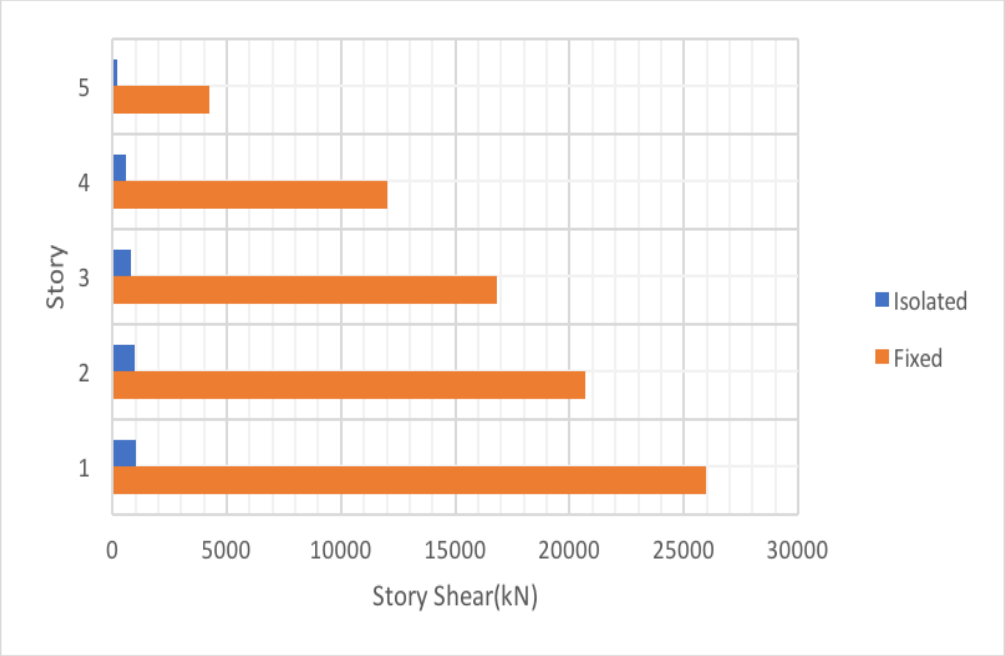

Figure 4.6: Maximum Base Shear Hector – X direction

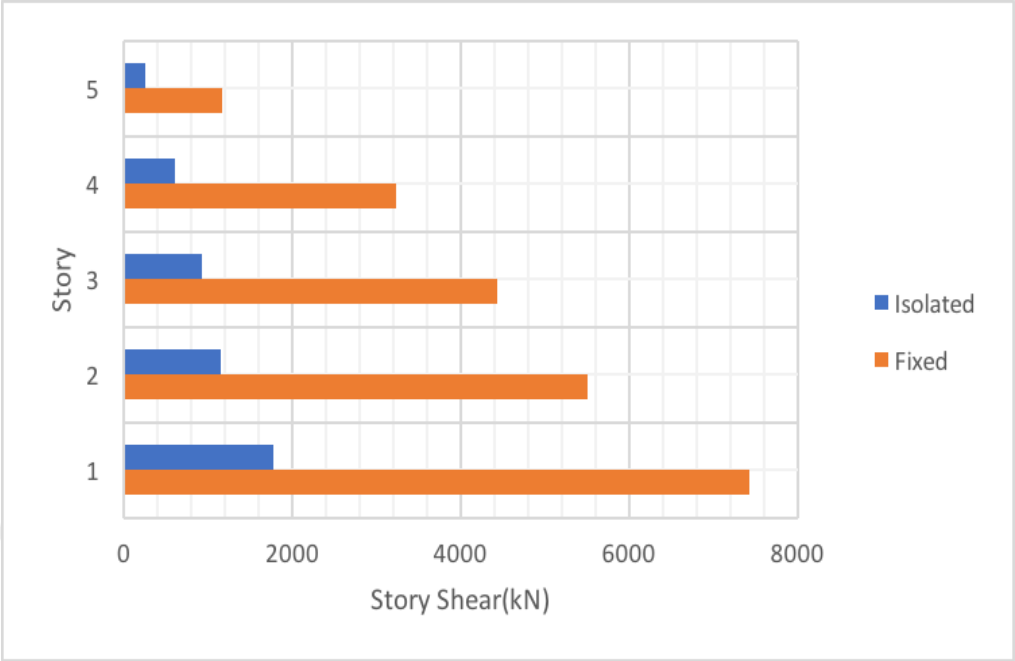

Figure 4.7: Maximum Base Shear L.A Hollywood – X direction

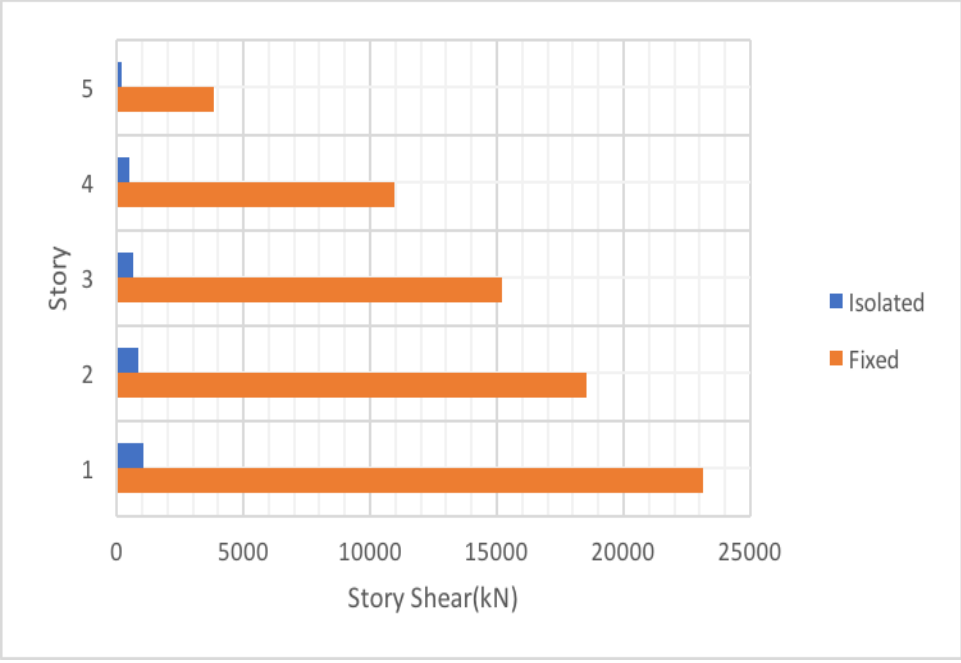

Figure 4.8: Maximum Base Shear Beverly Hills – X direction

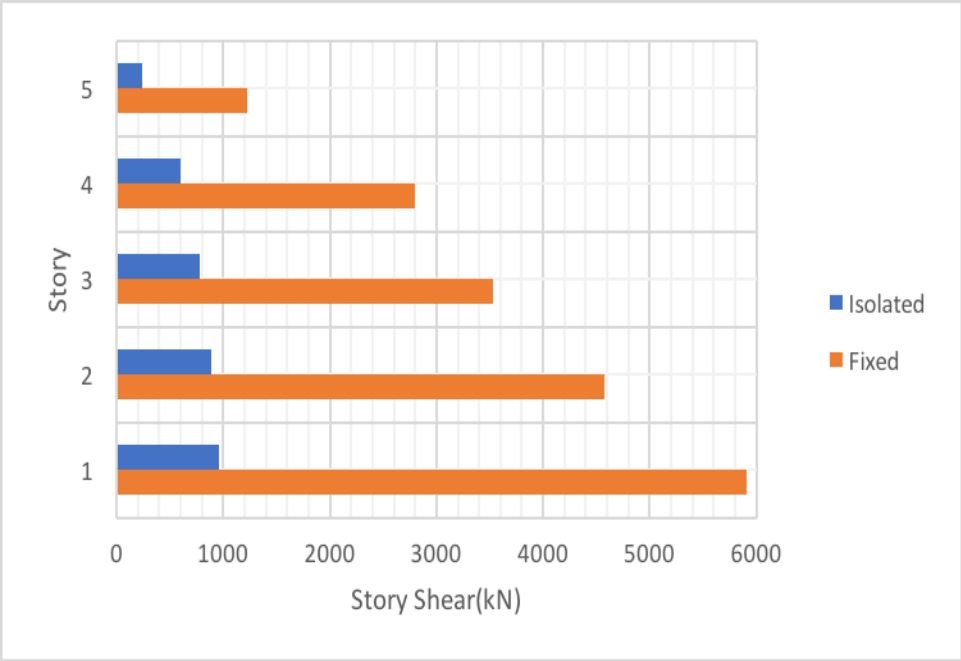

Figure 4.9: Maximum Base Shear Abbar – X direction

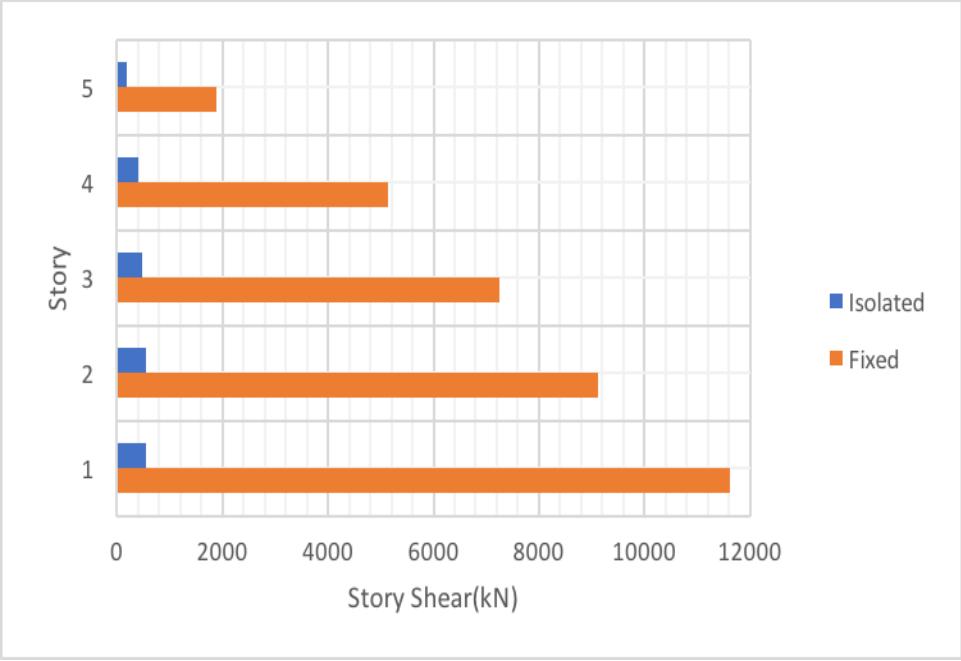

Figure 4.10: Maximum Base Shear Coolwater – X direction

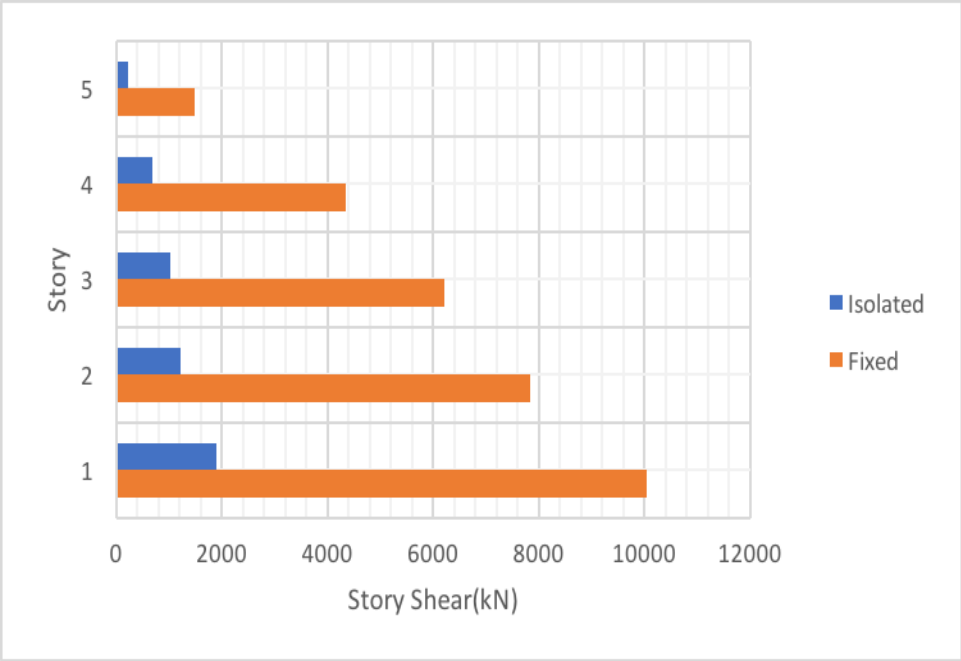

Figure 4.11: Maximum Base Shear Erzincan – X direction

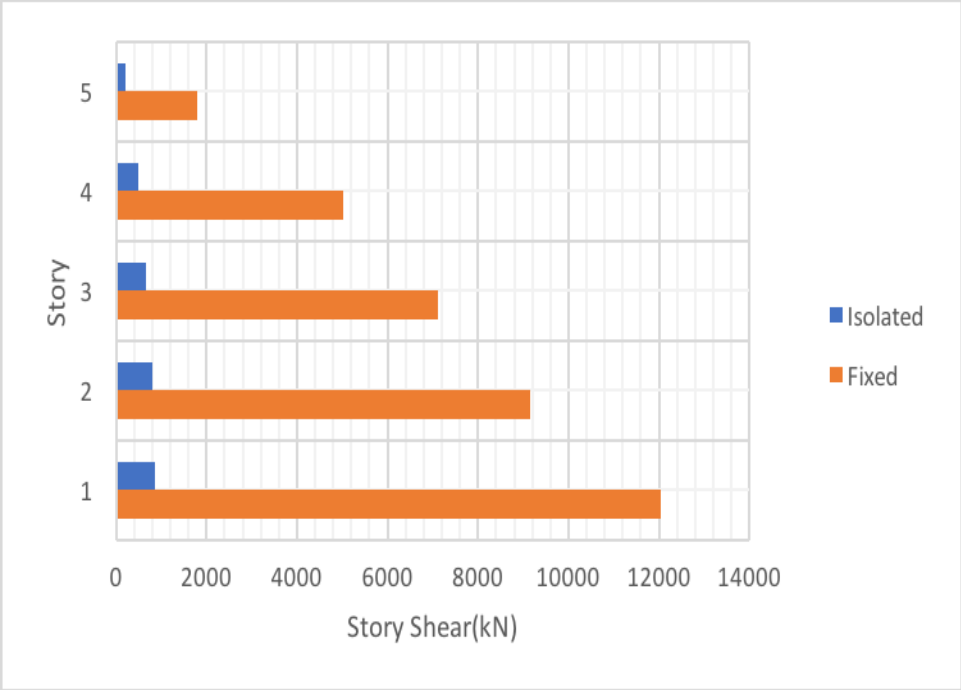

Figure 4.12: Maximum Base Shear Petrolia - X direction

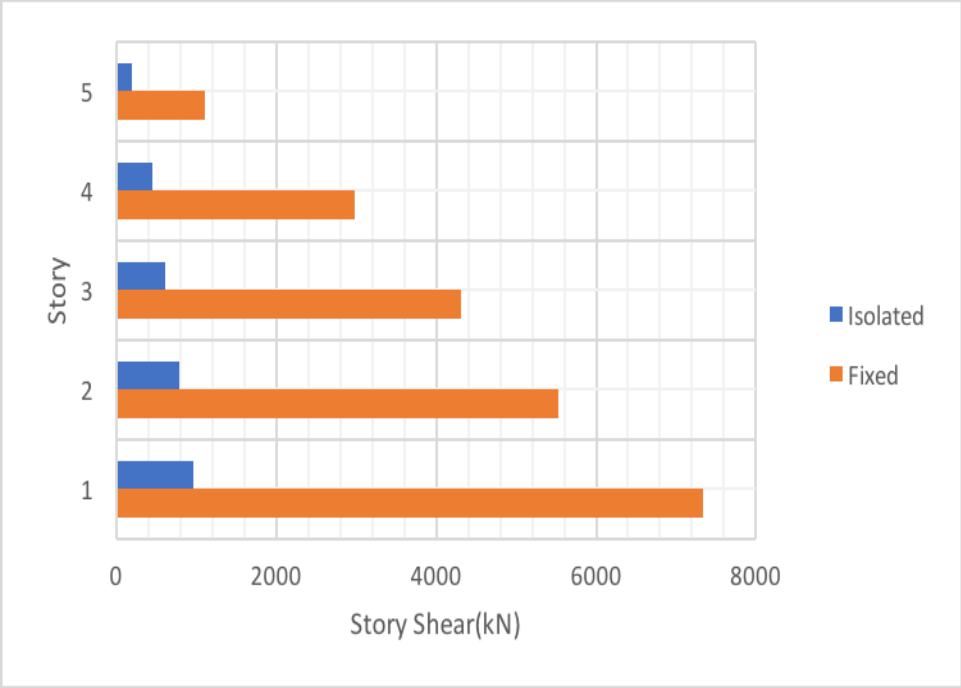

Figure 4.13: Maximum Base Shear Duzce - X direction

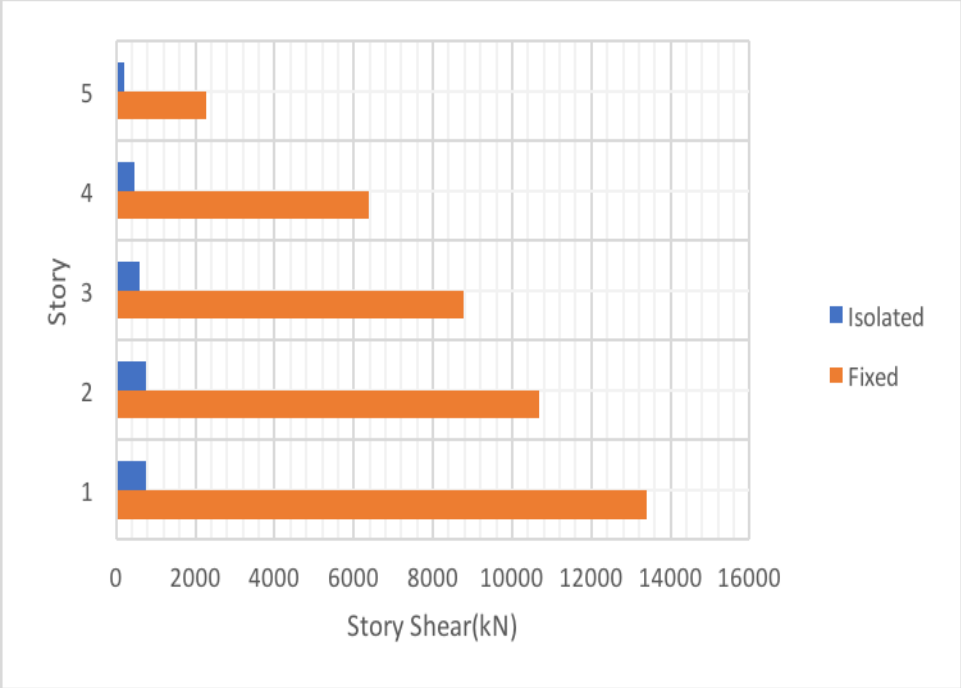

Figure 4.14: Maximum Base Shear Bonds Corner - X direction

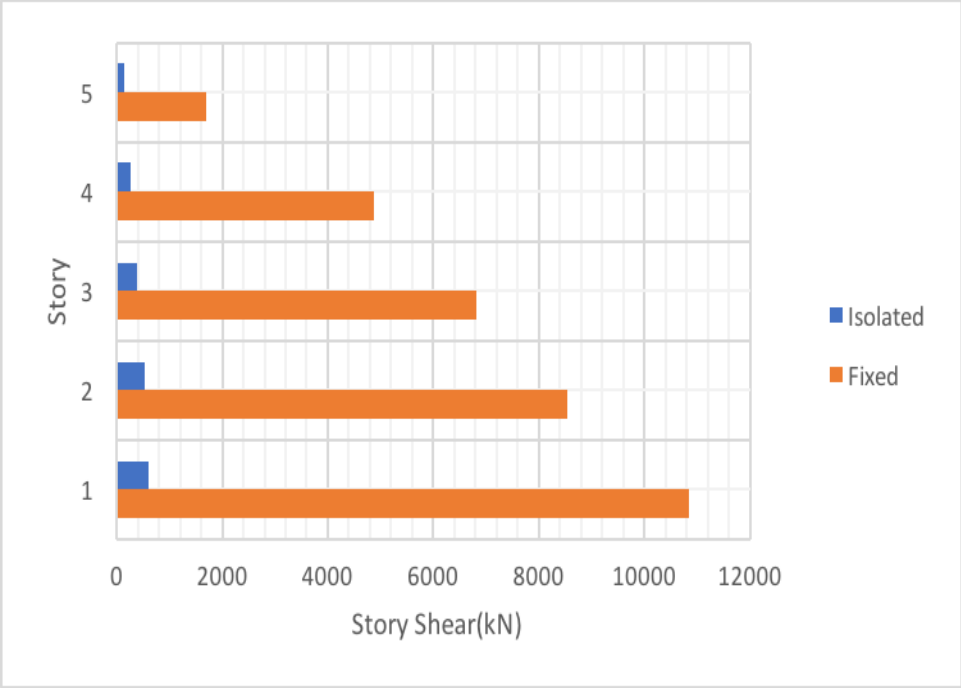

Figure 4.15: Maximum Base Shear Nahanni Site 2 - X direction

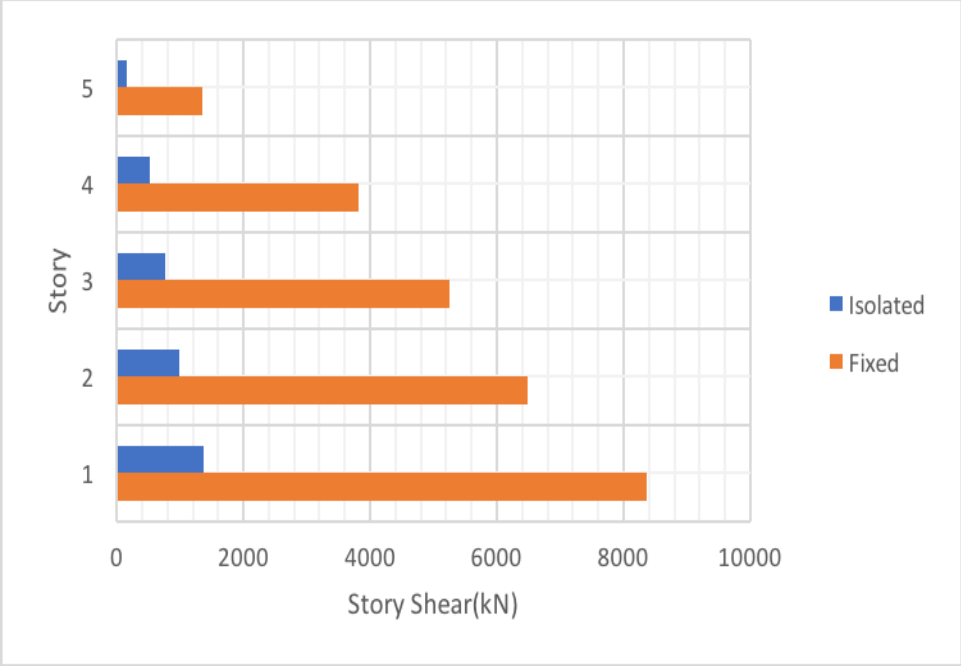

Figure 4.16: Maximum Base Shear ChiChi TCU067 - X direction

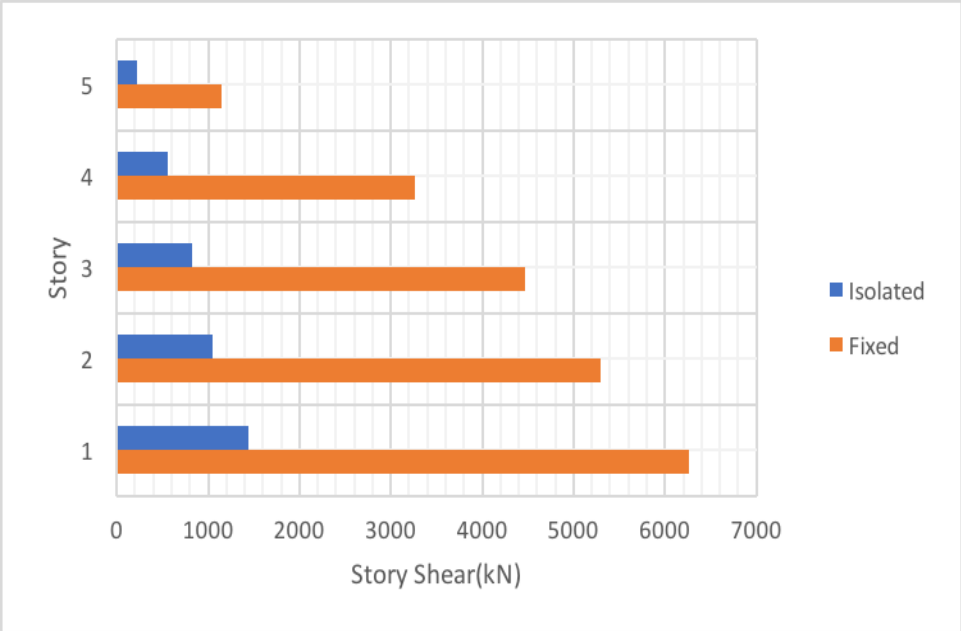

Figure 4.17: Maximum Base Shear Parachute Test Site - X direction

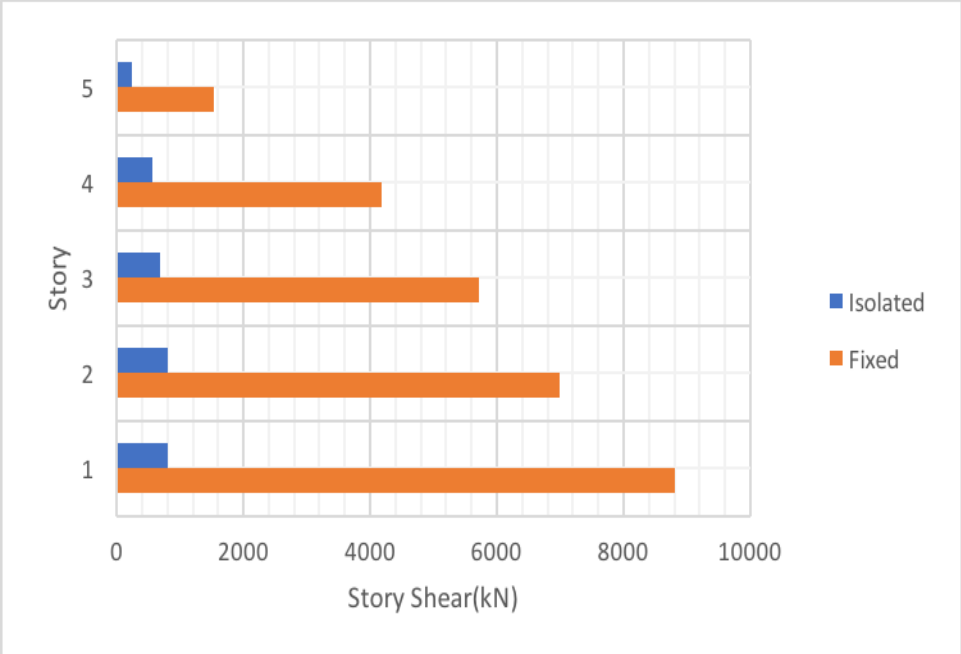

Figure 4.18: Maximum Base Shear Saratoga - X direction

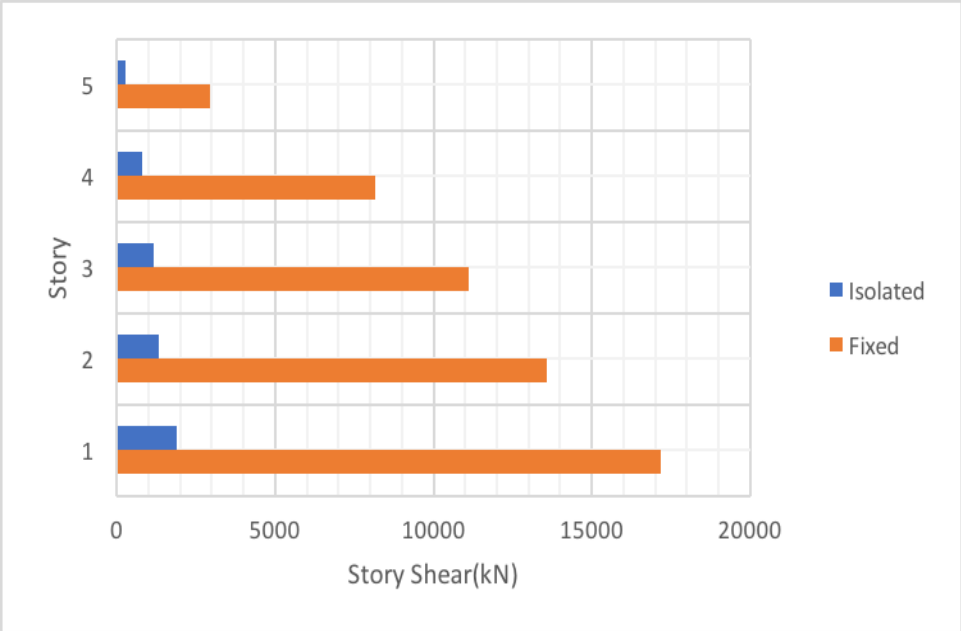

Figure 4.19: Maximum Base Shear Sylmar - X direction

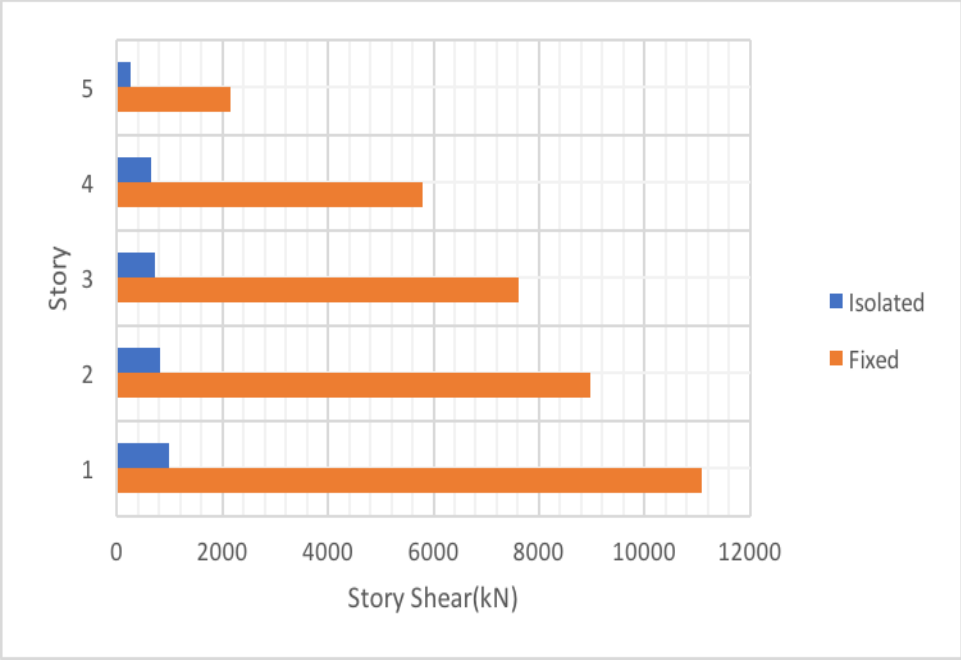

Figure 4.20: Maximum Base Shear Saticoy - X direction

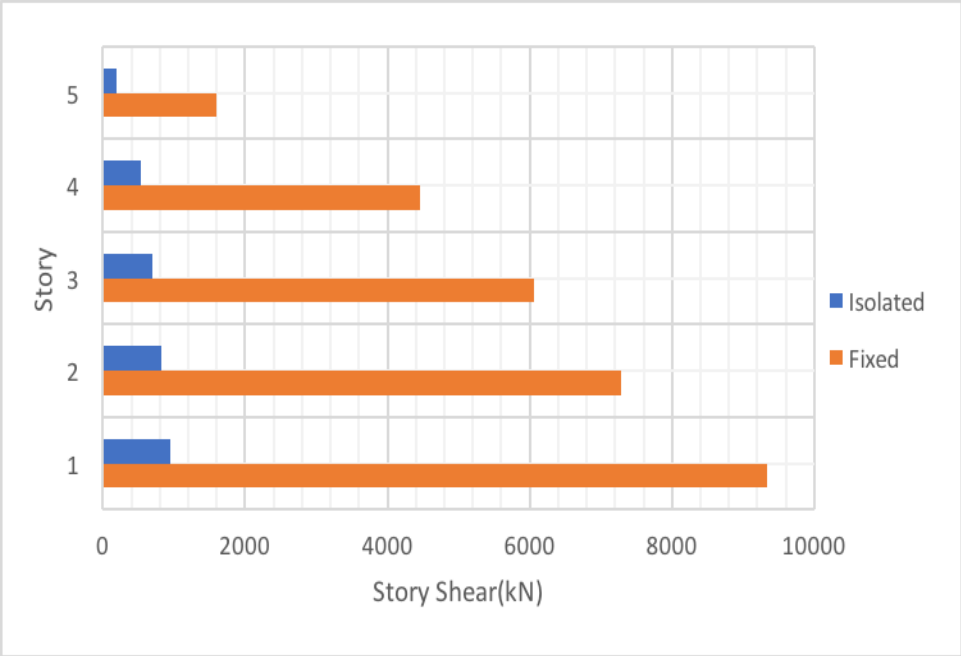

Figure 4.21: Maximum Base Shear Chihuahua - X direction

4.2.2 Inter-Story Drift

Peak inter-storey drift ratio is the maximum percentage drift between two floors divided by their storey height. The TFP isolated structure results show decrease in peak inter-story drift. Story drift for both isolated and fixed structures are shown in Figure 4.22 to Figure 4.42 decreasing at upper stories in a linear manner. Top floors have lesser story drifts compared to lower story drifts because of their low displacement values but in the case of fixed base L.A Hollywood, Abbar, Petrolia and Sylmar earthquake records, the inter-story drift of the first story is less than the second story inter-story drift which could be due to the contribution of higher modes.

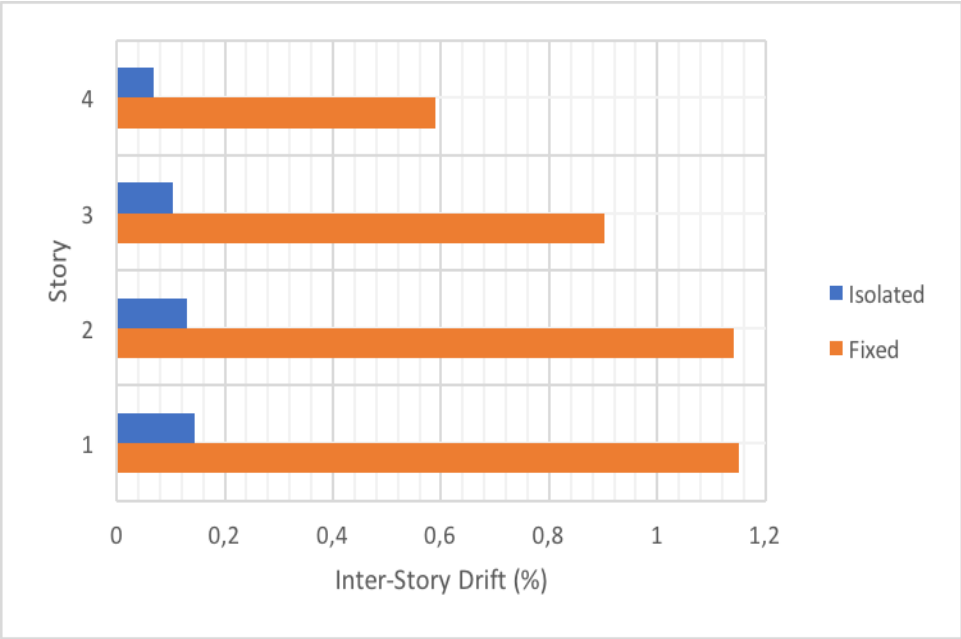

Figure 4.22: Peak Inter-Story Drift Bolu – X direction

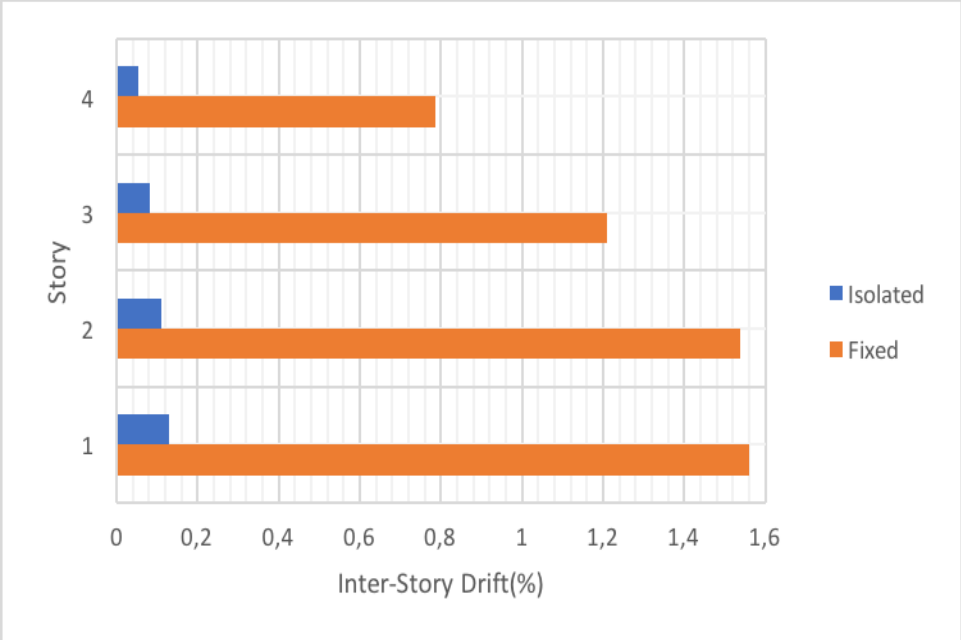

Figure 4.23: Peak Inter-Story Drift Nishi Akashi – X direction

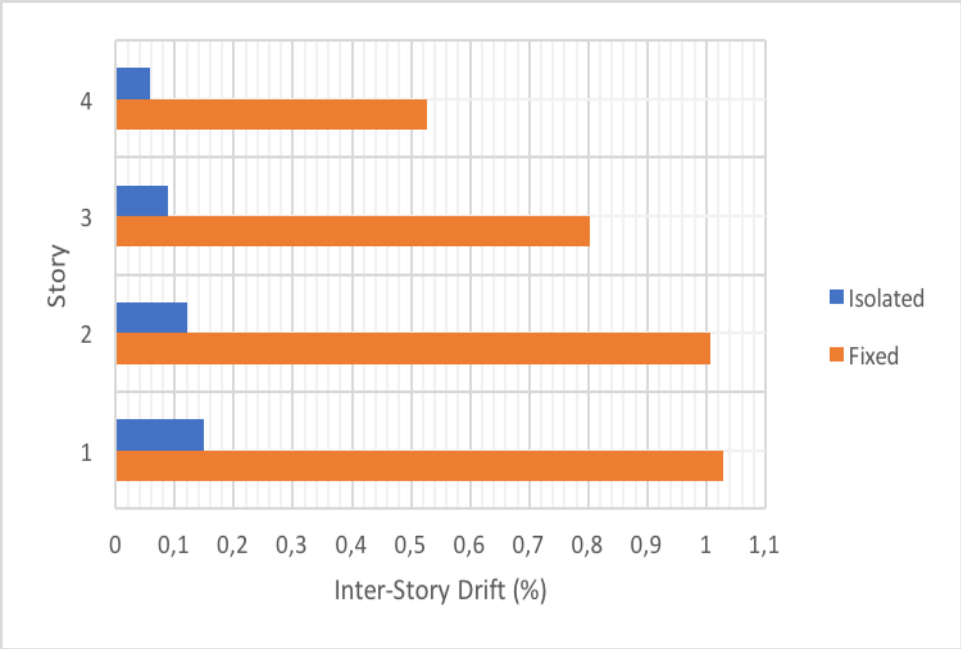

Figure 4.24: Peak Inter-Story Drift Shin Osaka – X direction

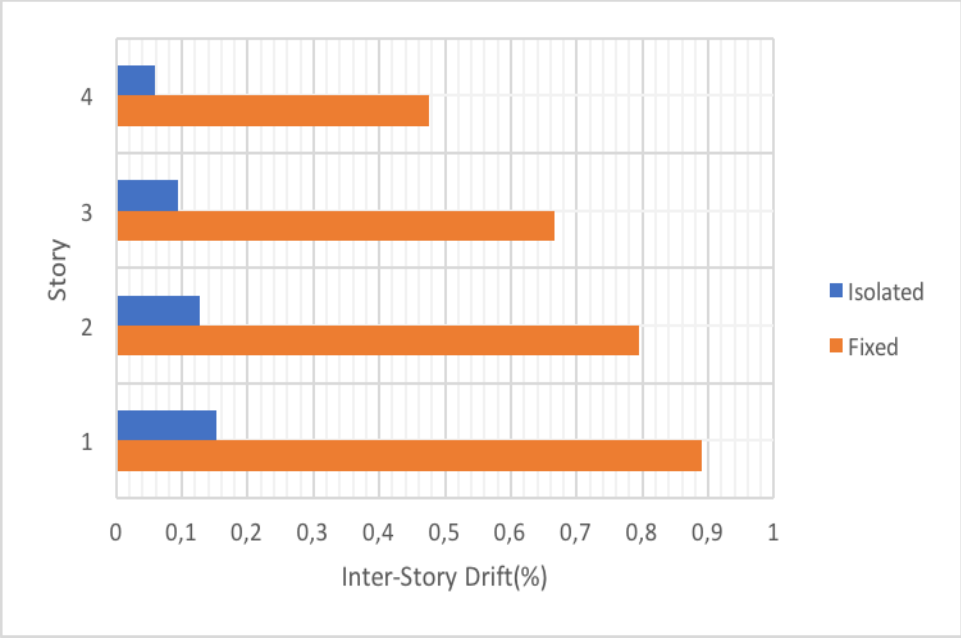

Figure 4.25: Peak Inter-Story Drift Arcelik – X direction

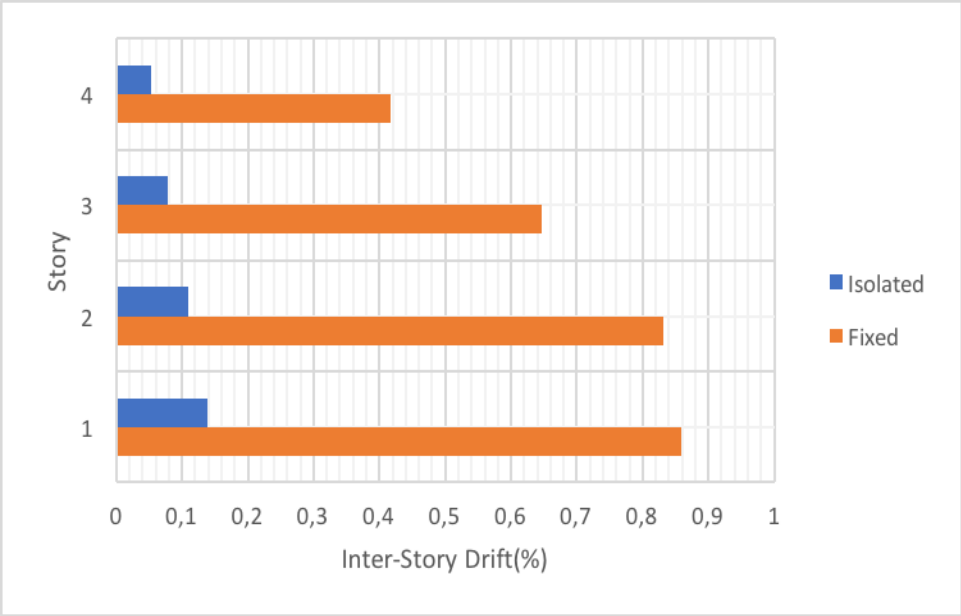

Figure 4.26: Peak Inter-Story Drift Delta – X direction

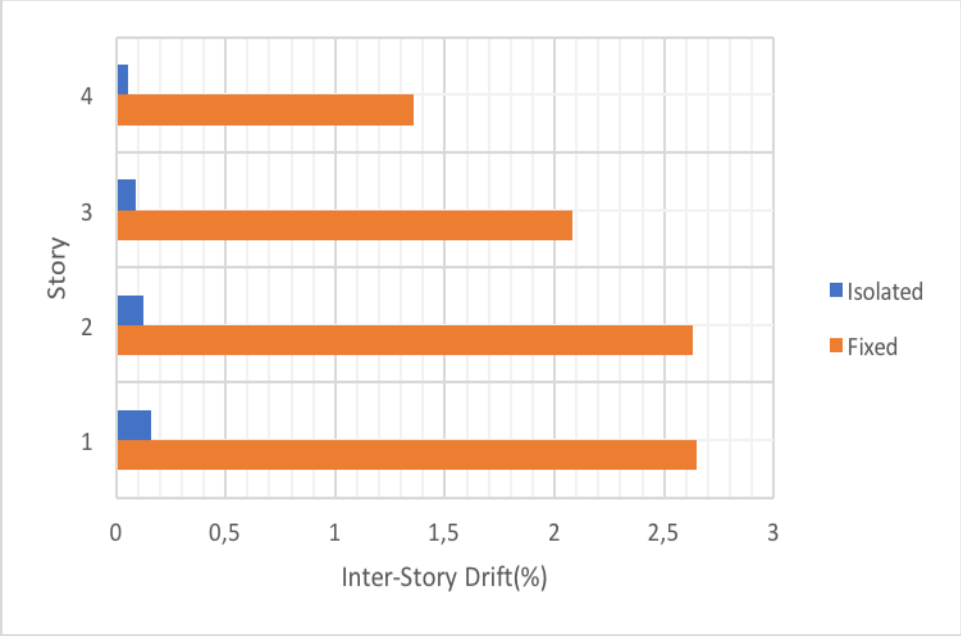

Figure 4.27: Peak Inter-Story Drift Hector – X direction

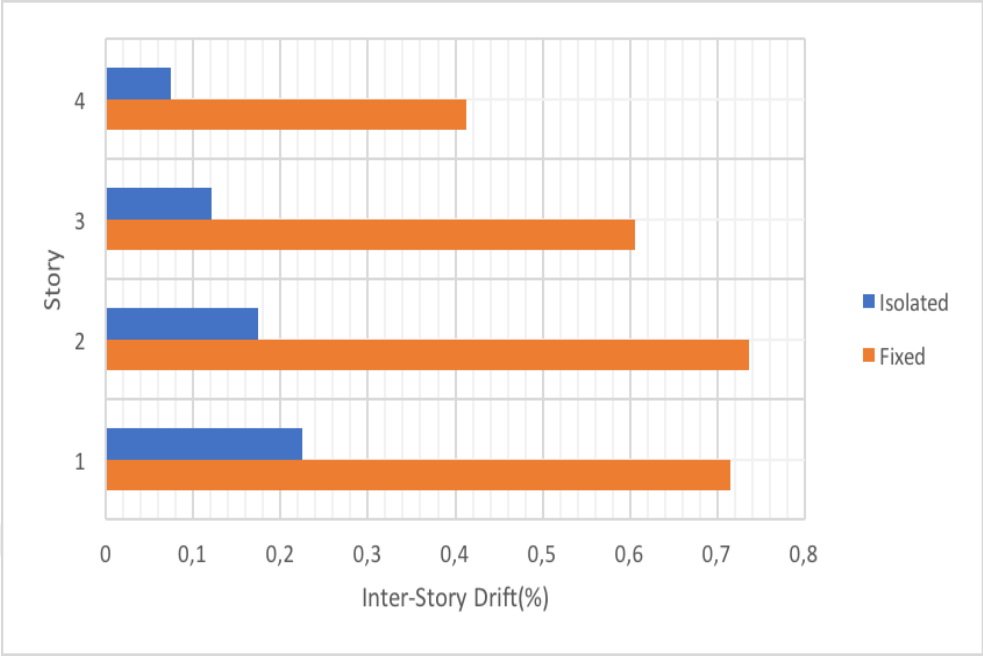

Figure 4.28: Peak Inter-Story Drift L.A Hollywood – X direction

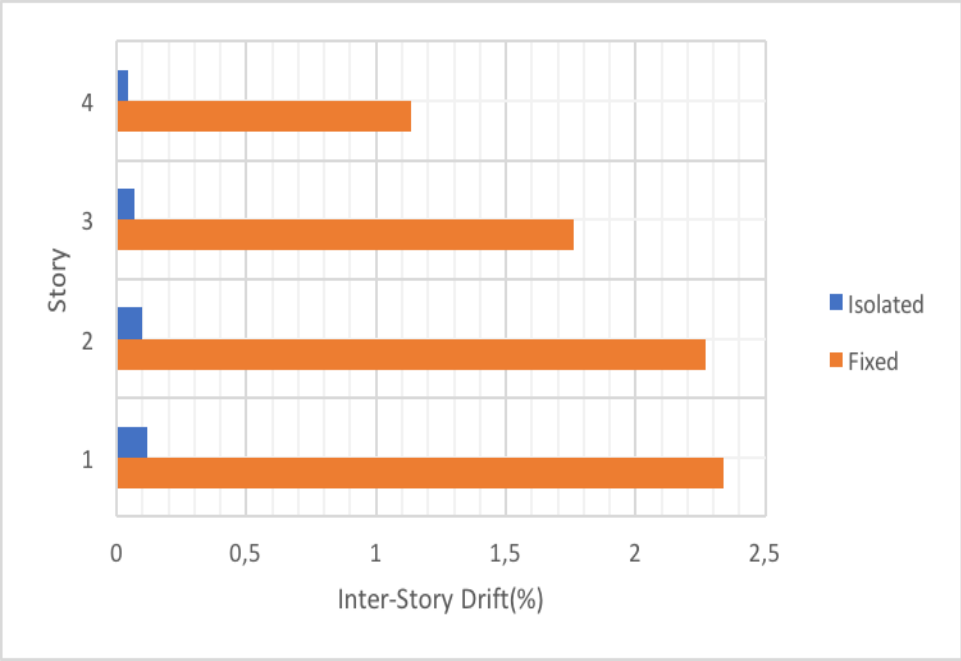

Figure 4.29: Peak Inter-Story Drift Beverly Hills – X direction

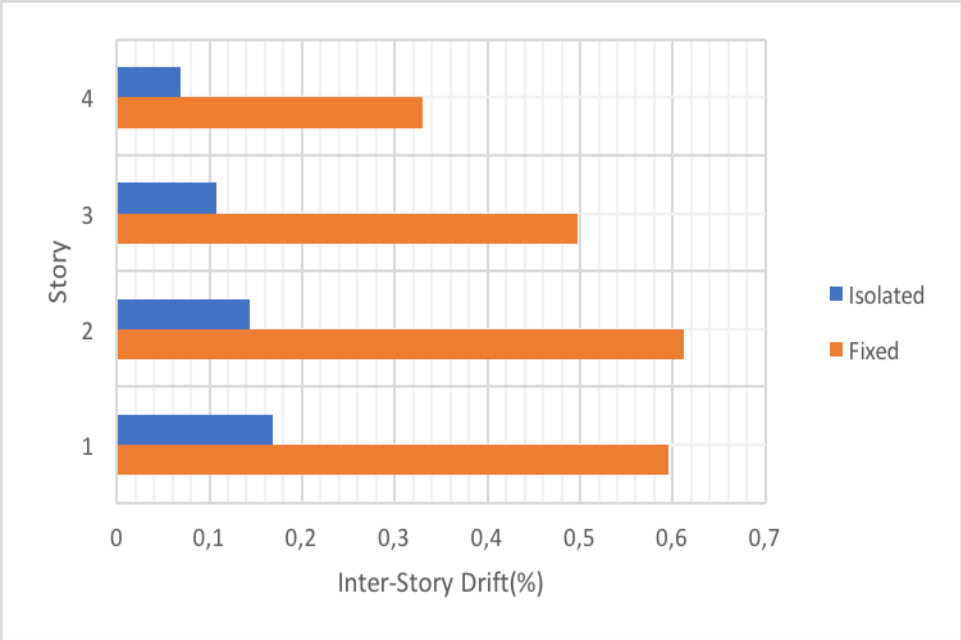

Figure 4.30: Peak Inter-Story Drift Abbar – X direction

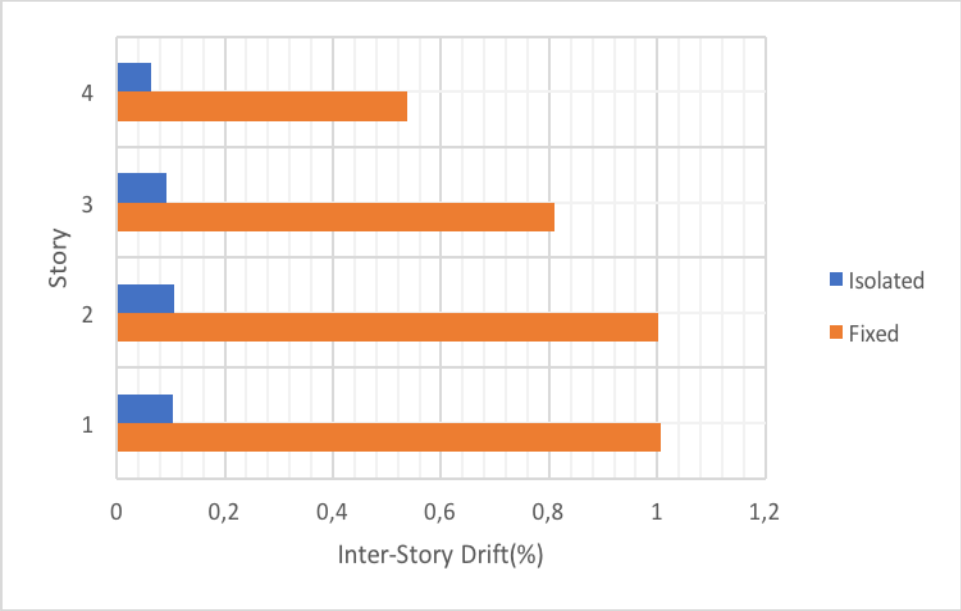

Figure 4.31: Peak Inter-Story Drift Coolwater – X direction

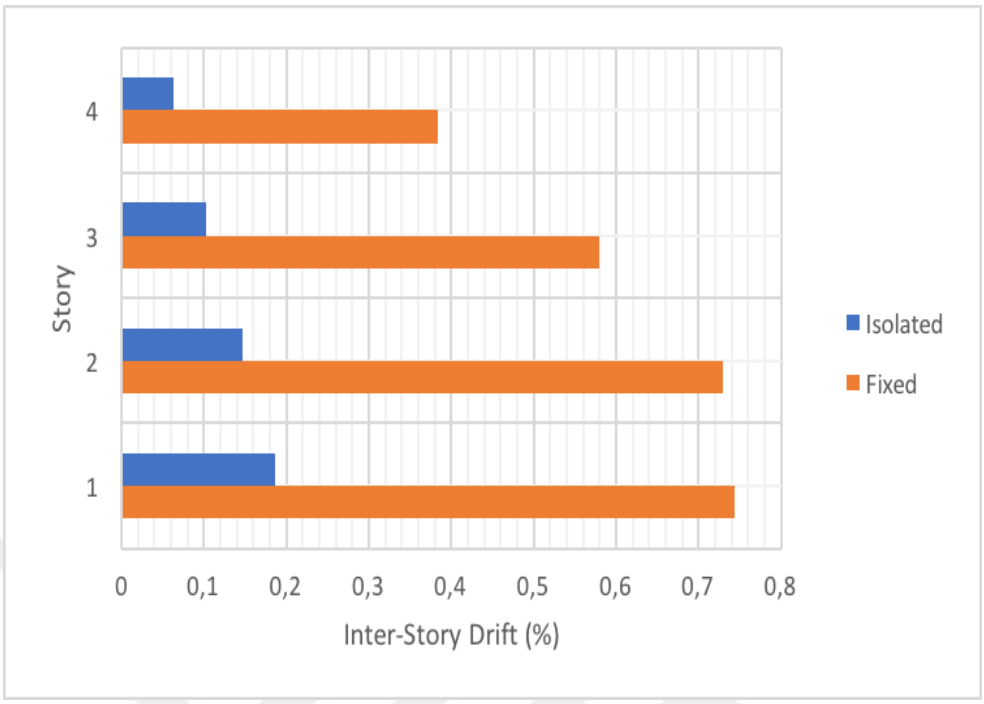

Figure 4.32: Peak Inter-Story Drift Erzincan – X direction

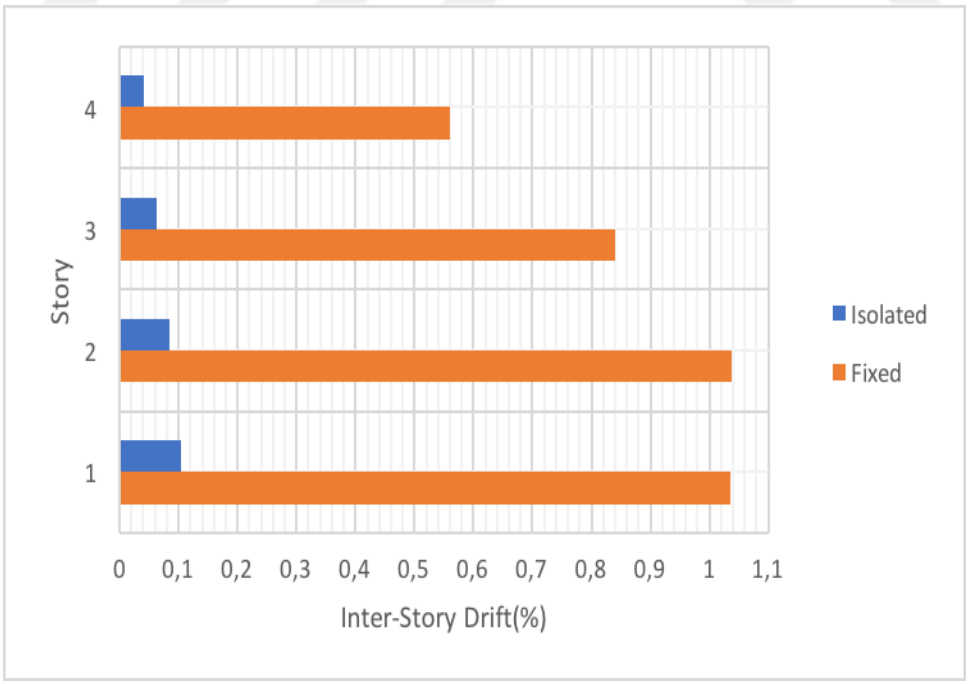

Figure 4.33: Peak Inter-Story Drift Petrolia – X direction

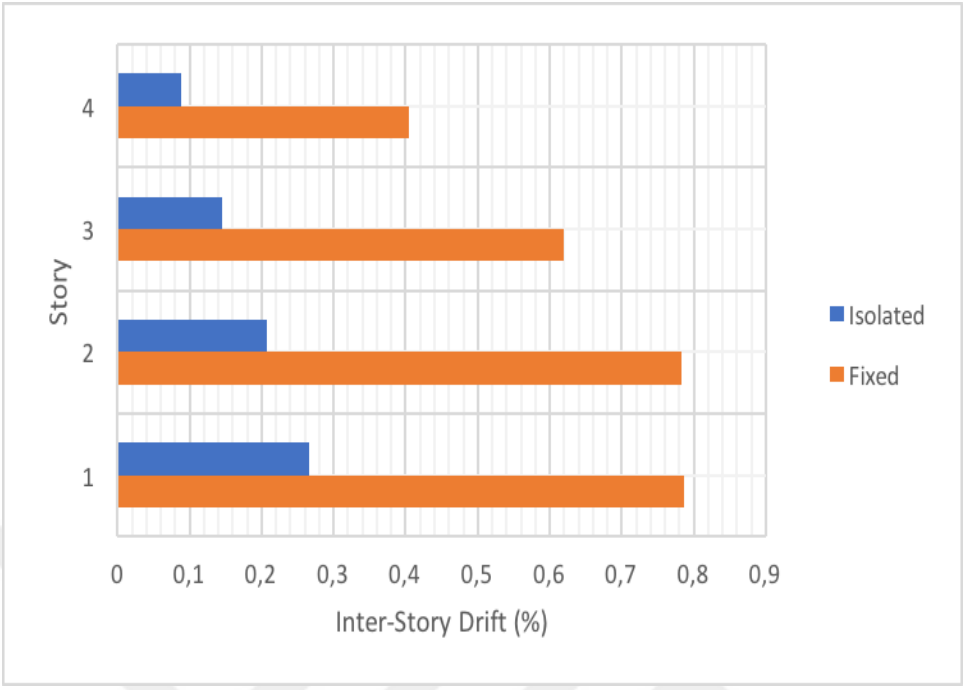

Figure 4.34: Peak Inter-Story Drift Duzce – X direction

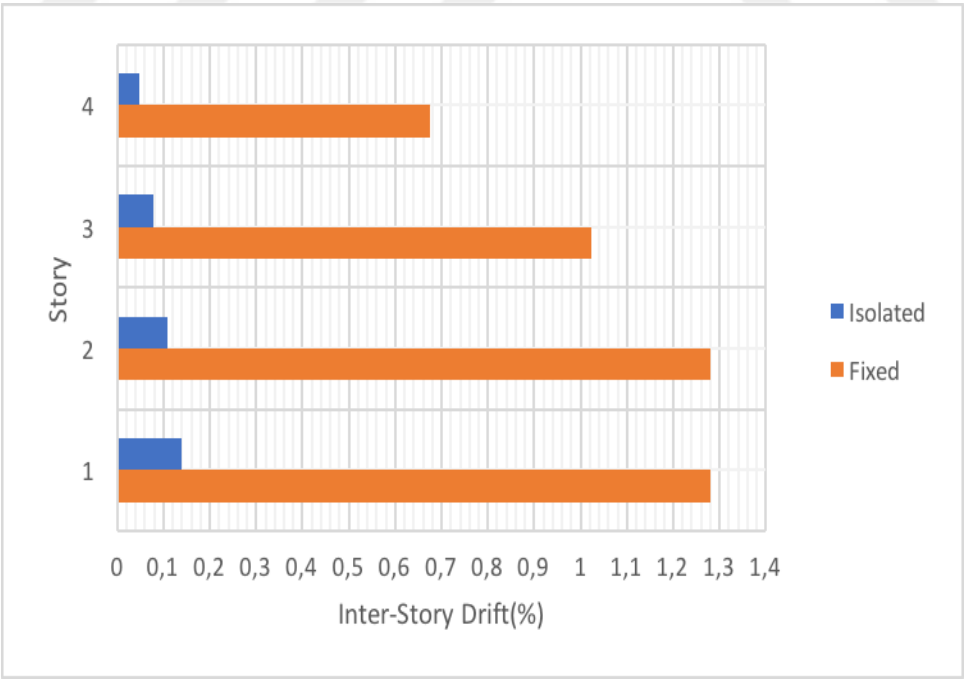

Figure 4.35: Peak Inter-Story Drift Bonds Corner – X direction

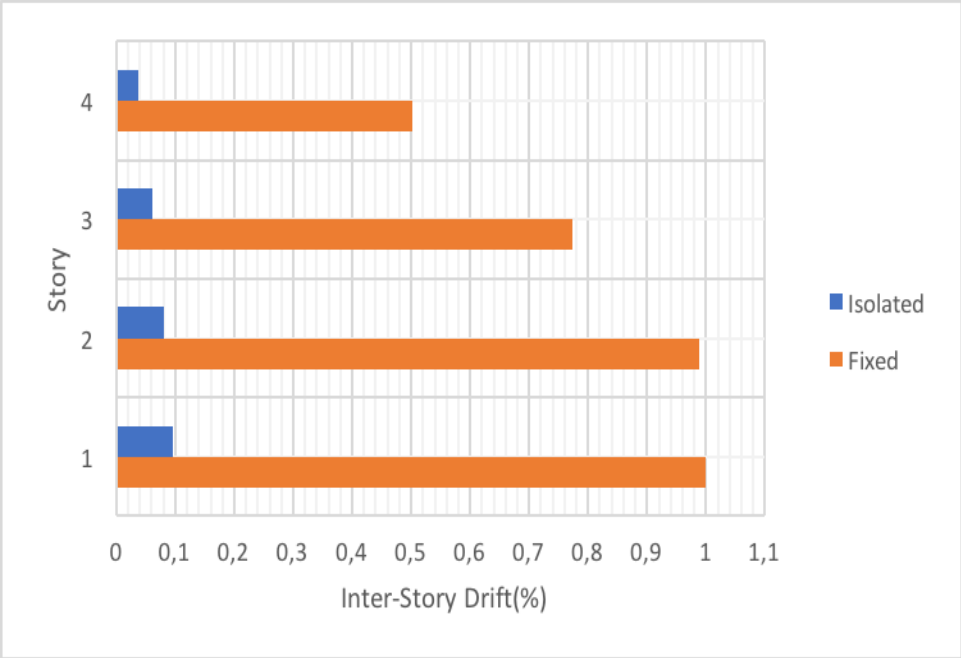

Figure 4.36: Peak Inter-Story Drift Nahanni Site 2 – X direction

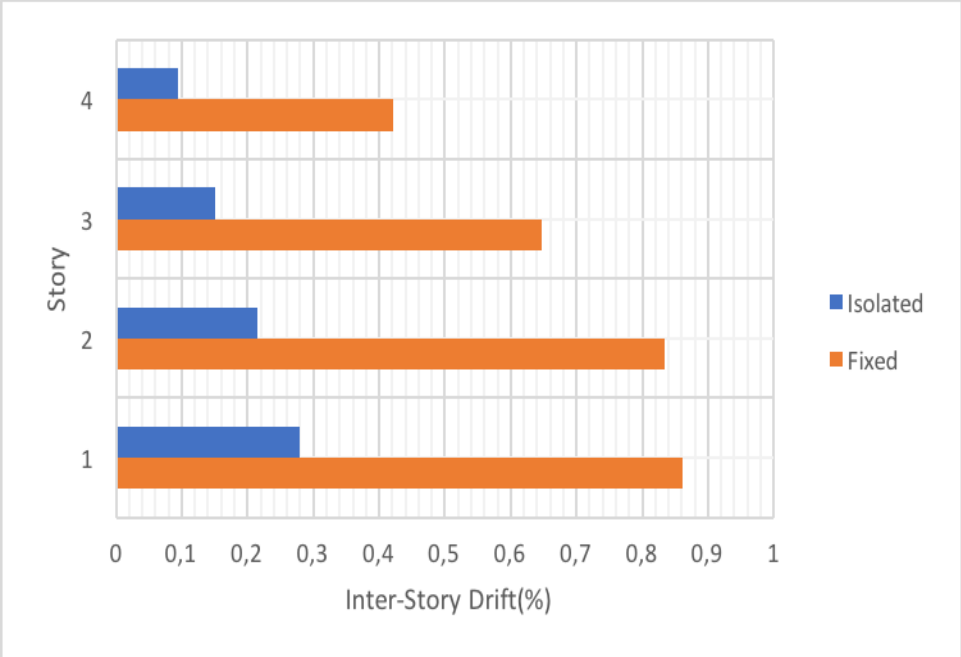

Figure 4.37: Peak Inter-Story Drift ChiChi TCU 067 – X direction

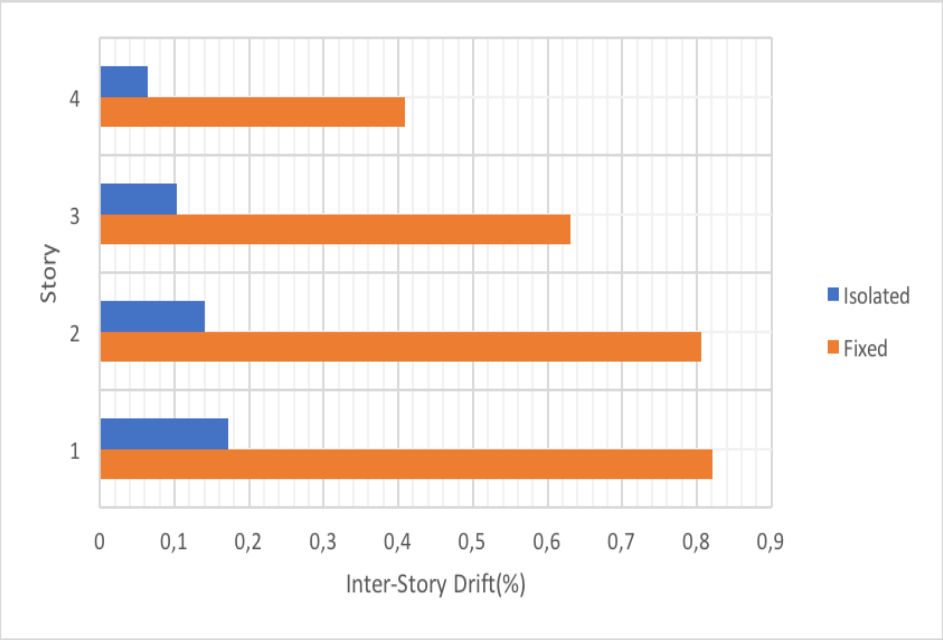

Figure 4.38: Peak Inter-Story Drift Parachute Test Site - X direction

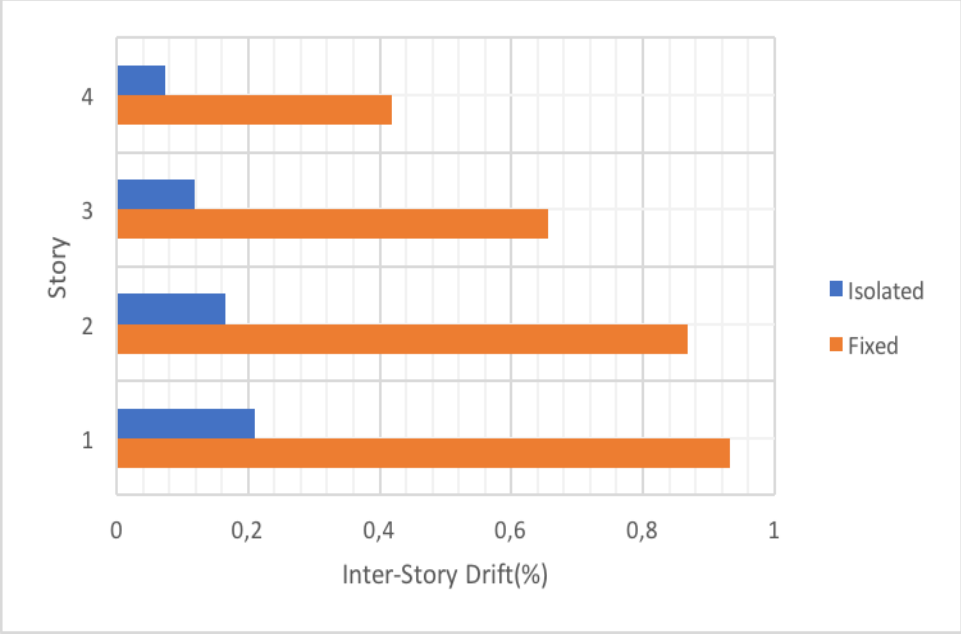

Figure 4.39: Peak Inter-Story Drift Saratoga - X direction

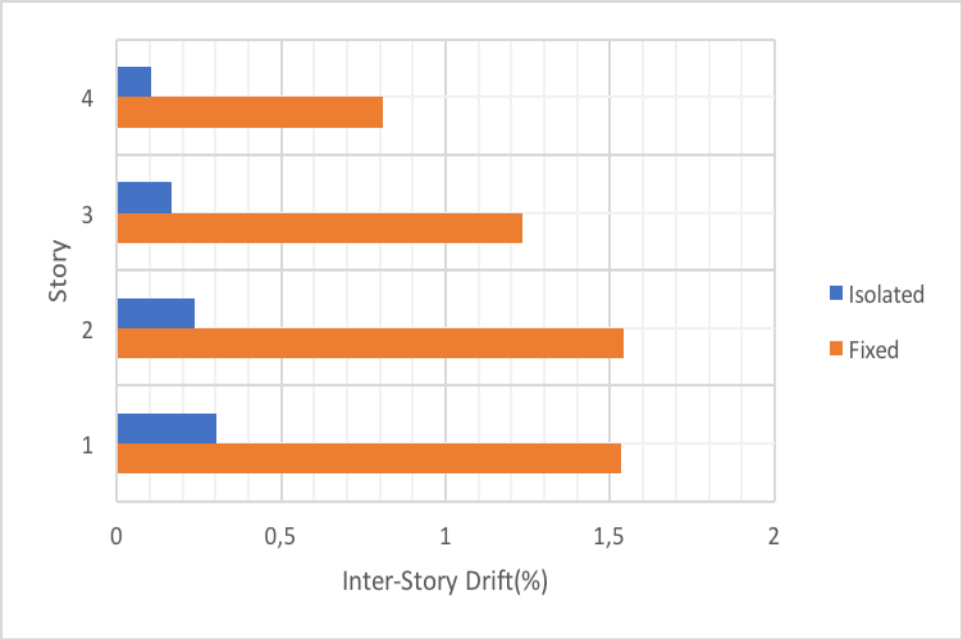

Figure 4.40: Peak Inter-Story Drift Sylmar - X direction

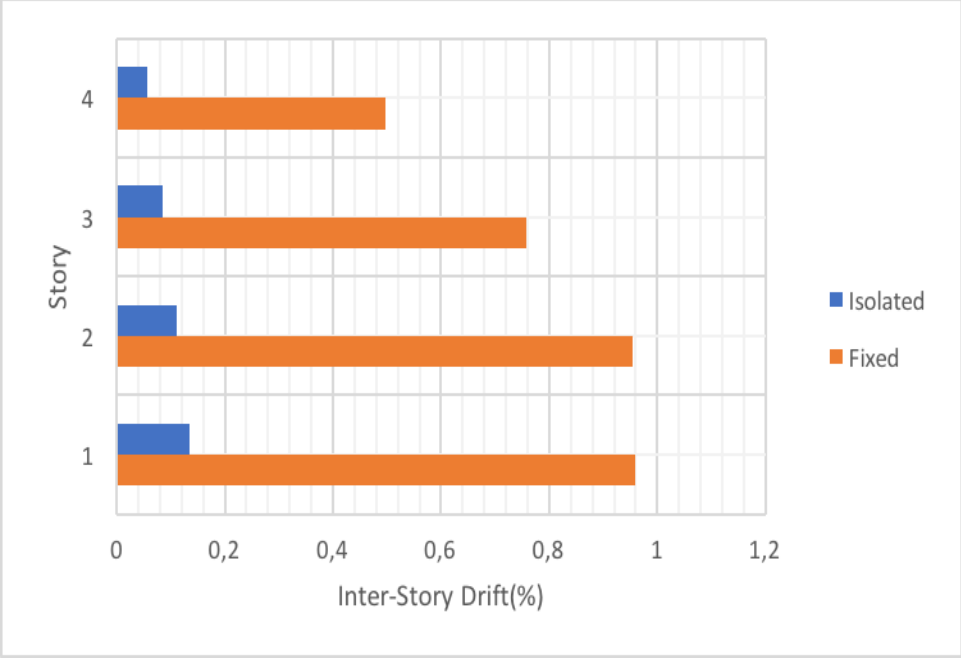

Figure 4.41: Peak Inter-Story Drift Saticoy - X direction

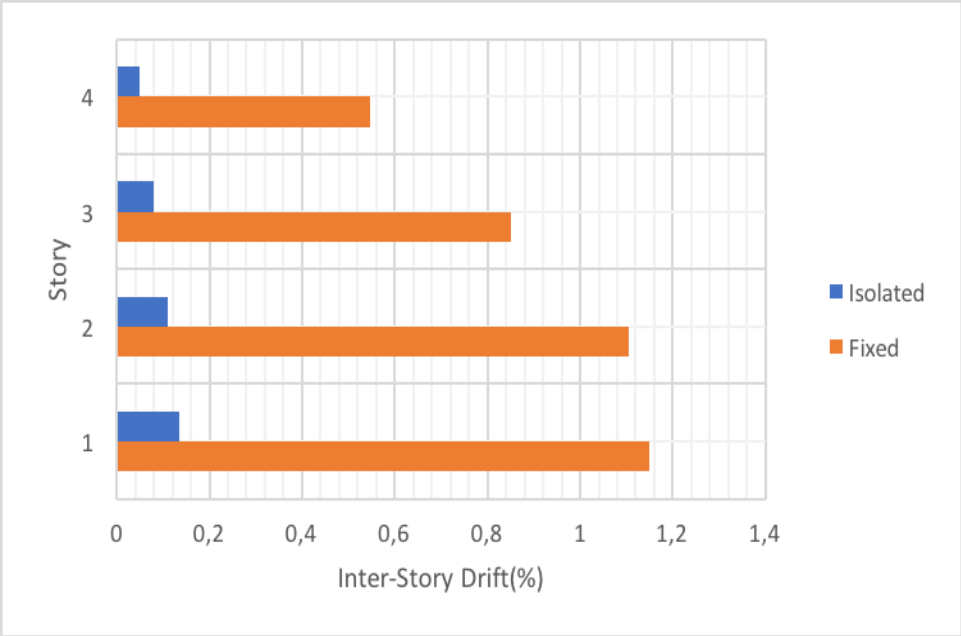

Figure 4.42: Peak Inter-Story Drift Chihuahua - X direction

4.2.3 Story Acceleration

Absolute maximum story acceleration is the absolute peak acceleration value of a horizontally excited earthquake record in both negative and positive axis. Story inertial forces are proportional to the accelerations, hence larger acceleration yield higher story forces. The maximum reduction in floor acceleration in far-field and near-field ground motions were observed to be 95% and 92% respectively. Furthermore, linear floor distribution is seen Figure 4.64 for Turkish and American codse using isolator equivalent lateral method while in isolator time history analysis of both far-field and near-field in Figure 4.65 and Figure 4.66 shows the floor distributions to be relative straight and approximate to each other. Moreover, in the case of fixed based Arcelik, Abbar, and Saratoga shows similar distribution behaviour as isolated structure.

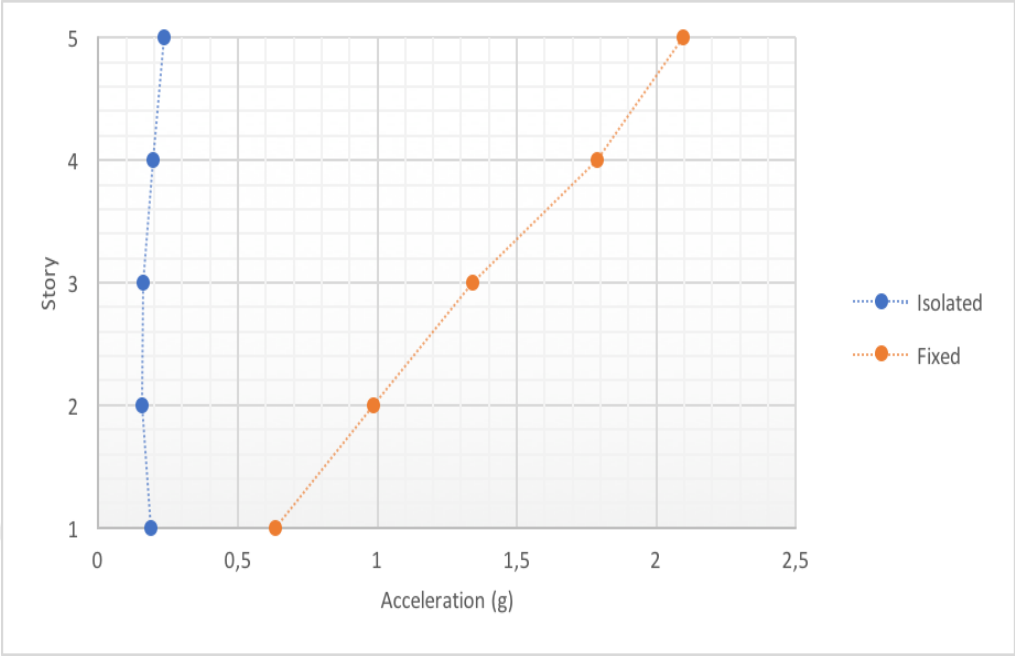

Figure 4.43: Absolute Maximum Story Acceleration Bolu – X direction

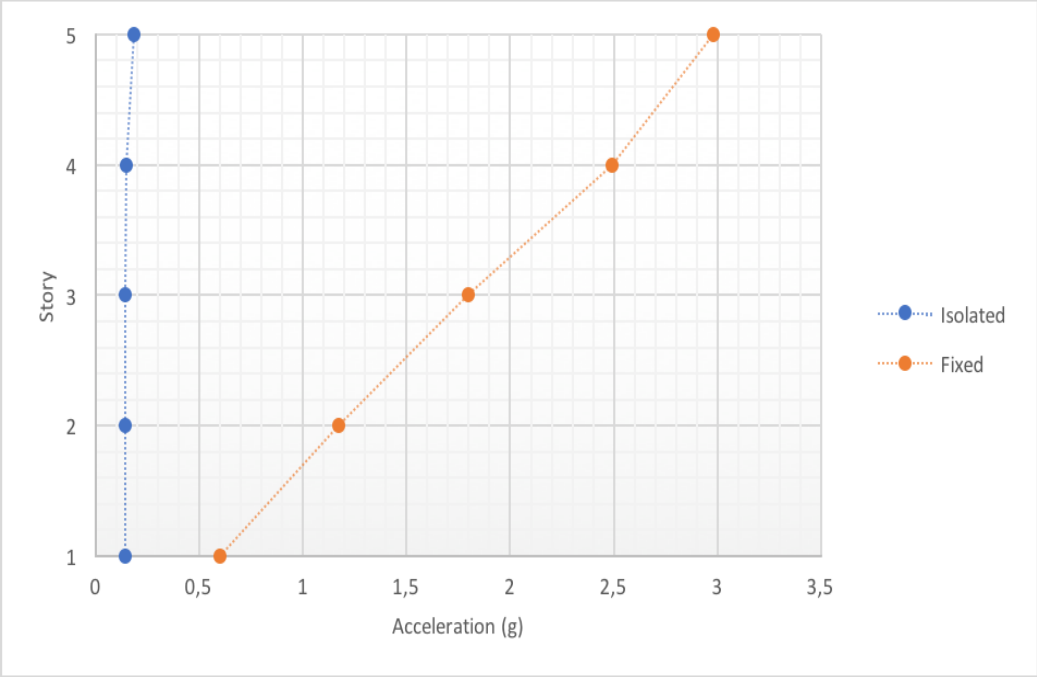

Figure 4.44: Absolute Maximum Story Acceleration Nishi Akashi – X direction

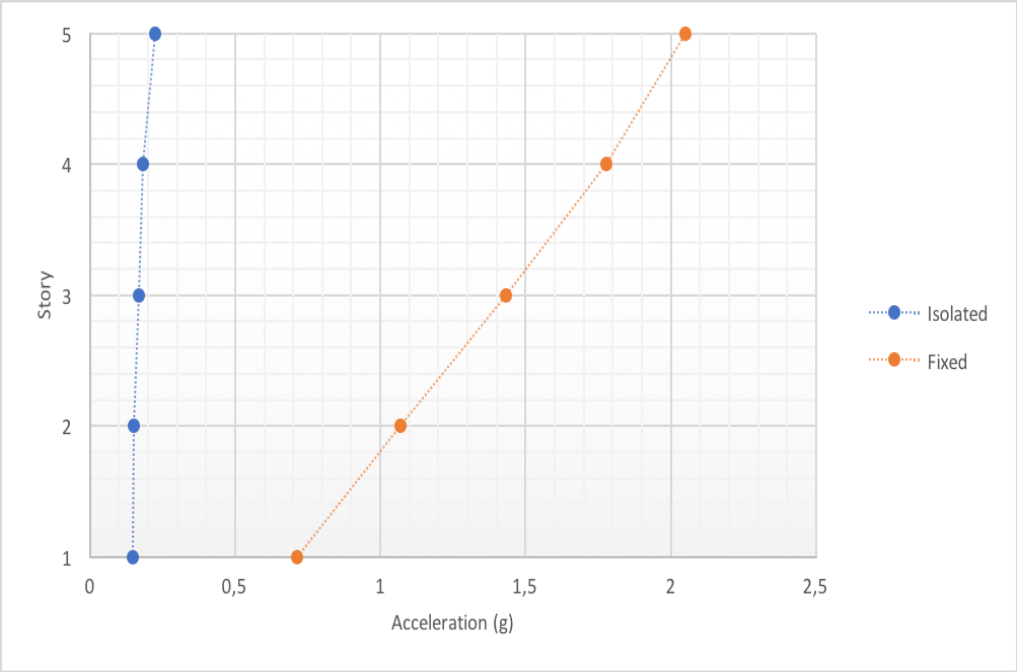

Figure 4.45: Absolute Maximum Story Acceleration Shin Osaka– X direction

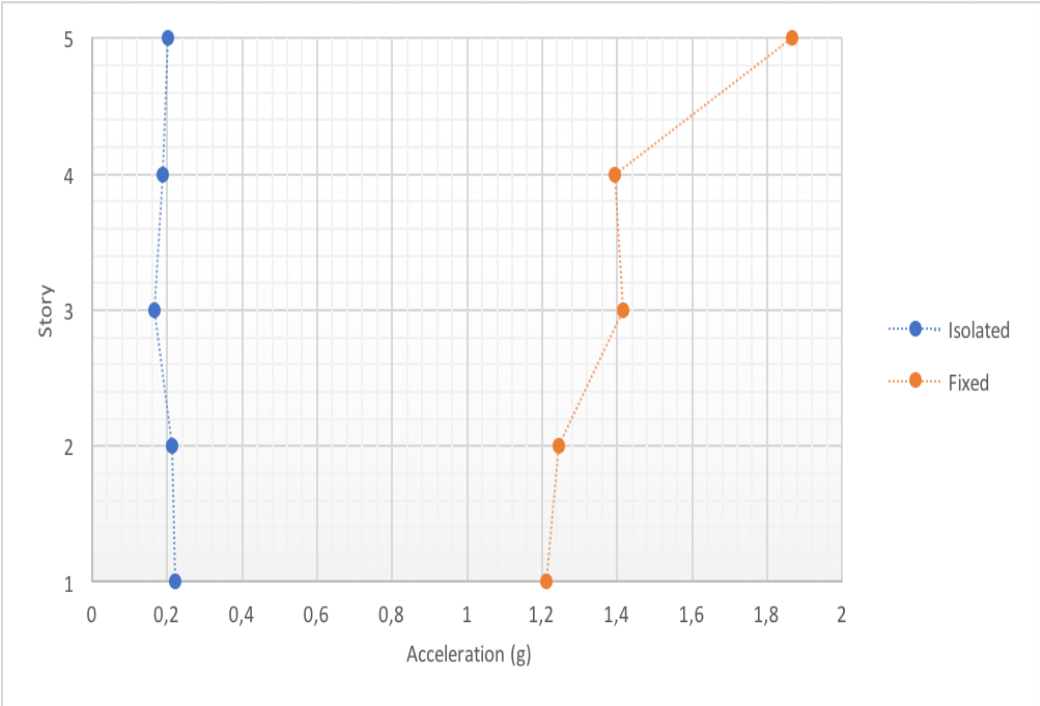

Figure 4.46: Absolute Maximum Story Acceleration Arcelik– X direction

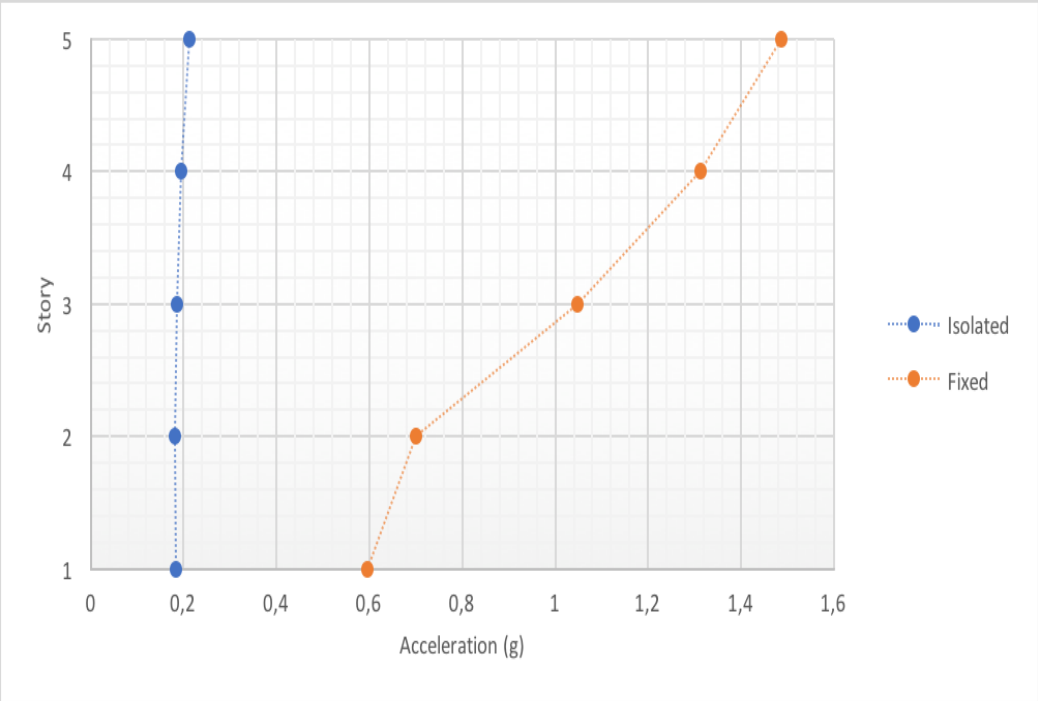

Figure 4.47: Absolute Maximum Story Acceleration Delta – X direction

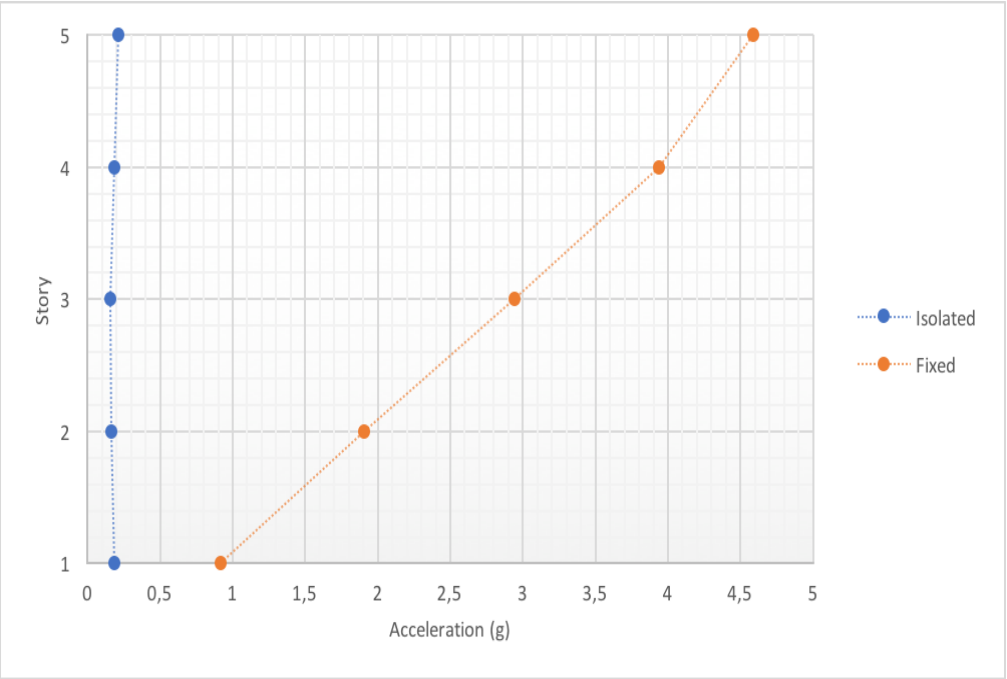

Figure 4.48: Absolute Maximum Story Acceleration Hector – X direction

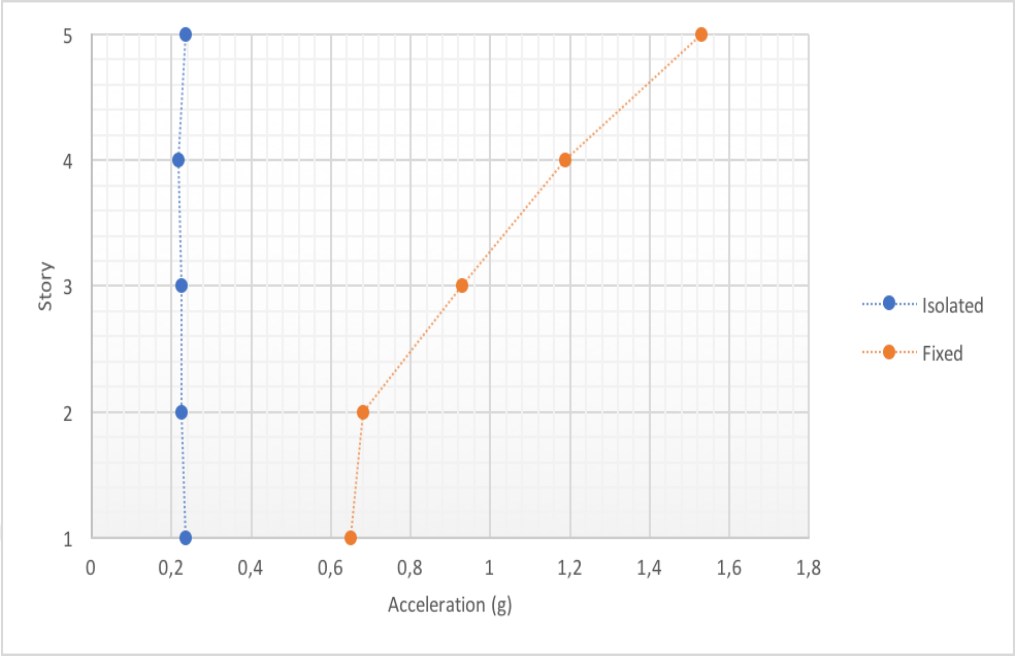

Figure 4.49: Absolute Maximum Story Acceleration L.A Hollywood – X direction

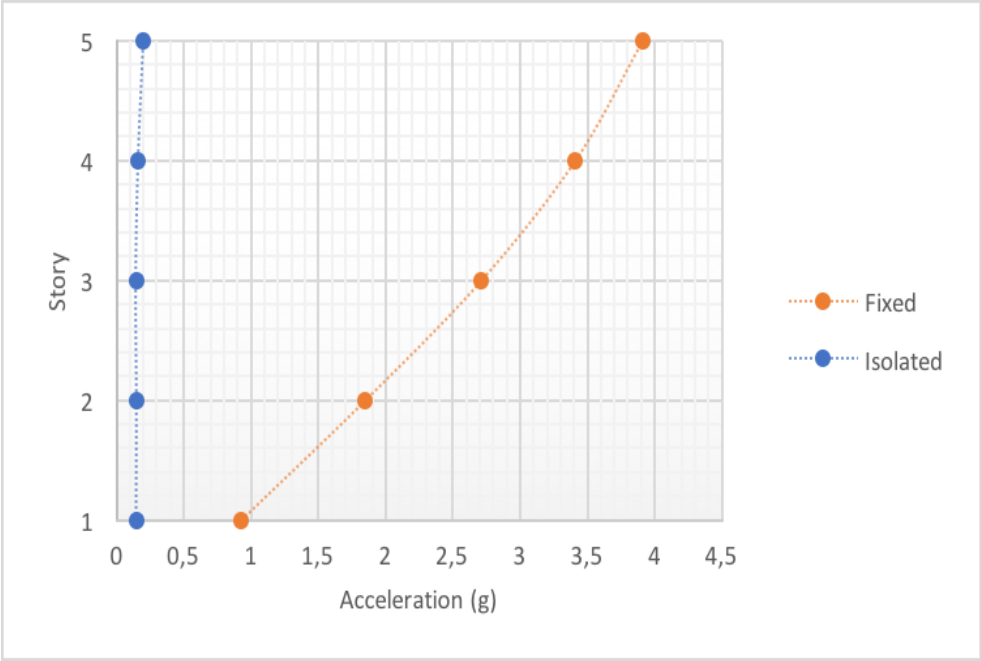

Figure 4.50: Absolute Maximum Story Acceleration Beverly Hills – X direction

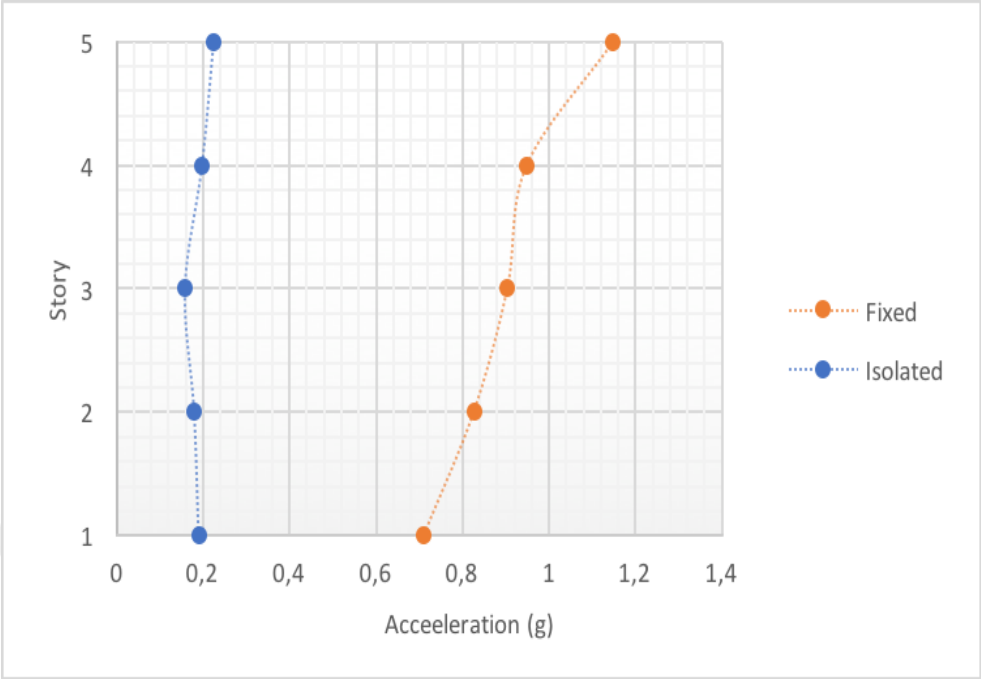

Figure 4.51: Absolute Maximum Story Acceleration Abbar – X direction

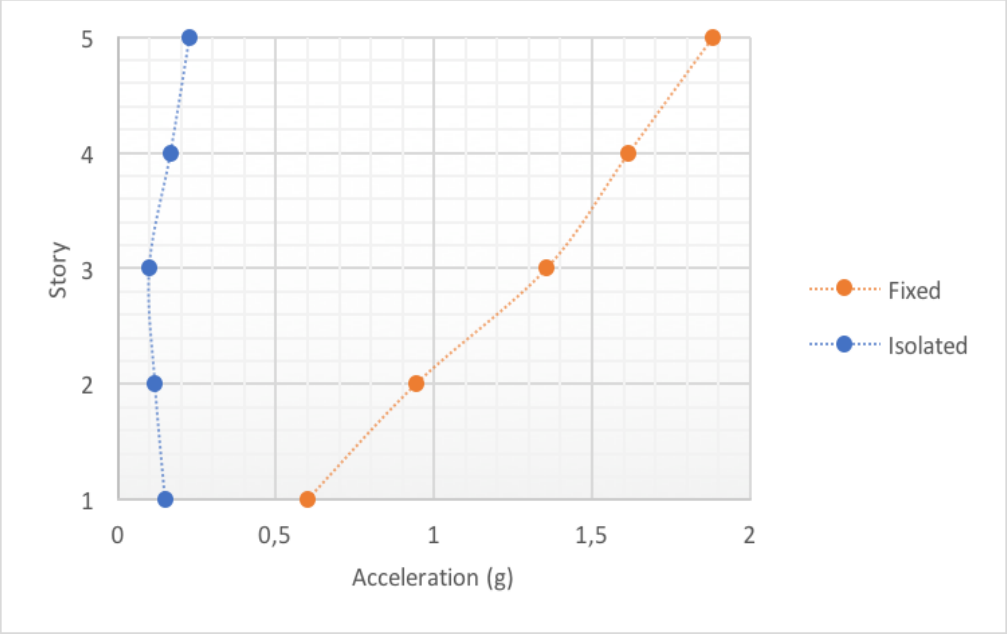

Figure 4.52: Absolute Maximum Story Acceleration Coolwater – X direction

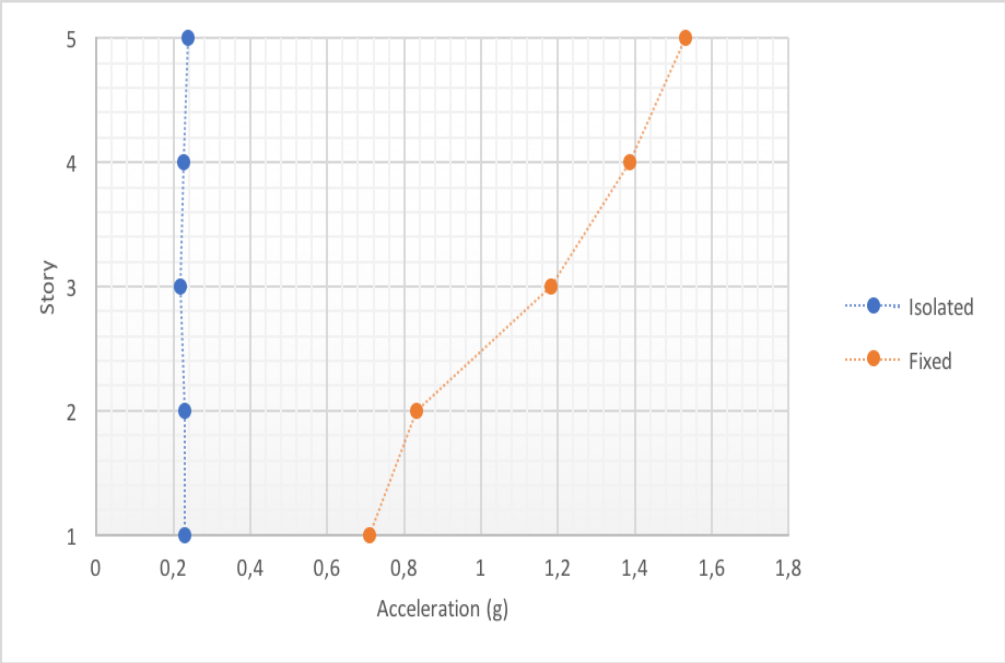

Figure 4.53: Absolute Maximum Story Acceleration Erzincan– X direction

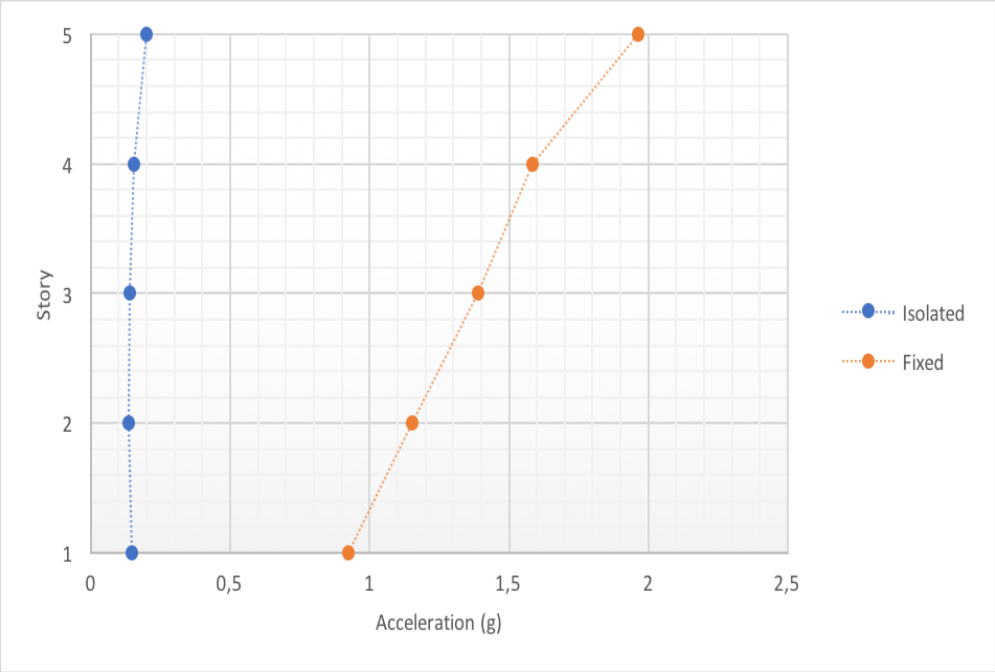

Figure 4.54: Absolute Maximum Story Acceleration Petrolia – X direction

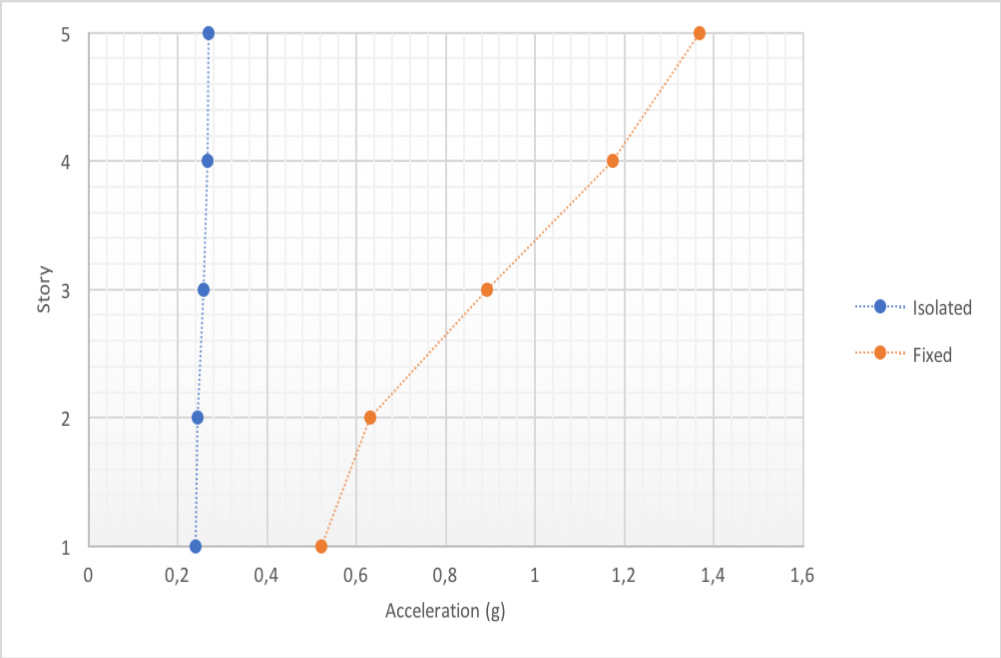

Figure 4.55: Absolute Maximum Story Acceleration Duzce – X direction

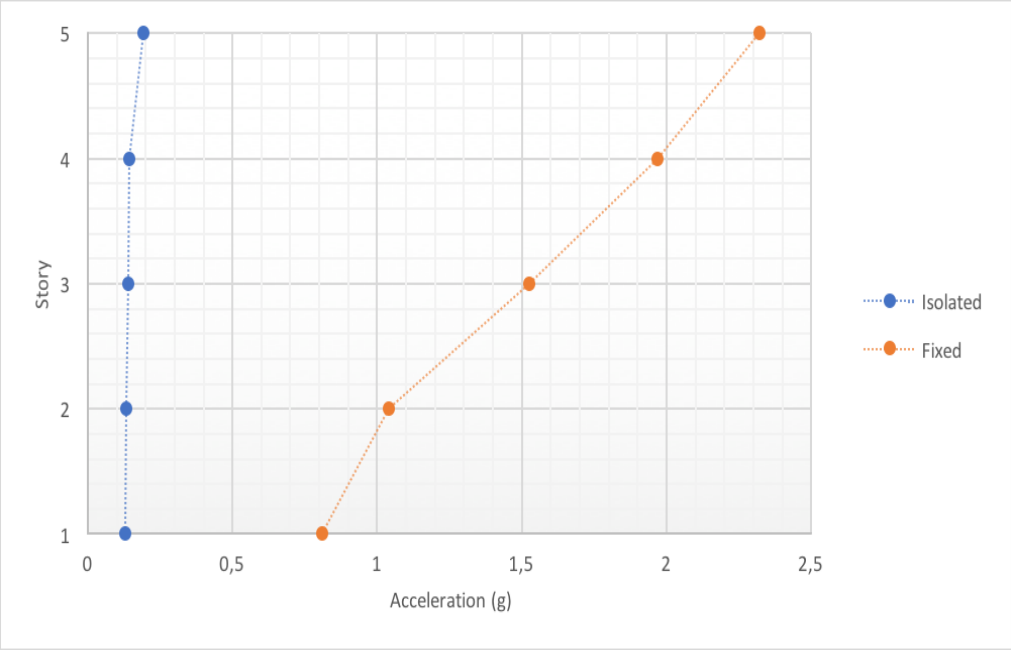

Figure 4.56: Absolute Maximum Story Acceleration Bonds Corner – X direction

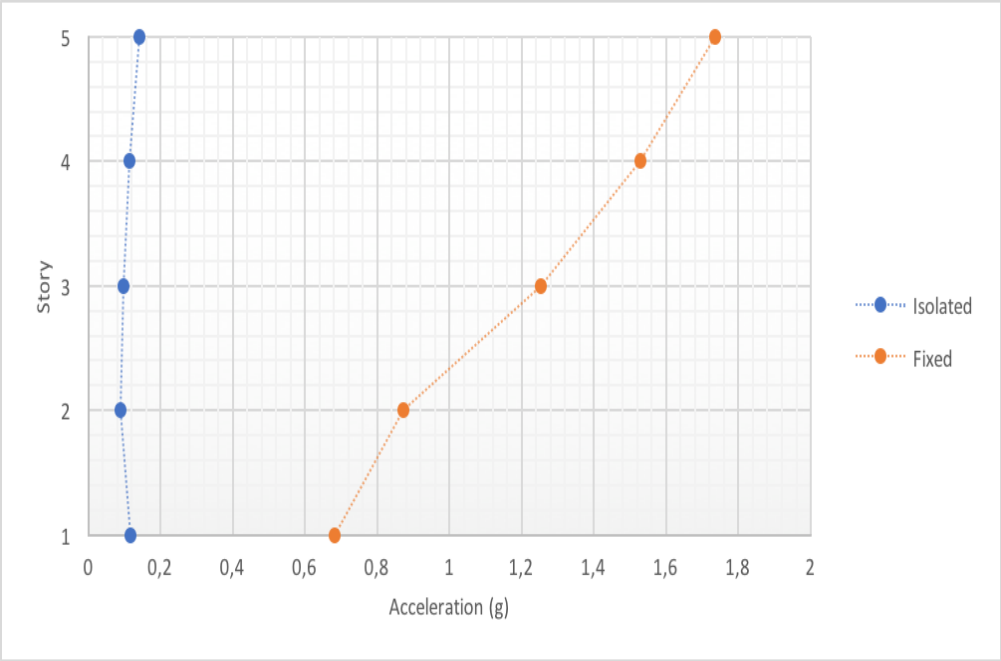

Figure 4.57: Absolute Maximum Story Acceleration Nahanni Site 2– X direction

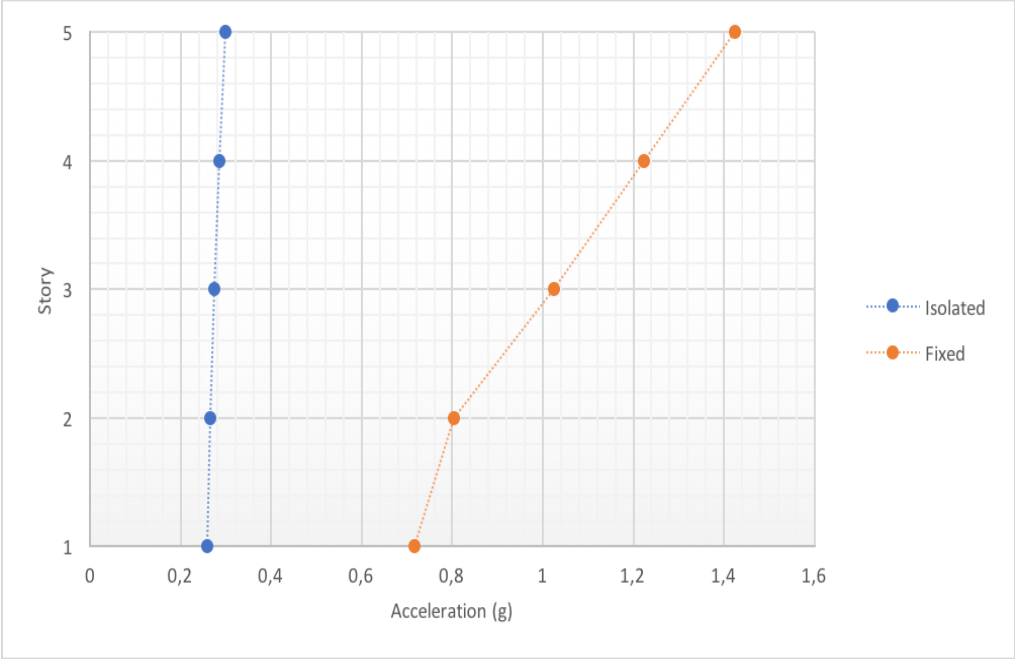

Figure 4.58: Absolute Maximum Story Acceleration ChiChi TCU067 – X direction

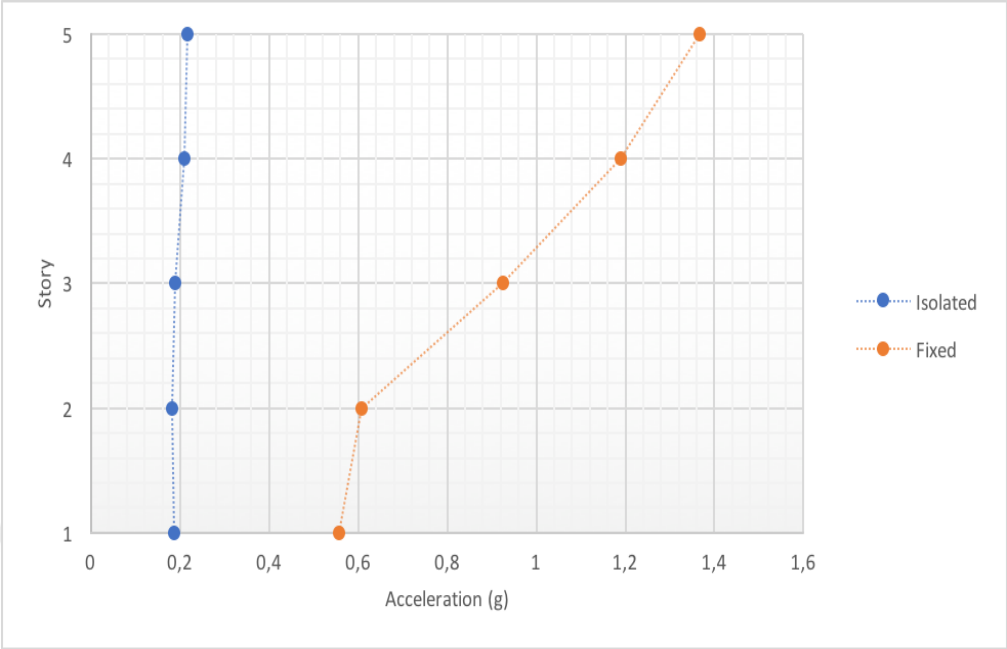

Figure 4.59: Absolute Maximum Story Acceleration Parachute Test Site – X direction

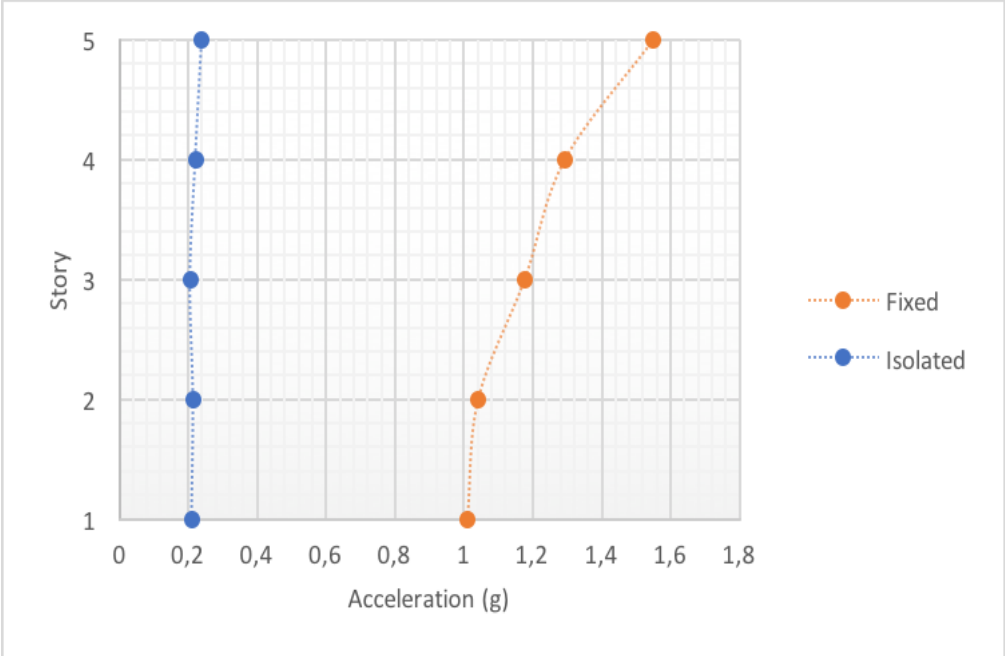

Figure 4.60: Absolute Maximum Story Acceleration Saratoga – X direction

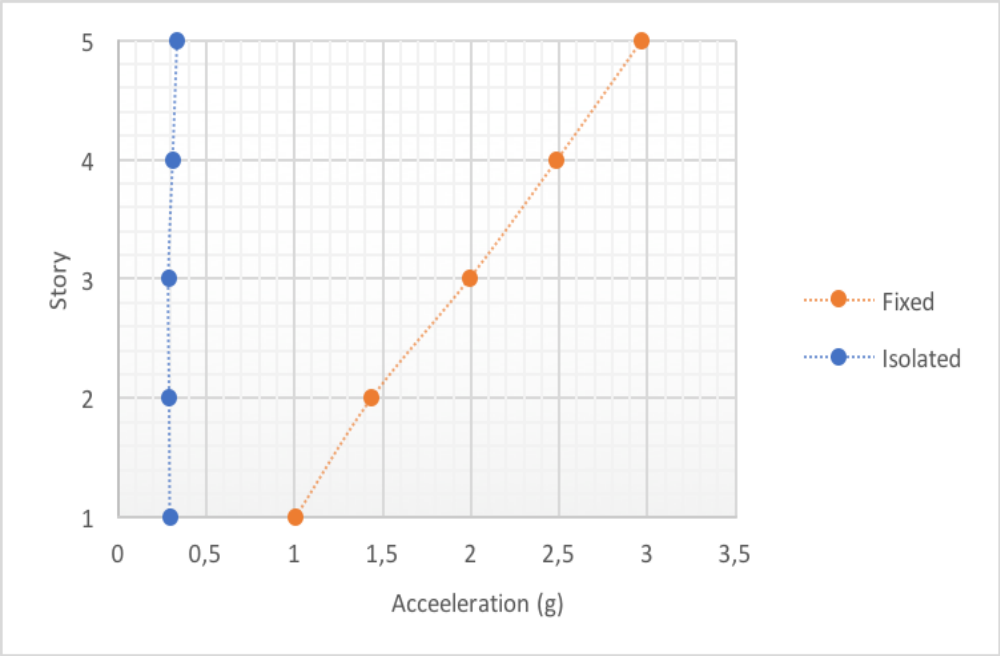

Figure 4.61: Absolute Maximum Story Acceleration Sylmar – X direction

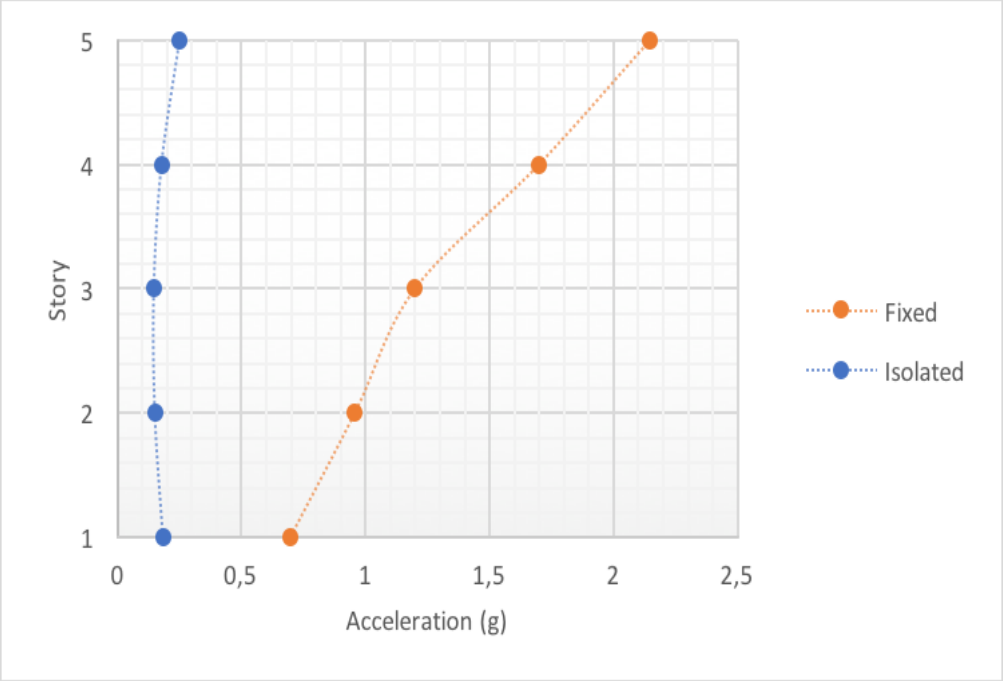

Figure 4.62: Absolute Maximum Story Acceleration Saticoy – X direction

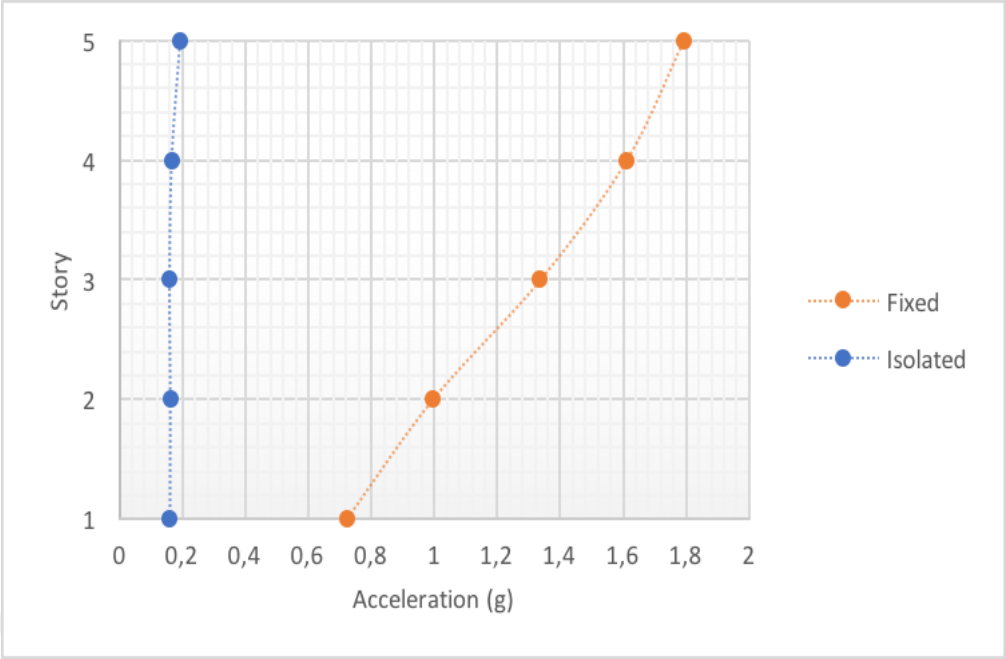

Figure 4.63: Absolute Maximum Story Acceleration Chihuahua – X direction

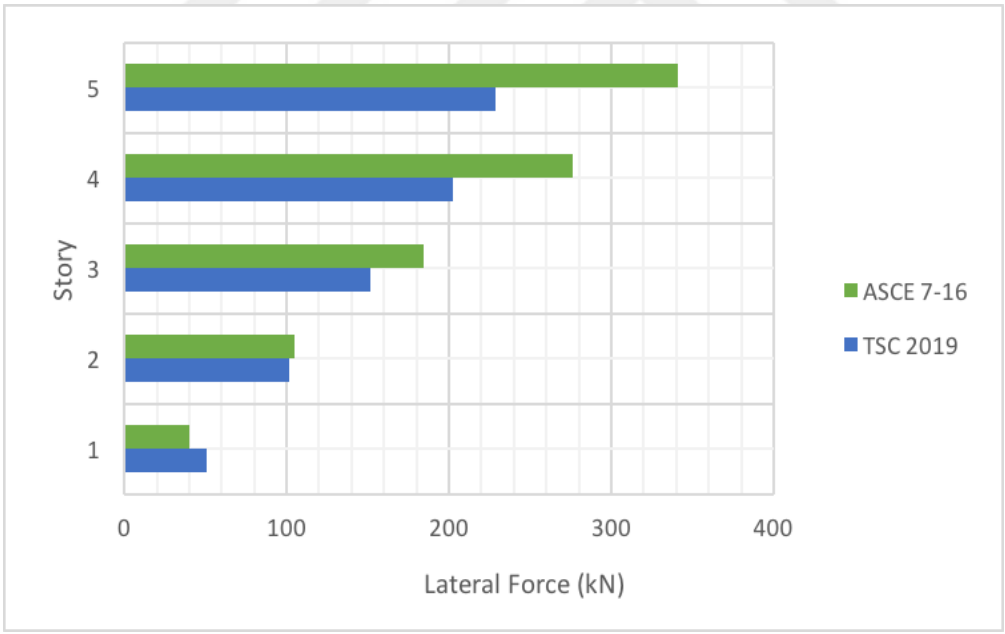

Figure 4.64: Equivalent Lateral Force Distribution

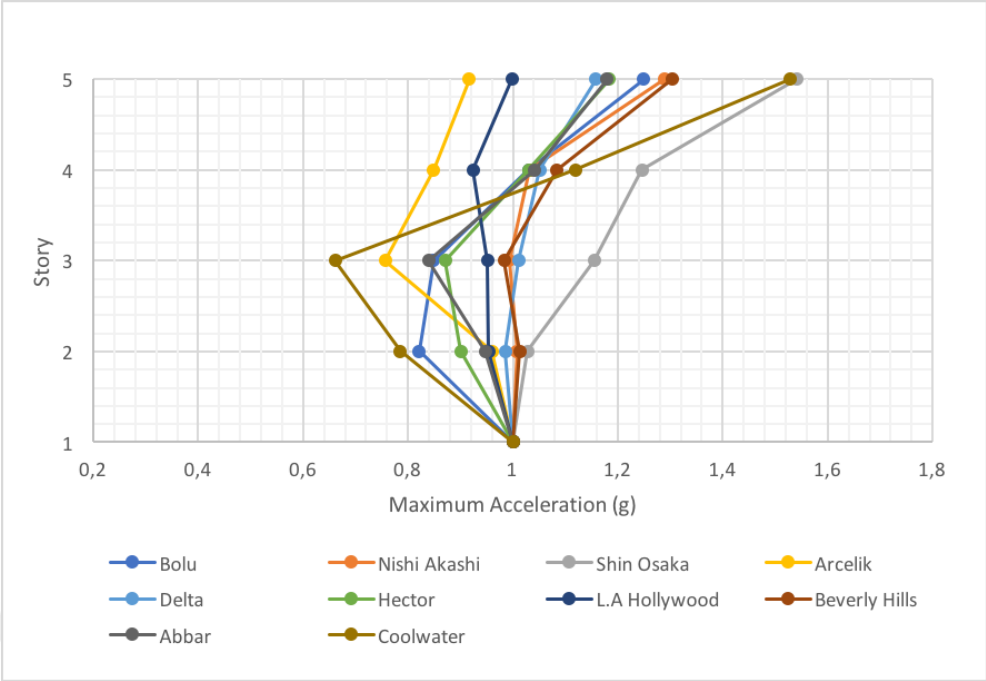

Figure 4.65: Far-Field Ground Motion Distribution

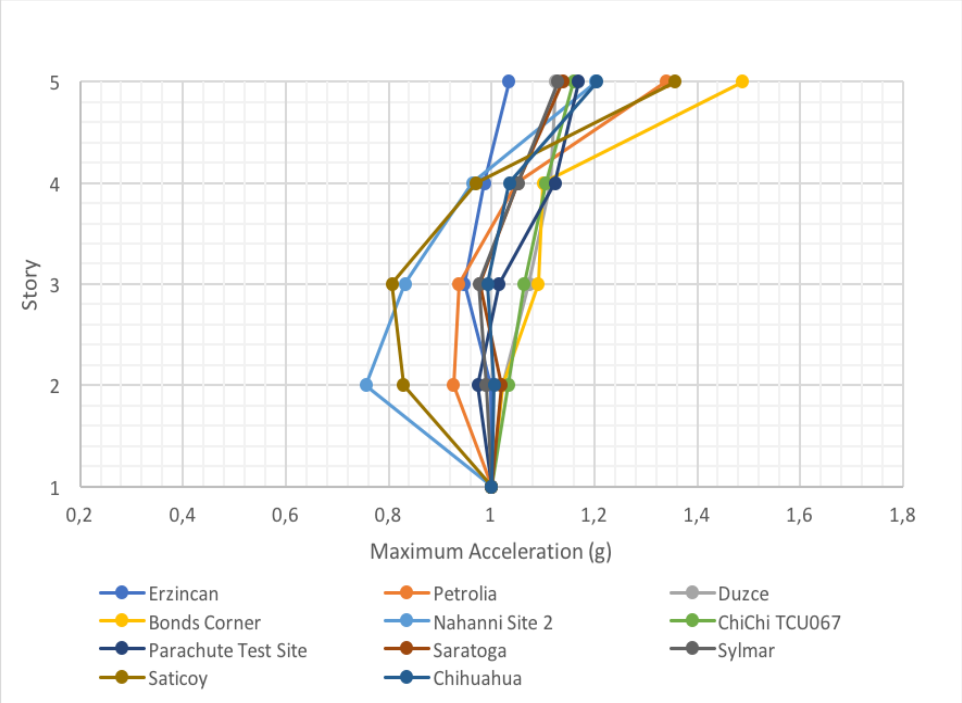

Figure 4.66: Near-Field Ground Motion Distribution

4.2.4 Force – Displacement Curves of the Isolators

Hysteretic loops illustrate the force displacement response of triple friction pendulum bearings. The hysteresis loops can be used to determine the energy dissipation per cycle and the effective damping provided by bearings. Displacements less than 300mm were observed in most motion records dissipating less energy and only triggers movement in the inner sliding surfaces. The maximum displacement observed in far-field and near-field are L.A Hollywood and Sylmar with 535mm and 720mm respectively. Sylmars displacement triggers most of the sliding regimes in the TFP isolated. Regime V is not necessarily triggered because TFP isolators are not typically designed to operate in that regime [70].

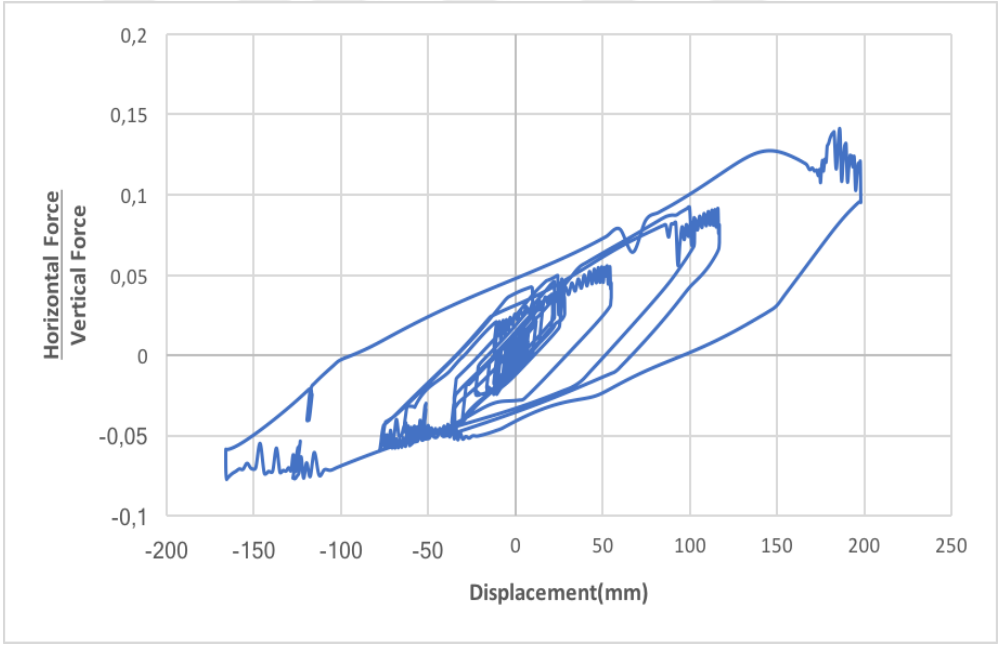

Figure 4.67: Bolu Hysteresis Loop – X direction

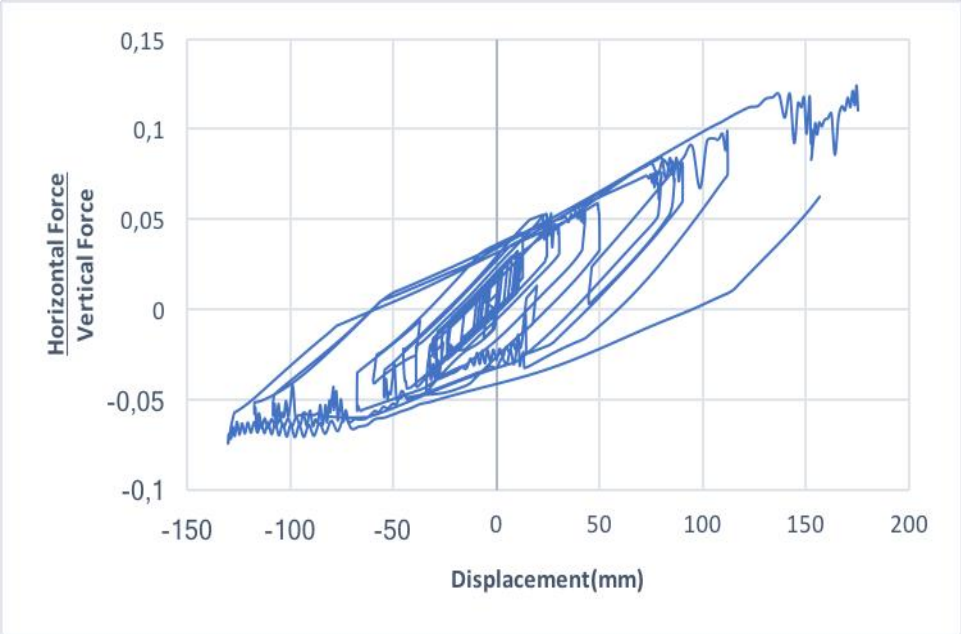

Figure 4.68: Nishi Akashi Hysteresis Loop – X direction

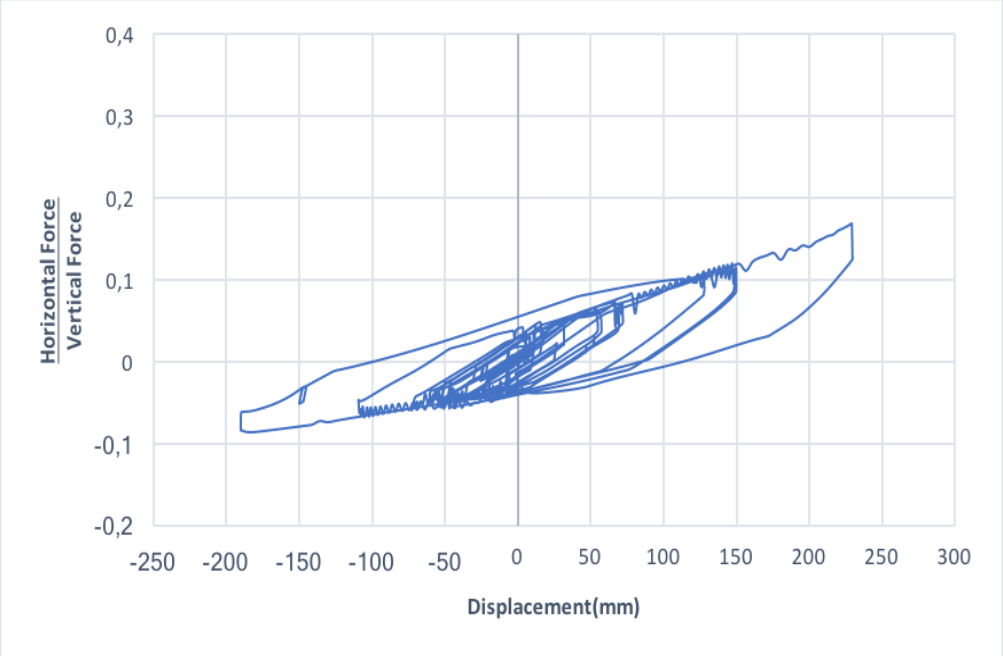

Figure 4.69: Shin Osaka Hysteresis Loop – X direction

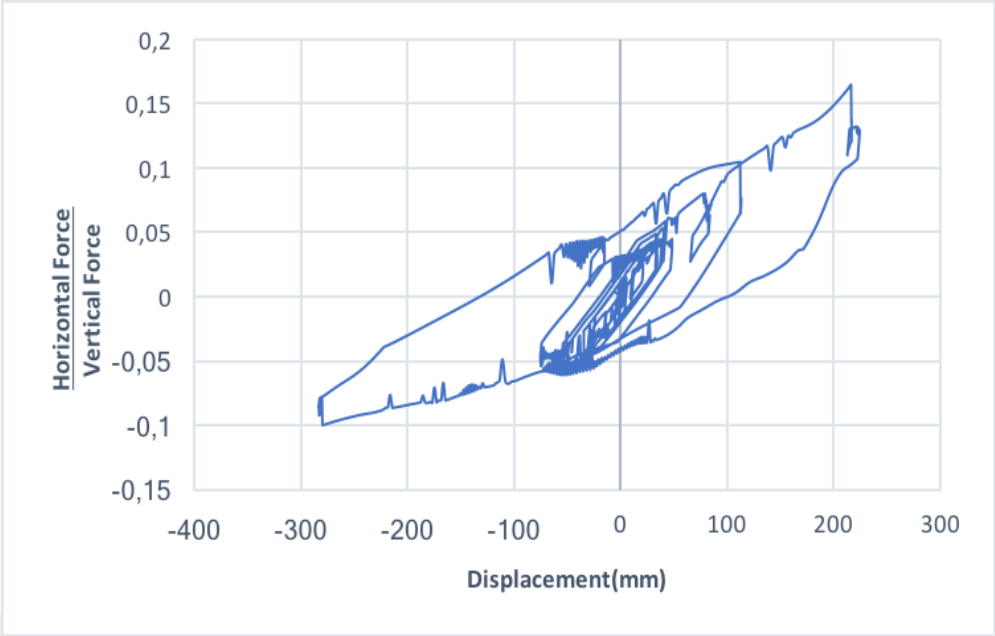

Figure 4.70: Arcelik Hysteresis Loop – X direction

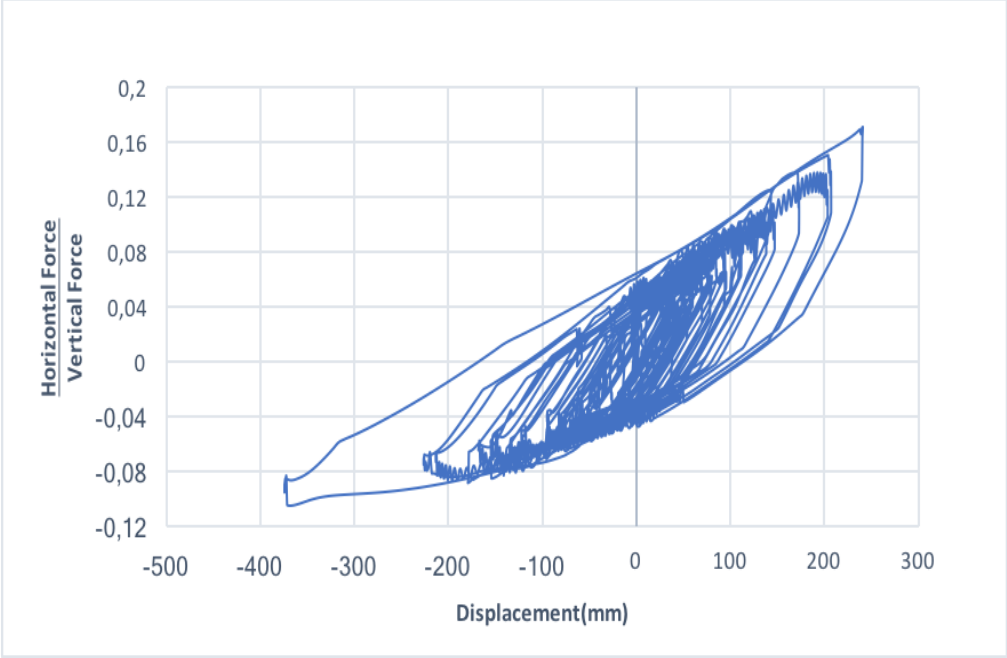

Figure 4.71: Delta Hysteresis Loop – X direction

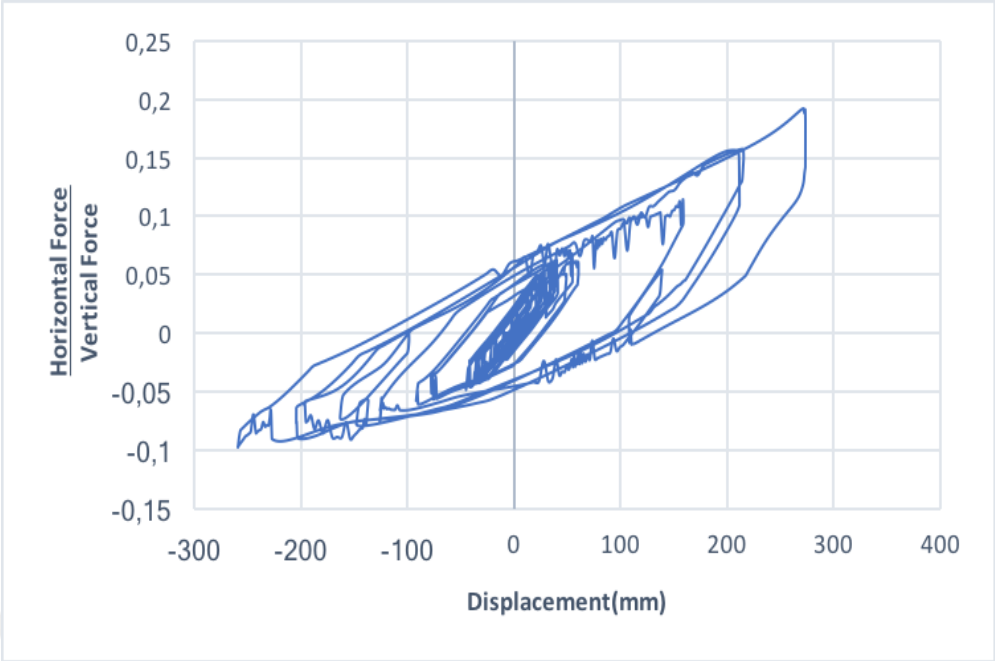

Figure 4.72: Hector Hysteresis Loop – X direction

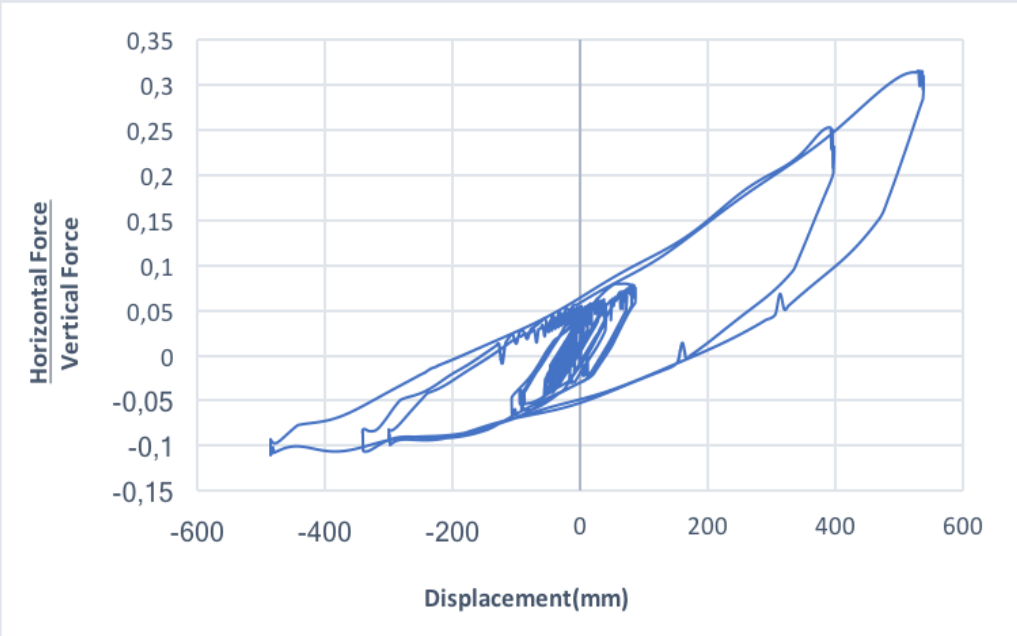

Figure 4.73: L.A Hollywood Hysteresis Loop – X direction

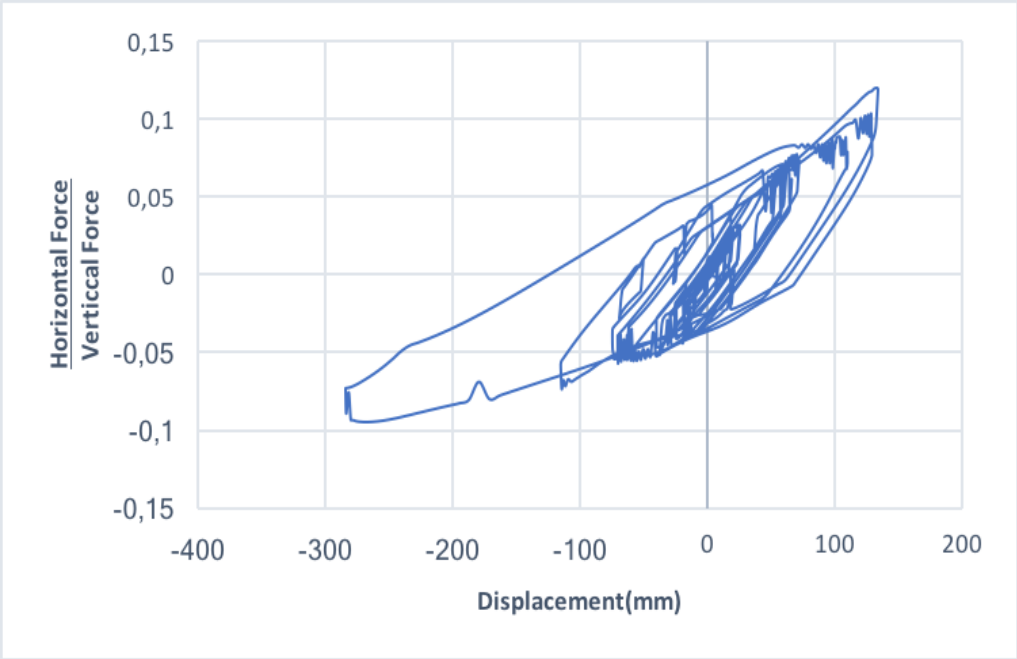

Figure 4.74: Beverly Hills Hysteresis Loop – X direction

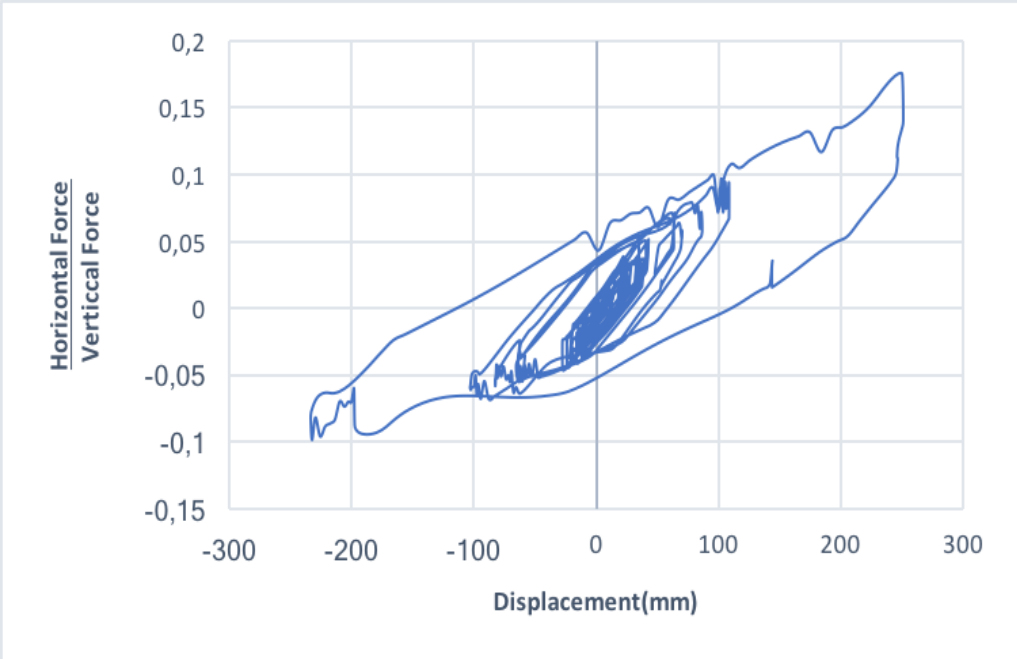

Figure 4.75: Abbar Hysteresis Loop – X direction

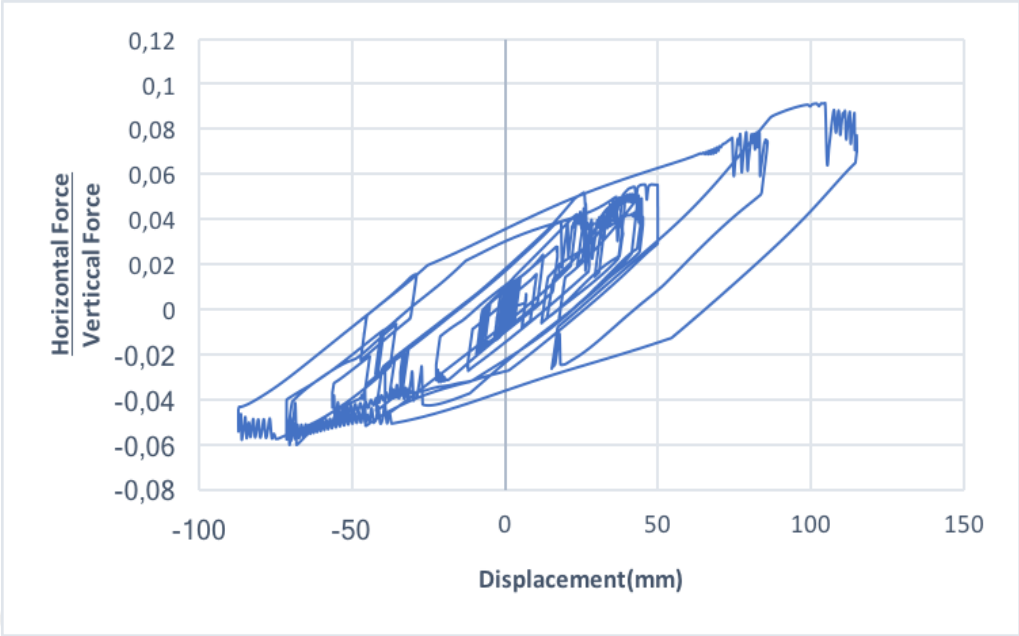

Figure 4.76: Coolwater Hysteresis Loop – X direction

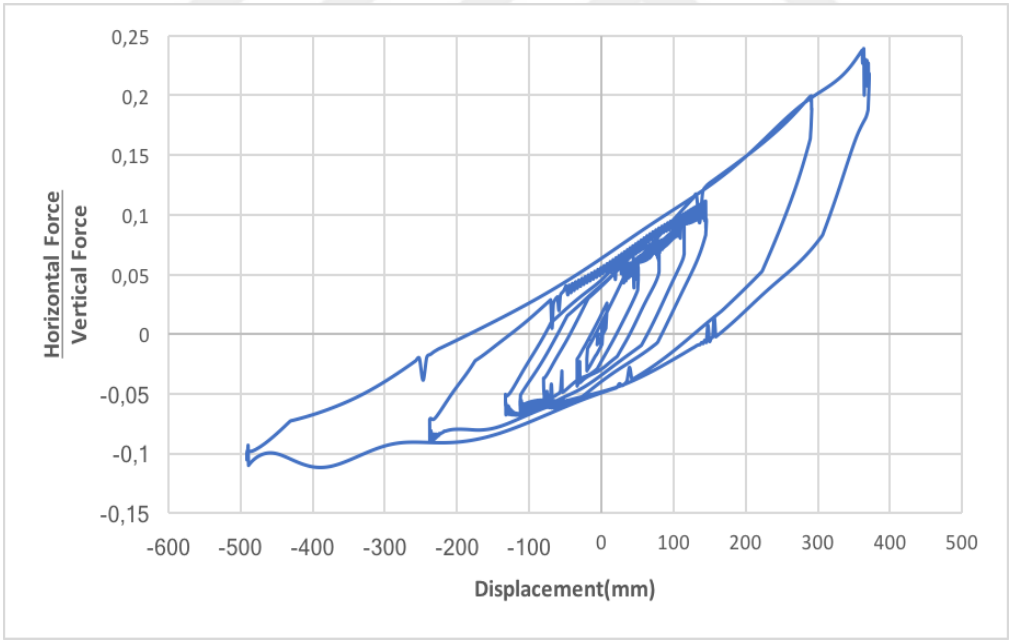

Figure 4.77: Erzincan Hysteresis Loop – X direction

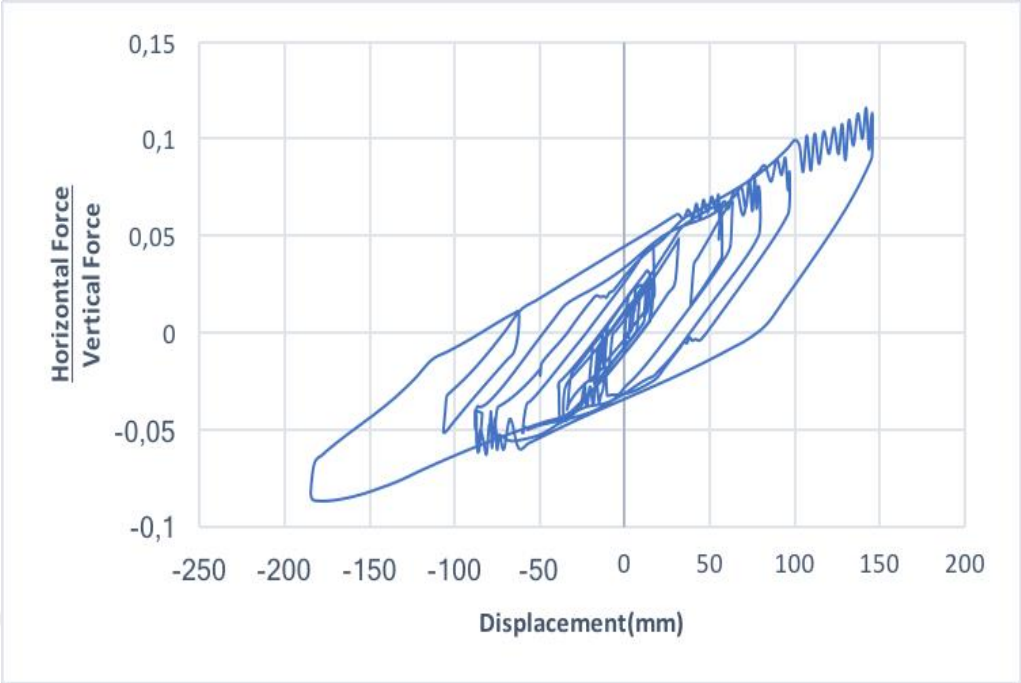

Figure 4.78: Petrolia Hysteresis Loop– X direction

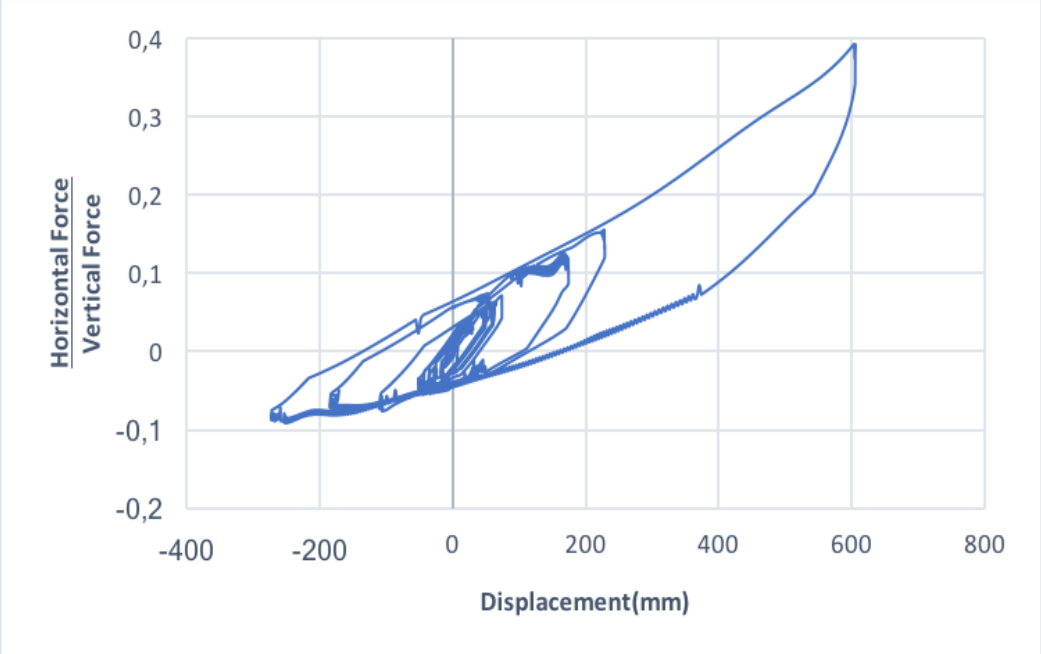

Figure 4.79: Duzce Hysteresis Loop – X direction

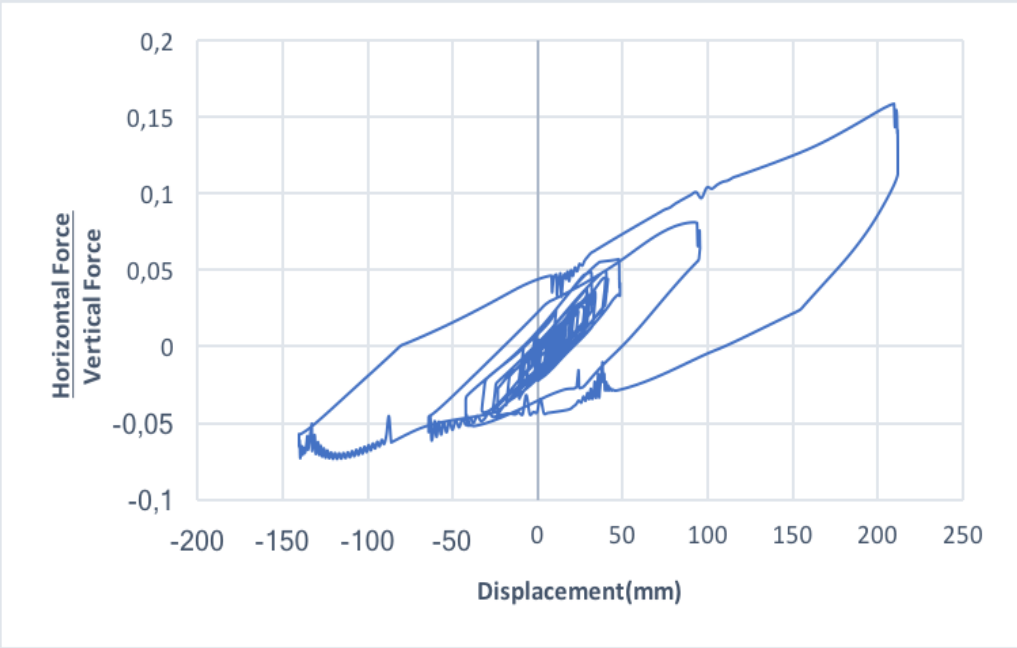

Figure 4.80: Bonds Corner Hysteresis Loop – X direction

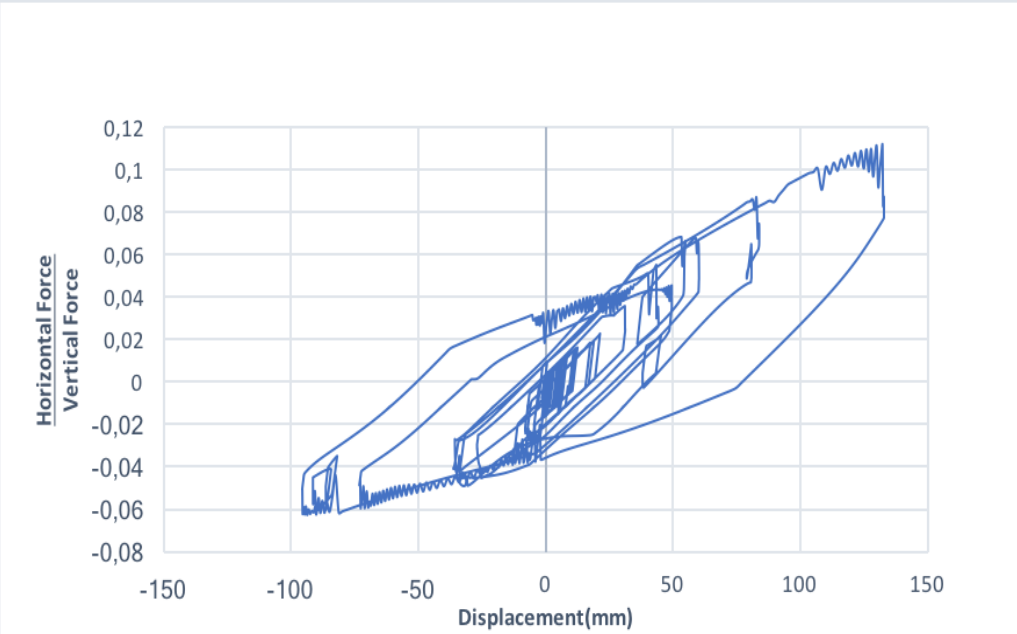

Figure 4.81: Nahanni Site 2 Hysteresis Loop – X direction

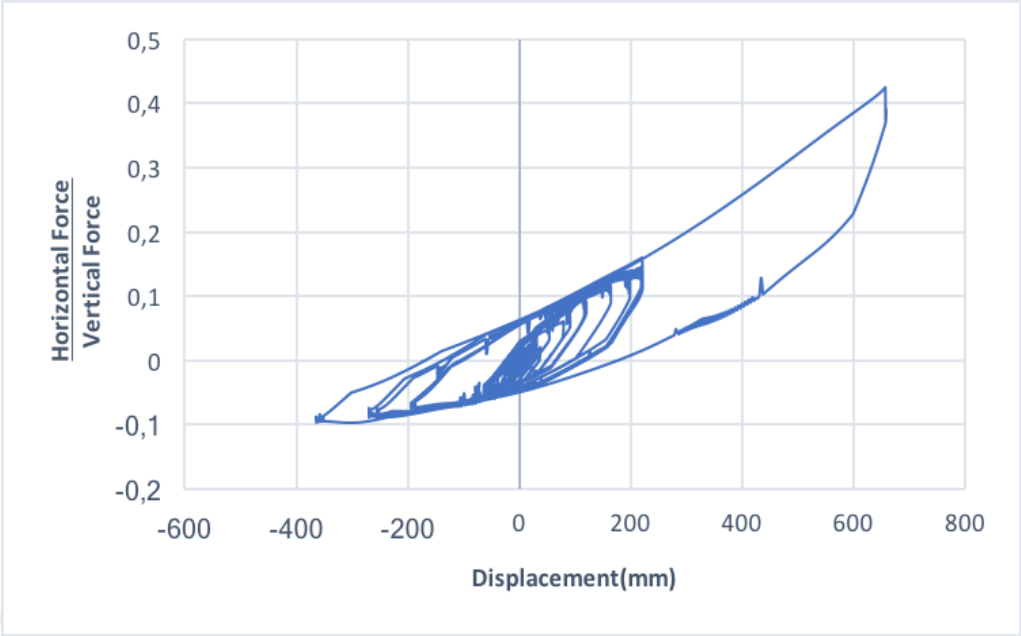

Figure 4.82: ChiChi TCU067 Hysteresis Loop – X direction

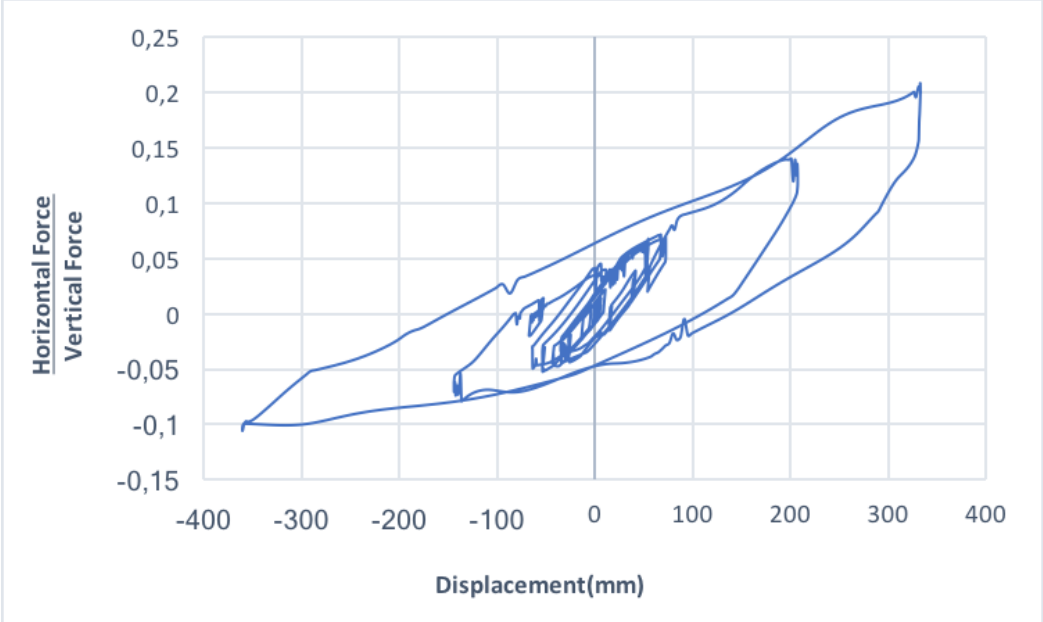

Figure 4.83: Parachute Test Site Hysteresis Loop – X direction

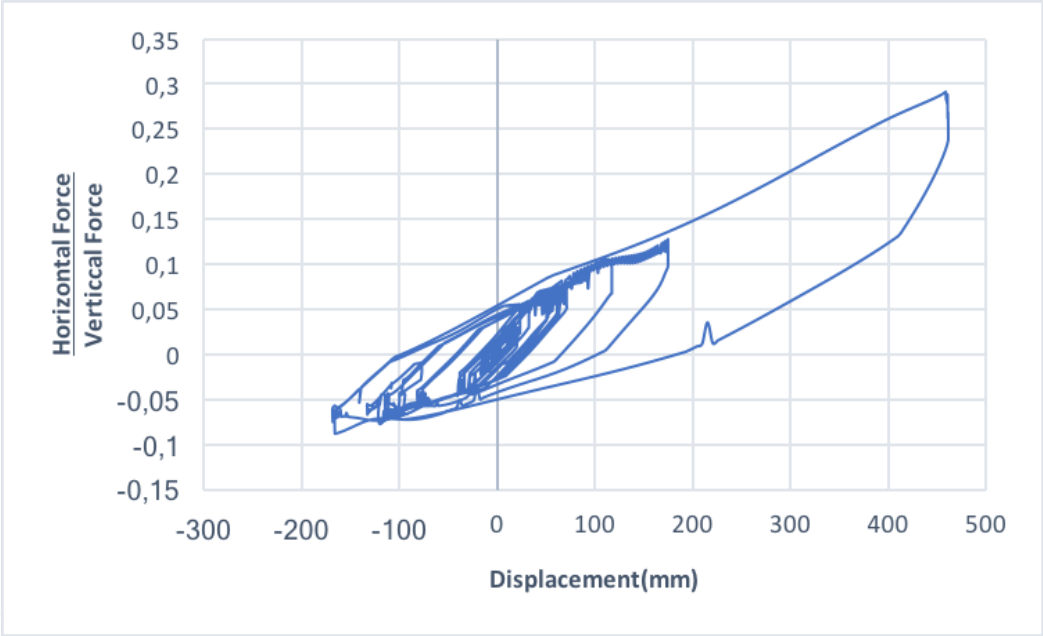

Figure 4.84: Saratoga Hysteresis Loop – X direction

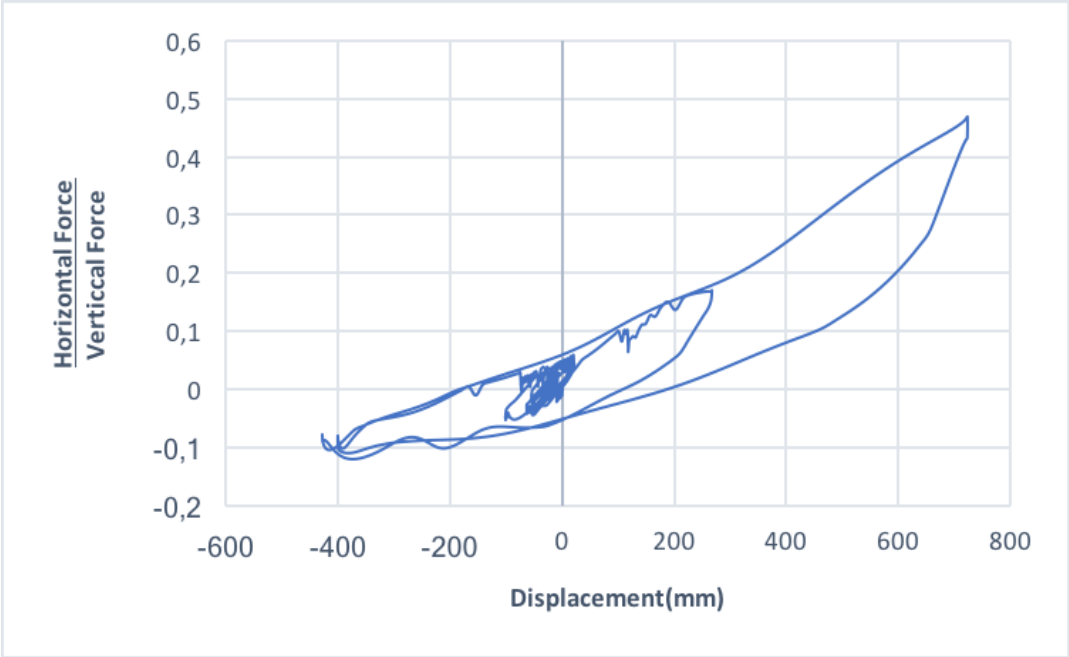

Figure 4.85: Sylmar Hysteresis Loop – X direction

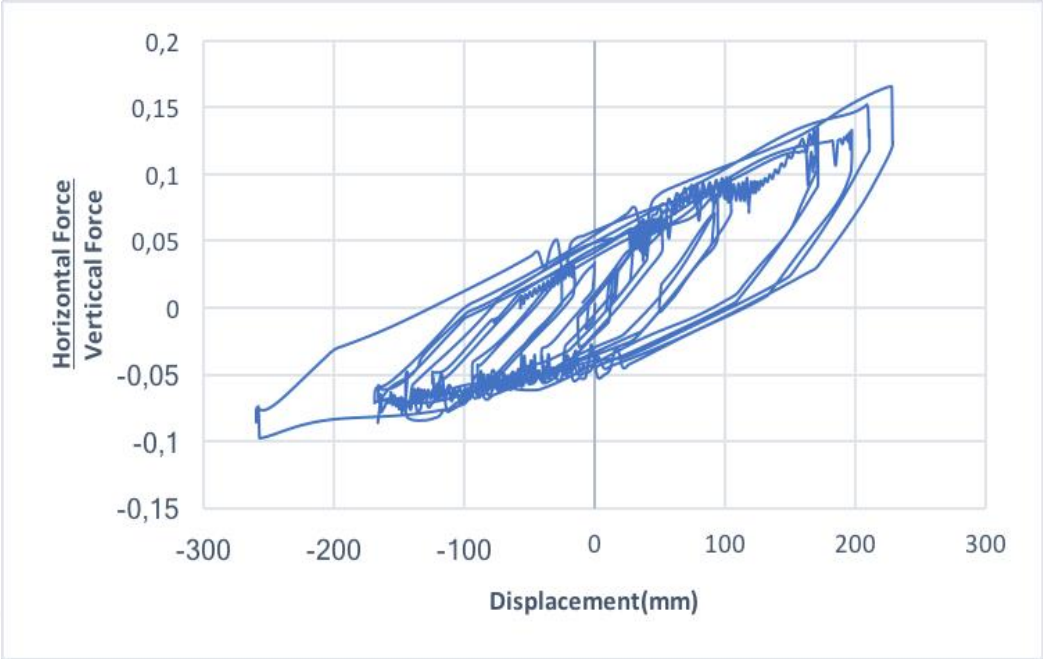

Figure 4.86: Saticoy Hysteresis Loop – X direction

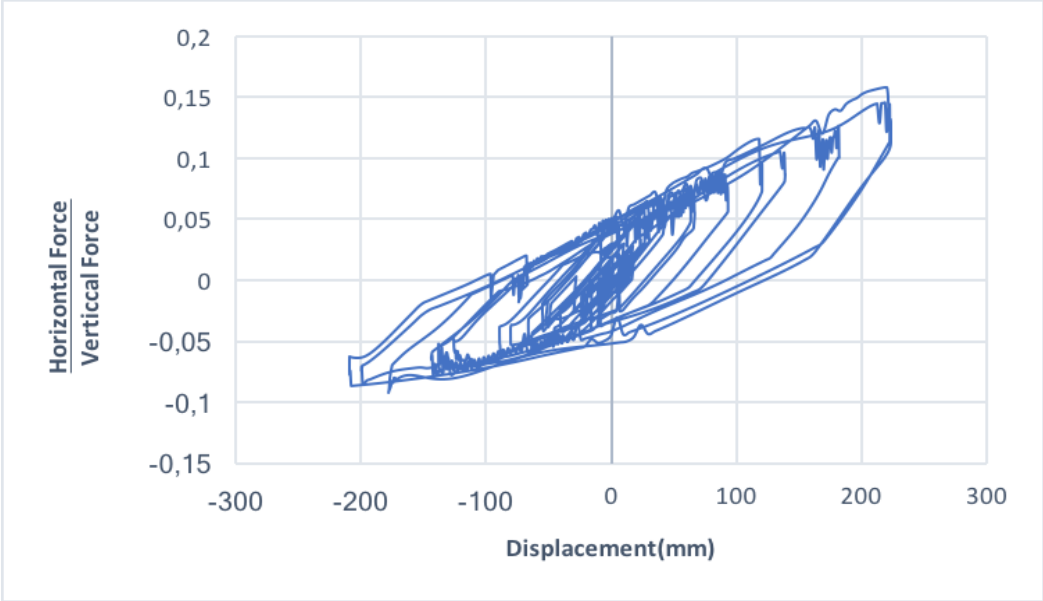

Figure 4.87: Chihuahua Hysteresis Loop – X direction

4.2.5 Influence of the Change in Friction Coefficient

Optimization on TFP isolator is conducted under scaled earthquake records in Table 4.1 to determine the base shear behaviour of the analysis model at different friction coefficient. The coefficient of friction is an important parameter that affects the structural response and the bearing displacements. The friction coefficients of the surfaces are maintained as ($\mu_2 = \mu_3 < \mu_1 < \mu_4$) throughout the analysis following the general design.

Table 4.1: Bearing Friction Coefficient Configurations

Bearing	Lower Bound (μ_{slow})				Upper Bound (μ_{fast})			
	μ_1	μ_2	μ_3	μ_4	μ_1	μ_2	μ_3	μ_4
Configuration 1	0.02	0.01	0.01	0.07	0.03-0.07	0.01	0.01	0.12
Configuration 2	0.02	0.01	0.01	0.07	0.07	0.01	0.01	0.08-0.12
Configuration 3	0.04	0.01-0.03	0.01-0.03	0.07	0.07	0.01-0.03	0.01-0.03	0.12

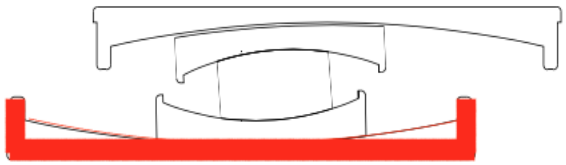

Figure 4.88: Configuration 1

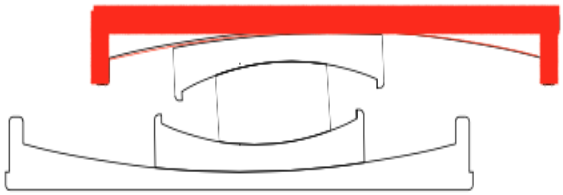

Figure 4.89: Configuration 2

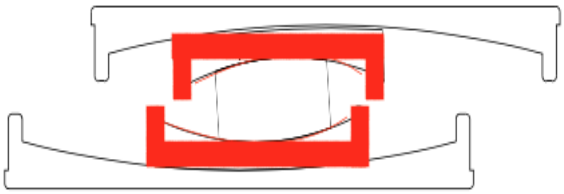

Figure 4.90: Configuration 3

Configuration 1 in Figure 4.85 has a constant lower and upper bound friction values for both inner surfaces and outer surface 4. The surface 1 lower bound friction value is also kept constant but the upper bound value is change at each analysis at a rate of 0.01. Similarly, Configuration 2 in Figure 4.86 has a constant lower and upper bound friction values for both inner surfaces and outer surface 1 whilst outer surface 4 upper bound value is also changed at a rate of 0.01. Furthermore, Configuration 3 in Figure 4.87 has a constant lower and upper bound friction coefficient for the outer surfaces with changing lower and upper bound friction coefficient for the inner surfaces.

Variation of Base Shear with Friction Coefficient

High base shear causes structural damage in buildings, to reduce this effect modification is made on friction coefficients to study the performance of the building at each configured analysis. Figure 4.91 and Figure 4.92 shows the earthquake records with configuration 1 friction coefficient and their mean at each friction point. The normalizing point is taken as 0.05, base shear decreases with increase in friction. Configuration 2 analysis in Figure 4.93 and Figure 4.94 shows reduction in mean base shear when the friction values increase. Moreover, configuration 3 in Figure 4.95 shows increase in base shear with increase in friction coefficient while Figure 4.96 shows ineffective variation on modifying the friction coefficient of the inner bearing surfaces.

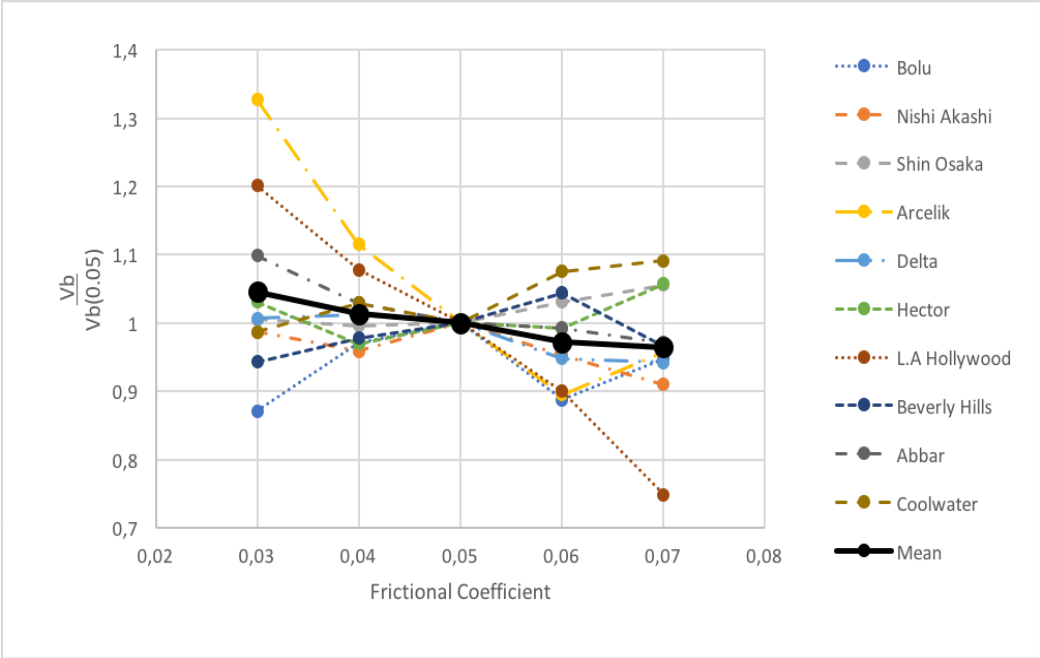

Figure 4.91: Far-Field Configuration 1 Maximum Base Shear – X direction

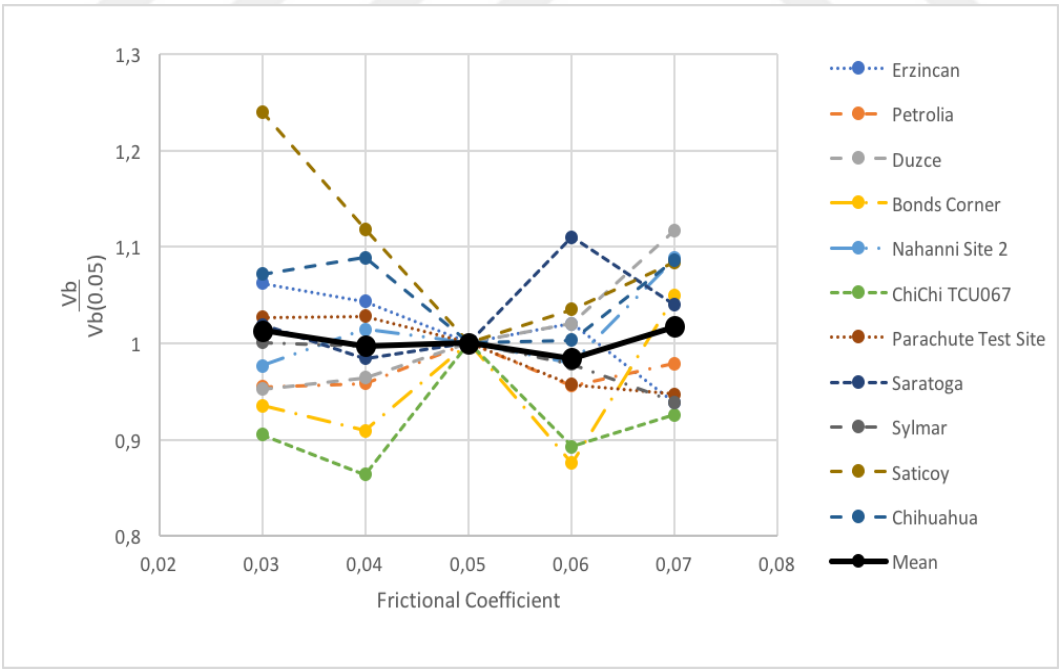

Figure 4.92: Near-Field Configuration 1 Maximum Base Shear – X direction

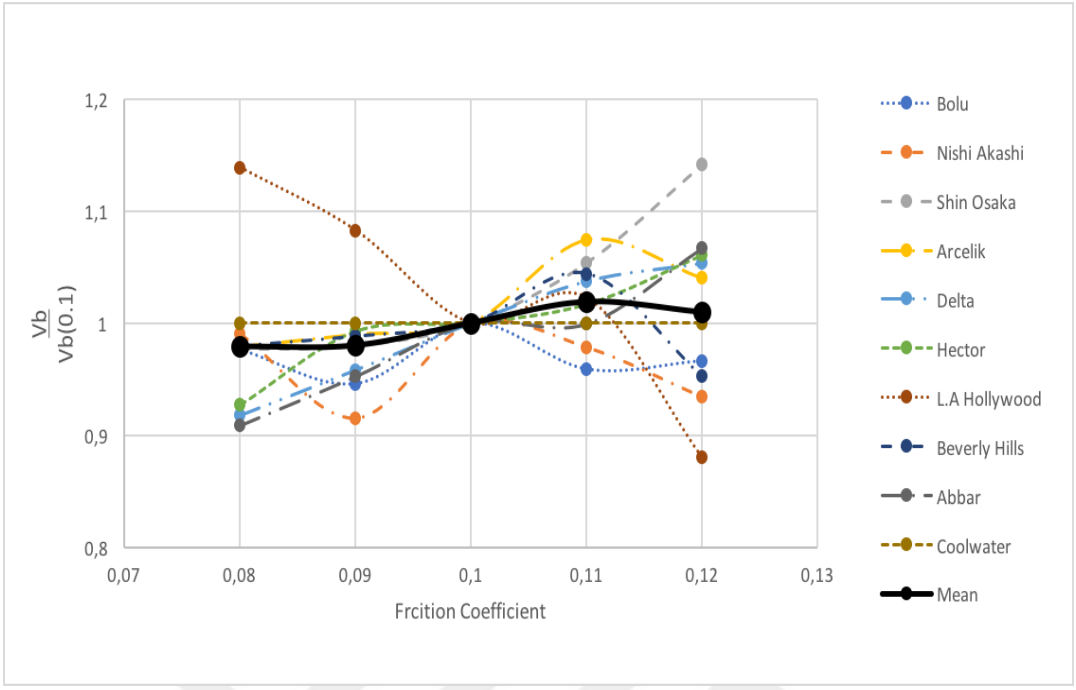

Figure 4.93: Far-Field Configuration 2 Maximum Base Shear – X direction

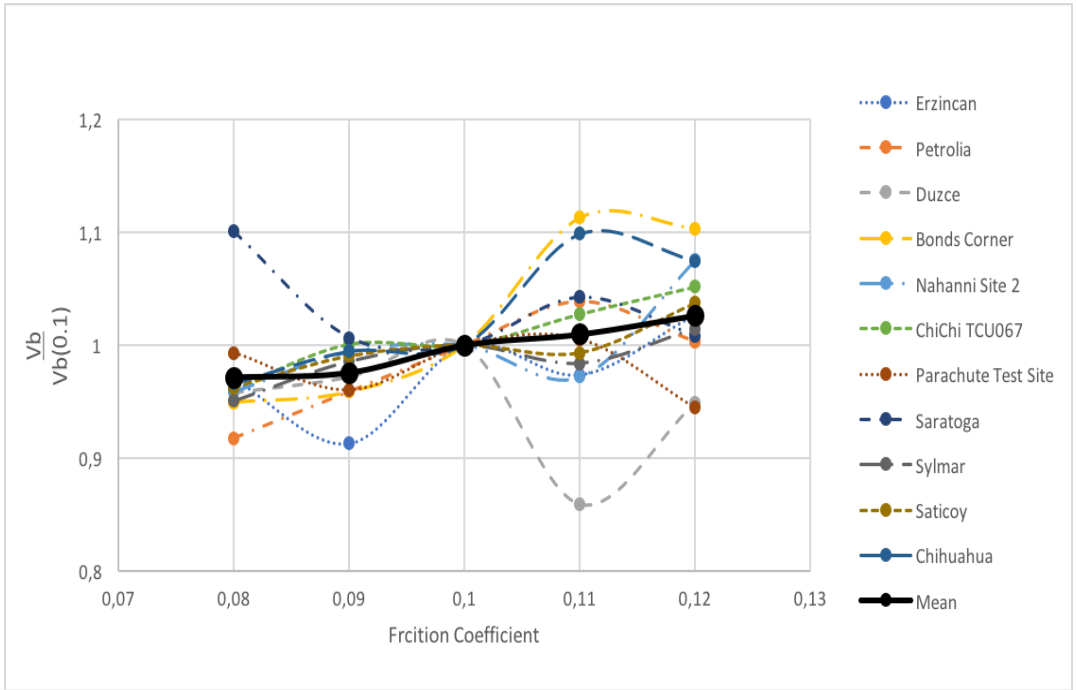

Figure 4.94: Near-Field Configuration 2 Maximum Base Shear – X direction

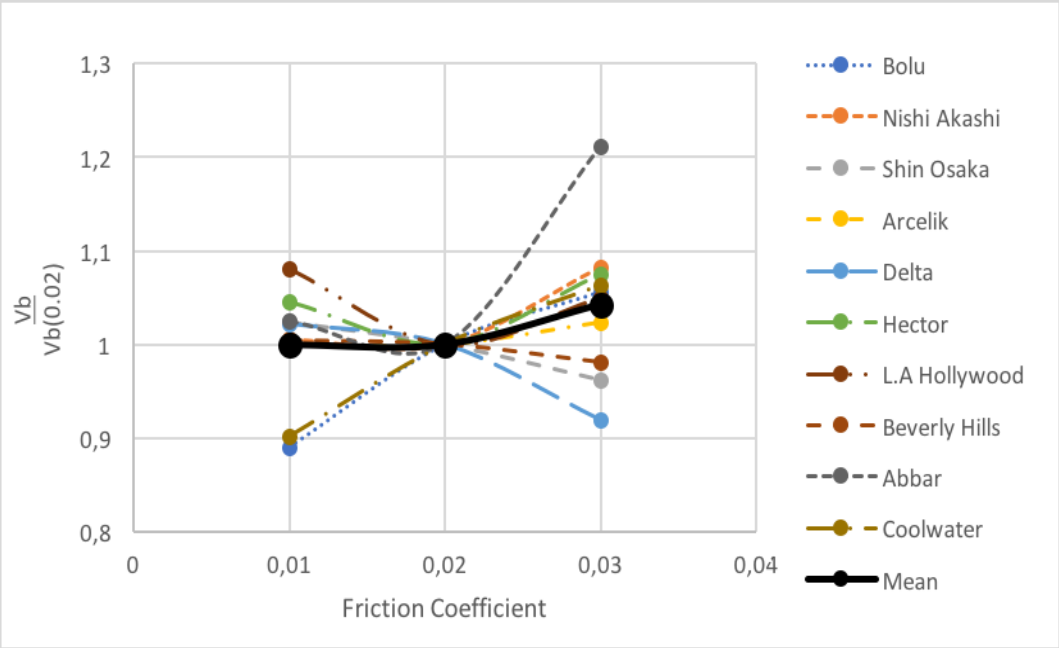

Figure 4.95: Far-Field Configuration 3 Maximum Base Shear – X direction

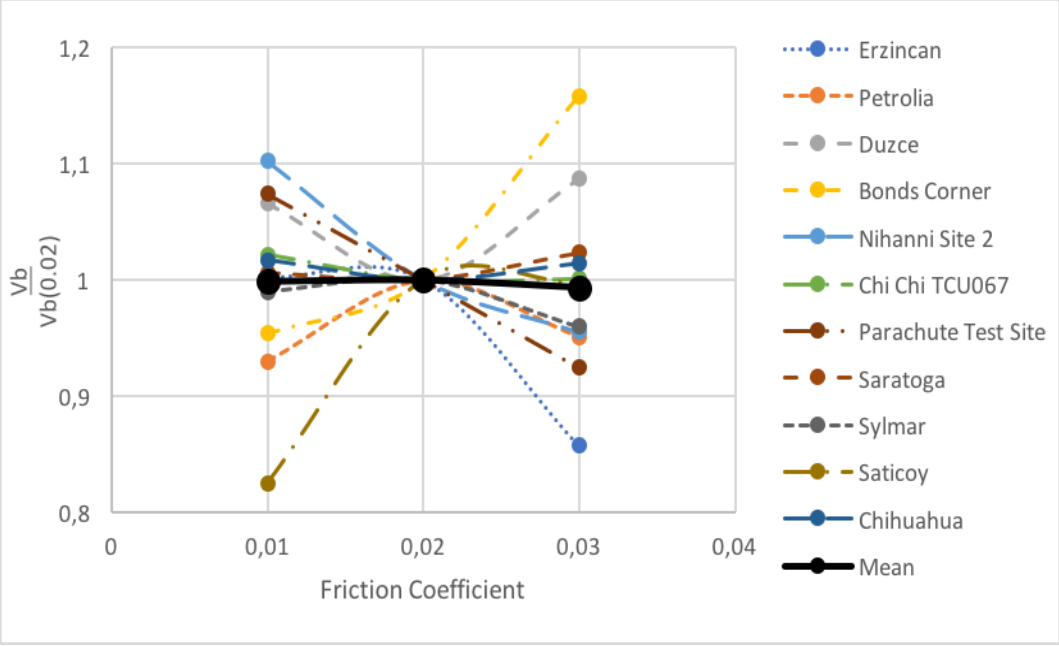

Figure 4.96: Near-Field Configuration 3 Maximum Base Shear – X direction

Variation of Bearing Displacement with Friction Coefficient

. The configuration 1 displacements in Figure 4.97 and Figure 4.98 shows that lower friction coefficient analysis below 0.05 have higher bearing displacement whereas past the normalizing friction coefficient the average displacement lessens. Furthermore, Configuration 2 displacement in Figure 4.99 and Figure 4.100 are less in the mid μ_{4fast} values but overall higher friction coefficient reduces more bearing displacement. Moreover, configuration 3 analysis in Figure 4.101 and Figure 4.102 shows a mean decrease in bearing displacement after increasing friction coefficient.

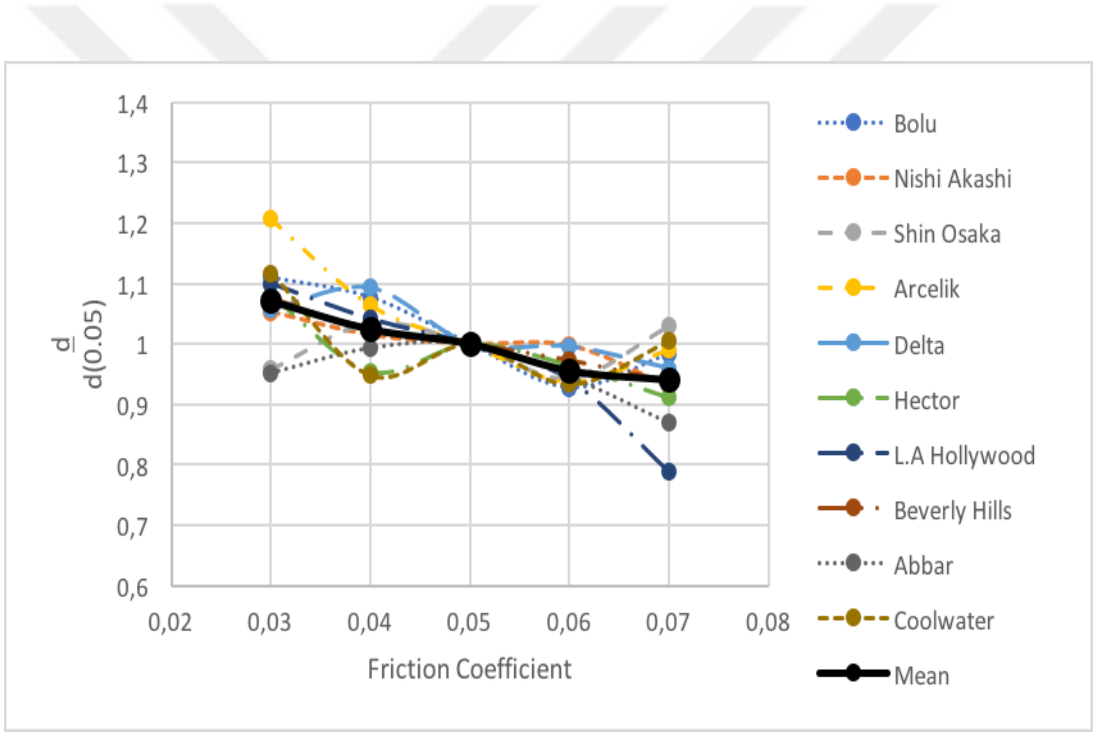

Figure 4.97: Far-Field Configuration 1 Bearing Maximum Displacement – X direction

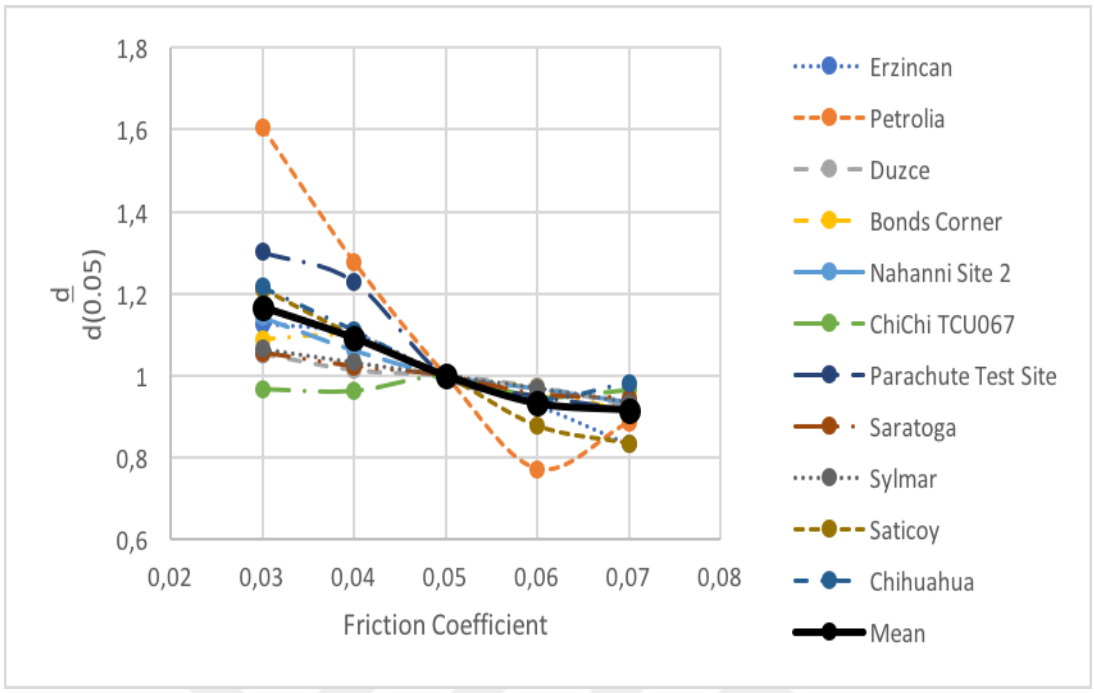

Figure 4.98: Near-Field Configuration 1 Bearing Maximum Displacement – X direction

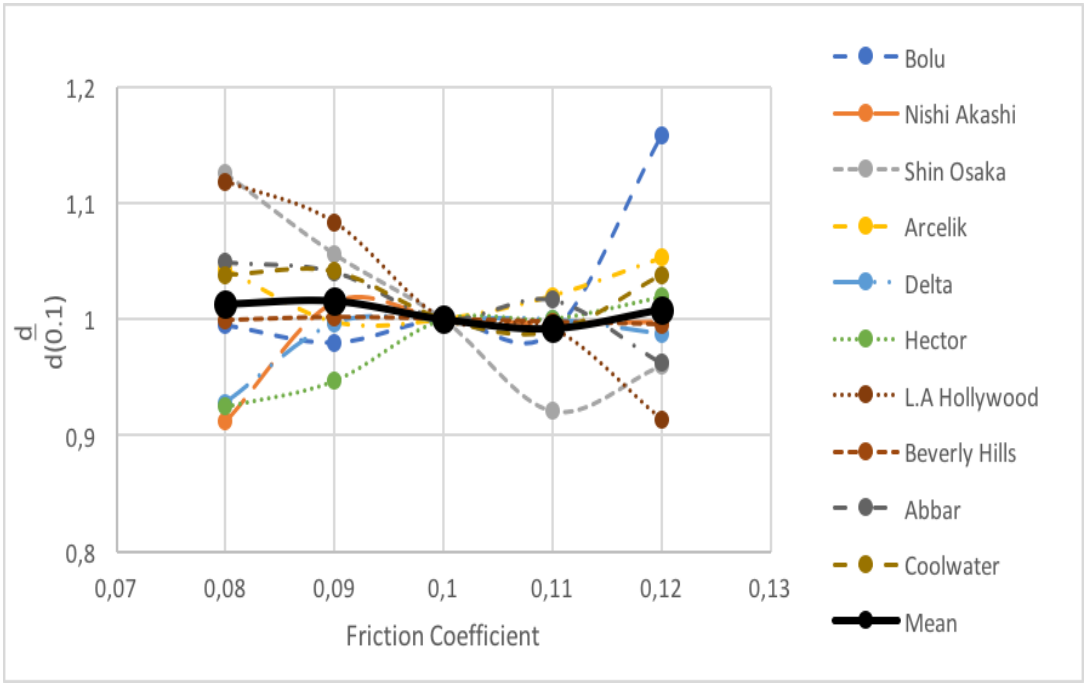

Figure 4.99: Far-Field Configuration 2 Bearing Maximum Displacement – X direction

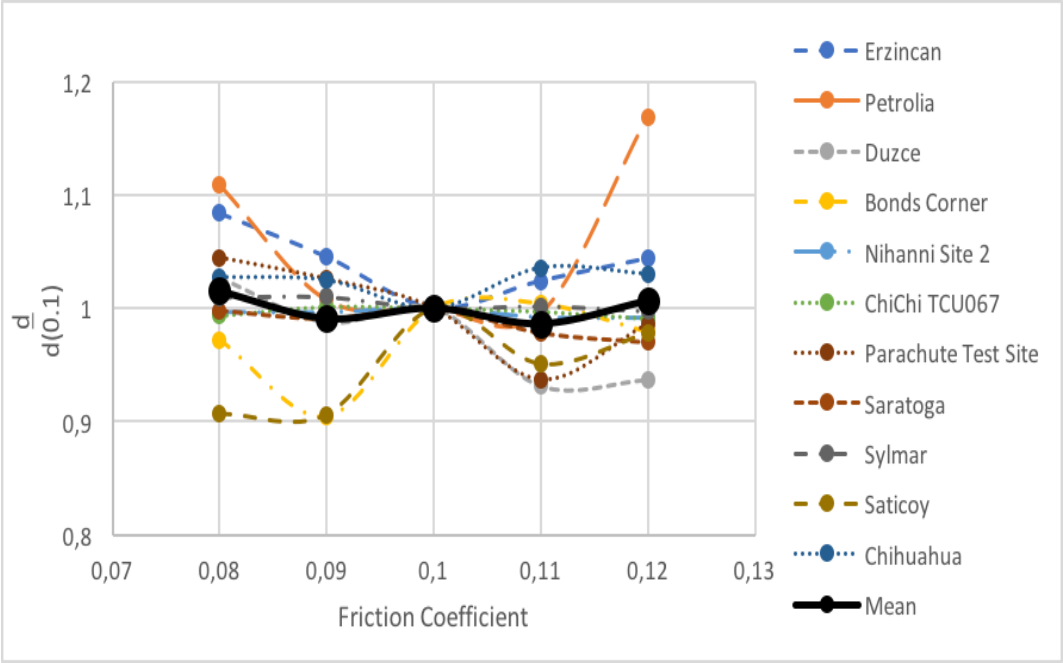

Figure 4.100: Near-Field Configuration 2 Bearing Maximum Displacement – X direction

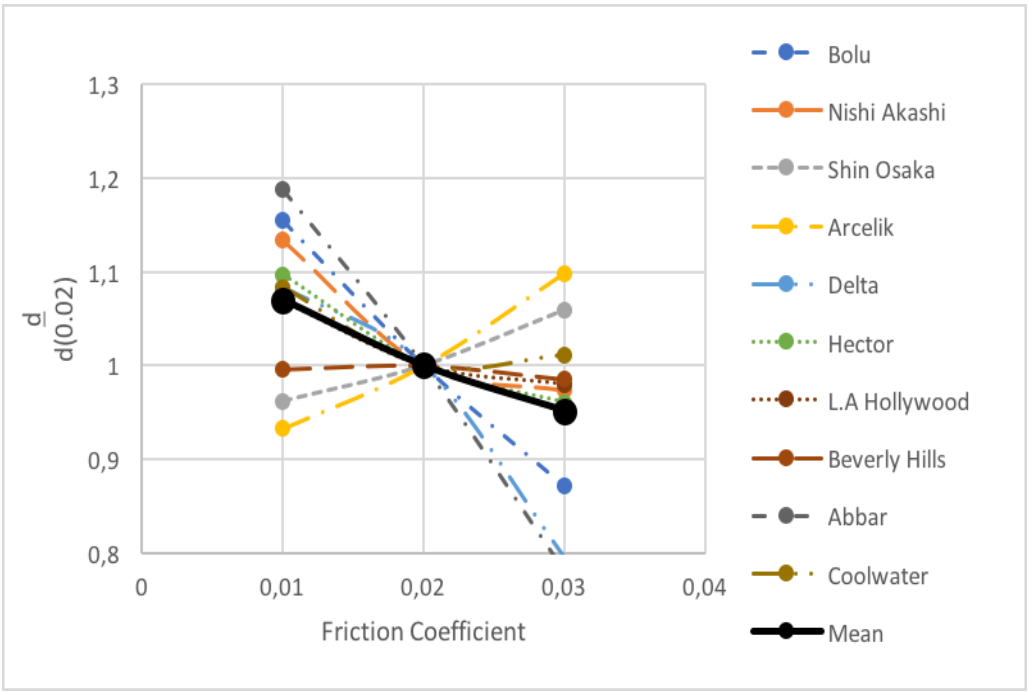

Figure 4.101: Far-Field Configuration 3 Bearing Maximum Displacement – X direction

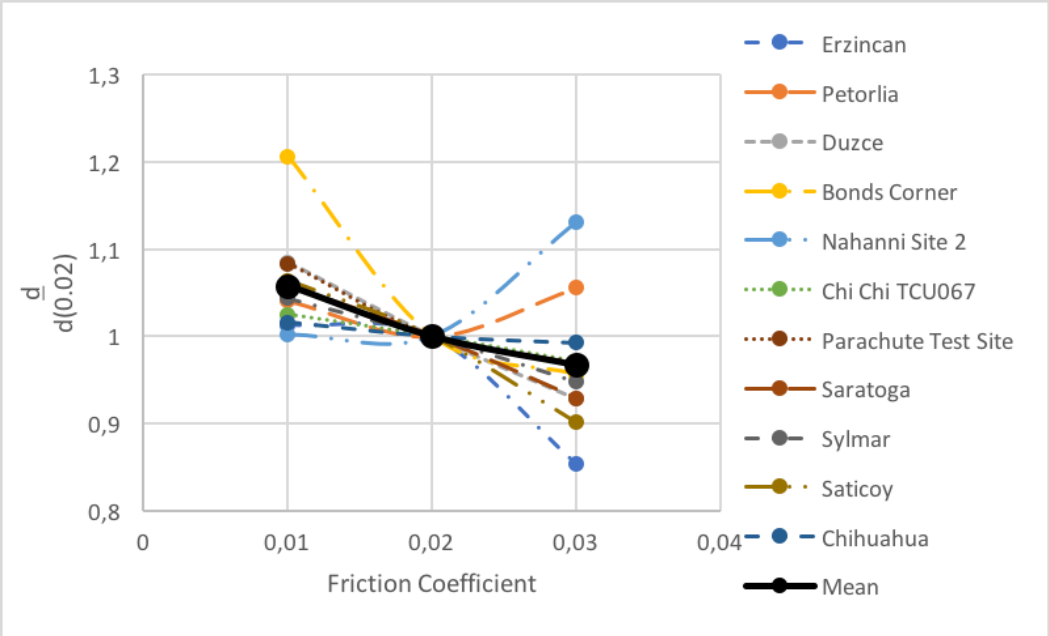

Figure 4.102: Near-Field Configuration 3 Bearing Maximum Displacement – X direction

4.2.6 Influence of Bearing Contamination

Bearing contamination happens when bearing surfaces are not protected allowing particles and other environmental factors affect the friction surface coating. Generally, triple friction pendulum bearing surfaces are rubber seal protected to keep the bearing from disintegration during shear and uplift [62]. These rubber seal also provides environmental protection to the bearing.

Table 4.2: Original and Configured Contaminated Bearings

Bearing	Lower Bound (μ_{slow})				Upper Bound (μ_{fast})			
	μ_1	μ_2	μ_3	μ_4	μ_1	μ_2	μ_3	μ_4
Normal	0.02	0.01	0.01	0.05	0.05	0.01	0.01	0.1
Configuration A	0.03-0.05	0.01	0.01	0.06-0.08	0.06-0.08	0.01	0.01	0.11-0.13
Configuration B	0.03-0.05	0.02-0.04	0.02-0.04	0.06-0.08	0.06-0.08	0.02-0.04	0.02-0.04	0.11-0.13

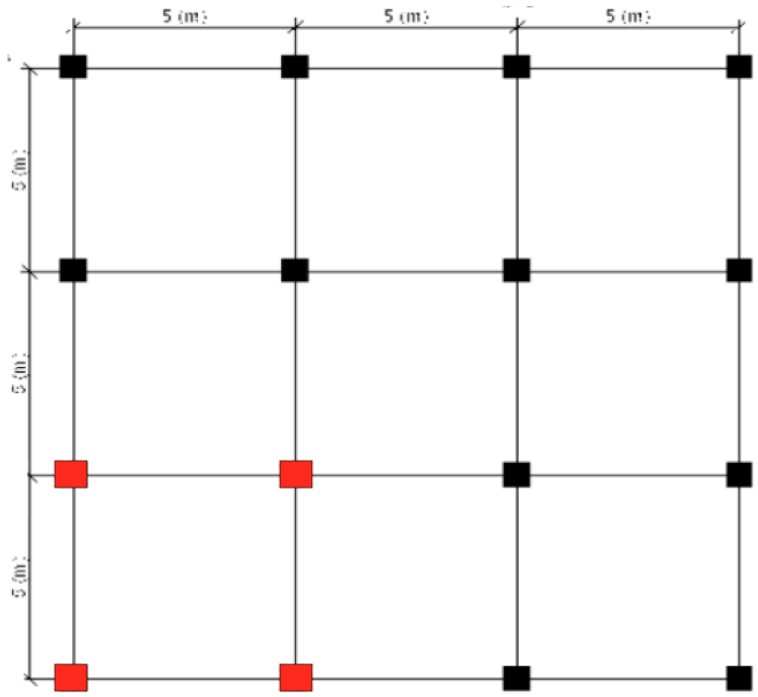

Figure 4.103: Case 1 X-Y Plan

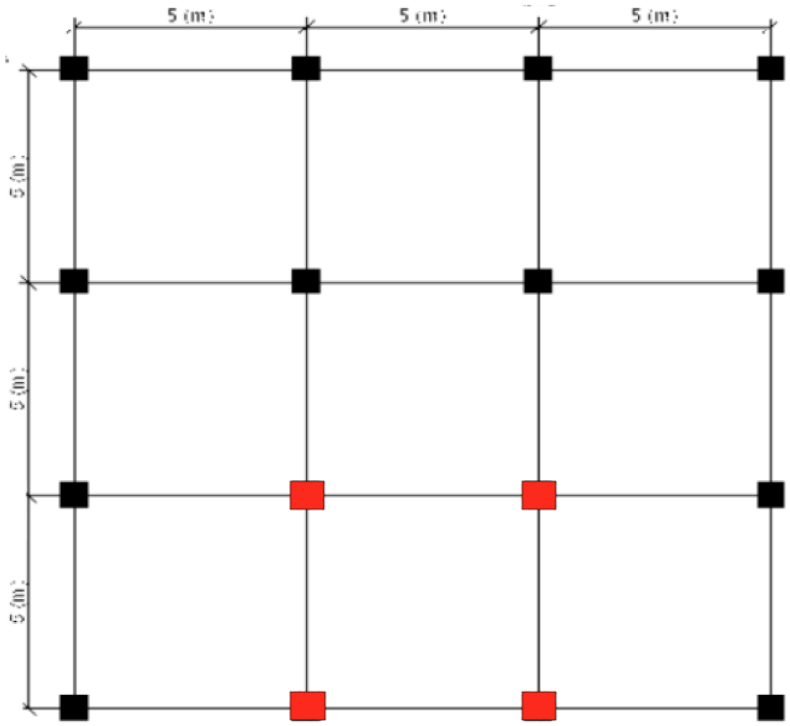

Figure 4.104: Case 2 X-Y Plan

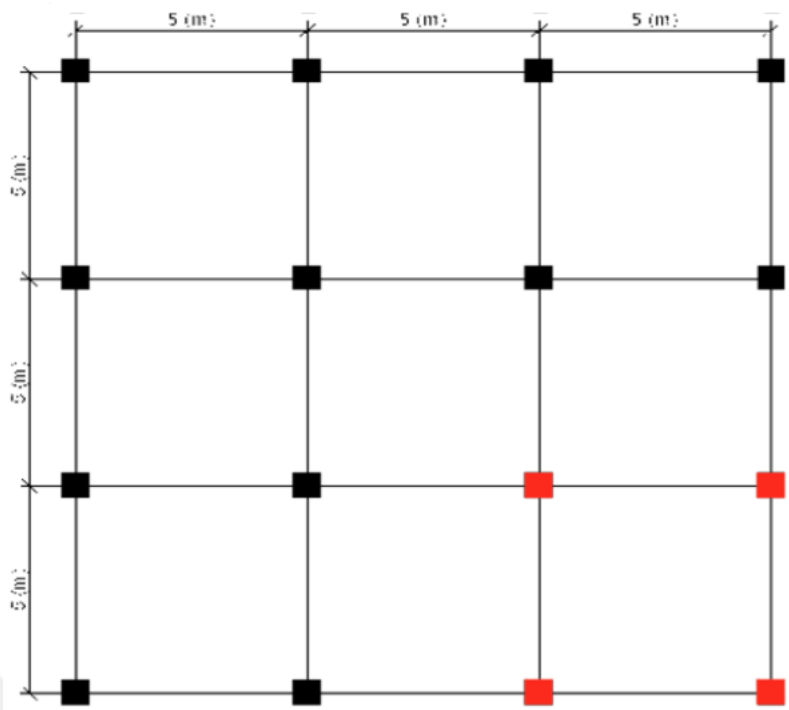

Figure 4.105: Case 3 X-Y Plan

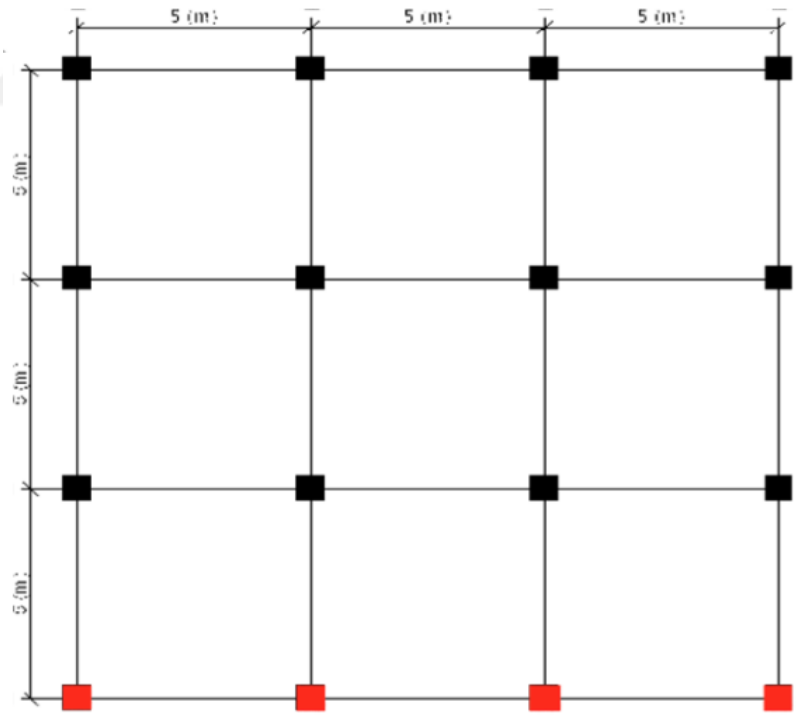

Figure 4.106: Case 4 X-Y Plan

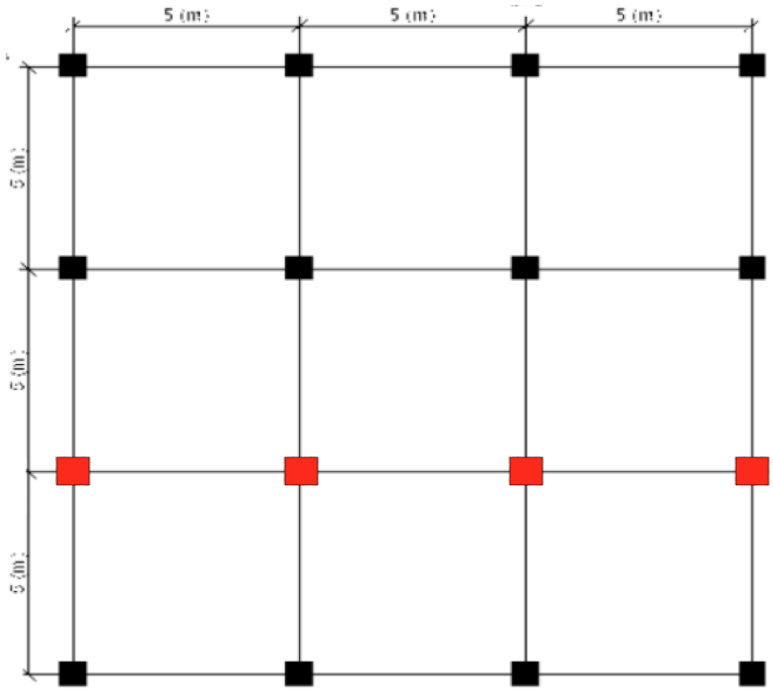

Figure 4.107: Case 5 X-Y Plan

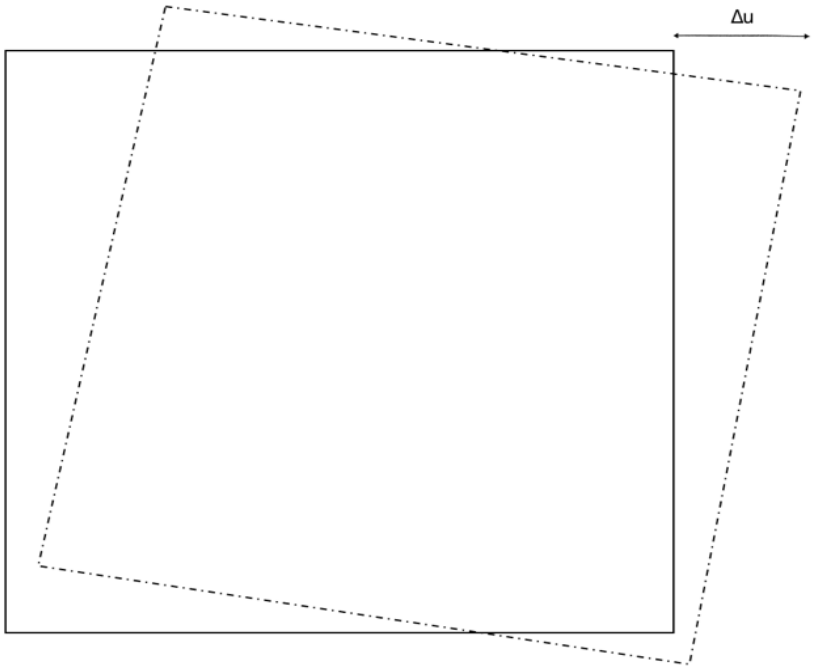

Figure 4.108: Plan Torsional Irregularity

Table 4.2 shows the bearing configurations; configuration A is for bearing protected internally disallowing any environmental effects on the inner surfaces but outer surfaces are left unprotected to be contaminated changing their friction coefficient (Δμ) at a rate of 0.01. Configuration B is a fully unprotected bearing allowing environmental effects on both inner and outer surfaces of the bearing leading to similar friction coefficient change. Effect of contaminated triple friction pendulum result to irregularity in Figure 4.108.

Effect of Contamination on Bearing Displacements

The non-uniformity of bearings is a factor that may cause damage to buildings due to torsion, the performance of the bearings with defect marked in red Figure 4.103 and Figure 4.107 are assessed for torsion effect. The vertical axis represents the percentages of displacement change of the cases in respect to the original bearing displacement. The analysis results also show that bearing displacements increase towards the vertical direction in each y-axis rows of the case plans. Configuration A for all cases show rise in displacement change with increase in contamination, the configuration has an average maximum increase of up to 6% of the original bearing displacement. Also, configuration B plots show average maximum of 11% displacement change percentage with contamination increase.

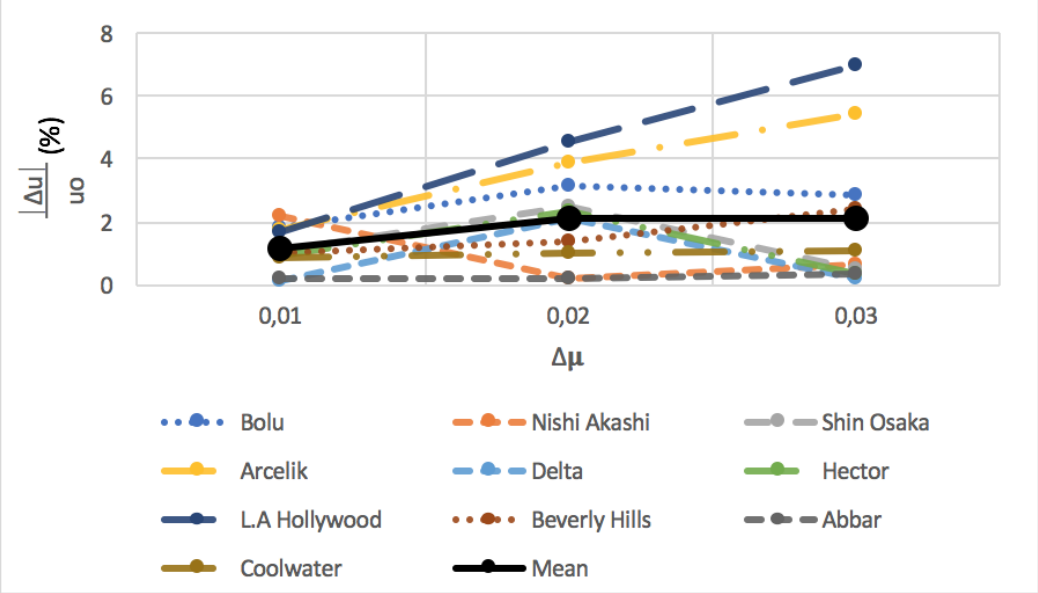

Figure 4.109: Far-Field Configuration A Case 1

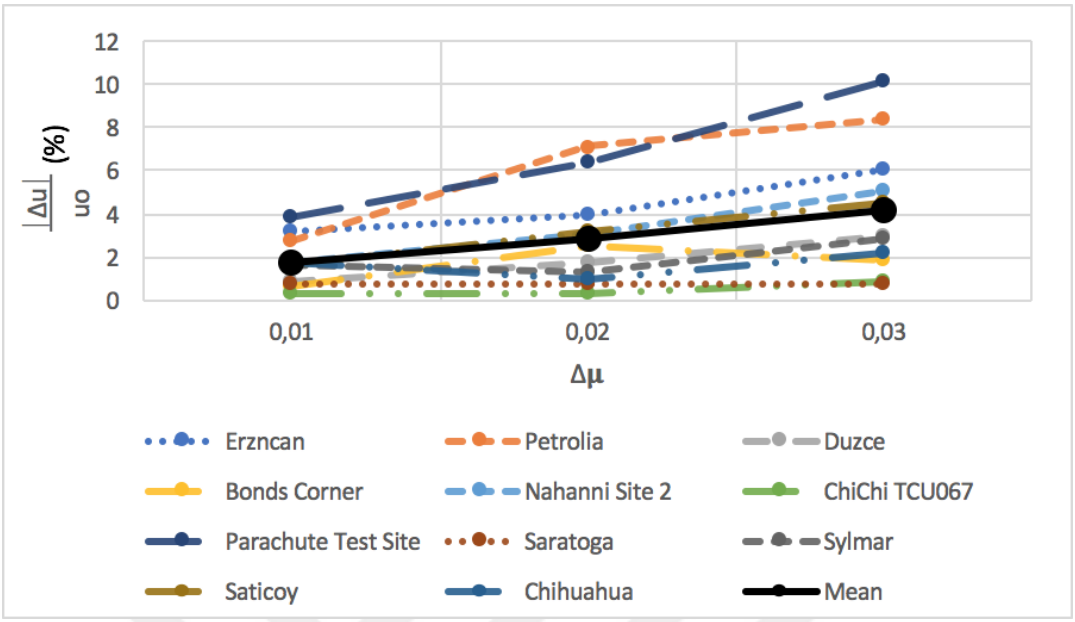

Figure 4.110: Near-Field Configuration A Case 1

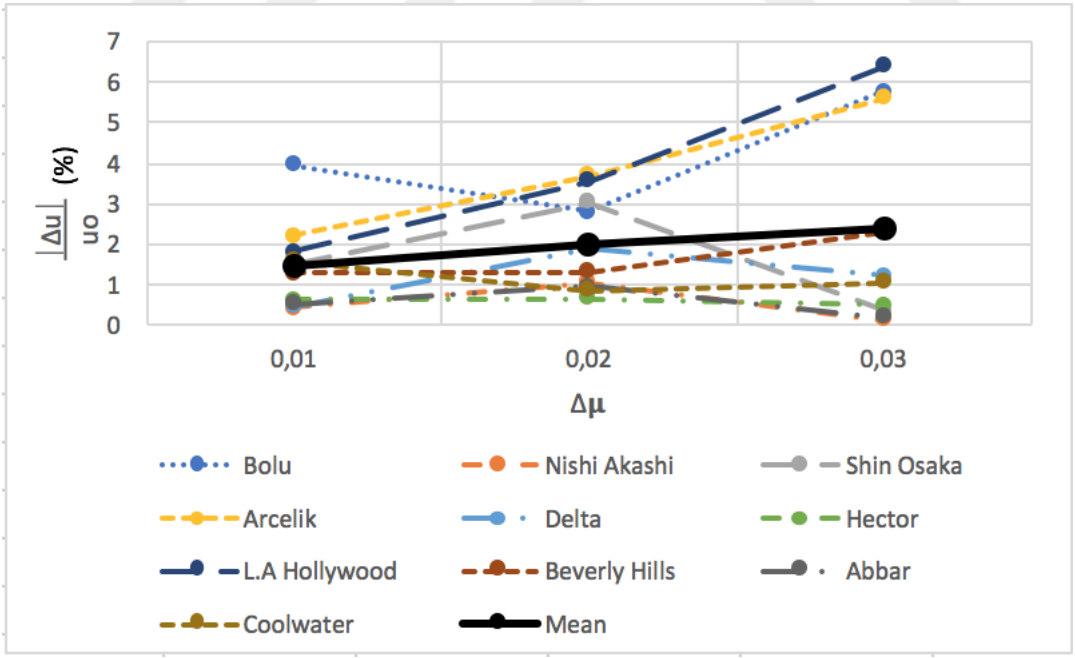

Figure 4.111: Far-Field Configuration A Case 2

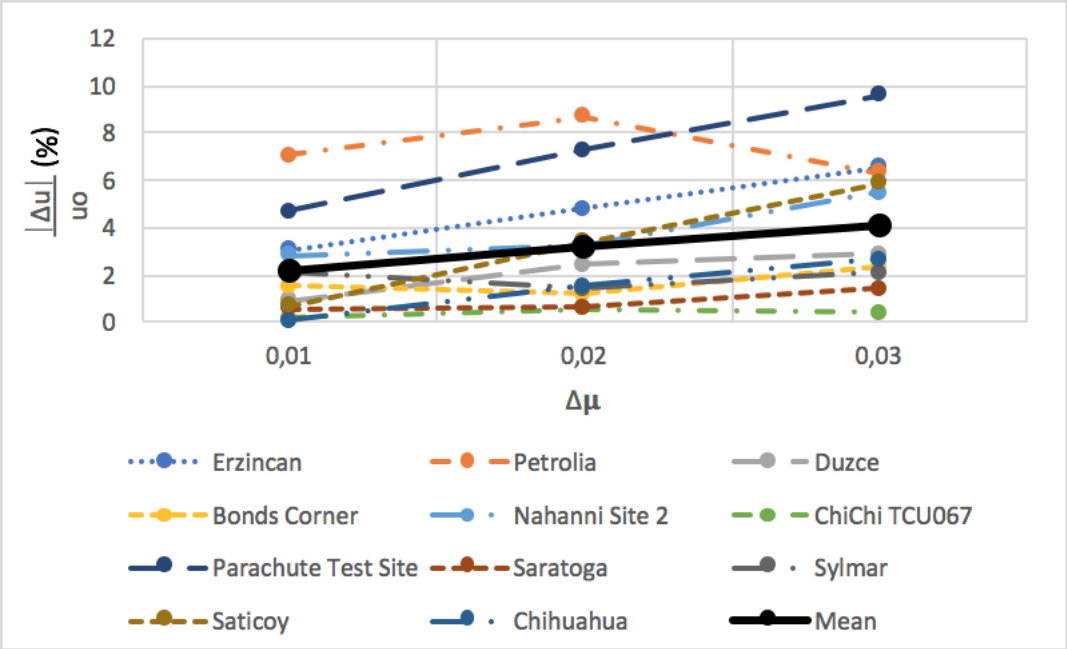

Figure 4.112: Near-Field Configuration A Case 2

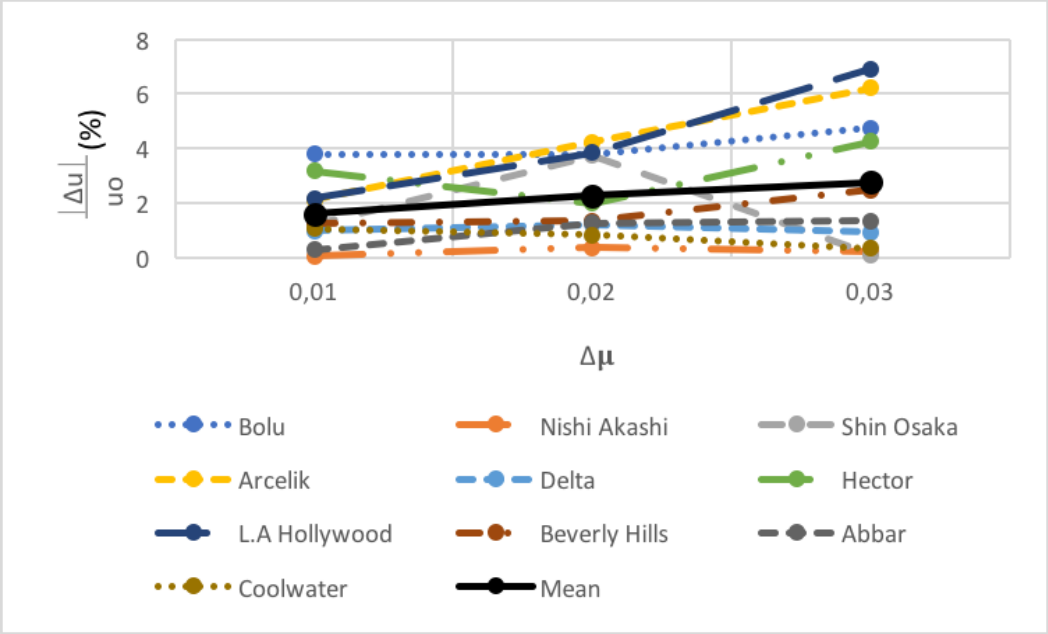

Figure 4.113: Far-Field Configuration A Case 3

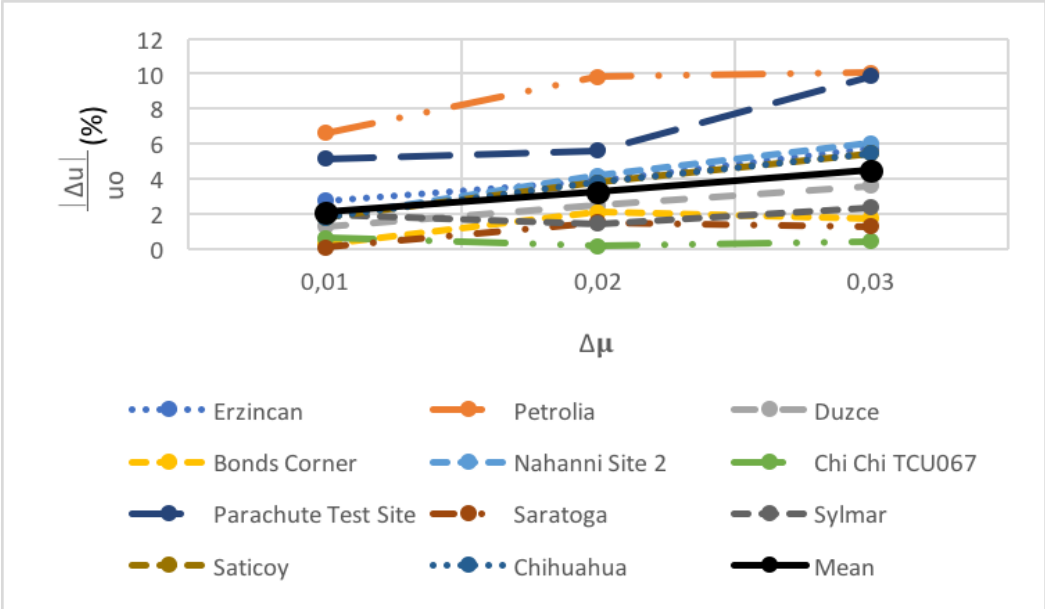

Figure 4.114: Near-Field Configuration A Case 3

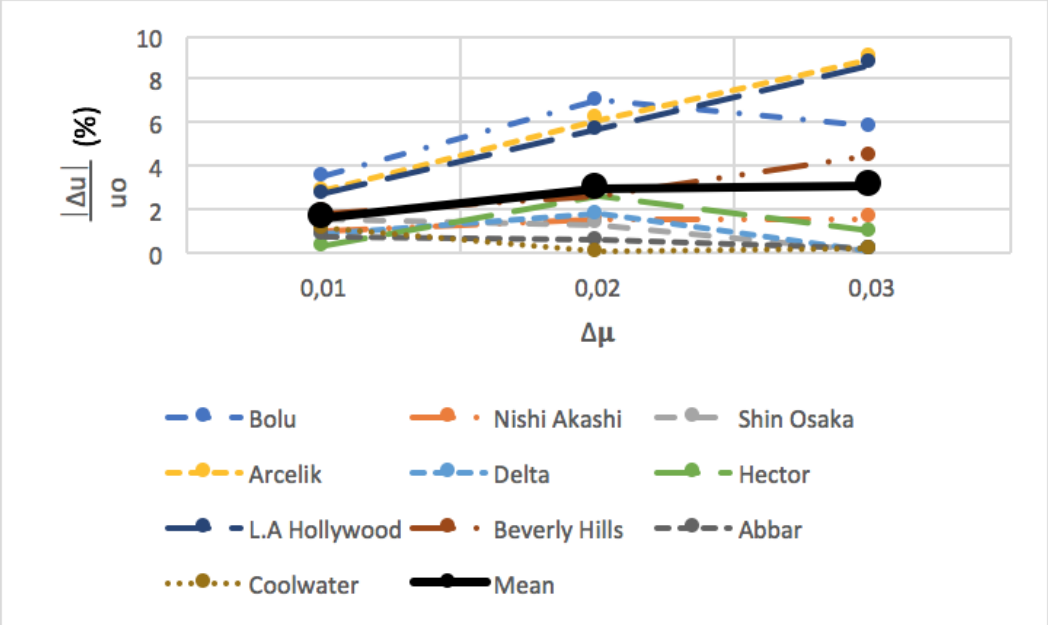

Figure 4.115: Far-Field Configuration A Case 4

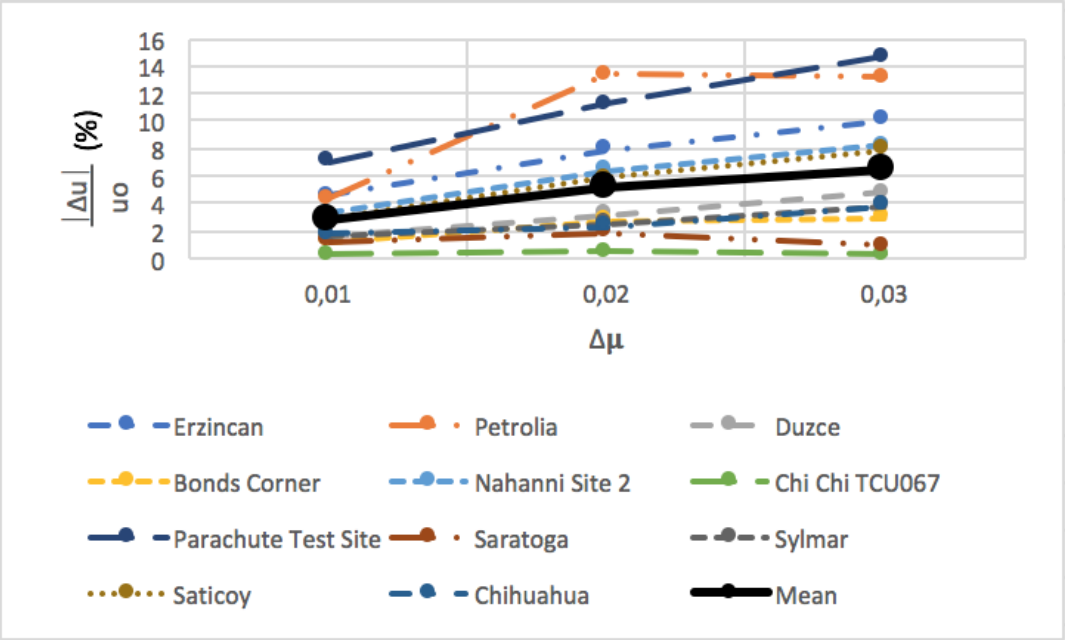

Figure 4.116: Near-Field Configuration A Case 4

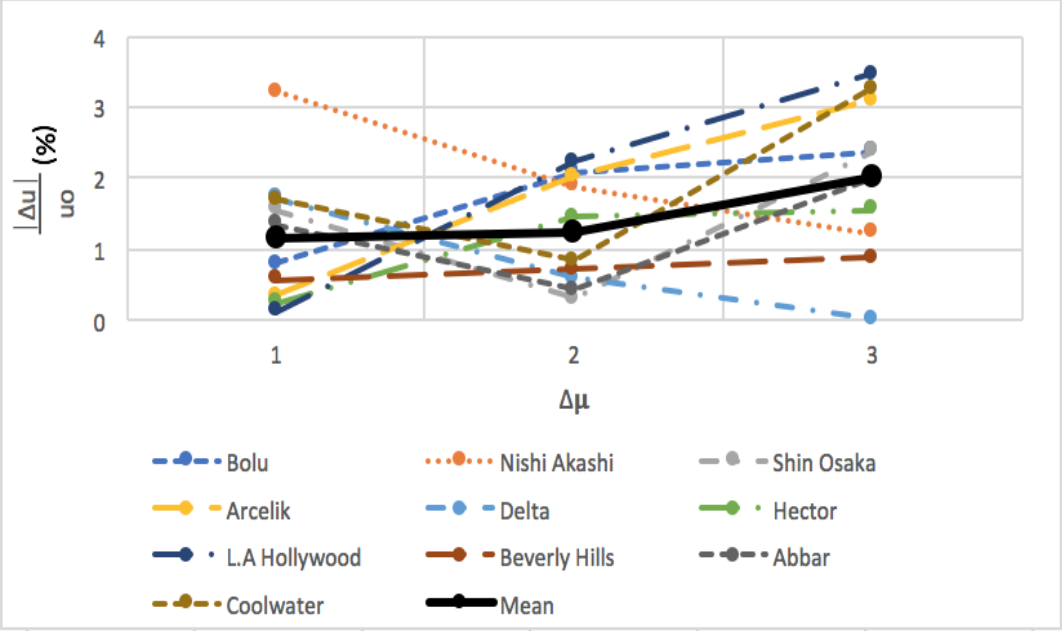

Figure 4.117: Far-Field Configuration A Case 5

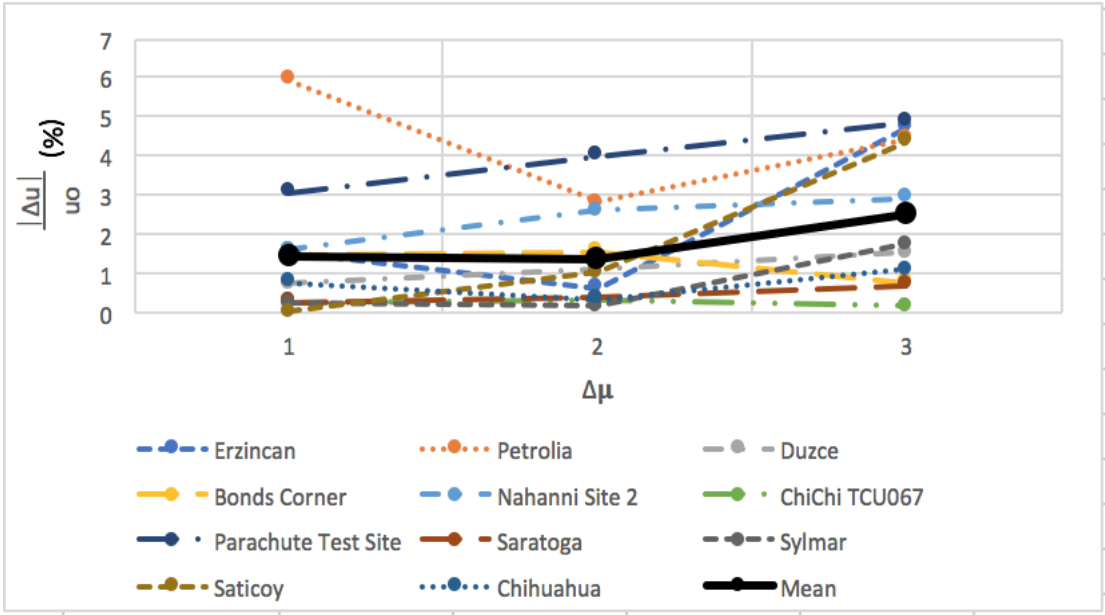

Figure 4.118: Near-Field Configuration A Case 5

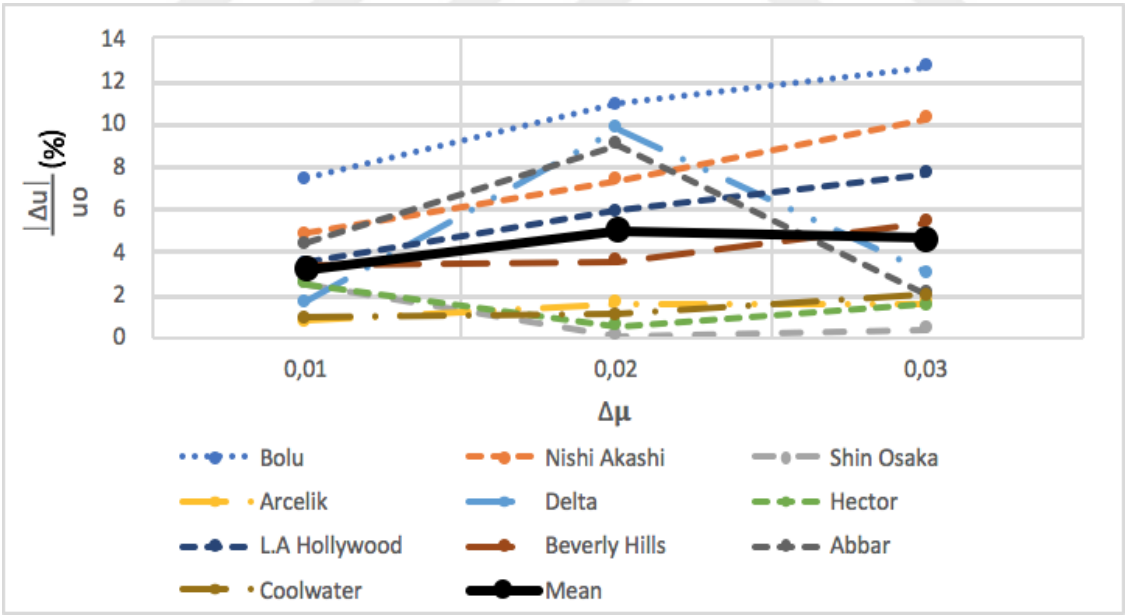

Figure 4.119: Far-Field Configuration B Case 1

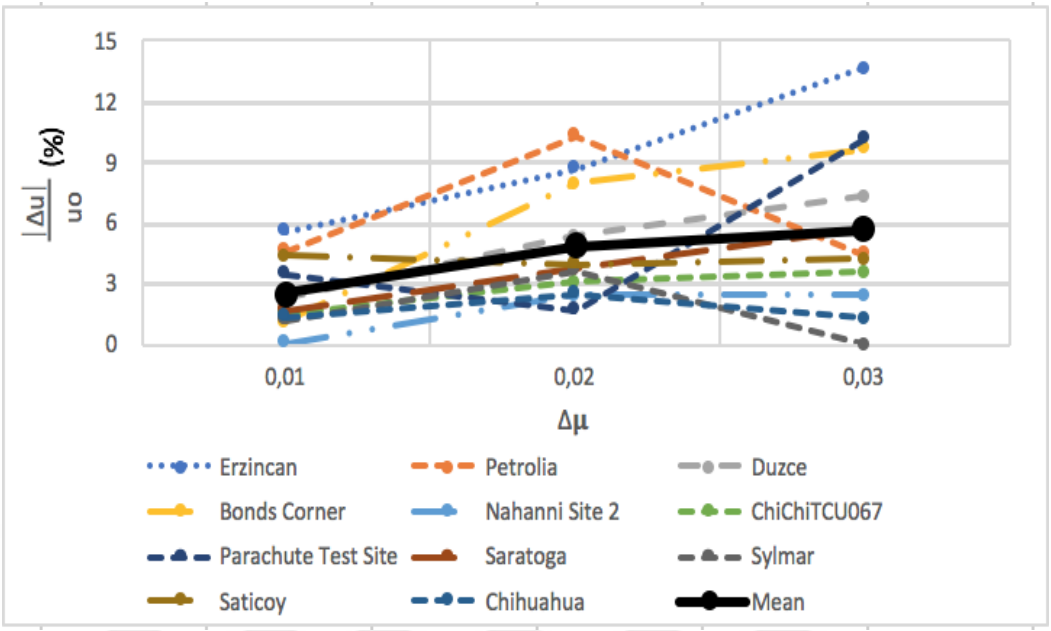

Figure 4.120: Near-Field Configuration B Case 1

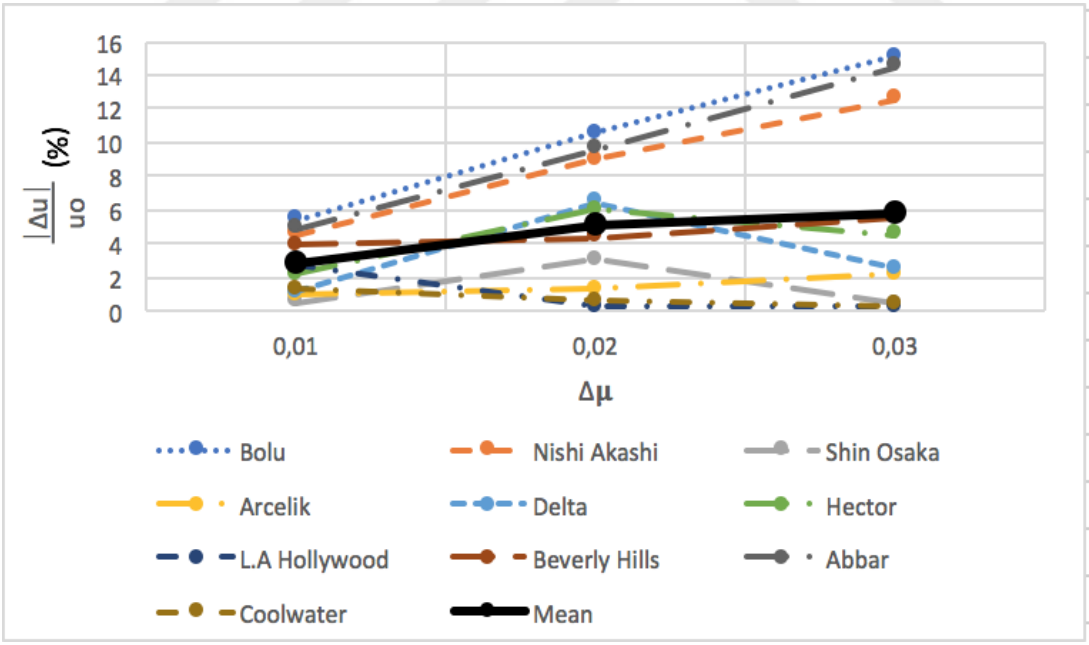

Figure 4.121: Far-Field Configuration B Case 2

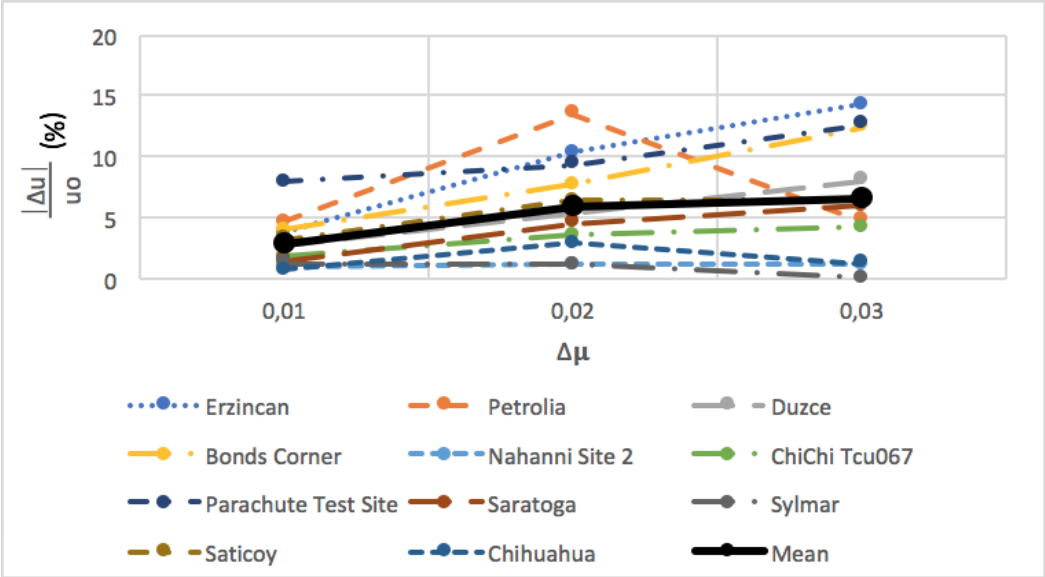

Figure 4.122: Near-Field Configuration B Case 2

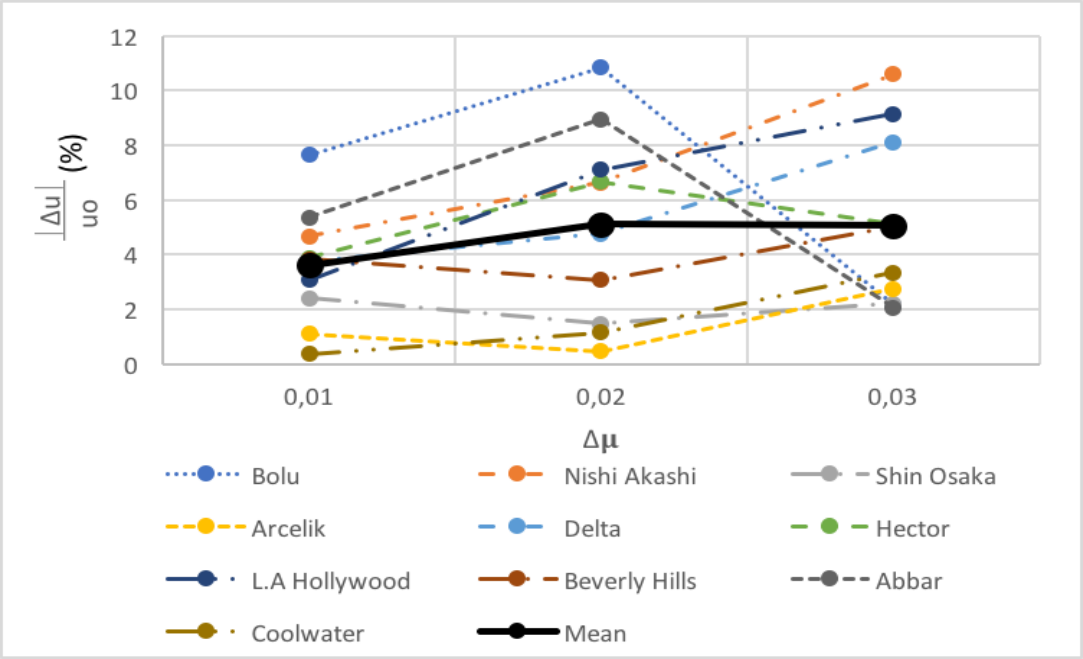

Figure 4.123: Far-Field Configuration B Case 3

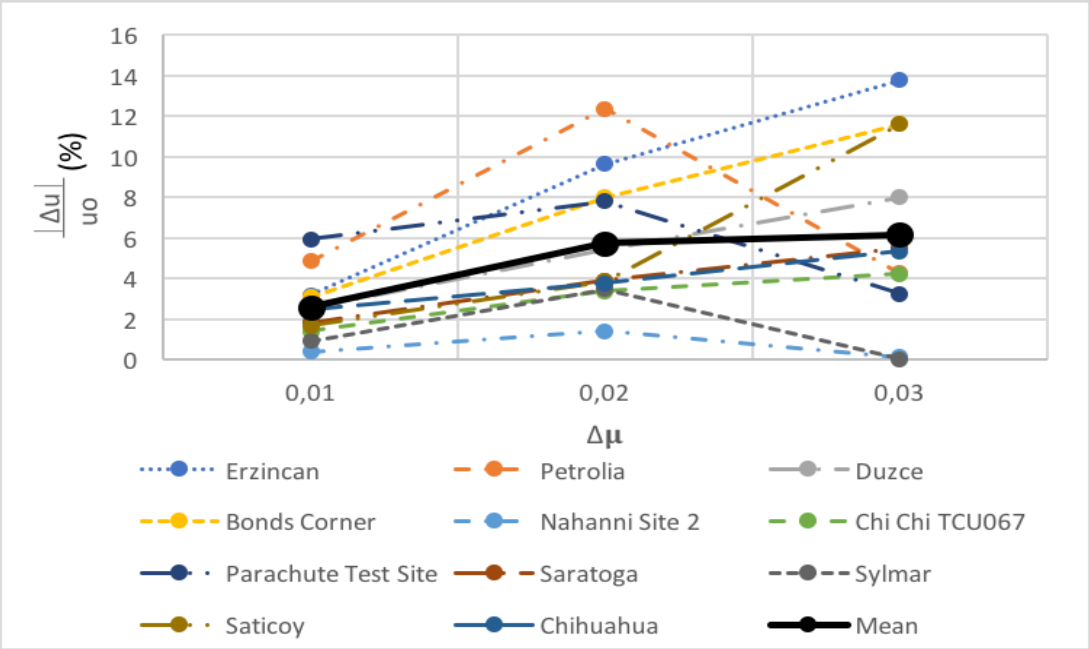

Figure 4.124: Near-Field Configuration B Case 3

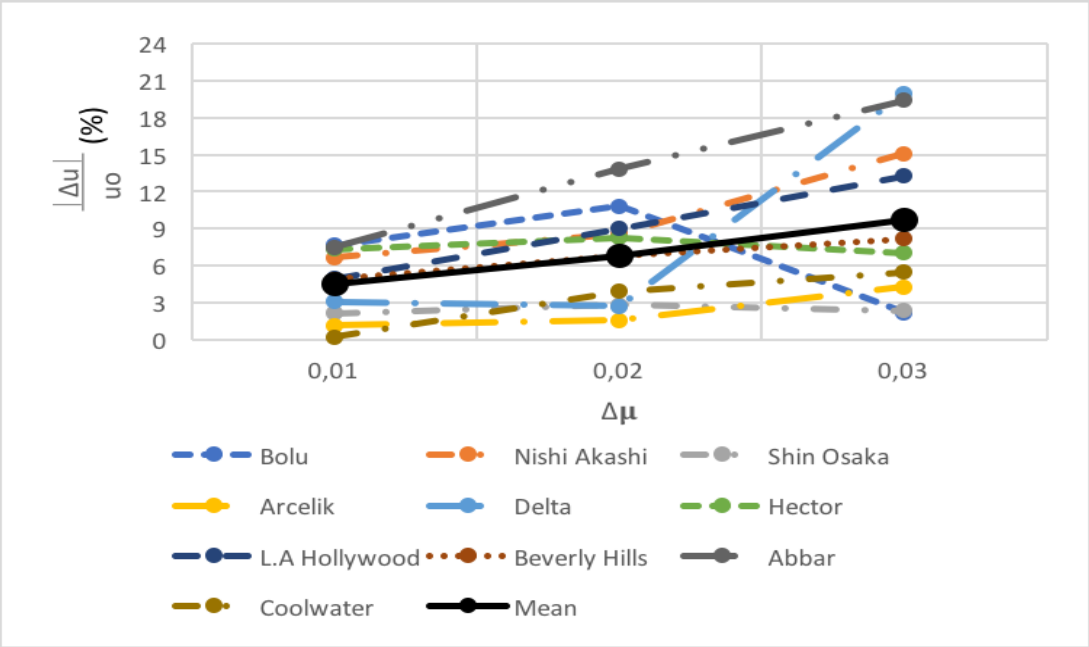

Figure 4.125: Far-Field Configuration B Case 4

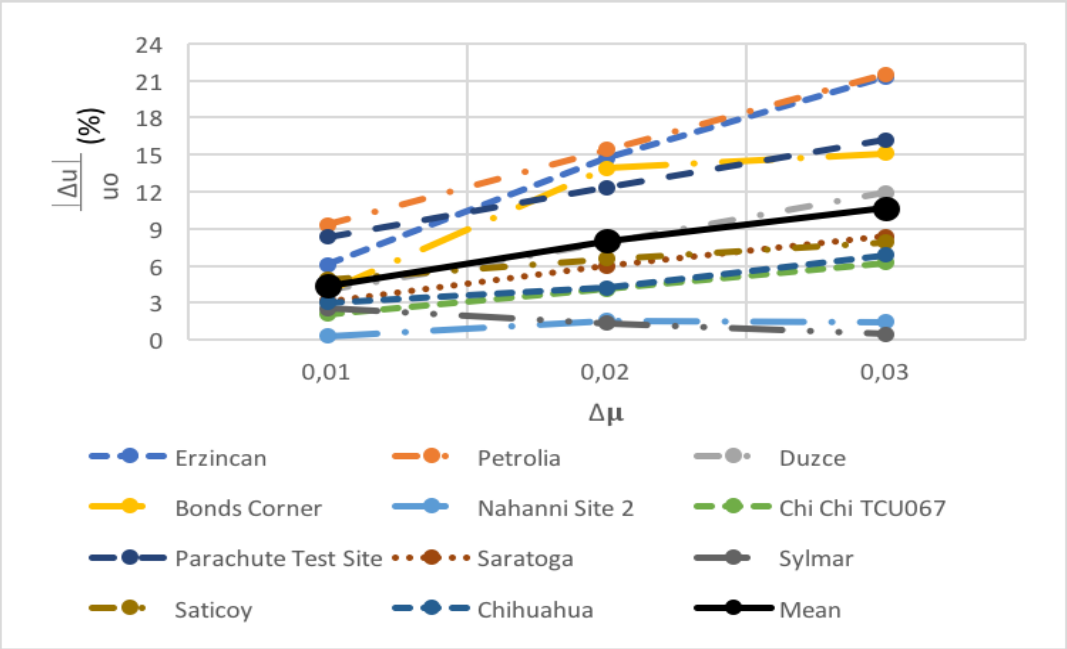

Figure 4.126: Near-Field Configuration B Case 4

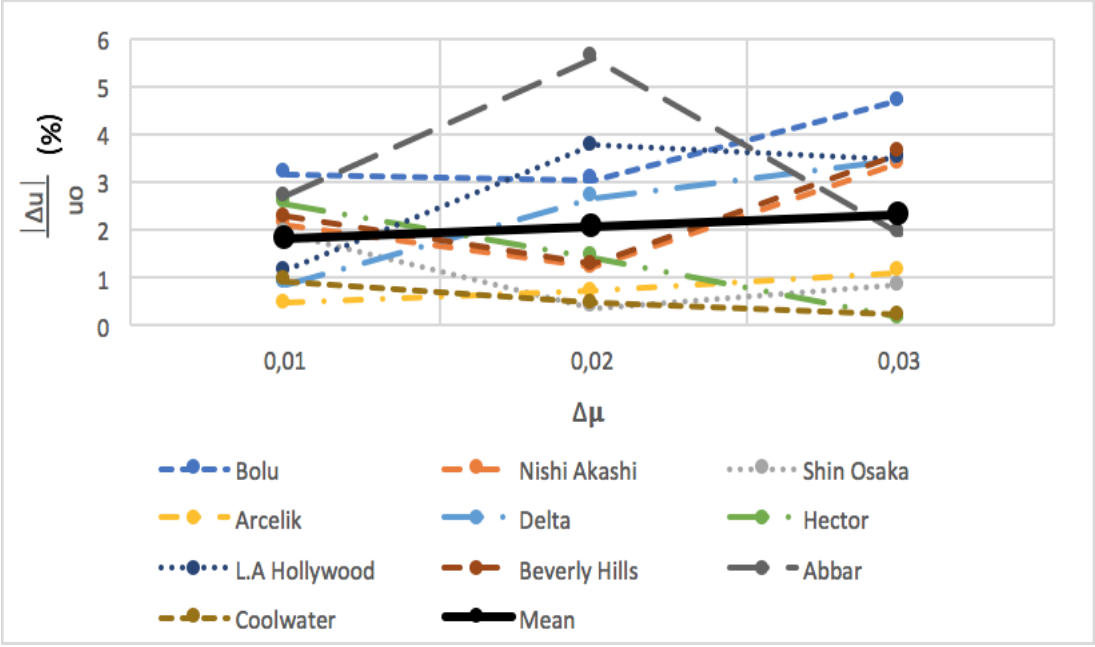

Figure 4.127: Far-Field Configuration B Case 5

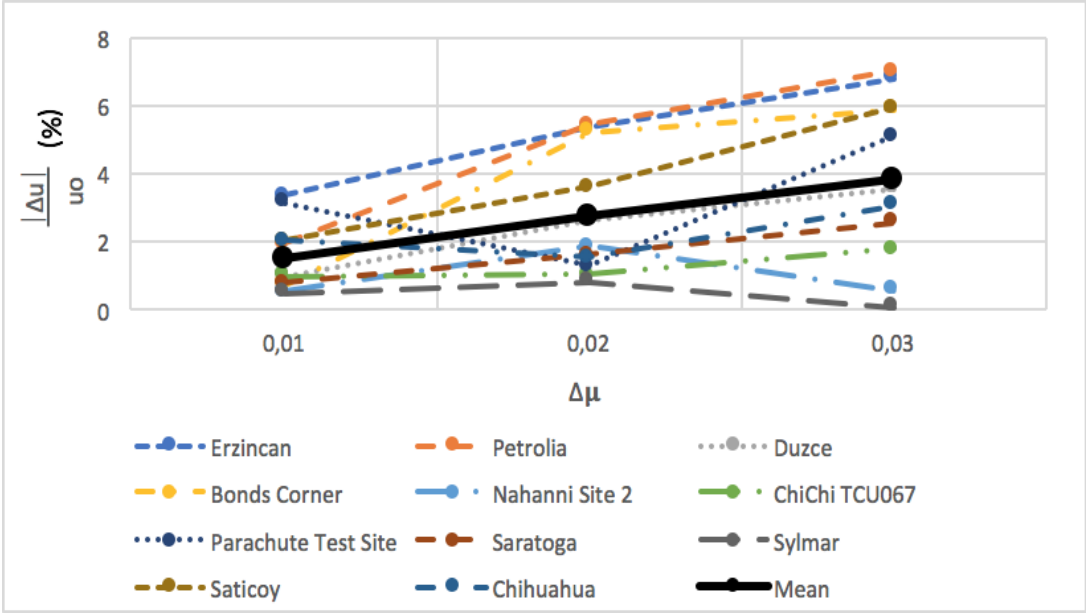

Figure 4.128: Near-Field Configuration B Case 5

CHAPTER 5

SUMMARY AND CONCLUSION

5.1 Summary and Conclusion.

In this thesis, the effect of seismic isolators in buildings and their advantages in comparison to the classic fixed based buildings are shown and discussed. The ideology behind seismic isolation, it is types used in structural engineering application and mechanical behaviour were reviewed. Moreover, the design and mathematical formulation are mentioned and explained. Furthermore, fixed and isolated building model with 10% probability of being exceeded in 50 years or 475-year return period was analysed with equivalent lateral method and time history analysis under ten (10) far-field and eleven (11) near-field ground motions. The analyses performed conclude that;

- The seismic isolation lateral equivalent method story forces distribution for both TSC2019 and ASCE 7-16 are linearly distributed. The absolute maximum floor acceleration values obtained from time history analyses of model structure were almost constant at each floor.

- Seismic isolation system performed well under earthquake. The reduction reached up to 95% in acceleration, 96% in story shear and inter-story drifts in analysed ground motions. Furthermore, absolute maximum acceleration did not exceed 0.3g and within the elements non-damage limit. On average, far-field ground motions reduce further 2% of base shear and 3% more inter-story drift in comparison to near-field ground motions

- Variation of outer surface 1 coefficient of friction on base shear shows increase in friction reduces the base shear. Outer surface 4 friction increment showed increase in base shear. Furthermore, inner surface friction change yields minor effect on base shear. Structural

displacement in all surfaces generally showed significant decrease when the friction coefficient is increased.

- Non-uniform contamination of the bearings in a seismic isolation system can cause torsional effects, which result in an increase in the estimated bearing displacements. Of the cases examined in this study, the case where all the bearings on the outer row were contaminated more than the remaining isolators produced the most unfavorable results. It was also observed that this effect was more pronounced in the case of near field motions.

References

[1] F. Naeim and J. M. Kelly, *Design of Seismic Isolated Structures: From Theory to Practice*, vol. 16, no. 3. 2000.

[2] P. Erformance, I. Aiken, and D. Ph, "No Title," no. March, pp. 10–13, 2012.

[3] "Earthquake in Turkey Article, Tectonics Information, Earthquake Facts -- National Geographic." [Online]. Available: https://www.nationalgeographic.com/science/earth/the-dynamic-earth/anatolian-fault/.

[4] "protamuhendislik." [Online]. Available: http://protamuhendislik.com.tr/EN/service/base-isolated-structures/projects.

[5] O. Gunes, "Case Studies in Construction Materials Turkey ' s grand challenge : Disaster-proof building inventory within 20 years §," *Case Stud. Constr. Mater.*, vol. 2, pp. 18–34, 2015.

[6] "İstanbul atatürk havalimani diş hatlar terminali," 2001.

[7] U. Akyuz, A. Caner, and A. Yakut, "A Comparative Study on Seismic Isolation Applications in Turkey," 2017, no. Asce 2010.

[8] C. Ozkaya, N. Celebi, and F. Tulumtas, "Hybrid seismic isolation design of Sakarya-II Viaduct in the proximity of the North Anatolian Fault," pp. 2391–2396, 2010.

[9] J. Kubin, D. Kubin, A. Özmen, O. B. Şadan, and E. Eroğlu, "Seismic Isolated Hospital Design Practice in Turkey : Erzurum Medical Campus."

[10] C. Yilmaz, E. Booth, and C. Sketchley, "(a joint event of the 13 th ECEE & 30 th General Assembly of the ESC) Paper Number : 1259 RETROFIT OF ANTALYA AIRPORT INTERNATIONAL TERMINAL BUILDING , TURKEY USING SEISMIC ISOLATION," 2006, no. September, pp. 3–8.

[11] "The 10 Largest Base-Isolated Buildings in the World | 2017-07-17 | ENR." [Online]. Available: https://www.enr.com/articles/42366-the-10-largest-base-isolated-buildings-in-the-world.

[12] A. D. N. P. P. P. Sa, “Adana Entegre Sağlık Kampü s ü Projesi Çevre sel ve Sosyal Etki Değerlendirmesi Teknik Olmayan Özet (TOÖ) Nihai ÇSED,” Adana, Turkey, 2014.

[13] U. Akyüz, A. Caner, A. Yakut, and S. Ozdemir, “TÜRKİYE ’ DEKİ SİSMİK İZOLASYON UYGULAMALARININ İNCELENMESİ INVESTIGATION ON SEISMIC ISOLATION APPLICATIONS IN TURKEY,” 2017, pp. 1–6.

[14] “Isparta City Hospital.” [Online]. Available: https://ispartasehir.saglik.gov.tr/EN,201189/isparta-city-hospital.html.

[15] H. Darama, “Implementation of Seismic Isolation in Turkey for Continued Functionality Implementation of Seismic Isolation in Turkey for Continued Functionality,” 2015, no. August.

[16] F. Devices, L. Augusto, and D. Osorio, “Optimization of Base Isolation Systems Using Low Cost,” 2001.

[17] M. Efiloglu, “Understanding the concept of base isolation,” 2013.

[18] O. Avsar, A. Yakut, and P. Gulkan, “Influence Of Seismic Isolation Level On A Building Response,” in *14th World Conference on Earthquake Engineering (14WCEE)*, 2008.

[19] N. Torunbalci and G. Ozpalanlar, “Earthquake Response Analysis of Mid-Story Buildings Isolated With Various Seismic Isolation Techniques Abstract :,” 2008.

[20] M. C. Constantinou, A. S. Whittaker, Y. Kalpakidis, D. M. Fenz, and G. P. Warn, *Performance of Seismic Isolation Hardware under Service and Seismic Loading - Technical Report MCEER-07-0012*. 2007.

[21] Seda Özdemir, “Investigation Of Seismic Isolation Efficiency For Building Structures(2016),” 2016.

[22] G. P. Warn and K. L. Ryan, “A Review of Seismic Isolation for Buildings: Historical Development and Research Needs,” *Buildings*, vol. 2, no. 4, pp. 300–325, 2012.

[23] A. Islam, M. Jameel, M. a Uddin, and S. I. Ahmad, “Simplified design guidelines for seismic base isolation in multi-storey buildings for Bangladesh National Building Code (BNBC),” *Int. J. Phys. Sci*, vol. 6, no. 23, pp. 5467–5486, 2011.

[24] A. Ezazi, “Dual Isolation for Enhanced Seismic Protection,” 2015.

[25] E. D. Wolff C. Ipek M. C. Constantinou and M. Tapan, “Effect of viscous damping devices on the response of seismically isolated structures,” no. July 2014, pp. 185–198, 2014.

[26] D. E. Nassani and M. W. Abdulmajeed, “Seismic Base Isolation in Reinforced Concrete Structures,” *Int. J. Res. Stud. Sci. Eng. Technol.*, vol. 2, no. 2, pp. 1–13, 2015.

[27] C. P. Ã. Providakis, “Effect of supplemental damping on LRB and FPS seismic isolators under near-fault ground motions,” vol. 29, pp. 80–90, 2009.

[28] F. Mazza, M. Mazza, and A. Vulcano, “Base-isolation systems for the seismic retro fi tting of r . c . framed buildings with soft-storey subjected to near-fault earthquakes,” *Soil Dyn. Earthq. Eng.*, vol. 109, no. February, pp. 209–221, 2018.

[29] C. Alhan and S. Öncü-davas, “Performance limits of seismically isolated buildings under near-field earthquakes,” *Eng. Struct.*, vol. 116, pp. 83–94, 2016.

[30] E. C. ALEMDAĞ, “a New Method To Increase Effectiveness of Base Isolation on,” 2016.

[31] M. Han, “Application of Base Isolation Systems To Reinforced Concrete,” 2017.

[32] C. S. Tsai, T. Chiang, and B. Chen, “Experimental Study for Multiple Friction Pendulum System,” in *13 th World Conference on Earthquake Engineering*, 2004, no. 669, p. 12.

[33] S. Arathy and P. M. Manju, “Analysis of friction pendulum bearing isolated structure,” pp. 317–322, 2016.

[34] F. Weber, J. Distl, and C. Braun, “Isolation Performance Assessment of Adaptive Behaviour of Triple Friction Pendulum,” *J. Civ. Eng. Res.*, vol. 7, no. 1, pp. 17–33, 2017.

[35] M. R. Marsico, “Seismic isolation and energy dissipation.”

[36] J. M. Kelly, “Base isolation: linear theory and design, J. Earthquake Spectra, 6, 223-244,” 1990.

[37] H. H. N. and J. L. Tassoulas., “Directional Effects of Shear Combined with Compression on Bridge Elastomeric Bearings.,” 2009.

[38] “Seismic Isolatotors.” 2016.

[39] T. C. Becker, “Advanced Modeling of the Performance of Structures Supported on Triple Friction Pendulum Bearings,” 2011.

[40] Opensees, “Flat Fricition Slider.” [Online]. Available: http://opensees.berkeley.edu/wiki/index.php/Flat_Slider_Bearing_Element.

[41] D. M. Fenz and M. C. Constantinou, *Mechanical Behavior of Multi-Spherical by*. 2008.

[42] D. Fenz and M. C. Constantinou, *Development, implementation and verification of dynamic analysis models for multi-spherical sliding bearings : Technical Report MCEER-08-0018*. 2008.

[43] H. Moeindarbari, “Optimum Design of Triple Friction Pendulum Bearing Subjected by Near-Field Ground Motions,” in *15th World Conference on Earthquake Engineering (15WCEE)*, 2012.

[44] P. M. Calvi and G. M. Calvi, “Historical development of friction-based seismic isolation systems,” *Soil Dyn. Earthq. Eng.*, vol. 106, no. August, pp. 14–30, 2017.

[45] G. M. Calvi *et al.*, *Seismic bridge design and retrofit – structural solutions*. 2007.

[46] J. E. Long, “The Performance of PTFE in Bridge Bearings.,” *Civ. Eng. Public Work. Rev.*, pp. 459–462, 1969.

[47] M. J. Campbell, T. I. and Fatemi, “Further Laboratory Studies of Friction in TFE Slide Surface of a Bridge Bearing.,” 1989.

[48] R. L. Mayes and D. Ph, “Chapter 14 Design of Structures with Seismic Isolation,” in *Design*, 2000.

[49] B. Sciences, *2003 Edition NEHRP RECOMMENDED PROVISIONS FOR SEISMIC REGULATIONS FOR NEW BUILDINGS AND OTHER STRUCTURES (FEMA 450)*, no. Fema 450. 2003.

[50] C. a Kircher and D. Ph, "Seismically Isolated Structures," in *FEMA P-751, NEHRP Recommended Provisions: Design Examples*, 2009, pp. 1–64.

[51] M. D. Loads and O. Structures, *Minimum Design Loads and Associated Criteria for Buildings and Other Structures*. .

[52] N. A. Deprem, D. Madde, U. Hayata, and A. Dolay, *DEPREM ETKİSİ ALTINDA BİNALARIN TASARIMI İÇİN ESASLAR*, vol. 30364, no. 1. 2018.

[53] ASCE, *Asce/Sei 7-05*. 2010.

[54] National Institute of Building Sciences, *Earthquake-Resistant Design Concepts, An Introduction to the NEHRP Recommended Seismic Provisions for New Buildings and Other Structures*, no. December. 2010.

[55] D. Mishne, *Formation control of satellites subject to drag variations and J(2) perturbations*, vol. 27, no. 4. 2004.

[56] I. W. Sengara, "Investigation on Risk-Targeted Seismic Design Criteria for a High-rise Building in Jakarta-Indonesia," in *15th World Conference on Earthquake Engineering (15WCEE)*, 2012.

[57] M. Malekzadeh and T. Taghikhany, "Multi-Stage Performance of Seismically Isolated Bridge Using Triple Pendulum Bearings," *Adv. Struct. Eng.*, vol. 15, no. 7, pp. 1181–1196, 2012.

[58] LATBSDC, *"An Alternative Procedure for Seismic Analysis and Design of Tall Buildings Located in the Los Angeles Region. Los Angeles, CA"*. 2014.

[59] A. Sei, *ASCE 7-12. Minimum Design Loads for Buildings and Other Structures. American Society of Civil Engineers. Reston,VA. 2016*. 2012.

[60] A. Zekioglu, H. Darama, and B. Erkus, "Performance-Based Seismic Design of a Large Seismically Isolated Structure : Istanbul Sabiha Gökçen International Airport Terminal Building," in *Building*, 2007, no. November, pp. 409–427.

[61] G. Mosqueda, A. S. Whittaker, and G. L. Fenves, “Characterization and Modeling of Friction Pendulum Bearings Subjected to Characterization and Modeling of Friction Pendulum Bearings Subjected to Multiple Components of Excitation,” vol. 9445, no. March, 2004.

[62] A. A. Sarlis and M. C. Constantinou, *Model of Triple Friction Pendulum Bearing for General Geometric and Frictional Parameters and for Uplift Conditions by*. 2013.

[63] M. C. Constantinou, I. Kalpakidis, A. Filiatrault, and R. A. E. Lay, *LRFD-Based Analysis and Design Procedures for Bridge Bearings and Seismic Isolators by*, no. 65. 2011.

[64] D. M. Fenz and M. C. Constantinou, “Modeling triple friction pendulum bearings for response-history analysis,” *Earthq. Spectra*, vol. 24, no. 4, pp. 1011–1028, 2008.

[65] N. A. Deprem, D. Madde, U. Hayata, and A. Dolay, “Resmî Gazete,” vol. 30364, no. 1, 2018.

[66] F. P. June *et al.*, “Quanti fi cation of Building Seismic Performance Factors,” no. June, 2009.

[67] S. Engineering, I. I. A. M. Kaynia, and E. E. Erduran, “Thesis.”

[68] A. Fathieh, “Nonlinear Dynamic Analysis of Modular Steel Buildings in Two and Three Dimensions,” 2013.

[69] N. Gcr, *Selecting and Scaling Earthquake Ground Motions for Performing Analyses*. .

[70] M. Malekzadeh and T. Taghikhany, “Multi-Stage Performance of Seismically Isolated Bridge Using Triple Pendulum Bearings,” no. June 2015, 2012.

[71] F. Weber, H. Distl, and C. Braun, “Isolation Performance of Optimized Triple Friction Pendulum,” vol. 5, no. 12, pp. 55–69, 2016.

APPENDIX A

PRELIMINARY DESIGN CALCULATION OF A TRIPLE FRICTION PENDULUM BEARING

This preliminary design is based on the guidelines presented in [60] [63] [71].

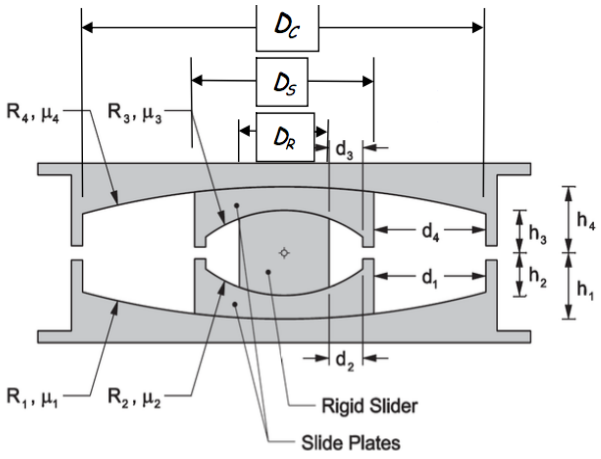

Figure A.1: Triple Friction Pendulum Parameters [63]

The design of triple friction bearing is mainly characterized by the effective outer radii R_{eff1} and R_{eff4}. In general, pendulum bearings period ranges from 3s-4s, also the coefficient of friction ranges between 0.01-0.12 in most researches. Furthermore, economically, the displacement capacity of FP bearings should at most be about 20% of the effective radius of curvature[63].

Let the design period T = 3.6s and $\boldsymbol{R_{eff1}} = \boldsymbol{R_{eff4}}$.

$$3.6 = 2 \times 3.14\sqrt{\frac{(R)}{9.81}}$$

$$R = 3.23m$$

$$R_{eff1} = R_{eff4} = \frac{1}{2} \text{ x } 3.23\text{m} = 1.62\text{m}$$

I. Effective Stiffness K_{eff}.

Based on Spectrum in Figure 3.3 and equation (2-8) the D_D= 0.421m

Let D_D < 20% R as advised.

lower bound friction μ = 0.05 and upper bound friction μ = 0.1.

Lower bound

$$K_{eff} = \frac{W}{R} + \frac{\mu W}{D_D} = \frac{821.201}{3.23} + \frac{0.05 \text{x} 821.201}{(0.421)} = 351.772 \text{ KN/m}$$

Upper bound

$$K_{eff} = \frac{W}{R} + \frac{\mu W}{D_D} = \frac{821.201}{3.23} + \frac{0.1 \text{x} 821.201}{(0.421)} = 449.301 \text{ KN/m}$$

II. Effective Period

Lower bound

$$T_{eff} = 2\pi \sqrt{\frac{W}{g K_{eff}}} = 2 \text{ x } 3.14 \sqrt{\frac{821.201}{9.81 \text{ x } 351.772}} = 3.1\text{s}$$

Upper bound

$$T_{eff} = 2 \text{ x } 3.14 \sqrt{\frac{821.201}{9.81 \text{ x } 449.301}} = 2.7\text{s}$$

III. Effective Damping

Lower bound

Energy dissipation per force-displacement circle:

$$\text{EDC} = 4\mu W D_D = 4 \text{ x } 0.05 \text{ x } 821.201 \text{ x } 0.421 = 69.145 \text{ KN.m}$$

$$\beta = \frac{EDC}{2\pi K_{eff} D_D^2} = \frac{69.145}{2 \text{ x } 3.14 \text{ x } 351.772 \text{ x } 0.421^2} = 0.177$$

Upper bound

Energy dissipation per force-displacement circle:

$$EDC = 4\mu W D_D = 4 \text{ x } 0.1 \text{ x } 821.201 \text{ x } 0.421 = 138.290 \text{ KN.m}$$

$$\beta = \frac{EDC}{2\pi K_{eff} D_D^2} = \frac{138.290}{2 \text{ x } 3.14 \text{ x } 449.301 \text{ x } 0.421^2} = 0.277$$

IV. Damping reduction factor

Lower bound

$$B_D = \left(\frac{\beta}{0.05}\right)^{0.3} = \left(\frac{0.177}{0.05}\right)^{0.3} = 1.461$$

Upper bound

$$B_D = \left(\frac{\beta}{0.05}\right)^{0.3} = \left(\frac{0.277}{0.05}\right)^{0.3} = 1.671$$

V. Response Spectrum Design Displacement Correction.

Sae values are according to spectrum in Figure 3.3.

Lower bound

Sa = $\frac{Sae}{B_D} = \frac{0.17g}{1.461}$ = 0.116g

Sd = $(\frac{T_{eff}}{2\pi})^2$ x Sa = $(\frac{3.1}{2 \text{ x } 3.14})^2$ x 0.116 x 9.81 m/s2 = 0.277m

Amplify Sd by 1.3

Sd = 0.277 x 1.3 = 0.36m

Add component in the orthogonal direction

Sd = $(\sqrt{(0.3 \text{ x } 0.36)^2 + 0.36^2})$ = 0.38m

Upper bound

Sa = $\frac{Sae}{B_D} = \frac{0.18g}{1.671}$ = 0.108g

Sd = $(\frac{T_{eff}}{2\pi})^2$ x Sa = $(\frac{2.7}{2 \text{ x } 3.14})^2$ x 0.108 x 9.81 m/s2 = 0.20m

Amplify Sd by 1.3

Sd = 0.20 x 1.3 = 0.26m

Add component in the orthogonal direction

Sd = $(\sqrt{(0.3 \text{ x } 0.26)^2 + 0.26^2})$ = 0.27m

VI. Maximum Displacement for 20% Response Spectrum

Lower bound

Sm = 1.5 x Sd = 1.5 x 0.38 = 0.57m

Upper bound

Sm = 1.5 x Sd = 1.5 x 0.27 = 0.41

Configuration: Reff1 = Reff4, Reff2 = Reff3, h1 = h4, h2 =h3.

It should be noted that Triple Friction Pendulum bearings are considerably more complicated than standard Friction Pendulum bearings and additional checks must conducted to ensure their stability.Table.A1 presents the parameters used for heights and the inner radius varies according to the triple friction pendulum overall sizes reported in literature. The ratio of Inner radius to outer radius range from 12-28% while the ratio of the outer radius to the height of the outer surface plate ranges between 4-9%. Furthermore, height between the articulate slider and the midpoint of the inner and the outer surface ratio vary between 50-75%. The inner radius and heights are matched to the isolator having similar parametric value as the designed isolator.

Table A.1: Triple Friction Pendulum Dimensions

Isolator Parameters	Reff1 (m)	Reff2 (m)	h1 (m)	h2 (m)	(Reff2/Reff1) x 100%	(h1/Reff1) x 100%	(h1/h2.) x 100%
Sarkisian.M, M.Constantinou (2012)	3.81	0.9906	0.1524	0.0762	26.0	4	50
F.Fadi, M.Constantinou (2010)	1.499	0.356	–	–	23.7	–	–
	2.085	0.3	–	–	14.4	–	–
	3.823	0.902	–	–	23.6	–	–

Table A.1 continued

D.Fenz,M.Constantinou (2008)	0.435	0.053	–	–	12.2	–	–
F.weber, J.Distl (2017)	0.435	0.053	0.038	0.023	12.2	8.7	60.5
H. Moeindarbari, T.Taghikhany (2012)	0.435	0.053	–	–	12.2	–	–
H.Darama, B.Erkus (2014)	2.0701	0.2921	0.1651	0.1143	14.1	8.0	69.2
M.Dhakot, D.soni (2016)	0.81	0.18	–	–	22.2	–	–
M.Malekzadeh, T.Taghikany (2012)	0.81	0.18	–	–	22.2	–	–
	1.62	0.405	–	–	27.8	–	–
M. C. Constantinou, I. Kalpakidis (2011)	2.1336	0.3302	0.1016	0.0762	15.5	4.8	75